



HAL
open science

Les systèmes eau-gaz-sels : modélisation des équilibres de phases et application aux fluides géologiques

Régis Thiéry

► **To cite this version:**

Régis Thiéry. Les systèmes eau-gaz-sels : modélisation des équilibres de phases et application aux fluides géologiques. Sciences de la Terre. Institut National Polytechnique de Lorraine, 1996. Français. NNT : 1996INPL089N . tel-01776385

HAL Id: tel-01776385

<https://hal.univ-lorraine.fr/tel-01776385v1>

Submitted on 24 Apr 2018

HAL is a multi-disciplinary open access archive for the deposit and dissemination of scientific research documents, whether they are published or not. The documents may come from teaching and research institutions in France or abroad, or from public or private research centers.

L'archive ouverte pluridisciplinaire **HAL**, est destinée au dépôt et à la diffusion de documents scientifiques de niveau recherche, publiés ou non, émanant des établissements d'enseignement et de recherche français ou étrangers, des laboratoires publics ou privés.



AVERTISSEMENT

Ce document est le fruit d'un long travail approuvé par le jury de soutenance et mis à disposition de l'ensemble de la communauté universitaire élargie.

Il est soumis à la propriété intellectuelle de l'auteur. Ceci implique une obligation de citation et de référencement lors de l'utilisation de ce document.

D'autre part, toute contrefaçon, plagiat, reproduction illicite encourt une poursuite pénale.

Contact : ddoc-theses-contact@univ-lorraine.fr

LIENS

Code de la Propriété Intellectuelle. articles L 122. 4

Code de la Propriété Intellectuelle. articles L 335.2- L 335.10

http://www.cfcopies.com/V2/leg/leg_droi.php

<http://www.culture.gouv.fr/culture/infos-pratiques/droits/protection.htm>

[M] 1996 THIÉRY, R.

INSTITUT NATIONAL
POLYTECHNIQUE DE LORRAINE

CENTRE DE RECHERCHES
SUR LA GÉOLOGIE DES
MATIÈRES PREMIÈRES
MINÉRALES ET ÉNERGÉTIQUES
GDR CNRS 077.

THÈSE PRÉSENTÉE À

L'INSTITUT NATIONAL POLYTECHNIQUE DE
LORRAINE

Pour l'obtention du titre de

DOCTEUR DE L'INSTITUT NATIONAL
POLYTECHNIQUE DE LORRAINE

EN "GÉOSCIENCES ET MATIÈRES PREMIÈRES"

Par

Régis THIÉRY

**LES SYSTÈMES EAU-GAZ-SELS.
MODÉLISATION DES ÉQUILIBRES DE PHASES
ET
APPLICATION AUX FLUIDES GÉOLOGIQUES.**

Soutenue publiquement le jeudi 12 septembre 1996
devant la Commission d'Examen :

Membres du Jury

MM. B. POTY	Directeur de recherches au CNRS	Président
J. DUBESSY	Directeur de recherches au CNRS	Directeur de Thèse
C. MONNIN	Chargé de recherches au CNRS	Rapporteur
F. MONTEL	Ingénieur de recherches à EAP	Rapporteur
B. YARDLEY	Professeur, Université de Leeds,	Rapporteur
E.U. FRANCK	Professeur, Université de Karlsruhe	Examineur
M. MAZUR	Professeur, Université d'Odessa	Examineur
J-P. SIMONIN	Chargé de recherches, Université de Paris VI	Examineur

Service Commun de la Documentation
INPL
Nancy-Brabois

AVANT-PROPOS

Ce travail a été réalisé au CREGU (Centre de Recherches sur la Géologie des Matières Premières Minérales et Énergétiques) avec le soutien financier du CNRS et de la société EAP, représentée par M. François Montel que je remercie tout particulièrement.

Je tiens à remercier M. Bernard Poty, qui m'a accueilli au CREGU et a accepté de présider le jury de thèse; et M. Jean Dubessy, mon directeur de thèse, qui a encadré ces recherches et sans qui rien n'aurait été fait.

Je tiens à remercier également MM. J. Vidal, A.M. van den Kerkhof et S.N. Lvov pour leur aide sur le système $CO_2-N_2-CH_4$ et le modèle MSA.

Enfin, je voudrais remercier l'ensemble du personnel du CREGU pour m'avoir apporté leur compétences et leur soutien tout au cours de ces travaux.

SOMMAIRE

Résumé.....	5
Abstract.....	6
Introduction.....	7
Chapitre 1. Une nouvelle librairie pour calculer analytiquement les propriétés thermodynamiques des fluides avec les équations d'état.....	16
• Résumé.....	17
• A new object-oriented library for calculating analytically high-order multivariable derivatives and thermodynamic properties of fluids with equations of state.....	19
Chapitre 2. La modélisation des équilibres de phases dans le système CO₂- CH₄-N₂ et application aux inclusions fluides.....	34
• Résumé.....	35
• Phase equilibria modelling applied to fluid inclusions: liquid-vapour equilibria and calculation of the molar volume in the CO ₂ -CH ₄ -N ₂ system.....	37
• Improved modelling of vapour-liquid equilibria up to the critical region. Application to the CO ₂ -CH ₄ -N ₂ system.....	47
• v-X properties of CH ₄ -CO ₂ and CO ₂ -N ₂ fluid inclusions: modelling for T < 31°C and P < 400 bars.....	60
Chapitre 3. Les équilibres de phases fluides dans le système ion-dipôle par un modèle MSA.....	79

• Résumé.....	80
• The global phase diagram of the ion-dipole mixture in the MSA.....	81
Chapitre 4. La modélisation des équilibres liquide-vapeur dans le système H ₂ O-NaCl à l'aide du modèle ion-dipôle.....	90
• Résumé.....	127
• Description of vapour-liquid equilibria of the H ₂ O-NaCl system with a thermodynamic model based on the MSA.....	130
Chapitre 5. Les hydrates de gaz.....	175
• Résumé.....	176
• Modelling of phase equilibria involving mixed gas clathrates: application to the determination of molar volume of the vapour phase and salinity of the aqueous solution in fluid inclusions.....	179
• Geochemistry of gas hydrates and associated fluids in the sediments of a continental margin (ODP Leg 64).....	191
Conclusion.	224

RÉSUMÉ

Les équilibres de phases dans les systèmes eau-gaz-sels et sous-systèmes associés jouent un rôle central en géochimie. Le développement d'un outil de calcul et trois applications de la modélisation thermodynamique de ces systèmes à partir des équations d'état font l'objet de cette thèse.

Le développement d'une **équation d'état à partir d'un modèle physique** passe toujours par une étape de calcul formel des fonctions thermodynamiques qui peut être fastidieuse pour les modèles complexes. C'est pourquoi, une **nouvelle méthode de calcul et de programmation** est proposée facilitant le calcul des fonctions thermodynamiques, des courbes critiques, des points tricritiques, des équilibres liquide-gaz et liquide-liquide-gaz, à partir de l'expression de l'énergie de Helmholtz.

La première application est le calcul des **équilibres de phases** liquide-gaz, solide-liquide, solide-liquide-gaz à basse température ($-180^{\circ}\text{C} < T < 31^{\circ}\text{C}$) dans le système **CO₂-CH₄-N₂** à l'aide d'une équation d'état cubique. L'introduction de deux paramètres d'interactions binaires ajustés hors zone critique et le long de la courbe critique a permis d'**améliorer sensiblement la reproduction des pressions dans le domaine critique**. Associé à un modèle de calcul de densité basé sur la méthode des états correspondants à trois paramètres, le modèle de Lee et Kessler (1975), les **projections volume molaire-composition** ont été construites pour chaque système binaire pour les besoins des analyses des inclusions fluides.

La deuxième application concerne la modélisation des **équilibres liquide-gaz des systèmes électrolytiques** à haute température ($100^{\circ}\text{C} < T < 700^{\circ}\text{C}$). Le modèle utilisé est celui de Lvov développé à partir de la théorie "**Approximation en champ sphérique moyen**" qui assimile le fluide à un mélange de dipôles et d'ions de tailles différentes. Dans une première étape, un diagramme de phases global a été établi afin de déterminer l'influence des paramètres physiques (moment dipolaire, diamètre des ions et des dipôles) sur la topologie des diagrammes de phases, en ne considérant que les équilibres des phases fluides. Ainsi, il a été démontré que le modèle prédit les différentes topologies des systèmes électrolytiques.

Appliqué au système **H₂O-NaCl**, le modèle reproduit de manière satisfaisante les équilibres liquide-gaz à condition de prendre en compte la **formation de paires d'ions** à haute température ($T > 400^{\circ}\text{C}$) ou dans les phases de faible densité. Le faible nombre de paramètres ajustables (taille des ions et dipôle, valeur du dipôle et de la constante d'association), qui ont tous une signification physique, montre la puissance de ce modèle et en fait un bon candidat pour la formulation d'une équation d'état non empirique pour les fluides d'intérêt géologique.

La troisième application concerne les équilibres de phases dans les systèmes eau-gaz-sels impliquant les **clathrates de gaz** à basse température ($T < 30^{\circ}\text{C}$), qui se forment dans les **inclusions fluides** et dans les **sédiments des marges continentales**. Un **modèle de stabilité des clathrates de gaz** a été construit et un logiciel de calcul permet de déterminer la salinité des inclusions fluides et la densité de la phase vapeur. Ce logiciel ainsi que celui relatif au système CO₂-CH₄-N₂ (première application) ont été **intégrés à un programme informatique général de modélisation de toutes les transitions de phases possibles** de basses températures ($T < 31^{\circ}\text{C}$) observables lors des études microthermométriques des inclusions fluides du systèmes H₂O-NaCl-CO₂-CH₄-N₂.

La distribution des clathrates de gaz, la composition des clathrates et des phases fluides à méthane dominant, **ont été mesurées dans des échantillons provenant de sondages réalisés dans la marge continentale passive (Blake Outer Ridge, au large de la Caroline) lors de la campagne ODP (leg 164)**. Les clathrates ont été localisés entre 190 et 450 mètres sous le fond de l'océan et constituent 1 à 3 % du volume total des sédiments. **Le réflecteur sismique BSR représente l'interface entre une couche contenant des hydrates et une zone sous-jacente sursaturée en gaz**. La richesse en gaz de la couche inférieure est un paramètre sensible pour l'identification de l'interface par sismique. La modélisation thermodynamique prédit la profondeur de la limite de stabilité des clathrates 28 mètres sous le BSR pour le site 997. En revanche, pour le site 995, l'écart est de 86 mètres: s'agit-il d'erreurs dans la mesure des températures lors du sondage? La modélisation thermodynamique montre que **la richesse en méthane est un paramètre essentiel pour la formation des clathrates**. On montre aussi que les clathrates contrôlent pour partie l'évolution du rapport entre méthane, éthane et dioxyde de carbone. Enfin, leur présence diminue la perméabilité des sédiments, ce qui modifie sensiblement la circulation des fluides.

ABSTRACT

Phase equilibria in water-gas-salts systems and associated subsystems play a central role in geochemistry. A new tool for the thermodynamic calculations and three applications of the thermodynamic modelling of fluids with the help of equations of state are presented in this thesis.

The development of **an equation of state from a physical model** requires always a step of symbolic calculation of thermodynamic functions, that may be painful for complex models. This is the reason why **a new method of calculation and programming** is proposed, that facilitates the derivation of thermodynamic functions and calculations of critical curves, tricritical points, liquid-gas and liquid-liquid-gas equilibria from the expression of the Helmholtz free energy.

The first application is the calculation of liquid-gas, solid-liquid-gas, solid-liquid, and solid-gas **phase equilibria** at low temperatures ($-180^{\circ}\text{C} < T < 31^{\circ}\text{C}$) in the $\text{CO}_2\text{-CH}_4\text{-N}_2$ system with the help of a cubic equation of state. The introduction of two binary interaction parameters fitted respectively in the noncritical region and along the critical curve allows one to **improve significantly the reproduction of pressures in the critical region**. Associated with a density calculation model based on the three-parameters corresponding states principle (Lee and Kesler, 1975), **molar volume-composition projections** have been built for each binary system for the purposes of fluid inclusions analyses.

The second application is about the modelling of **liquid-gas phase equilibria of electrolytic systems** at high temperatures ($100^{\circ}\text{C} < T < 700^{\circ}\text{C}$). The model of Lvov for the ion-dipole mixture based on the **Mean Spherical Approximation** is used. To a first step, the global phase diagram has been built in order to determine the influence of physical parameters (dipole moment, ion and dipole diameters) on the topology of phase diagrams by considering only fluid phase equilibria. It has been demonstrated that the model predicts the different topologies of electrolytic systems.

Applied to the **H₂O-NaCl** system, the model reproduces satisfactorily liquid-gas phase equilibria if the **formation of ion pairs** is taken into account at high temperatures ($T > 400^{\circ}\text{C}$) or in the phases of low density. The small number of fitting parameters (sizes of the ions and dipoles, dipole moment and association constant) and their physical meaning show the power of the model. Therefore, the model is a good candidate for the formulation of a non-empirical equation of state for geologic fluids

The third application is about the phase equilibria in the water-gas-salts systems involving **gas hydrates** at low temperatures ($T < 30^{\circ}\text{C}$), that form in **fluid inclusions** and in **the sediments of continental margins**. A **stability model for gas hydrates** has been built and a calculation software has been written that allows the determination the bulk salinity and the density of the volatile part of fluid inclusions. This software as well the first one developed for the $\text{CO}_2\text{-CH}_4\text{-N}_2$ system (see above) have been gathered into a **general program for the interpretation of all phase transitions** that are observable during the microthermometric analyses of fluid inclusions at low temperatures in the $\text{H}_2\text{O-NaCl-CO}_2\text{-CH}_4\text{-N}_2$ system.

The distribution and composition of gas hydrates and associated fluid phases **have been measured in the samples that have been recovered during the drillings of a continental passive margin (Blake Outer Ridge, near the Carolina coast) during an ODP campaign (Leg 164)**. Gas hydrates have been localized between 190 and 450 meters below the sea bottom and represent one to three percent of the bulk volume of sediments. A **seismic reflector (the BSR) represents the interface between a gas hydrates-bearing layer and an underlying zone oversaturated in gas**. The gas quantity in this zone is a key parameter for the identification of this interface on seismic records. Thermodynamic modelling predicts that the deeper occurrence of gas hydrates should occur at 28 meters at Site 997, and 86 meters at Site 995 below the BSR. The large discrepancy observed at Site 997 may be due to errors of the in-situ temperature measurements. Thermodynamic modelling shows that **the amount of methane is a key parameter for the formation of gas hydrates**. Gas hydrates control partially the variations of the ratios between methane, ethane and carbon dioxide. Finally, their occurrence decreases the permeability of sediments, and thus modifies clearly the circulation of fluids.

INTRODUCTION

Introduction

L'importance des fluides eau-gaz-sels en géologie

Depuis longtemps, il est reconnu que les fluides jouent un rôle central dans de nombreux processus géologiques de la croûte. Les espèces chimiques les plus fréquemment rencontrées dans les fluides sont l'eau, les sels, les gaz (CO_2 , CH_4 , N_2 , ...) et les hydrocarbures. Entre la surface terrestre et l'interface croûte-manteau, les conditions de pression-température-composition sont extrêmement variées et d'importantes circulations de fluides prennent place dans la croûte. De nombreux échanges entre les fluides et les roches se produisent lors de ces circulations. Ainsi, par exemple, d'importantes quantités de volatiles (H_2O , CO_2 , ...) sont libérées (réactions de dévolatilisation) lors de l'enfouissement des roches dans des niveaux profonds (par exemple, lors d'une subduction de croûte océanique, ...). Dans les bassins sédimentaires et les marges continentales, de grandes quantités d'eau sont également expulsées lors de la compaction des roches; et du dioxyde de carbone et du méthane sont générés par les réactions biochimiques. De même, la matière organique enfouie occupe une part importante dans la génération de fluides. Sous l'action de réactions chimiques et biochimiques, elle se transforme en kérogène. Le kérogène est soumis à des températures et des pressions de plus en plus fortes lors de son enfouissement, conduisant à de profondes altérations chimiques. Dans un premier temps, des composés inorganiques (H_2O , CO_2 , ...) sont produits aux faibles profondeurs. Ensuite, lorsque la température dépasse les 100°C , du pétrole est produit. Enfin, du méthane est généré au stade ultime de la dégradation du kérogène. Dans les sédiments des marges continentales, les importantes quantités de méthane produites peuvent conduire à la formation d'hydrates de gaz. La présence de ces hydrates de gaz dans les sédiments est susceptible aussi de modifier la circulation des fluides. Un autre exemple de l'importance des systèmes eau-gaz-sels est fourni par les systèmes géothermiques. Des fluides salés remontent des profondeurs, et des émulsions liquide-

vapeur se produisent lors de la baisse de pression induite. Ceci entraîne une diminution drastique de la solubilité des espèces dissoutes, et des dépôts de métaux se produisent.

Tous ces exemples montrent qu'une bonne compréhension des équilibres de phases dans les systèmes eau-gaz-sels est nécessaire en géologie. Mais, il y a encore un autre domaine, où une bonne connaissance des systèmes eau-gaz-sels est requise. C'est celui des inclusions fluides et de leur analyse par microthermométrie. Les inclusions fluides sont des microcavités, dans lesquelles les fluides peuvent être piégés lors de la croissance ou la recristallisation des minéraux. L'étude des inclusions fluides peuvent donc fournir des informations clés sur les paléofluides qui ont circulé dans la roche (Hollister et Crawford, 1981; Roedder, 1984; Pagel et al., 1986). Les analyses des inclusions fluides repose en grande partie sur les mesures microthermométriques. La microthermométrie consiste en l'observation des changements de phases se produisant lors de changements de température contrôlés entre -180°C et 600°C (Chaixmeca © : Poty et al., 1976; Linkham ©: Shepherd, 1981; USGS-Fluid Inc. ©: Werre et al., 1976). L'interprétation des températures des transitions de phase est basée sur l'hypothèse que les inclusions fluides se comportent comme des systèmes à masse et volume constants. Ceci nécessite donc une bonne connaissance des transitions de phase et propriétés v-x (volume molaire - composition) des fluides eau-gaz-sels.

Les fluides, les forces intermoléculaires, et les équilibres de phase.

Les fluides représentent un état de la matière, où les molécules sont animées d'une importante énergie cinétique. Cette énergie est proportionnelle à la température absolue. C'est pourquoi l'état fluide est associé à des domaines de plus fortes températures que l'état solide. Mais entre les molécules s'exercent aussi des forces. Ces forces ont des origines différentes et sont plus ou moins fortes. Les plus importantes sont les forces électrostatiques s'exerçant entre les ions. Les plus faibles sont les forces de dispersion s'exerçant entre les molécules monoatomiques, dont la couche externe électronique est saturée (par exemple, l'argon). Entre ces deux extrêmes se situe tout l'éventail des

différents types de forces intermoléculaires (interactions ion-dipôle, dipôle-dipôle, ion-quadrupôle, dipôle-quadrupôle, liaisons hydrogène, forces d'induction, ...). Ce sont ces forces intermoléculaires qui sont à l'origine des formes condensées de la matière. L'état de la matière résulte donc d'un équilibre entre l'agitation thermique et les forces moléculaires. Une transition de phase s'opère donc lorsque par une variation de température, de pression ou de composition du système, cet équilibre entre ces deux effets antagonistes est bouleversée, et une nouvelle phase caractérisée par une distribution différente de l'énergie cinétique et potentielle devient stable. C'est ce qui se passe lors des équilibres liquide-vapeur. Ainsi, dans un gaz, l'énergie cinétique occupe une part prédominante sur l'énergie potentielle intermoléculaire; tandis que dans un liquide, c'est l'énergie potentielle générée par les interactions moléculaires qui prédomine sur l'énergie cinétique. Ceci a aussi des conséquences importantes sur la distribution des différentes espèces chimiques entre les phases en équilibre. Une ségrégation des différentes molécules se produit en effet entre les différentes phases en fonction des interactions moléculaires.

La modélisation.

La description de ces transitions de phase constitue donc un important domaine de la chimie et de la thermodynamique. Historiquement, il y a eu (et il y a encore) deux façons principales de traiter un problème de transition de phases. La première est basée sur la quantification des phénomènes macroscopiques accompagnant les transitions de phases (transfert de chaleur, changement de densité, ...). Ceci est à l'origine de la thermodynamique classique, et a permis de mettre en évidence les premier et second principes de la thermodynamique, avec pour corollaire, l'existence de fonctions d'état. La deuxième méthode tente d'utiliser une description à l'échelle moléculaire de la matière. Cette voie apparaît très séduisante, car il suffirait en effet de connaître uniquement les potentiels intermoléculaires pour être capable de prédire les transitions de phase en résolvant les équations du mouvement de Newton. Mais très vite, il est apparu qu'une telle méthode se heurte à des difficultés pratiques colossales. En effet, la matière est composée

d'un grand nombre de molécules, et dont les mouvements fluctuent à des intervalles de temps extrêmement courts. Néanmoins, grâce l'apparition de moyens de calculs puissants, cette approche a pu récemment se développer avec les simulations par ordinateur (Monte-Carlo, dynamique moléculaire). Cependant, une telle méthode demande des moyens lourds, et est donc inadaptée à la résolution des problèmes de transition de phases, qui se posent quotidiennement. Une résolution rigoureuse et exacte des équations de Newton est donc hors de portée (sauf dans le cas très simple du gaz parfait), et des simplifications doivent être adoptées. C'est là que réside toute la difficulté : comment dériver les propriétés macroscopiques d'un fluide à partir de la connaissance de ses potentiels intermoléculaires, par ailleurs mal connus ? C'est dans la résolution de ce problème, que la mécanique statistique tente d'apporter des solutions. Le premier pas dans ce domaine a été marqué par l'équation de van der Waals. Elle est basée sur une vision simpliste des interactions moléculaires et elle a été construite en suivant une démarche plus intuitive que rigoureuse; mais elle permet déjà de rendre compte des principales caractéristiques des fluides à un seul constituant (courbe de saturation, point critique, ...). L'équation de van der Waals a servi de base à toute une famille d'équations d'état, communément appelées équations cubiques et très utilisées dans le domaine pétrolier sur les mélanges d'hydrocarbures (Soave, 1972; Peng et Robinson, 1976), les systèmes eau-gaz (Daridon, 1992) et les systèmes eau-gaz-sels (Bowers et Helgeson, 1983; Søreide et Whitson, 1992). Les équations d'état cubiques actuelles parviennent à une bonne reproduction des données expérimentales, mais ceci se fait en ayant recours à des développements souvent empiriques et en utilisant un grand nombre de paramètres d'ajustements. De telles équations d'état ne sont plus alors extrapolables en dehors des conditions de pressions et températures, dans lesquelles elles ont été ajustées. Mais, depuis l'équation de van der Waals, de nombreuses avancées ont été réalisées sur le plan théorique en mécanique statistique. Des méthodes mathématiques ont été établies permettant de calculer de manière plus réaliste les propriétés thermodynamiques d'un fluide à partir de ses potentiels intermoléculaires. Ainsi, de nouvelles équations d'état reposant sur de solides bases théoriques peuvent être mises au point. C'est en particulier

une de ces nouvelles équations d'état, construites pour modéliser les propriétés thermodynamiques d'un mélange d'ions et de dipôles, qui a été utilisée dans ce travail pour les équilibres liquide-vapeur des fluides H₂O-NaCl.

Les interactions moléculaires dans les fluides eau-gaz-sels.

La difficulté de la modélisation des fluides eau-gaz-sels provient principalement du fait que l'eau, les gaz (CO₂, CH₄, N₂, ...) et les sels représentent trois types très différents de molécules. Les constituants, regroupés sous le nom de "gaz" (CO₂, CH₄, N₂, ...) constituent les espèces chimiques les plus simples. Les molécules de méthane et d'azote sont des molécules nonpolaires interagissant par des forces de dispersion et des forces quadrupôle-quadrupôle, quadrupôle-octopôle, ... Leur point critique est situé à des températures très basses (-146.95°C pour l'azote, -82.55°C pour le méthane). La molécule de dioxyde de carbone est un quadrupôle fort, et elle est donc capable de développer des interactions plus fortes, comme le révèle la valeur plus haute de la température critique du CO₂ (31.1°C). Depuis longtemps, l'eau est reconnue comme étant un fluide avec des propriétés uniques. Son point critique est situé à haute température (374°C), ce qui traduit l'existence de liaisons fortes entre les molécules d'eau. La molécule d'eau est en effet fortement polaire ($\mu = 1.83$ Debye), et elle est capable de former des interactions, dites liaisons hydrogène, avec d'autres molécules d'eau. C'est en raison de ces liaisons hydrogène, que les molécules d'eau ont tendance à former des groupements tétraédriques. C'est ce qui se passe dans des phases condensées comme la glace ou les hydrates de gaz, où les molécules d'eau constituent un réseau dilaté reliées entre elles par des liaisons hydrogène. Et enfin, les espèces ioniques représentent les molécules développant les interactions les plus fortes. La température critique des sels n'est pas connue avec précision, mais elle se situe probablement autour de 3000°C pour le chlorure de sodium. Des interactions moléculaires fortes se développent aussi entre l'eau et les sels. L'eau est un liquide à constante diélectrique élevée. De cette propriété provient sa forte propension à dissoudre les sels. De plus, les molécules d'eau ont tendance à former des sphères

d'hydratation autour des ions. Par contre, la solubilité des gaz est plus limitée dans les solutions aqueuses. Cette rapide revue donne une idée de la diversité des interactions moléculaires s'exerçant dans les fluides eau-sels-gaz; et il n'est donc pas étonnant de constater que la modélisation de tels fluides soit difficile.

Dans ce mémoire, trois applications différentes de la modélisation des fluides eau-gaz-sels à partir des équations d'état sont développées. Mais, auparavant, le premier chapitre décrit un nouvel outil de programmation permettant de faciliter grandement le calcul des dérivées et des fonctions thermodynamiques à partir des équations d'état. Cet outil s'est révélé très utile lors des calculs de diagrammes de phase et de la mise au point d'équations d'états. La première application est développée dans le deuxième chapitre et est consacrée aux équilibres de phase du système $\text{CO}_2\text{-CH}_4\text{-N}_2$ et à la détermination des propriétés volume molaire-composition ($v\text{-}x$) des parties volatiles des inclusions fluides. La deuxième application, développée dans les troisième et quatrième chapitres, concerne l'application d'un modèle thermodynamique dérivé de la mécanique statistique aux équilibres liquide-gaz des systèmes eau-sels. Et enfin, la troisième application, décrite dans le cinquième chapitre, donne deux exemples de l'utilisation d'un modèle de stabilité des hydrates de gaz, d'une part pour déterminer la salinité globale et la densité de la partie non-aqueuse de certains types d'inclusions fluides, et d'autre part pour interpréter les mesures de composition des fluides échantillonnés lors de forages du Leg ODP 164 (Ocean Drilling Program) consacré aux hydrates de gaz marins.

Références.

Bowers, T.S. et Helgeson, H.C. (1983) Calculation of the thermodynamic properties and geochemical consequences of nonideal mixing in the system $\text{H}_2\text{O-CO}_2\text{-NaCl}$ fluids at high pressures and temperatures. *Geochim. Cosmochim. Acta* **47**, 1247-1275.

Crawford, M.L. (1981) Phase equilibria in aqueous fluid inclusions. In L.S. Hollister et M.L. Crawford, eds. : Short course in fluid inclusions: applications to petrology. Mineralogical Association of Canada, v. **6**, pp 75-100.

Daridon, J.L. (1992) Mesure et représentation des équilibres de phase sous pression de mélanges d'eau, de paraffines et de dioxyde de carbone. Thèse de doctorat de l'Université de Pau et des Pays de l'Adour, 177 p.

Pagel, M., Walgenwitz, F. et Dubessy, J. (1986) Fluid inclusions in oil and gas-bearing sedimentary formations. In J. Burruss, eds : Thermal modeling in sedimentary basins. Editions Technip, pp 565-583.

Peng, D. et Robinson, D.B. (1976) A new two constants equation of state. Ind. Eng. Chem. Fundam. **15**, 59-64.

Poty, B., Leroy, J. and Jackimowicz, L. (1976) Un nouvel appareil pour la mesure des températures sous le microscope: l'installation de la microthermométrie Chaixmeca. Bull. Min. **99**, 182-186.

Roedder, E. (1984) Fluid inclusions. Reviews in Mineralogy, v. **12**, 644 p.

Shepherd, T.J. (1981) Temperature-programmable heating-freezing stage for microthermometric analysis of fluid inclusions. Econ. Geol., **76**, 1244-1247.

Soave, G. (1972) Equilibrium constants from a modified Redlich-Kwong equation of state. Chem. Eng. Sci. **27**, 1197-1203.

Søreide, I. and Whitson, C.H. (1992) Peng-Robinson predictions for hydrocarbons, CO₂, N₂, and H₂S with pure water and NaCl brine. *Fluid Phase Equilibria* **77**, 217-240.

Werre, R.W., Bodnar, R.J., Betke, P.M. and Barton, P.B. (1979) A novel gas-flow fluid inclusion heating/freezing stage; *In Geol. Soc. Am. Abstr. Programs*, vol. **11**, pp 539.

CHAPITRE 1

**Une nouvelle librairie
pour calculer analytiquement
les propriétés thermodynamiques
des fluides
avec les équations d'état.**

Résumé

Les équations d'état non-empiriques et s'appuyant sur un modèle physique des fluides sont le plus souvent exprimées sous la forme d'une expression de l'énergie d'Helmholtz en fonction de la température, du volume molaire et de la composition. Cette formulation est commode, car toutes les propriétés thermodynamiques peuvent être alors obtenues par simple différentiation de l'énergie d'Helmholtz. Cependant, dans la pratique, le calcul formel des propriétés thermodynamiques peut représenter une grosse charge de travail. En effet, la complexité des expressions mathématiques croît de manière exponentielle avec l'ordre de dérivation et il n'est pas rare d'avoir à calculer des dérivées jusqu'à l'ordre quatre. Ainsi, les calculs d'équilibres de phase nécessitent de connaître les dérivées de l'énergie d'Helmholtz jusqu'à l'ordre deux, et les dérivées du quatrième ordre sont requises pour les calculs de courbes critiques. Et dans certains cas particuliers (par exemple, le calcul de points tricritiques, cf Chapitre 3), les dérivées d'ordre six sont également nécessaires. Parallèlement à cela, la complexité des équations d'état actuelles croît de manière considérable. Il suffit de comparer l'équation de van der Waals et le modèle MSA décrit dans le Chapitre 3 pour se rendre compte du degré de complexité atteint aujourd'hui par les modèles dérivés de la mécanique statistique. Le calcul formel à la main des dérivées de l'énergie d'Helmholtz du modèle MSA (chapitre 3) jusqu'à l'ordre quatre nécessite des semaines de travail, et les erreurs sont inévitables. Par conséquent, il est nécessaire d'utiliser une méthode. Des logiciels de calcul formel existent à l'heure actuelle et permettent d'obtenir les expressions mathématiques des dérivées seulement jusqu'au troisième ordre (Deiters, 1994, communication privée) si l'équation d'état n'est pas trop complexe. Une alternative aux logiciels de calcul formel est présentée ici et elle est utilisable sous la forme d'une librairie informatique orientée objet. Les dérivées jusqu'à l'ordre quatre des opérateurs mathématiques (somme, produit, division, puissance, sommes multiples,...) les plus usuellement utilisés dans les équations d'état sont

préprogrammées. Il n'y a donc plus besoin d'exécuter de longues et fastidieuses dérivations des expressions mathématiques. Le travail du concepteur de l'équation d'état se limite alors à programmer la succession des opérations mathématiques requises pour le calcul de l'énergie d'Helmholtz. Cette étape se fait en représentant l'énergie d'Helmholtz sous la forme d'un "arbre", dont chaque noeud représente une opération mathématique, et chaque lien un paramètre. La librairie utilise cette représentation de l'énergie d'Helmholtz sous forme d'arbre pour calculer les dérivées. Cette librairie est couramment testée et utilisée depuis deux ans au CREGU avec de nombreux modèles thermodynamiques différents, et elle permet des gains de temps appréciables dans la programmation des équations d'état. L'ensemble de ce travail fait l'objet d'une publication actuellement sous presse (Thiéry, 1996).

Références.

Thiéry, R. (1996) A new object-oriented library for calculating analytically high-order multivariable derivatives and thermodynamic properties of fluids with equations of state. *Computer & Geosciences* (sous presse).



A NEW OBJECT-ORIENTED LIBRARY FOR CALCULATING ANALYTICALLY HIGH-ORDER MULTIVARIABLE DERIVATIVES AND THERMODYNAMIC PROPERTIES OF FLUIDS WITH EQUATIONS OF STATE

RÉGIS THIÉRY

CREGU, BP 23, F-54501 Vandœuvre-lès-Nancy Cedex, France

(Received 25 May 1995; Accepted 13 January 1996)

Abstract—A new global approach for calculating thermodynamic properties of fluids with equations of state is proposed. This method uses an object-oriented library, written in C++, and containing a number of routines that facilitate thermodynamic calculations. It is applicable to any equation of state formulated by an analytical expression of the Helmholtz free energy. The programming work of the user is limited to the building of a parse representation of the Helmholtz free energy. This parse graph is then processed by the program for analytically calculating the required derivatives and thermodynamic properties of fluids. A demonstration of this library is made with the Anderko and Pitzer equation of state for H₂O–NaCl–KCl fluids. The Helmholtz free energy has been differentiated analytically up to the fourth order with respect to the temperature, molar volume, and composition. Calculated derivatives are used to calculate the critical line of H₂O–NaCl mixtures and other thermodynamic properties, which otherwise would be difficult to obtain.

Key Words: Equations of state, Thermodynamics, Critical state, H₂O–NaCl fluids, Object-oriented programming

INTRODUCTION

Knowledge of the thermophysical properties of geological fluids is required for the understanding of chemical and mechanical processes occurring in various environments. The equilibrium state of a fluid mixture of N components is defined entirely by a set of $(N + 1)$ intensive variables that can be either TVx_i , PTx_i , SVx_i , or SPx_i (where T is the temperature, V is the molar volume, P is the pressure, S is the molar entropy of the system, and x_i is the mole fraction of the i th component in the mixture). Any expression of the form $F(a_1, a_2, \dots) = 0$ in which the a_i are the $(N + 1)$ variables defining the equilibrium state of the system is termed an equation of state (EOS). Its formulation can be empirical or guided by theoretical expressions. In TVx_i coordinates, EOS may be given by expressions of the Helmholtz free energy, A from which all desired quantities can be obtained by classical thermodynamic relationships.

$$A = A(T, V, x_i) \quad (1)$$

Such a formulation, referred to as the fundamental equation, is more convenient than $P = P(T, V, x_i)$ as all thermodynamic properties of the fluid are obtained by simple differentiation with respect to the TVx_i variables. This formulation is now used by most recently published EOS, and has been chosen for this study.

A great deal of the work of the thermodynamist consists of differentiating the fundamental equation to obtain all the desired thermodynamic properties. This can represent a large amount of time, as specific mathematical formulations of EOS are rarely simple. Recent advances in statistical mechanics lead to efficient, but complex expressions, which are cumbersome to differentiate. A good illustration of this is given by the Anderko and Pitzer (1993a), (1993b) EOS for the H₂O–NaCl–KCl system above 300°C. This EOS is successful in calculating liquid–vapor phase equilibria and adequately predicts the densities of liquids and vapors. However, for deriving the molar enthalpy, H , from the Helmholtz free energy (Eq. 2), Anderko and Pitzer remark that “the temperature dependency of some of the terms of A is so complex that the derivative was determined numerically rather than analytically”.

$$H = -T^2 \left(\frac{\partial(A/T)}{\partial T} \right)_{V, x_i} - V \left(\frac{\partial A}{\partial V} \right)_{T, x_i} \quad (2)$$

Generally, other important parameters such as the pressure and the chemical potential of a component are easy to obtain by simple first-order differentiation:

$$P = - \left(\frac{\partial A}{\partial V} \right)_{T, x_i} \quad (3a)$$

$$\mu_i = \left(\frac{\partial A}{\partial n_i} \right)_{T,V,x_j} = \frac{1}{n} \left[\left(\frac{\partial A}{\partial x_i} \right)_{T,V,x_j} - \sum_k \left(\frac{\partial A}{\partial x_k} \right)_{T,V,x_j} \right], \quad (3b)$$

where n and n_i stand, respectively, for the total number of moles and the number of moles of the i th component in the system. The complexity of expressions increases rapidly with the order of differentiation (see later), and differentiation up to the fourth order is required. Indeed, efficient algorithms for calculating fluid phase equilibria (Peng and Robinson, 1977; Asselineau, Bogdanic, and Vidal, 1979) require second-order differentiates of the Helmholtz free energy. Critical phenomena play an important role in geochemical processes (Bischoff, Rosenbauer, and Pitzer, 1986; Johnson and Norton, 1991), and the location of critical points of fluid mixtures requires differentiates at least up to the third order (Huron, Dufour, and Vidal, 1977; Baker and Luks, 1978; Heidemann and Khalil, 1980; Michelsen, 1980; Michelsen and Heidemann, 1981; Eaton, 1988).

There are three methods to obtain analytical expressions of the derivatives of the free energy. The first one is hand calculation, which can be lengthy and painstaking. The second one is numerical differentiation. As shown previously, this method is sometimes used for first-order differentiate calculations, but should be discarded for calculating higher-order differentiates. Three-point and five-point finite-centered formulae are not reliable enough for determining the second- and third-order differentiates, which are necessary for locating a critical point (Heilig, 1988; Heilig and Franck, 1990). Differentiates from the third order up to the sixth order have been obtained by Deiters and Pegg (1989) by using optimized numerical differentiation formulas, but this requires more computing time. The third method involves the use of computer programs that perform analytical calculations, such as Mathematica (Wolfram, 1991), Reduce (Hearn, 1987), Matlab (Chen and Moler, 1993),... such programs are termed symbolic calculation software, and are used with some success (Heilig, 1988; Heilig and Franck, 1990; Deiters, pers. comm., 1994); however, they are not free of critics. The main problem is that these programs require extensive of memory for complicated EOS. Thus, the analytical expressions of

derivatives that can be produced with these programs are limited mostly to the third order (Deiters, pers. comm., 1994). Therefore, the creation of new programming tools devoted specifically to EOS would be a great help.

This paper describes a new tool, which is now used in our laboratory for calculating analytically the differentiates of the Helmholtz free energy and the thermodynamic properties of fluids. This method uses an object-oriented library, written in C + +. It is based on an algorithm which looks similar to the one used by symbolic calculation software. However, our library overcomes the shortcomings of these programs and is able to handle the most complex EOS and to calculate multivariable differentiates up to the fourth order (and higher, if required) with respect to the T , V and x_i . First, a brief explanation of the differentiation algorithm will be given. Differences between our library and symbolic calculation programs are pointed out. Then, the use of this library is illustrated with the Anderko and Pitzer 1993a), 1993b) EOS.

PRINCIPLES OF THE DIFFERENTIATION ALGORITHM

The difficulty of differentiating a complex arithmetic expression is the number of terms, which grows exponentially each time the order of differentiation is incremented (Norris, 1981). For a small subexpression such as the product of two multivariable functions, such as $u \cdot v$, the first-order derivative involves 4 terms, the second order 8 terms, the third order 16 terms,...; and hence, the number of operations is multiplied by two at each differentiation step. The situation is worse for the division operator, where the number of operations is multiplied practically by three at each step. Thus, even after simplification and factorization of the expressions, the fourth-order derivative of u/v involves at least 131 terms. Most specific statements of the Helmholtz free energy function contain many terms and operators. Some of these statements have been listed in Table 1 together with the number of mathematical operations required for calculating the Helmholtz free energy. Cubic EOS require relatively few operations, which make them useful for practical calculations (Thiéry,

Table 1. Number (No.) of mathematical operations required for calculating the Helmholtz free energy of some EOS

EOS	No.
Cubic EOS, attractive part	10
Boublik EOS (1970) for hard-spheres mixtures	20
Anderko and Pitzer, 1993a), dipole-dipole interaction for H ₂ O-NaCl system	21
Anderko and Pitzer, 1993a), dispersion interactions for H ₂ O-NaCl system	52
IUPAC EOS for CH ₄ (Angus, Armstrong, and de Reuck, 1978)	53
IUPAC EOS for CO ₂ (Angus, Armstrong, and de Reuck, 1976)	58
Kcenan EOS (1969) for H ₂ O	55
Haar-Gallager-Kell EOS (1984) for H ₂ O	85
Hill EOS (1990) for H ₂ O (outside the critical region)	91
The MSA ion-dipole model (Lvov and Wood, 1990) for H ₂ O-NaCl solutions	133

Vidal, and Dubessy, 1994; Thiéry, Kerkhof, and Dubessy, 1994; Thiéry and Dubessy, submitte, 0). However, some recently published EOS (Angus, Armstrong, and de Reuck, 1976, 1978; Keenan and others, 1969; Boublik, 1970; Haar, Gallagher, and Kell, 1984; Hill, 1990; Anderko and Pitzer, 1993a, 1993b) require many more operations. Now, new efficient EOS (Lvov and Wood, 1990; Harvey, 1991), which are based on recent advances of statistical mechanics, are more complex still. Thus, it is not a surprise that the differentiation of such a function becomes quickly impracticable.

A first answer to this type of problem has been given by symbolic calculation software. These programs are all based on an algorithm used widely in computer science (Haugeland, 1985; Sedgewick, 1992). The principle of this algorithm is simple: a complex task can always be decomposed into elementary operations and decomposition is conveniently visualized by a hierarchical representation. For instance, consider how a simple arithmetic expression is split into smaller subexpressions (Fig. 1A):

$$f(x,y,z) = u \times v + v/u \times w, \quad (4)$$

where f , u , v and w are a function of three variables, x , y and z . This is how symbolic calculation programs store an arithmetic expression in memory. This type of representation is termed a parse tree (Sedgewick, 1992). Each box is termed a node and refers to an arithmetic operation (an addition, a multiplication, the logarithm of a quantity,...). The upper node is the root and it contains the expression to be decomposed. Bifurcation starts from the root and continues so long as it is possible to decompose a subexpression further. Terminal nodes are termed the leaves and contain irreducible expressions. Now, for calculating a first-order differentiate, symbolic calculation programs traverse the parse tree from the leaves up to the root. At each node of the parse tree, a simple first-order derivation rule is applied. The result is the construction of a new parse tree. Fig. 1B shows the parse tree obtained for the first-order partial derivative $(\partial f/\partial x)_{y,z}$ denoted as f_x (derivatives are written using the convention, where subscripts designate the differentiation variables). The root of this new parse tree contains the desired arithmetic expression of the first-order differentiate. It is worth noting that the parse tree of a first-order differentiated expression grows already considerably in size. For calculating a derivative of order n , symbolic calculation programs apply this algorithm n times. Thus, there is no theoretical limit for the order of differentiates that can be calculated. However, memory requirements of this algorithm may be so great that expressions of fourth- and higher-order differentiates cannot be obtained (Deiters, pers. comm., 1994).

This leads us to think about an alternative method for calculating analytical values of differentiates. Our

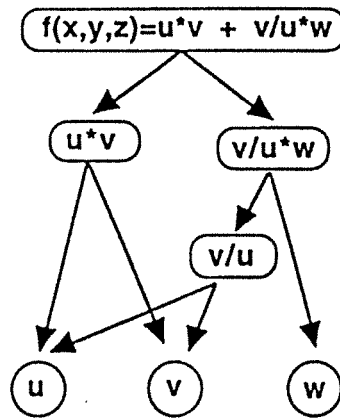
method uses parse representations, too; but there are large differences with respect to the method used by symbolic calculation software. As shown above, these programs manipulate only strings of characters, which are arithmetic expressions of the derivatives. These strings of characters then can be inserted in the source code of the calculation programs. On the contrary, our library does not try to obtain the analytical expressions of the partial derivatives, it calculates only analytically their numerical values. Symbolic calculation software is able only to apply first-order derivation rules to a given parsed expression. In our library package, the source code for calculating the first-, second-, third-, and fourth-order derivatives has been written for a large number of operators. Such a mode of operation has several advantages. First, memory requirements of our library are smaller. For each derivative, symbolic calculation software produce a new parse tree, which is progressively more complex each time that the differentiation order is increased (Fig. 1B). With this library, no parse tree for the partial differentiates is constructed. Indeed, for calculating a differentiate of order n , the library uses only the parse tree of the arithmetic expression, that has been built by the user (Fig. 1C). Of course, the order of differentiates that can be obtained at this time is limited to the fourth order, but, if necessary, this limit could be increased to a higher order. It would require to write only the source code of higher derivatives. Another shortcoming of symbolic calculation programs is that they give complex and lengthy analytical expressions for the differentiated expressions. Many repetitions can be observed in the source code produced by symbolic calculation software. These expressions should be simplified and factorized in order to produce an efficient and rapid program, but, as pointed out by specialists of symbolic calculation, the automatic simplification of arithmetic expressions remains a difficult problem of computer science. For now, symbolic calculation software is not able to factorize simple expressions effectively. In our library, this problem is solved, as simplifications and factorizations have been achieved at the stage of writing the source code.

Our library has been written in C++ (Stroustrup, 1991), an object-oriented extension of the C language (Kernighan and Ritchie, 1978). Because users of this library will have to write some instructions in C++, it is important to explain how this library is organized and constructed.

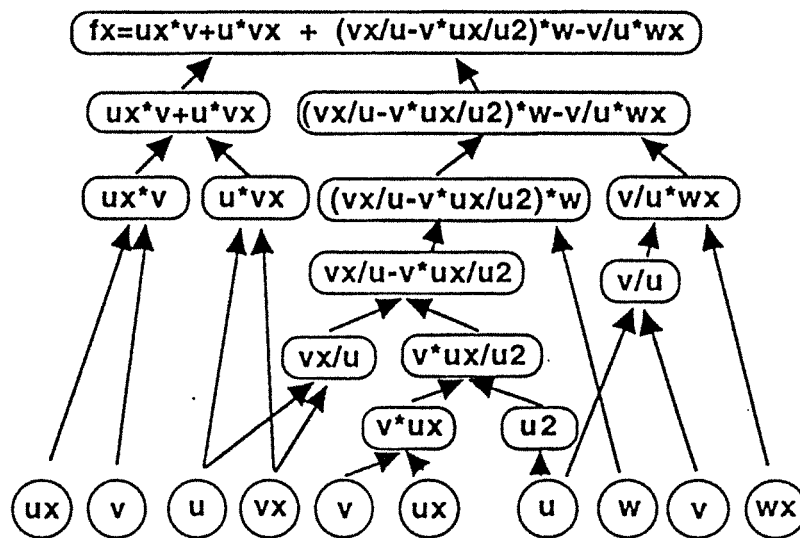
ORGANIZATION OF THE LIBRARY

This library (Fig. 2) is composed of two modules interacting with each other: the first module applies to the calculation of analytical differentiates, the second module calculates thermodynamic properties of fluids. The first module contains only source code for calculating the differentiates of a generic product,

A



B



C

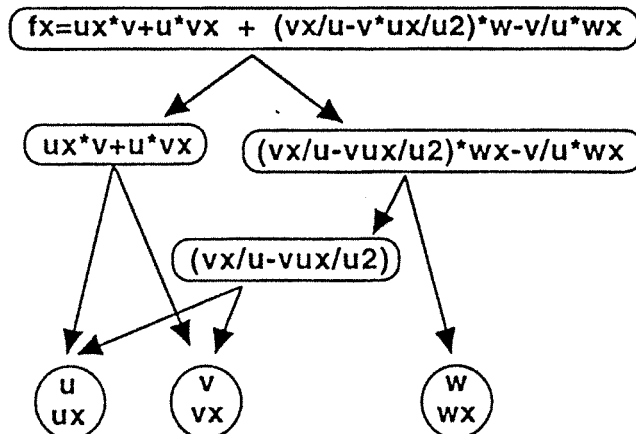


Fig. 1. Comparison of differentiation algorithms between symbolic calculation software and our library. (A) Start point is same: arithmetic expression is decomposed into smaller elementary subexpressions (boxes) which are easier to process. Irreducible subexpressions, called "leaves", are represented by circles. Arrows and numbers indicate the direction and order of the decomposition (from the root up to the leaves). (B) Symbolic calculation software build new parse tree for each differentiate. Here is represented parse tree of differentiated function with respect to one variable. Parse tree is obtained by applying simple first-order differentiation rules on parse tree of Figure 1A. Growth of parse tree starts from leaves and ends at root. (C) Our library uses same parse tree as Figure 1A for calculating any differentiate of n -order. Differentiates are obtained by applying differentiation rules that have been programmed in library. Notations ux , vx , wx , $u2$ are used respectively for u , v , w and u^2 functions.

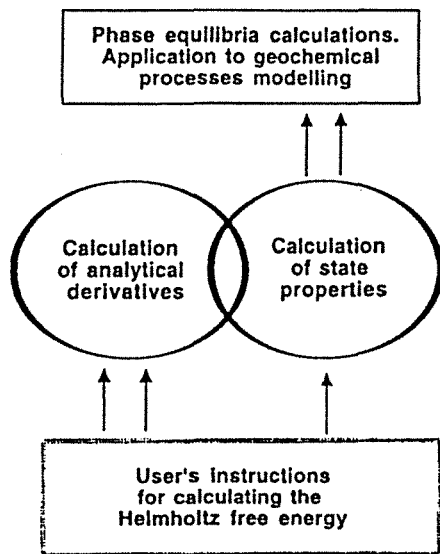


Fig. 2. Organization of library. Two main modules make up core of library 1/ calculation of differentiates of simple expressions, like product of two functions,... and 2/ calculation of state properties of fluids as a function of partial derivatives of Helmholtz free energy. Library communicates by means of (1) user's instructions for constructing parse tree of any EOS, and with (2) other specialized libraries of geochemical calculations.

a sum, a ratio,... In the second module, all state parameters of interest for the thermodynamics of fluid have been expressed as a function of partial differentiates of the Helmholtz free energy. The source code is applicable to any EOS, expressed by means of the Helmholtz free energy. The first step for using this library is to write C++ instructions for constructing the parse tree of the specific Helmholtz free energy function of interest. Then, the user must compile the source file with a C++ compiler and link it with the library. After this step, the user can call all the available subroutines of thermodynamic calculations. This library and the user's code can be linked to other specialized libraries for geochemical process modelling.

USE OF THE DIFFERENTIATION LIBRARY

A detailed example

The use of the differentiation module will be illustrated with the simple function, given by Equation (4). Using C++, one defines, and manipulates entities, termed objects, that combine variables and functions. Thus, the first step is the creation of an "object". This is what is shown in the following example. The keyword "struct" indicates that a new object is being defined. "AnExample" is the name of the new defined object. Variables and functions are declared between the brackets. Comments are introduced with the characters '//'.

```

//-----
//      struct AnExample : public Equation
//-----
{
// Declaration of the nodes of the parse tree

Sum2 f ;           // f = uv + vuw
Product uv ;      // uv = u * v
Product vuw ;     // vuw = vu * w
Division vu ;     // vu = v/u

// Declaration of the leaves of the parse tree
//      u(x,y,z) = 2.0 * x * x ;
//      v(x,y,z) = x + y + z
//      w(x,y,z) = x - y * z

Leaf u ;
Leaf v ;
Leaf w ;

// The differentiation variables

double x ;
double y ;
double z ;

// Declaration of the functions

AnExample () ;
void calculate_the_leaves () ;
void calculate_the_partial_differentiates () ;
void check_derivatives () ;
} ;
  
```

The second step is to construct a C++ representation of the parse tree. The method used here is similar to that used by symbolic calculation softwares. This is performed in our example by the function AnExample ().

```

//-----
//      AnExample :: AnExample () : Equation ()
//-----
//      Construction of the parse tree (Fig 1A)
//-----
{
f . tie ( uv , vuw ) ;           // f = uv + vuw
f . set_scalars ( 1.0 , 1.0 , 0.0 ) ;

uv . tie ( u , v ) ;           // uv = u * v
vuw . tie ( vu , w ) ;        // vuw = vu * w
vu . tie ( v , u ) ;           // vu = v / u

//      There are three differentiation variables (x,y and z)
f . number_of_variables ( 3 ) ;
}
  
```

The tie () function connects the nodes. After the parse graph has been defined entirely, the number of differentiation variables must be specified by calling the number_of_variables () function.

Finally, in the third step, the user writes the function that calculates the partial differentiates of irreducible expressions. This is carried out by the calculate_the_leaves () function. (see page 6)

Variables for which derivatives are to be calculated are given arbitrary identification numbers, starting from zero. These numbers are used as index numbers for referencing a specific derivative value. An important remark is given here: the user must specify differentiation variables of any derivative in a decreasing order (for example, for referring to the $e_{,}$ derivative, and by using the following identification numbers (x,0), (y,1) and (z,2), the user will have to write w(2,1) and not w(1,2)).

```

//-----
// void AnExample :: calculate_the_leaves ()
//-----
// Calculation of partial differentiates of irreducible
// expressions
// Indexes of the differentiation variables are :
// 0 : the x variable
// 1 : the y variable
// 2 : the z variable
//-----
{
// u(x,y,z) = 2.0 * x * x ;
// v(x,y,z) = x * y * z
// w(x,y,z) = x - y * z

u () = 2.0 * x * x ;
v () = x * y * z ;
w () = x - y * z ;

j (0) = 2.0 * x ;
j (0,0) = 2.0 ;

v (0) = 1.0 ;
v (1) = 1.0 ;
v (2) = 1.0 ;

w (0) = 1.0 ;
w (1) = -z ;
w (2) = -y ;
w (2,1) = -1.0 ;

// Other derivatives are equal to zero, by default.
}

```

Now, it remains to call the library functions that calculate the partial differentiates. This is performed by the following three instructions in the `calculate_the_partial_differentiates ()` function.

```

//-----
// void AnExample :: calculate_the_partial_differentiates ()
//-----
// Calculation of the partial differentiates.
//-----
{
int n_order = 4 ; // the differentiation order
f . initialize_the_graph () ;
calculate_the_leaves () ;
f . calculate ( order ) ;
}

```

The `initialize_the_graph ()` function resets an internal flag that prevents repetitive expressions from being recalculated.

Here is the subroutine for calculating and displaying the f_x , and f_{xy} partial differentiates:

```

//-----
// void main ()
//-----
{
AnExample example ;
example . calculate_the_partial_differentiates () ;
printf ("%lg %lg", example . f (1,0) , example . f (2,1,0) ) ;
}

```

Some useful functions

In this section, some useful functions available within the differentiation library are addressed. First, it may happen that some irreducible expressions do not depend on some variables. For instance, in the previous model, where the leaf referred to as u does not depend on the y and z variables. Thus, calculation of differentiates with respect to these variables is redundant. For this reason, the user has the option to specify to the library whether an expression really is a function of a given variable

or not. This is achieved with the following instructions:

```

u . specify_variable_dependency ( 1 , FALSE ) ;
v . specify_variable_dependency ( 2 , FALSE ) ;
// 1 and 2 are the indexes of the y and z variables
// in the array of differentiation variables

```

In this example, the user indicates that the expression u is not dependent on the y variable. After all specifications have been set, the user can request an analysis of the dependencies of the nodes of the parse tree by calling the `analyze_dependencies ()` function

```
f . analyze_dependencies () ;
```

Another important group of functions furnished by this library concerns the detection of mistakes made by the user. Possible errors are of two types. The first type occurs when the user forgets to define one connection between two nodes. The user should therefore be careful when the parse graph contains many nodes. Two utility functions are given for detecting this type of error (the `print ()` and `check_pointers ()` function).

```
f . print ( file ) ;
```

```
f . check_connections ( file ) ;
```

The `print ()` function writes on a file the list of the nodes with their connections. Memory addresses and the nature of the nodes are indicated. The `check_connections ()` function detects whether a connection is lacking. The second type of error involves differentiation mistakes of the leaves. This library provides a method for detecting them. The user can carry out a systematic checking of differentiates of a given node by calling the `check1 ()`, `check2 ()`, `check3 ()`, and `check4 ()` functions, respectively for checking first-, second-, third, and fourth- order derivatives. Each of these functions compares values of derivatives, calculated with the library and by a finite-centered difference method. Analytical and numerical values are then reported on an ASCII file specified by the user. If the number digits are not identical (except for the last digit), there is an error in the derivatives of the "leaves" expressions. (see opposite)

The list of operators and functions

The list of available operators and functions is given in Table 2, and covers most of the situations encountered in thermodynamic modelling. Note that although exponentiation `Pow0` and `Power` objects look similar, they do not have the same behavior. `Power` objects accept only positive values of $(u + b)$ expressions, whereas `Pow0` objects accept positive

```

//-----
void AnExample :: check_derivatives ()
//-----
{
FILE * report = fopen ( "Derivatives.note" , "w" ) ;
double var [3], dvar [3] ;

var [0] = 200.0 ;           // the x variable
var [1] = 40.0 ;           // the y variable
var [2] = 500.0 ;           // the z variable

dvar [0] = 1.0e-6 ;        // step parameters used
dvar [1] = 1.0e-6 ;        // for calculating numerical
dvar [2] = 1.0e-6 ;        // differentiates

f . check1 ( report , var , dvar ) ;
f . check2 ( report , var , dvar ) ;
f . check3 ( report , var , dvar ) ;
f . check4 ( report , var , dvar ) ;

fclose (report) ;
}

```

and negative values. However Power objects accept any value for the exponent, and Powo objects accept only exponents which can be expressed by a ratio of two integers ($c = n/m$ where c is the exponent, n denotes any integer, and m is an odd integer). For constructing a parse tree for any arithmetic expression, the knowledge of Table 2 and of two important functions (`tie ()` and `set_scalars ()` functions) is sufficient. The `tie ()` function connects a parental node (denoted as P) to one or two subexpressions (denoted as u and v).

```

Node P, u, v ;
P . tie ( u ) ;           // if P connects to only one node
P . tie ( u , v ) ;       // or if P connects to two nodes

```

Arithmetic expressions involve always scalar parameters. These are always specified by calling the `set_scalars ()` function.

```

Node P ;
double a, b, c, d ;       // scalar parameters, as defined
                           // by Table 2

P . set_scalars ( a ) ;
    // if P is a Cube object, for instance

P . set_scalars ( a, b ) ;
    // if P is an Inverse object, for instance

P . set_scalars ( a, b, c ) ;
    // if P is a Power object, for instance

P . set_scalars ( a, b, c, d ) ;
    // if P is an Exponential object, for instance

```

Other operators are more complex, and their use must be defined explicitly. These are the Sum, LineaX2, LineaX3, SumX2, SumX3, SumX4, and SumX5 types of nodes. They are used mostly to extend EOS to fluid mixtures. They involve multiple summations through the components of the system. The different steps required for using these objects are

summarized in Appendix A for the Sum object, in Appendix B for the LineaX and LineaX2 objects, and in Appendix C for the SumX2, SumX3, SumX4 and SumX5 objects.

USE OF THE MODULE FOR THERMODYNAMIC CALCULATIONS

In representing and calculating the thermodynamic properties of fluids, it is usual to split molecular interactions within a fluid into several contributions; for instance, the repulsive contribution, the dispersion, the dipole-dipole interaction, the dipole-quadrupole contribution, and others. This has been considered in the construction of our library. Two basic objects have been implemented: the Interaction and FluidPhase objects. The Interaction object is used for modelling different types of interactions, whereas the FluidPhase object contains all basic variables and functions for implementing an EOS. What the user must do for implementing a new thermodynamic model, is to construct new objects inherited from the Interaction and FluidPhase objects. A typical inherited FluidPhase object uses one or more different Interaction objects. It is worth noting that the only significant amount of programming work is the construction of parse trees. A large number of variables and functions are predefined in the Interaction and FluidPhase objects that the user need not recreate. The most important of these functions involve:

- the calculation of chemical potentials, fugacities, and activities, and their first-order differentiates with respect to the temperature, molar volume, pressure, and mole fraction;
- the calculation of the molar volume, given the temperature and the pressure;
- the calculation of liquid-gas, liquid-liquid, and liquid-liquid-gas equilibria (Asselineau, Bogdanic, and Vidal, 1979), including the calculation of various phase diagrams (isotherms, isobars, and isopleths for binary and ternary systems);
- the calculation of the critical curve of binary fluids.

APPLICATION TO THE ANDERKO AND PITZER EQUATION OF STATE

As an illustration of the usefulness of this library, the Anderko and Pitzer 1993a), 1993b) EOS has been chosen. It applies to the H₂O-NaCl-KCl system above 300°C. This ternary system is representative of fluids that are met in a wide variety of geological environments. In particular, near-critical conditions of this system are important for the understanding of boiling seafloor geothermal systems and of many hydrothermal deposits (Bischoff, Rosenbauer, and

Table 2. List of available objects in library for user. a , b , c and d stand for scalars involved in arithmetic expressions. u and v are used for "children" subexpressions

Object	Arithmetic expression
Cube	$a(u+b)^3$
Exponential	$a \exp(bu+c)$
Inverse	$a/(u+b)$
Inverse2	$a/(u+b)^2$
Logarithm	$a \log(u+b)$
Power	$a(u+b)^c$
Powo	$a(u+b)^c$ with $c = n/m$ and m is an odd integer
Square	$a/(u+b)^2$
Sum1	$au+b$
Sum2	$au+bu+c$
Sum	$\sum a_i$
Division	au/v
Product	auv
LineaX2	$\sum \sum a_i x_j$
LineaX3	$\sum \sum \sum a_i x_j x_k$
SumX2	$\sum \sum x_j x_k$
SumX3	$\sum \sum \sum x_j x_k x_l$
SumX4	$\sum \sum \sum \sum x_j x_k x_l x_m$
SumX5	$\sum \sum \sum \sum \sum x_j x_k x_l x_m x_n$

Pitzer, 1986). Our library has been used for solving two difficult problems:

- calculation of the critical locus curve of the H₂O–NaCl system,
- calculation of thermodynamic properties, requiring differentiation of the Helmholtz free energy with respect to the temperature, such as the enthalpy, and others

Calculation of derivatives of the Helmholtz free energy

The Anderko and Pitzer EOS considers the H₂O–NaCl–KCl system above 573 K as a mixture of H₂O molecules and the ion pairs NaCl and KCl. The Helmholtz free energy of H₂O–salts mixtures is split into three contributions:

$$A = A_{repulsion} + A_{dipole} + A_{dispersion}, \quad (5)$$

where $A_{repulsion}$ is a result of the repulsion between molecules and ion pairs, A_{dipole} is representative of dipole–dipole interactions, and $A_{dispersion}$ stands for the attractive dispersion forces. For programming this EOS, three separate Interaction—type objects have been defined for the intermolecular repulsion, dipolar, and dispersion forces. The source code for the repulsive part is given in Appendix D. Appendix E gives the source code for the Anderko and Pitzer, 1993a) EOS. Some information about the construction of the parse trees of these three interactions is summarized here.

The repulsion contribution. The arithmetic expressions for the evaluation of $A_{repulsion}$ are given by Anderko and Pitzer 1993a), 1993b) following the theory of hard spheres (Boublik, 1970; Mansoori and others, 1971):

$$\frac{A^{rep}}{RT} = \frac{\frac{3DE}{F} \eta - \frac{E^3}{F^2}}{1 - \eta} + \frac{\frac{E^3}{F^2}}{(1 - \eta)^2} + \left(\frac{E^3}{F^2} - 1 \right) \ln(1 - \eta), \quad (6)$$

where η is the reduced density,

$$\eta = \frac{b}{4V} \quad (7)$$

and b is the covolume of the mixture,

$$b = \sum_i x_i b_i, \quad (8)$$

where x_i is the mole fraction of the i th component and b_i is the covolume.

The b_i covolumes and the σ_i hard sphere diameters are related by:

$$b_i = \frac{2}{3} \pi N_A \sigma_i^3, \quad (9)$$

where N_A is the Avogadro number.

The parameters D , E , and F are given by:

$$D = \sum_i x_i \sigma_i, \quad (10a)$$

$$E = \sum_i x_i \sigma_i^2, \quad (10b)$$

$$F = \sum_i x_i \sigma_i^3 \quad (10c)$$

The procedure for calculating the differentiates of the $A_{repulsion}$ has been completely developed in Appendix D. Fig. 3 can be used as a guide for following the construction of the parse representation.

The dipole contribution. The Helmholtz energy difference between dipolar hard spheres and simple hard spheres is expressed as (Stell, Rasaiah, and Narang, 1972; Rushbrooke, Stell, and Høye, 1973; Stell, Rasaiah, and Narang, 1974):

$$\frac{A^{dip}}{RT} = \frac{A_2}{1 - \frac{A_1}{A_2}} \quad (11a)$$

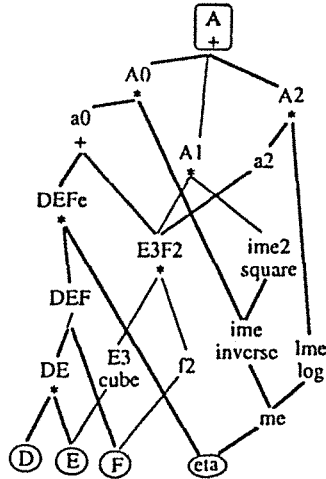


Fig. 3. Parse tree of Helmholtz free energy for a mixture of hard spheres, following theory of Boublik (Boublik, 1970; Anderko and Pitzer, 1993a, Anderko and Pitzer, 1993b). Leaves are surrounded by circles, and root is surrounded by rectangular frame. Function performed by each node is indicated by symbol below name of each subexpression. Notations are those used in declaration of Boublik object (see Appendix C).

where

$$A_2 = K_2 \eta I_2(\eta), \quad (11b)$$

$$A_3 = K_3 \eta^3 I_3(\eta), \quad (11c)$$

$I_2(\eta)$ and $I_3(\eta)$ are empirical functions of the η density. Auxiliary functions, termed K_2 and K_3 have been introduced in order to simplify expressions:

$$K_2 = \sum_i \sum_j k_{2,ij} x_i x_j, \quad (12a)$$

where

$$k_{2,ij} = -\frac{4}{3} \left(\frac{\sigma_i^3 \sigma_j^3}{\sigma_{ij}^6} \right) \frac{\eta_{ij}}{\eta} \tilde{\mu}_i^2 \tilde{\mu}_j^2 \quad (12b)$$

and

$$K_3 = \sum_i \sum_j \sum_k k_{3,ijk} x_i x_j x_k, \quad (13a)$$

where

$$k_{3,ijk} = \frac{10}{9} \left(\frac{\sigma_i^3 \sigma_j^3 \sigma_k^3}{\sigma_{ijk}^9} \right) \frac{\eta_{ijk}^2}{\eta^2} \tilde{\mu}_i^2 \tilde{\mu}_j^2 \tilde{\mu}_k^2 \quad (13b)$$

η_{ij} and η_{ijk} are functions of the density and of the composition of the mixture, $\tilde{\mu}_i$ is a function of the dipole moment of the i th component, K_2 is a quadratic function of the composition, and K_3 is a cubic function of the composition. For handling these finite summations, LineaX2 and LineaX3 objects of the library have been used.

The dispersion contribution.

$$\frac{A^d}{RT} = -\frac{1}{RT} \left(\frac{a}{V} + \frac{acb}{4V^2} + \frac{adb^2}{16V^3} + \frac{acb^3}{64V^4} \right), \quad (14)$$

where

$$b = \sum_i x_i b_i, \quad (15)$$

$$a = \sum_i \sum_j x_i x_j a_{ij}, \quad (16)$$

$$c = \frac{1}{ab} \sum_i \sum_j \sum_k x_i x_j x_k (ac)_{ijk} b_{ijk}, \quad (17)$$

$$d = \frac{1}{ab^2} \sum_i \sum_j \sum_k \sum_l x_i x_j x_k x_l (ad)_{ijkl} b_{ijkl}, \text{ and} \quad (18)$$

$$e = \frac{1}{ab^3} \sum_i \sum_j \sum_k \sum_l \sum_m x_i x_j x_k x_l x_m (ae)_{ijklm} b_{ijklm}^3, \quad (19)$$

Calculation of derivatives of the a , c , d and e summations requires respectively the use of SumX2, SumX3, SumX4, and SumX5 objects, as explained in Appendix C.

Calculation of the critical curve

A binary mixture of components 1 and 2 is in a critical state if the two following relations S_1 and S_2 are equal to zero (Heilig, 1988):

$$S_1(T, V, x_2) = A_{x_2 x_2} A_w - A_{V x_2} = 0 \quad (20a)$$

$$S_2(T, V, x_2) = A_{x_2 x_2 x_2}^2 - 3A_{V x_2} A_{V x_2 x_2} + 3A_{V V x_2} A_{V x_2}^2 - A_{V V V} A_{x_2 x_2} A_{V x_2} = 0, \quad (20b)$$

where A is the free Helmholtz energy of the mixture, as given by the EOS. This set of non-linear equations has been solved by the Newton method with the x_2 mole fraction as a given parameter, and the temperature T and the molar volume V as unknowns.

Once a solution has been obtained, it is still necessary to check the stability of this critical point by considering the following condition (Heilig, 1988; Heilig and Franck, 1990):

$$A_{x_2 x_2 x_2 x_2} - 4q A_{V x_2 x_2 x_2} + 6q^2 A_{V V x_2 x_2} - 4q^3 A_{V V V x_2} + q^4 A_{V V V V} \geq 0, \quad (21a)$$

$$\text{with } q = \frac{A_{V x_2}}{A_{V V}} \quad (21b)$$

Thus, derivatives up to the fourth order with respect to the temperature, the molar volume, and the composition are required and are calculated with our library. When a critical point has been determined, it is possible to estimate the variation of critical temperature and molar volume for a small change of the composition. This possibility is interesting, as it allows the estimation of suitable values of T and V for the Newton algorithm of the next critical point on

the critical curve. The solution of the following linear system is required:

$$\begin{bmatrix} \left(\frac{\partial S_1}{\partial T}\right)_{T,x_2} & \left(\frac{\partial S_1}{\partial V}\right)_{T,x_2} \\ \left(\frac{\partial S_2}{\partial T}\right)_{T,x_2} & \left(\frac{\partial S_2}{\partial V}\right)_{T,x_2} \end{bmatrix} \begin{bmatrix} \left(\frac{\partial T}{\partial x_2}\right)_{S_1,S_2} \\ \left(\frac{\partial V}{\partial x_2}\right)_{S_1,S_2} \end{bmatrix} = \begin{bmatrix} -\left(\frac{\partial S_1}{\partial x_2}\right)_{T,V} \\ \left(\frac{\partial S_2}{\partial x_2}\right)_{T,V} \end{bmatrix}. \quad (22)$$

This result is obtained by writing the Taylor series of S_1 and S_2 functions along the critical line, truncated after the first term:

$$dS_1 = 0 = \left(\frac{\partial S_1}{\partial T}\right)_{T,x_2} dT + \left(\frac{\partial S_1}{\partial V}\right)_{T,x_2} dV + \left(\frac{\partial S_1}{\partial x_2}\right)_{T,V} dx_2, \quad (23a)$$

$$dS_2 = 0 = \left(\frac{\partial S_2}{\partial T}\right)_{T,x_2} dT + \left(\frac{\partial S_2}{\partial V}\right)_{T,x_2} dV + \left(\frac{\partial S_2}{\partial x_2}\right)_{T,V} dx_2. \quad (23b)$$

It is worth noting that the left-hand matrix (Eq. 22) is calculated for the solving the nonlinear system (Eq. 20) with the Newton algorithm. Thus, this method permits a fast and stepwise calculation of the critical line of a binary mixture. It is particularly valuable for water-salts systems, where a small increment of the x_2 ($= x_{NaCl}$) mole fraction value results in a large variation of critical P and T variables near the H_2O critical point. $T - x_{NaCl}$ and $P - T$ projections of the critical curve of the H_2O - $NaCl$ system calculated with the Anderko and Pitzer, 1993a) EOS are given in Fig. 4.

Calculation of the isobaric expansivity

The isobaric expansivity (or thermal expansion coefficient) exemplifies an important thermodynamic parameter, which is difficult to extract from the Anderko and Pitzer 1993a), 1993b) EOS, as its calculation involves a temperature differentiation of the Helmholtz free energy. This parameter is required for calculating the Rayleigh-Darcy number, which is a key parameter in modelling fluid circulations in the crust (Johnson and Norton, 1991), in particular for locating the transition between conductive and convective regimes. The expansion coefficient is defined as:

$$\alpha = \frac{1}{V} \left(\frac{\partial V}{\partial T}\right)_P, \quad (25)$$

$(\partial V/\partial T)_P$ can be obtained from the Helmholtz free energy by noting that:

$$\left(\frac{\partial V}{\partial T}\right)_P = \frac{\left(\frac{\partial P}{\partial T}\right)_V}{\left(\frac{\partial P}{\partial V}\right)_T} = -\frac{\left(\frac{\partial^2 A}{\partial T \partial V}\right)}{\left(\frac{\partial^2 A}{\partial V^2}\right)_T} \quad (26)$$

Illustration of the variation of the isobaric expansivity as a function of the temperature and the $NaCl$ mole fraction is given in Fig. 5.

CONCLUSION

This library is used currently in our laboratory and it can be applied to a large variety of theoretical and applied geochemical problems, including, for example:

- phase topology studies of fluid mixtures, where derivatives up to the seventh order are sometimes required, whatever the complexity of the EOS (Deiters and Pegg, 1989; Van Pelt and de Loos, 1992; Thiéry and Lvov, submitte, 0).

- characterization of fluid inclusions where critical and retrograde condensation conditions can be determined accurately with models developed for CO_2 - CH_4 - N_2 fluid inclusions (Thiéry, Vidal, and Dubessy, 1994; Thiéry, Kerkhof, and Dubessy, 1994; Thiéry and Dubessy, submitte, 0).

Advantages of this library are numerous. First, it is reliable. Checking functions are supplied which allow analytical and numerical values to be compared. Detection of mistakes is easy, as each node of the parse graph can be checked individually. Secondly, it is a versatile tool. In research, it is often necessary to test between several hypotheses. With such a library, it is straightforward, for instance, to modify the temperature law for one of the parameters of the EOS, or to modify a mixing rule. Without this library, an extensive reprogramming of the computer code would be required in some situations. Next, this library is able to take into account complex operators such as simple finite summation (Σ), double summation ($\Sigma\Sigma$),... up to the quintuple summation ($\Sigma\Sigma\Sigma\Sigma\Sigma$). These operators are, indeed, widespread in modelling fluid properties. Finally, this library is an efficient and helpful tool for programming thermodynamic models. Before, one week of painstaking code development and testing was necessary to differentiate the Helmholtz free energy function, such as the one proposed for hard spheres mixtures (Boublik, 1970), which can now be achieved in two hours. Moreover, when combined with our library of thermodynamic calculations, any complex thermodynamic function is derived automatically. Another point of interest is that programs that implement an EOS based on this library will share the same routines and interface. This is an important consideration for implementing and updating calculation programs.

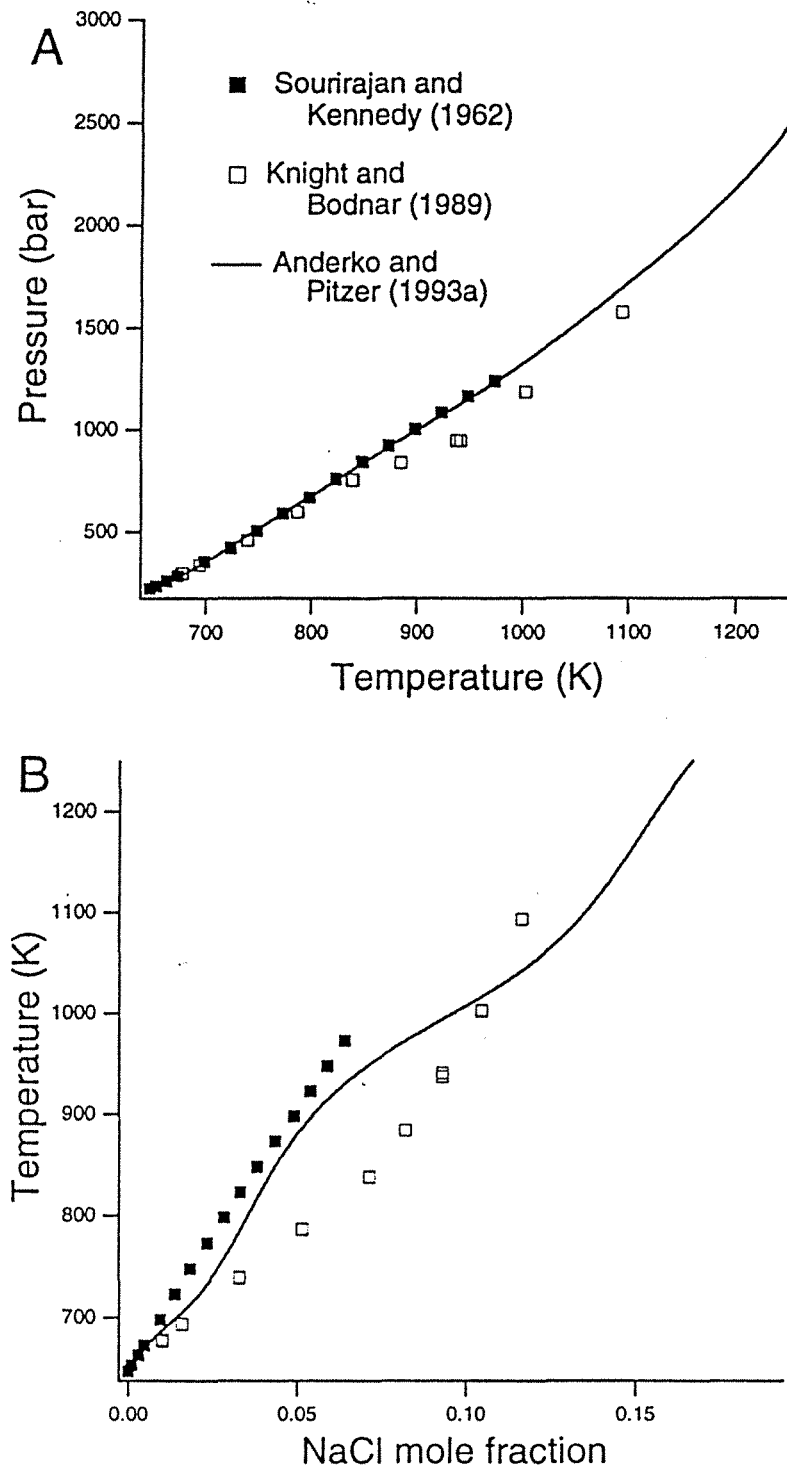


Fig. 4. H₂O-NaCl critical line in P-T diagram (A), and T-X NaCl diagram (B) calculated by Anderko and Pitzer EOS with aid of this library. Experimental data are those of Sourirajan and Kennedy (1962), of Knight and Bodnar (1989).

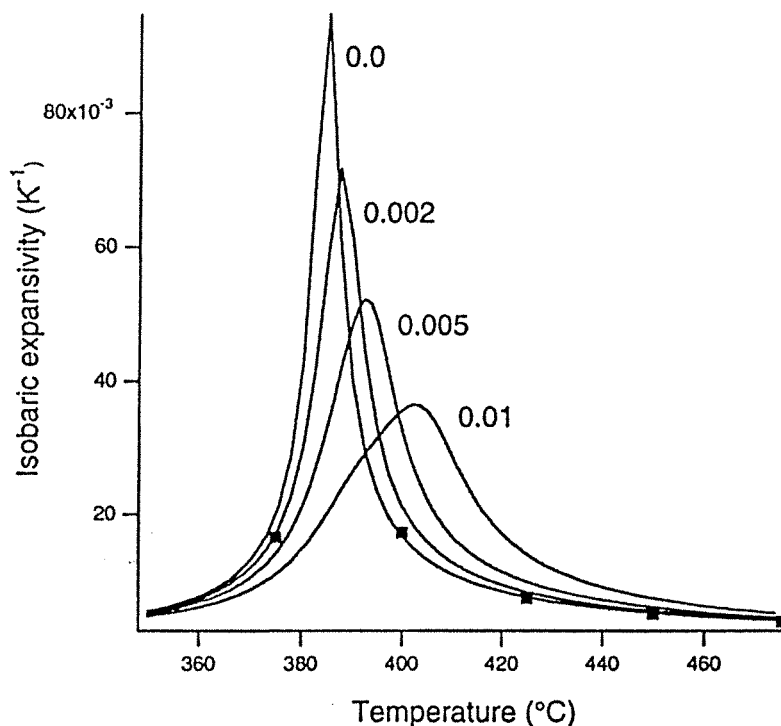


Fig. 5. Isobaric expansivity (K^{-1}) as function of temperature and NaCl mole fraction. Curves have been calculated with Anderko and Pitzer, 1993a) EOS for a pressure of 250 bars, i.e., above critical pressure of H_2O ($P_c = 217.6\text{bar}$). Numbers indicate NaCl mole fraction of aqueous solution. Full squares represent isobaric expansivity calculated for pure H_2O fluid with Haar, Gallagher and Kell EOS (Haar, Gallagher, and Kell, 1984), reported by Johnson and Norton (1991).

Note. The source code of the library and detailed examples are available on the anonymous FTP site "iamg.org".

Acknowledgements—This work has been supported financially by CNRS and Elf Aquitaine Production. The paper has benefited greatly from fruitful discussions and careful reviews of earlier drafts with Christophe Monnin, Ronald Bakker and Jean Dubessy. The two anonymous reviewers are thanked for their comments and suggestions for improving the manuscript.

REFERENCES

- Angus, S., Armstrong, B., and de Reuck, K. M., 1976, Carbon dioxide: International Thermodynamic Tables of the Fluid State, v. 3, Pergamon Press, Oxford, 385 p.
- Angus, S., Armstrong, B., and de Reuck, K. M., 1978, Methane: International Thermodynamic Tables of the Fluid State, v. 5, Pergamon Press, Oxford, 251 p.
- Anderko, A. and Pitzer, K. S., 1993, Equation-of-state representation of phase equilibria and volumetric properties of the system $\text{NaCl-H}_2\text{O}$ above 573 K. *Geochim. Cosmochim. Acta*, v. 57, no. 8, p. 1657-1680.
- Anderko, A. and Pitzer, K. S., 1993, Phase equilibria and volumetric properties of the systems $\text{KCl-H}_2\text{O}$ and $\text{NaCl-KCl-H}_2\text{O}$ above 573 K, Equation of state representation. *Geochim. Cosmochim. Acta*, v. 57, no. 20, p. 4885-4897.
- Asselineau, L., Bogdanic, G. and Vidal, J., 1979, A versatile algorithm for calculating vapour-liquid equilibria. *Fluid Phase Equilibria*, v. 3, p. 273-290.
- Baker, L. E., and Luks, D., 1978, Critical point and saturation pressure calculations for multicomponent systems: *Soc. Petrol. Eng. Jour.*, p. 1-9.
- Bischoff, J. L., Rosenbauer, R. J. and Pitzer, K. S., 1986, The system $\text{NaCl-H}_2\text{O}$: relations of vapor-liquid near the critical temperature of water and of vapor-liquid-halite from 300 to 500°C. *Geochim. Cosmochim. Acta*, v. 50, no. 7, p. 1437-1444.
- Boublik, T., 1970, Hard sphere equation of state. *Jour. Chem. Phys.*, v. 53, no. 1, p. 471-472.
- Chen, D., and Moler, C., 1993, Symbolic math toolbox user's guide: The MathWorks, Inc., Natick, Massachusetts, 166 p.
- Deiters, U. K. and Pegg, I. L., 1989, Systematic investigation of the phase behavior in binary fluid mixtures. 1. Calculations based on the Redlich-Kwong equation of state. *Jour. Chem. Phys.*, v. 90, no. 11, p. 6632-6641.
- Eaton, B. E., 1988, On the calculation of critical points by the method of Heidemann and Khalil: National Bureau of Standards, Technical Note 1313, 52 p.
- Haar, L., Gallagher, J. S., and Kell, G. S., 1984, NBS/NRC steam tables: thermodynamic and transport properties and computer programs for vapor and liquid of water in SI Units: Hemisphere Publishing Corporation, New York, 320 p.
- Harvey, A. H., 1991, Phase equilibria and critical lines in model water/salt mixtures. *Jour. Chem. Phys.*, v. 95, no. 1, p. 479-484.
- Haugeland, J., 1985, Artificial intelligence, the very idea: the Massachusetts Institute of Technology, Cambridge, 345 p.
- Hearn, A. C., 1987, Reduce users manual version 3.3: The Rand Corporation, Santa Monica, 243 p.
- Heidemann, R. A. and Khalil, A. M., 1980, The calculation of critical points. *Am. Inst. Chem. Eng. Jour.*, v. 26, p. 769-779.
- Heilig, M., 1988, Berechnung und experimentelle bestimmung von Zustandsdiagrammen fluider mehrkomponenten-

- tensysteme bis 400°C und 2500 bar: Ph.D. thesis, Univ. Karlsruhe, Karlsruhe, Germany, 143 p.
- Heilig, M. and Franck, E. U., 1990, Phase equilibria of multicomponent fluid systems to high pressures and temperatures. *Ber. Bunsenges. Phys. Chem.*, v. 94, p. 27-35.
- Hill, P. G., 1990, A unified fundamental equation for the thermodynamic properties of H₂O. *Jour. Phys. Chem. Ref. Data*, v. 19, no. 5, p. 1233-1274.
- Huron, M. J., Dufour, G.-N. and Vidal, J., 1977, Vapour-liquid equilibrium and critical locus curve calculations with the Soave equation for hydrocarbons systems with carbon dioxide and hydrogen sulphide. *Fluid Phase Equilibria*, v. 1, p. 247-265.
- Johnson, J. W. and Norton, D., 1991, Critical phenomena in hydrothermal systems: state, thermodynamic, electrostatic and transport properties of H₂O in the critical region. *Am. Jour. Sci.*, v. 291, p. 541-648.
- Kecnan J. H., Keyes, F. G., Hill, P. G., and Moore, J. G., 1969, Steam tables: thermodynamic properties of water including vapor, liquid and solid phases (English units): John Wiley and Sons, New York, 162 p.
- Kernighan, B. W., and Ritchie, D. M., 1978, The C programming language: Prentice-Hall, Inc., Englewood Cliffs, New Jersey, 228 p.
- Knight, C. L. and Bodnar, R. J., 1989, Synthetic fluid inclusions. IX. Critical PVTX properties of NaCl-H₂O solutions. *Geochim. Cosmochim. Acta*, v. 53, no. 1, p. 3-8.
- Lvov, S. N. and Wood, R. H., 1990, Equations of state of aqueous NaCl solutions over a wide range of temperatures, pressures and concentrations. *Fluid Phase Equilibria*, v. 60, p. 273-287.
- Mansoori, G. A., Carnahan, N. F., Starling, K. E. and Leland, T. W., 1971, Equilibrium thermodynamics of the mixture of hard-spheres. *Jour. Chem. Phys.*, v. 54, no. 4, p. 1523-1525.
- Michelsen, M. L., 1980, Calculation of phase envelopes and critical points for multicomponent mixtures. *Fluid Phase Equilibria*, v. 4, p. 1-10.
- Michelsen, M. L. and Heidemann, R. A., 1981, Calculation of critical points from cubic two-constant equations of state. *Am. Inst. Chem. Eng. Jour.*, v. 27, p. 521-523.
- Norris, A. C., 1981, Computational chemistry, an introduction to numerical methods: John Wiley and Sons, New York, 454 p.
- Peng, D. Y. and Robinson, D. E., 1977, A rigorous method for predicting the critical properties of multicomponent systems from an equation of state. *Am. Inst. Chem. Eng. Jour.*, v. 23, p. 137-144.
- Rushbrooke, G. S., Stell, G. and Ho, J. S., 1973, Theory of polar fluids I. Dipolar hard spheres. *Jour. Molecular Phys.*, v. 26, p. 1199-1215.
- Sedgewick, R., 1992, Algorithms in C++: Princeton University, Addison-Wesley, Reading, Massachusetts, 656 p.
- Sourirajan, S. and Kennedy, G. C., 1962, The system H₂O-NaCl at elevated temperatures and pressures. *Am. Jour. Sci.*, v. 260, p. 115-141.
- Stell, G., Rasaijah, J. C. and Narang, H., 1972, Thermodynamic perturbation theory for simple polar fluids. *Jour. Molecular Phys.*, v. 23, p. 393-406.
- Stell, G., Rasaijah, J. C. and Narang, H., 1974, Thermodynamic perturbation theory for simple polar fluids II. *Jour. Molecular Phys.*, v. 27, p. 1393-1414.
- Stroustrup, B., 1991, The C++ programming language (2nd ed.): Addison-Wesley, Reading, Massachusetts, 284 p.
- Thiery, R., Vidal, J. and Dubessy, J., 1994, Phase equilibria modelling applied to fluid inclusions. Liquid-vapour equilibria and calculation of the molar volume in the CO₂-CH₄-N₂ system. *Geochim. Cosmochim. Acta*, v. 58, no. 3, p. 1073-1082.
- Thiery, R., Kerkhof van den, A. M. and Dubessy, J., 1994, vX properties modelling of the CO₂-CH₄ and CO₂-N₂ fluids up to 31°C. *Eur. Jour. Mineral.*, v. 6, p. 753-771.
- Thiery, R., and Dubessy, J. (submitted to Fluid Phase Equilibria), Improved liquid-vapour phase equilibria modelling in the CO₂-CH₄-N₂ system for critical and noncritical conditions.
- Thiery, R., and Lvov, S. N. (submitted to Fluid Phase Equilibria), The ion-dipole model based on the mean spherical approximation. I. the global phase diagram.
- Van Pelt, A. and de Loos, Th. W., 1992, Connectivity of critical lines around the van Laar point in T X projections. *Jour. Chem. Phys.*, v. 97, no. 2, p. 1271-1281.
- Wolfram, S., 1991, Mathematica, a system for doing mathematics by computer (2nd ed.): Addison-Wesley Publishing Co., Redwood City, California, 1056 p.

APPENDIX

For constructing the parse representation of a sum, such as:

$$P = P_1 + 2P_2 - P_3 + 5P_4 + 3,$$

here is what the user must do:

```
//-----
// Use of the Sum object
//-----

// the declarations of nodes

Sum P ;
Leaf P1, P2, P3, P4 ;

// Instructions to insert at the
// beginning of the program

P . number_of_terms ( 4 ) ;

P . tie ( & P1, & P2, & P3, & P4 ) ;
P . set_scalars ( 1.0, 2.0, -1.0, 5.0, 3.0 ) ;
```

For constructing the parse representations of expressions such as:

$$K_2 = \sum_i \sum_j x_i x_j k_{2ij}, \text{ and}$$

$$K_3 = \sum_i \sum_j \sum_k x_i x_j x_k k_{3ijk},$$

where k_{2ij} and k_{3ijk} are scalars, the user must write the following instructions:

```
//-----
// Use of the LineaX2 and LineaX3 objects
//-----

// the declarations of variables

int N = 5 ; // the number of components
int ix = 2 ; // the index of the first composition
// variable

double ** k2, *** k3 ; // the array of scalars

LineaX2 K2 ;
LineaX3 K3 ;

// Instructions to insert at the
// beginning of the program

K2 . dimension (N) ;
K3 . dimension (N) ;

K2 . starting_index (ix) ;
K3 . starting_index (ix) ;
```



```

(Out*) A) -> set_relations_with (this);
:
//-----
void Boublík :: number_of_components ( int ncomp )
//-----
{
Interaction :: number_of_components (ncomp);
sig = allocate (N);
bi = allocate (N);
A -> number_of_variables ( 2*N );
//-----
// Gives useful indications of the dependency
// on the variables
//-----
// For the leaves
mlogV . specify_variable_dependency ( iC, 0 );
eta . specify_variable_dependency ( iC, 0 );
D . specify_variable_dependency ( iC, 0 );
E . specify_variable_dependency ( iC, 0 );
F . specify_variable_dependency ( iC, 0 );

D . specify_variable_dependency ( iV, 0 );
E . specify_variable_dependency ( iV, 0 );
F . specify_variable_dependency ( iV, 0 );

for ( int i = 0 ; i < N ; i ++ )
mlogV . specify_variable_dependency ( ix+i, 0 );

A > analyze_dependencies ( );
}

//-----
void Boublík :: calculate_fixed_parameters ( )
//-----
//
// Calculates parameters which are volume-independent.
//-----
{
RT = R * T ;
int i ;
double sigi, Dval, Eval, Fval ;
b = Dval = Eval = Fval = 0.0 ;
for ( i = 0 ; i < N ; i ++ )
{
b += x [i] * bi [i] ;
sigi = sig [i] ;

Dval += x [i] * sigi ;
Eval += x [i] * sigi * sigi ;
Fval += x [i] * sigi * sigi * sigi ;
}
D () = Dval ;
E () = Eval ;
F () = Fval ;
}

//-----
void Boublík :: calculate_volume_dependent_parameters ( )
//-----
{
int i ;
double sigi ;
double V2, V3, V4 ;

V2 = V * V ;
V3 = V2 * V ;
V4 = V3 * V ;

mlogV () = - log ( V ) ;
mlogV (iV) = - 1 / V ;
mlogV (iV,iV) = 1.0 / V2 ;

for ( i = 0 ; i < N ; i ++ )
{
sigi = sig [i] ;

eta (ix+i) = bi [i] / ( 4.0 * V ) ;

eta (ix+i,iV) = - bi [i] / ( 4.0 * V2 ) ;
eta (ix+i,iV,iV) = bi [i] / ( 2.0 * V3 ) ;
eta (ix+i,iV,iV,iV) = - 3.0 * bi [i] / ( 2.0 * V4 ) ;

D (ix+i) = sigi ; // Derivatives wrt to composition
F (ix+i) = sigi * sigi ;
F (ix+i,iV) = sigi * sigi * sigi ; // derivatives of higher order are zero
}

eta () = b / ( 4.0 * V ) ;
eta (iV) = - b / ( 4.0 * V2 ) ;
eta (iV,iV) = b / ( 2.0 * V3 ) ;
}

//-----
void Boublík :: calculate_high_order_parameters ( )
//-----
{
int i ;
double sigi ;
double V2, V3, V4, V5 ;
V2 = V * V ;
V3 = V2 * V ;
V4 = V3 * V ;
V5 = V4 * V ;

mlogV (iV,iV,iV) = - 2.0 / V3 ;
mlogV (iV,iV,iV,iV) = 6.0 / V4 ;

for ( i = 0 ; i < N ; i ++ )
{
sigi = sig [i] ;
eta (ix+i,iV,iV) = bi [i] / ( 2.0 * V3 ) ;
eta (ix+i,iV,iV,iV) = - 3.0 * bi [i] / ( 2.0 * V4 ) ;
}

#ifdef _ANDERKO_H
#define _ANDERKO_H

#include "FluidPhase.h"
#include "Interaction.h"
#include "NewtonRaphsor.h"
#include "Newton.h"

//-----
class Anderko : public FluidPhase
//-----
// Modelling of the H2O-NaCl-KCl system
//-----
{
public :
// Different types of interactions
Interaction * repulsion ; // between hard spheres

Interaction * dipole ; // between dipoles
Interaction * dispersion ; // dispersion forces

// Parameters of the Anderko & Pitzer's EOS
// 1 : H2O
// 2 : NaCl
// 3 : KCl

double b1 ; // Covolumes
double b2 ;
double b3 ;
double m1 ; // Dipole moments
double m2 ;
double m3 ;

Anderko (int) ;
} ;

#include "Anderko.h"
#include "Boublík.h"
#include "Dipole.h"
#include "H2ONaClDisp.h"

//-----
Anderko :: Anderko (int nphase) : FluidPhase (3,nphase)
//-----
{
interaction [0] = repulsion = new Boublík ;
interaction [1] = dipole = new Dipole ;
interaction [2] = dispersion = new H2ONaClDisp ;
}

```

CHAPITRE 2

**La modélisation
des équilibres de phases
dans le système CO₂-CH₄-N₂
et
application aux inclusions fluides.**

Résumé

Il arrive fréquemment que de petites quantités des paléofluides soient piégées dans des inclusions fluides lors des croissances ou recristallisations des minéraux. L'étude de ces inclusions fluides peut alors fournir des informations clé sur l'histoire de la roche. Cependant, la petite taille de ces cavités (comprise le plus souvent entre le micron et le millimètre) et la faible quantité des fluides piégés requièrent la mise au point et l'utilisation de méthodes d'analyses et d'interprétations spécifiques. Actuellement, deux méthodes d'analyse sont employées pour l'étude de la partie non-aqueuse riche en volatiles (CO_2 , CH_4 , N_2 , ...). La première technique est la microspectrométrie Raman, qui permet de mesurer la composition des fluides en éléments volatiles (CO_2 , CH_4 , N_2 , C_2H_6 , ...). La deuxième technique est la microthermométrie, qui consiste en la mesure des températures des transitions de phase. Les inclusions fluides se comportent généralement comme des systèmes à masse et volume constants lors de l'étude microthermométrique. Par conséquent, l'interprétation des mesures microthermométriques peut fournir des informations sur le volume molaire (v) et la composition (x) des fluides. Ceci nécessite donc de bien connaître les propriétés v - x des fluides CO_2 - CH_4 - N_2 . Les données expérimentales relatives à ce système sont peu nombreuses, et il est donc nécessaire de passer par une modélisation thermodynamique.

Le système CO_2 - CH_4 - N_2 est constitué de molécules nonpolaires, et c'est pour ce type de système que les équations d'état cubiques donnent généralement les meilleurs résultats. Une équation d'état cubique à deux paramètres (Soave, 1972) a donc été utilisée pour modéliser les équilibres de phases dans ce système. Une première modélisation, basée sur l'équation de Soave (1972) est décrite (Thiéry et al., 1994a). Cependant, le domaine critique est caractérisé par des fluctuations fortes et de longue portée de la densité. Les équations d'état cubiques, basées sur l'hypothèse dite "du champ moyen" de l'énergie potentielle intermoléculaire, sont incapables d'en

rendre compte. Ceci entraîne donc une forte dégradation des prédictions des équations cubiques dans la région critique. Une modification du modèle est décrite, améliorant nettement les calculs dans le domaine critique (Thiéry et Dubessy, 1996). Le modèle est utilisé pour calculer les équilibres de phases (liquide-gaz, liquide-liquide, solide-liquide-gaz, solide-liquide, solide-gaz) en dessous de 31°C dans le système CO₂-CH₄-N₂. Le modèle de Lee and Kesler (Lee et Kesler, 1975), basé sur le principe des états correspondants, est utilisé ensuite pour le calcul des densités dans le système CO₂-CH₄-N₂. Les diagrammes v-x, utilisables directement pour l'étude des inclusions fluides, ont été établis pour chacun des systèmes binaires CH₄-N₂, CO₂-CH₄ et CO₂-N₂. et sont décrits dans dernière publication présentée dans ce chapitre (Thiéry et al., 1994b).

Références

- Lee, B.I et Kesler, M.G. (1975) A generalized thermodynamic correlation based on three-parameter corresponding states. *AIChE J.* **21**, 510-527.
- Soave, G (1972) Equilibrium constants from a modified Redlich-Kwong equation of state. *Chem. Eng. Sci.*, **27**, 1197-1203.
- Thiéry, R., Vidal, J. et Dubessy, J. (1994a) Phase equilibria modelling applied to fluid inclusions: Liquid-vapour equilibria and calculation of the molar volume in the CO₂-CH₄-N₂ system. *Geochim. et Cosmochim. Acta*, **58**(3), 1073-1082.
- Thiéry, R., van den Kerkhof, A.M., et Dubessy, J. (1994b) vX properties of CH₄-CO₂ and CO₂-N₂ fluid inclusions: modelling for T < 31°C and P < 400 bars. *Eur. J. Mineral.*, **6**, 753-771.
- Thiéry, R. et Dubessy, J. (1996) Improved modelling of vapour-liquid equilibria up to the critical region. Application to the CO₂-CH₄-N₂ system. *Fluid Phase Equilibria* (sous presse).



Phase equilibria modelling applied to fluid inclusions: Liquid-vapour equilibria and calculation of the molar volume in the CO₂-CH₄-N₂ system*

R. THIERY,¹ J. VIDAL,² and J. DUBESSY¹

¹CREGU, Centre de Recherche sur la Géologie des Matières Minérales et Énergétiques, BP-23, 54501 Vandœuvre-les-Nancy Cedex, France
²Laboratoire de thermodynamique, IFP, BP-311, Rueil Malmaison Cedex, France

(Received August 31, 1992; accepted in revised form March 20, 1993)

Abstract—Quantitative use of fluid inclusions requires the determination of composition and molar volume. The molar volume can be calculated in the CO₂-CH₄-N₂ system from both the determination of the temperature of a $L + V \rightarrow L$ (or V) equilibrium if the composition is known independently, provided an equation of state (EOS) reproduces the P - V - T - X properties of each phase at equilibrium. This study is applicable to fluids for which the sequence of phase transition is $S_{CO_2} + L + V \rightarrow L + V \rightarrow L$ (or V) at increasing temperature. The molar volume is determined by following a two-step algorithm: (1) the pressure is calculated from a two-parameter cubic EOS with interaction parameters optimised along experimental L - V isotherms; (2) the molar volume is then calculated by the correlation of LEE and KESLER (1975) with the pressure calculated in the first step. Projections of polybaric L - V isotherms in v - X diagrams of the CO₂-CH₄, CO₂-N₂, and CH₄-N₂ systems can be directly applied to fluid inclusion studies. In addition, it is shown that the molar volume of CO₂-rich fluids ($X_{CO_2} > 0.6$) in the ternary system can be estimated with sufficient accuracy using empirical formulae relating to the v - X diagrams of the CO₂-CH₄ and CO₂-N₂ binary systems.

INTRODUCTION

CONTRARY TO SOLID PHASES for which the molar volume and its variation with pressure (P) and temperature (T) are usually well known, the complete characterization of paleofluids, presently found as relicts in fluid inclusions, requires the determination of both molar volume (v) and composition (X). The determination of the fluid v - X properties is essential for any quantitative P - T reconstruction since fluid inclusions are considered constant volume and mass systems to a first approximation. In a previous work, the determination of the molar volume of vapour phase was addressed from phase equilibria involving clathrate (DUBESSY et al., 1992). As popularised by BURRUSS (1981), v - X diagrams are most appropriate for quantitative interpretation of phase equilibria occurring in fluid inclusions since they are constant volume and mass systems. The first aim of this study is to produce projections of isotherms of liquid-vapour equilibria in the v - X plane for the three binary systems of the CO₂-CH₄-N₂ system.

The available experimental data are not numerous enough for an accurate interpretation of phase equilibria carried out simply by linear interpolation. Therefore, v - X diagrams must be constructed with thermodynamic models (e.g., HEYEN et al., 1982; HERSKOWITZ and KISCH, 1984; DARIMONT and HEYEN, 1988). However, no v - X diagram is available for the CH₄-N₂ system, which is commonly encountered fluid in inclusions as verified by microthermometric and Raman analysis. The ternary CO₂-CH₄-N₂ system is also very common in fluid inclusions representative of diagenetic, hydrothermal, or metamorphic fluids. No two-dimensional graph-

ical solution can be used to determine the molar volume in a ternary system. Therefore, a computer code which models liquid-vapour equilibria, with appropriate equations of state (EOS), is necessary to characterize complex paleofluids.

Previously, most calculations of thermodynamic properties on the CO₂-CH₄-N₂ system have been made using a single cubic EOS (HEYEN et al., 1982; HERSKOWITZ and KISCH, 1984; DARIMONT and HEYEN, 1988). As it has been shown (VIDAL, 1983), it is not possible to build a cubic EOS which is able to reproduce all the thermodynamic properties of a fluid. Therefore, instead of using only one EOS, two different thermodynamic models are successively applied in this work on the CO₂-CH₄-N₂ system. The first step is the calculation of the saturation pressure of a mixture of known composition and temperature by a two-parameter cubic EOS. Then, the molar volume is calculated from the previous computed pressure with a model based on the corresponding states principle (PRAUSNITZ et al., 1986), the correlation developed by LEE and KESLER (1975). Such a method is expected to improve the accuracy of all the calculations. Indeed, two-parameter cubic EOS are known to be efficient in modelling the P - T - X properties of liquid-vapour equilibria; and the Lee-Kesler method is a successful model when it is applied to the calculation of bulk properties such as the molar volume or enthalpy. Existing experimental data were evaluated in order to determine optimum binary interaction parameters which best reproduce the properties of the mixture. Finally, we show that the calculation of molar volumes of CO₂-rich fluid in the ternary system can be greatly simplified by projecting ternary compositions onto the two binary CH₄-CO₂ and N₂-CO₂ v - X diagrams.

SYMBOLS

L : liquid phase
 V : vapour phase

* Presented at the fourth biennial Pan-American Conference on Research on Fluid Inclusions (PACROFI IV), held May 22-24, 1992, at the UCLA Conference Center, Lake Arrowhead, California, USA.

X_i :	mole fraction of component i in a fluid phase
P :	pressure (bar)
v :	molar volume
T :	temperature (K)
$Z = Pv/(RT)$:	compressibility factor
R :	gas constant, $8.31441 \text{ J K}^{-1} \text{ mol}^{-1}$
T_c, P_c, v_c, Z_c :	critical temperature (K), pressure (bar), molar volume ($\text{cm}^3 \cdot \text{mol}^{-1}$), and compressibility factor
$T_c^*, P_c^*, v_c^*, Z_c^*$:	pseudo-critical temperature, pressure, molar volume and, compressibility factor
$T_r = T/T_c$:	reduced temperature
$P_r = P/P_c$:	reduced pressure
ω :	acentric factor = $-\log(P_{\text{sat}}(T_r=0.7)) - 1$; P_{sat} : saturation pressure at $T_r = 0.7$
k_{ij} :	interaction parameter characteristic of components i and j used in cubic EOS
ξ_{ij} :	interaction parameter characteristic of components i and j used in the MBWR EOS
U_{exp} :	experimental value of U
U_{calc} :	value of U calculated by the model
	$[\Delta P/P]\% = 100 \{P_{\text{exp}} - P_{\text{calc}}\}/P_{\text{calc}}$
	$[\Delta v/v]\% = 100 \{v_{\text{exp}} - v_{\text{calc}}\}/v_{\text{calc}}$
U_m :	value of U calculated in a mixture using proper mixing rules

USE OF CUBIC EQUATIONS OF STATE: A REVIEW

Two-Parameter Cubic EOS

Microthermometric studies provide temperatures of the phase transitions which can be converted to saturation pressure and molar volume with the aid of a thermodynamic model, provided the composition of the fluid is known. Cubic EOS are derived from the famous EOS of van der Waals,

$$P = RT/(v - b) - a/v^2, \quad (1)$$

which was the first EOS to improve prediction of the properties of liquid and vapour. Cubic EOS are the sum of two distinct terms:

$$P = P_{\text{repulsion}} + P_{\text{attraction}}. \quad (2)$$

The Soave-Redlich-Kwong (SRK) or the Peng-Robinson (PR) are the most popular EOS (PENG and ROBINSON, 1976; SOAVE, 1972):

$$\text{SRK} \quad P = RT/[v - b] - a/[v(v + b)], \quad (3)$$

$$\text{PR} \quad P = RT/[v - b] - a/[v(v + b) + b(v - b)], \quad (4)$$

where a is a temperature-dependent parameter, adjusted in order to reproduce the saturation pressure of a pure component, and b , the covolume, is a volume-dimension constant. The dependence of a with the temperature is usually described by the relation

$$a(T) = a_c \alpha(T) = [1 + F(1 - T_r^{1/2})]^2, \quad (5)$$

where a_c is the value of a at the critical point, and F is a quantity adjusted to best reproduce saturation pressure data of the pure component. The function F has been regressed to a second degree polynomial of the acentric factor ω (SOAVE, 1972; PENG and ROBINSON, 1976):

$$\text{(SRK): } F = 0.48 + 1.574\omega - 0.176\omega^2, \quad (6)$$

$$\text{(PR): } F = 0.3764 + 1.54226\omega - 0.26992\omega^2. \quad (7)$$

Thermodynamic stability criteria at the critical point

$$(\partial P/\partial v)_{T_c} = 0 \quad (8)$$

$$\text{and } (\partial^2 P/\partial v^2)_{T_c} = 0, \quad (9)$$

constrain the values of the a_c and b parameters (REID et al., 1977):

$$a_c = \Omega_A (RT_c)^2 / P_c, \quad (10)$$

$$b = \Omega_B (RT_c) / P_c, \quad (11)$$

where Ω_A and Ω_B are dimensionless constants:

$$\Omega_A(\text{SRK}) = 0.42748; \quad \Omega_A(\text{PR}) = 0.45724;$$

$$\Omega_B(\text{SRK}) = 0.08664; \quad \Omega_B(\text{PR}) = 0.07780.$$

EOS can be applied to mixtures, provided that mixing rules are available, to relate the a and b parameters to the composition of the mixture. A quadratic mixing rule applies to a and an arithmetic mixing rule to b :

$$a_m = \sum \sum x_i x_j a_{ij}, \quad \text{where } a_{ij} = (1 - k_{ij})(a_i a_j)^{1/2} \quad (12)$$

$$\text{and } b_m = \sum x_i b_i. \quad (13)$$

k_{ij} is an interaction parameter characteristic of each component i and j , and it is determined by adjusting experimental liquid-vapour equilibria for the binary system ($i - j$). Application of such mixing rules are equivalent to considering the mixture as a regular solution (VIDAL, 1978; LERMITE and VIDAL 1988). The mixing rules proposed by HEYEN (1981), based on a local composition model (LERMITE and VIDAL, 1988), are more sophisticated. These mixing laws have been applied to the $\text{CO}_2\text{-CH}_4$ and the $\text{CO}_2\text{-N}_2$ systems by several authors (HEYEN et al., 1982; HERSKOWITZ and KISCH, 1984; HEYEN and DARIMONT, 1988), but they have not been used in this work.

Three-Parameter EOS

As shown by several authors, SRK and PR EOS are quite successful in describing liquid-vapour equilibria of nonpolar mixtures, except in the critical region. However, prediction of the molar volumes of saturated liquids is quite poor and the compressibility factor Z_c at the critical point is equal for all components, which is not consistent with experimental data. PENELOUX et al. (1982) proposed a correction for the molar volumes of saturated liquids calculated by the two-parameter EOS by replacing v with $v - c$ for pure components. This translation has a negligible effect on the molar volumes of the vapour phase and the calculation of liquid-vapour equilibria is not modified, provided that for mixtures, the c parameter is calculated using an arithmetic mixing rule:

$$c_m = \sum x_i c_i. \quad (14)$$

PATEL and TEJA (1982) EOS (PT) and Heyen EOS (H) are similar to translated two-parameter EOS:

$$\text{(PT): } P = RT/(v - b) - a/(v(v + b) + c(v - b)), \quad (15)$$

$$\text{(H): } P = RT/(v - c) - a/(v(v + b) + c(v - b)). \quad (16)$$

Thermodynamic stability criteria at the critical point provide only two equations (eqns. 8 and 9) which do not permit the values of a at the critical point (a_c) and of b and c to be determined. Applications of Eqns. 8 and 9 show that a_c , b , and c are a function of P_c , T_c , and Z_c . A third relation is necessary to constrain the values of a_c , b and c . PATEL and TEJA (1982) did not use the experimental value of Z_c but adjusted it to best reproduce the saturated liquid molar volume. HEYEN (1981) used the experimental critical compressibility factor and correlated the b parameter to temperature.

CALCULATIONS OF PRESSURE AND COMPOSITION OF L-V EQUILIBRIA

Unary Systems

Cubic EOS were evaluated on their ability to reproduce the saturation pressures of pure components CO_2 , CH_4 , and N_2 (regression of experimental data reported by ANGUS et al., 1976, 1978, and 1979). Relative deviations do not exceed 2% (Fig. 1a, b, c) except for the SRK EOS at 100 K for CH_4 , where the relative error is larger than 8% (but even in this case, the prediction is good, since the absolute error does not

exceed 0.03 bar). Therefore, only the SRK EOS has been retained for modelling the saturation pressure of the mixture.

Calculation Procedure Used for the Binary Systems

For each binary system, an optimum interaction parameter k_{ij} has been recalculated to optimize the fit to the experimental data for vapour-liquid isotherms for only the SRK EOS. All the calculations were carried out using the computer program of Institut Français du Pétrole, described by ASSELINEAU et al. (1979).

Interaction parameters k_{ij} were obtained by minimizing the objective function SQ :

$$SQ = 1/N_d \left[\sum \left(\frac{P_{exp} - P_{calc}}{P_{calc}} \right)^2 + \sum (y_{i,calc} - y_{i,exp})^2 \right], \quad (17)$$

where N_d is the number of experimental data and $y_{i,calc}$ and $y_{i,exp}$ are, respectively, the calculated and the experimental mole fraction of component i in the liquid phase.

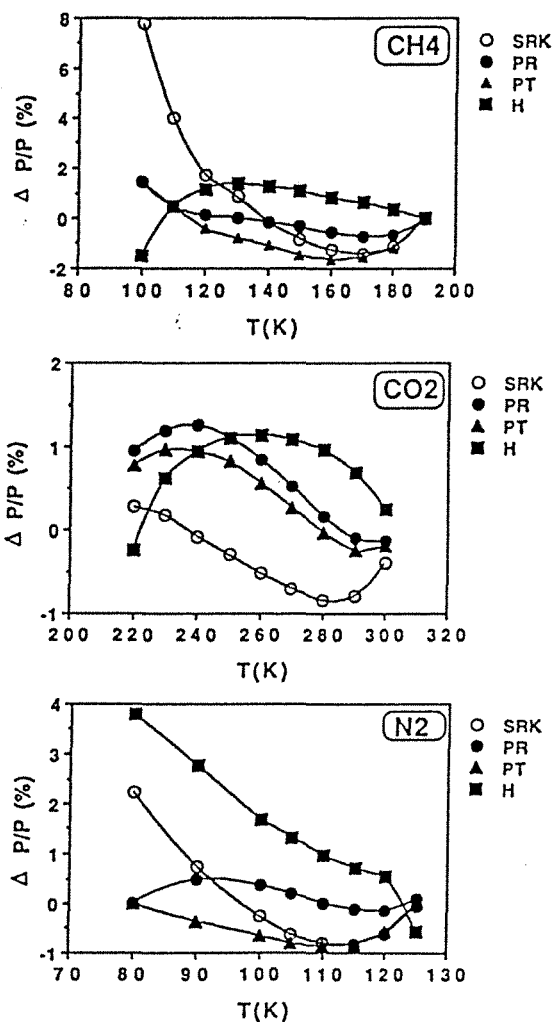


FIG. 1. Relative deviations ($\Delta P/P$ (%)) of the saturation pressure of the pure components (CH₄, N₂, CO₂) calculated by the four cubic EOS with respect to the values given by ANGUS et al. (1976, 1978, 1979). SRK: Soave-Redlich-Kwong; PR: Peng-Robinson; PT: Patel-Teja; H: Heyen.

Table 1: experimental data for the CH₄-N₂ system. #: number of data points.

T (K)	#	Pmin-Pmax (bar)	Source
95.00	9	0 - 5	Parrish and Hiza (1974)
99.82	11	1 - 7	Cines et al. (1953)
100.00	11	0 - 8	Parrish and Hiza (1974)
99.82	4	1 - 7	Bloomer et al. (1955)
105.00	9	1 - 11	Parrish and Hiza (1974)
110.00	11	1 - 15	Parrish and Hiza (1974)
110.93	14	2 - 14	Cines et al. (1953)
110.93	6	1 - 14	Bloomer et al. (1955)
113.15	8	11 - 18	Skripka et al. (1972)
115.00	10	1 - 20	Parrish and Hiza (1974)
120.00	10	2 - 25	Parrish and Hiza (1974)
122.04	7	3 - 28	Chang and Lu (1967)
122.00	13	2 - 28	Stryjek et al. (1974)
122.04	14	3 - 28	Cines et al. (1953)
122.04	8	3 - 28	Bloomer et al. (1955)
126.04	15	3 - 31	Cines et al. (1953)
127.59	17	3 - 35	Stryjek et al. (1974)
130.00	15	5 - 35	Cines et al. (1953)
138.46	10	6 - 38	Stryjek et al. (1974)
140.00	14	7 - 42	Kidnay et al. (1975)
144.26	9	10 - 38	Bloomer et al. (1955)
144.26	12	9 - 41	Cines et al. (1953)
149.83	10	10 - 46	Stryjek et al. (1974)
150.00	12	10 - 46	Kidnay et al. (1975)
155.37	10	14 - 45	Bloomer et al. (1955)
160.00	14	16 - 49	Kidnay et al. (1975)
160.93	13	16 - 49	Stryjek et al. (1974)
166.48	9	20 - 46	Bloomer et al. (1955)
170.00	13	24 - 50	Kidnay et al. (1975)
171.43	20	24 - 50	Chang and Lu (1967)
172.04	10	25 - 50	Stryjek et al. (1974)
172.04	6	27 - 45	Cines et al. (1953)
177.59	6	31 - 48	Bloomer et al. (1955)
177.59	12	30 - 49	Stryjek et al. (1974)
183.15	9	36 - 49	Stryjek et al. (1974)

The experimental data used to determine the interaction parameters k_{ij} are given in Tables 1, 2, and 3. Experimental data are usually reported with a relative deviation error of 0.5% in temperature, and 1% in pressure and mole fraction. The temperature and the composition of the liquid phase are given, and the computer program calculates the pressure (P_{calc}) and the composition of the vapour phase ($y_{i,calc}$). The fitting procedure was applied to each isothermal data set, in order to see whether a correction for the temperature dependence of the k_{ij} parameter was needed. The fitting was not performed in the critical region since it poorly constrains the value of k_{ij} for the other parts of the phase diagram. Moreover, such a procedure enables us to exclude experimental data which seem to be inconsistent with other data.

The CH₄-N₂ System

The interaction parameter was calculated for each isotherm from a set of 414 experimental data from 95 K up to 183.15 K (Table 1). In the 95–150 K temperature range, k_{ij} varies rather erratically between 0.029 and 0.034 (Fig. 2a). For temperatures higher than 150 K, k_{ij} increases to 0.06. The quality of fit is illustrated in Fig. 3a for an isotherm. The value of $[\Delta P/P]$ % is around 1%, except in the critical region.

The CO₂-CH₄ System

The interaction parameter was calculated for each isotherm from a set of 104 experimental data from 208.45 K to 270.00 K (Table 3): it varies between 0.092 and 0.111 (Fig. 2b). The value of $[\Delta P/P]$ % is around 1% (Fig. 3b), except in the critical region.

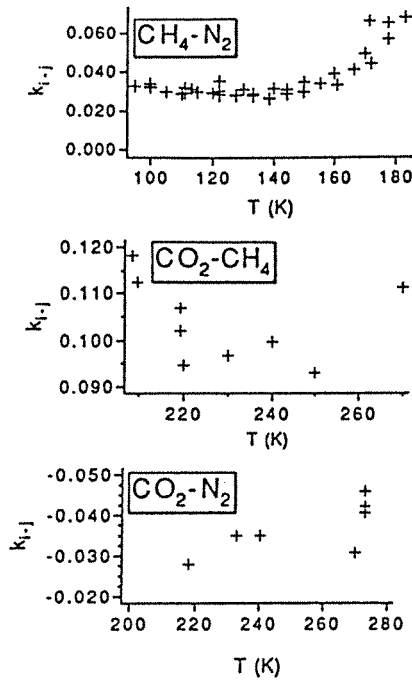


FIG. 2. Binary interaction parameters k_{ij} of the quadratic mixing rules associated with the SRK EOS, as a function of temperature calculated with experimental data listed in Tables 1, 2, and 3, for the $\text{CH}_4\text{-N}_2$, $\text{CH}_4\text{-CO}_2$, $\text{CO}_2\text{-N}_2$ systems.

The $\text{CO}_2\text{-N}_2$ System

The interaction parameter was calculated for each isotherm from a set of 105 experimental data from 218.15 K up to 273.15 K (Table 2): it varies between -0.028 and -0.046 (Fig. 2c). The quality of fit is not as good as for the other systems since $[\Delta P/P]\%$ reaches 4% and the critical pressure is strongly overestimated (Fig. 3c).

Calculations over the three binary systems show that it is not necessary to add a term for the temperature dependence of k_{ij} because relative deviations are not sensitive to the variation of k_{ij} around its mean value. Hence, it is possible to select a constant and optimal value of k_{ij} over the considered temperature range for each binary system: $k_{ij}(\text{CH}_4\text{-N}_2) = 0.03$; $k_{ij}(\text{CO}_2\text{-CH}_4) = 0.1$; $k_{ij}(\text{CO}_2\text{-N}_2) = -0.035$.

The Ternary $\text{CO}_2\text{-CH}_4\text{-N}_2$ System

Calculations assume that molecular interactions in the ternary system can be adequately described with the binary k_{ij} interaction parameters calculated previously. The predictions of each EOS were checked over a set of 182 experimental

Table 2 : experimental data for the $\text{CO}_2\text{-N}_2$ system. #: number of data points.

T (K)	#	Pmin-Pmax (bar)	Source
218.15	7	5 - 132	Zenner and Dana (1963)
232.85	8	10 - 139	Zenner and Dana (1963)
240.00	18	13 - 162	Al-Sahhaf et al. (1983)
270.00	34	32 - 125	Somait and Kidnay (1978)
273.15	4	55 - 120	Muirbrook and Prausnitz (1965)
273.15	10	35 - 120	Zenner and Dana (1963)
273.15	16	35 - 118	Yorizane et al. (1971)

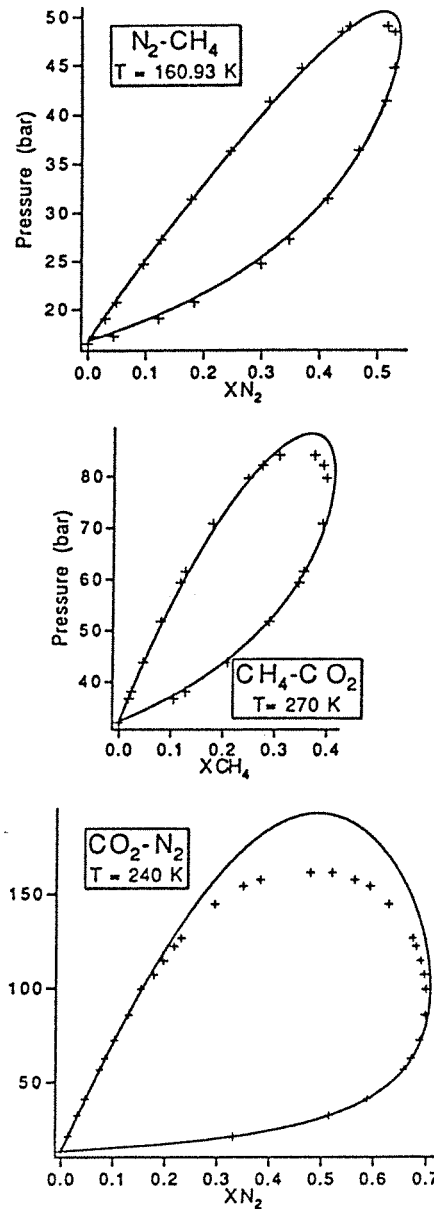


FIG. 3. $P\text{-}X$ isothermal curves of the binary systems. +: experimental data points; the curve is calculated with the SRK EOS. $\text{CH}_4\text{-N}_2$, $T = 161$ K, +: STRYKEK et al. (1974). $\text{CH}_4\text{-CO}_2$, $T = 270$ K, +: AL-SAHHAFF et al. (1983); $\text{CO}_2\text{-N}_2$, $T = 240$ K; +: AL-SAHHAFF et al. (1983).

data (Table 4). This results in a small increase in $[\Delta P/P]\%$ of about 2–3% on average and always smaller than 5%. This agreement is acceptable for the SRK EOS and indicates that it is not necessary to consider a three-body interaction by incorporation of a ternary interaction parameter, at least for the range of density and composition investigated in this work.

CALCULATIONS OF MOLAR VOLUMES

A Correlation Based on the Three-Corresponding State Principle (LEE and KESLER, 1975)

The use of a three-state corresponding principles method, such as the correlation of LEE and KESLER (1975), has been

Table 3 : experimental data for the CH₄-CO₂ system. #: number of data points.

T (K)	#	Pmin-Pmax (bar)	Source
208.45	9	51 - 61	Neumann and Walch (1968)
209.75	7	50 - 62	Neumann and Walch (1968)
219.26	12	58 - 65	Mraw et al. (1978)
219.26	6	6 - 40	Al-Sahhaf et al. (1983)
219.85	11	44 - 69	Neumann and Walch (1968)
230.00	15	9 - 71	Davalos et al. (1976)
240.00	13	13 - 78	Al-Sahhaf et al. (1983)
250.00	11	18 - 81	Davalos et al. (1976)
270.00	10	32 - 85	Davalos et al. (1976)
270.00	10	32 - 84	Somait and Kidnay (1978)
270.00	11	32 - 84	Al-Sahhaf et al. (1983)

recommended for the calculation of bulk properties of non-polar mixtures (LERMITE and VIDAL, 1988). LEE and KESLER (1975) calculate the compressibility factor ($Z(P_r, T_r)$) of the given fluid with an acentric factor ω , by linear interpolation between the compressibility factors of two reference fluids. One reference fluid has a spherical molecule (Ar or CH₄) with an acentric factor $\omega^{(s)} = 0$ and the other one is represented by a nondipolar and nonspherical molecule such as *n*-octane with an acentric factor $\omega^{(ns)} = 0.3978$:

$$(LK): Z(P_r, T_r) = Z^{(s)}(P_r, T_r) + [\omega/\omega^{(ns)}] \times [Z^{(ns)}(P_r, T_r) - Z^{(s)}(P_r, T_r)], \quad (18)$$

where $Z^{(s)}(P_r, T_r)$ is the compressibility factor of the reference fluid with a spherical molecule and $Z^{(ns)}(P_r, T_r)$ is the compressibility factor of the reference fluid with a nonspherical molecule. It is worth noting that reduced pressure and temperature of the mixture are calculated from the pseudocritical pressure and temperature of the mixture using the mixing rules proposed by LEE and KESLER (1975), which are described by Eqns. 19 to 25.

First, the pseudocritical compressibility factor $Z_{c_i}^*$ of each *i* component is calculated from Eqn. 19 using the corresponding acentric factor ω_i :

$$Z_{c_i}^* = 0.2905 - 0.085\omega_i. \quad (19)$$

The pseudocritical molar volume $v_{c_i}^*$ of component *i* is calculated using Eqn. 20:

$$v_{c_i}^* = Z_{c_i}^* RT_{c_i} / P_{c_i}, \quad (20)$$

where T_{c_i} and P_{c_i} are, respectively, the critical temperature and pressure of component *i*.

The pseudocritical properties of the mixture ($P_{c_m}^* - v_{c_m}^* - T_{c_m}^* - Z_{c_m}^*$) are calculated using the combining rules

$$v_{c_m}^* = 1/8 \sum \sum x_j x_k (v_{c_j}^{*1/3} + v_{c_k}^{*1/3})^3, \quad (21)$$

$T_{c_m}^*$

$$= 1/[8v_{c_m}^*] \cdot \sum \sum x_j x_k (v_{c_j}^{*1/3} + v_{c_k}^{*1/3})^3 \cdot (T_{c_j} T_{c_k})^{1/2}, \quad (22)$$

$$\omega_m^* = \sum x_j \omega_j, \quad (23)$$

where ω_m^* is the pseudo-acentric factor of the mixture

$$Z_{c_m}^* = 0.2905 - 0.085\omega_m^*, \quad (24)$$

$$P_{c_m}^* = Z_{c_m}^* RT_{c_m}^* / v_{c_m}^*. \quad (25)$$

A small modification of the original Lee-Kesler mixing rules was made by incorporating a new interaction parameter ξ_{ij} in Eqn. 22 in order to improve the accuracy of the cal-

culations in the critical region. The equation used for the calculation of $T_{c_m}^*$ was the following:

$$T_{c_m}^* = 1/[8v_{c_m}^*] \sum \sum x_j x_k (v_{c_j}^{*1/3} + v_{c_k}^{*1/3})^3 \times (T_{c_j} T_{c_k})^{1/2} (1 - \xi_{ij}). \quad (26)$$

Comparison with experimental data of ARAI et al. (1971) has shown that a non-zero ξ_{ij} was only necessary for the CO₂-N₂ system ($\xi_{CO_2-N_2} = -0.05$).

The compressibility factors of the reference fluids are calculated using a modified EOS of Benedict, Webb, and Rubin (BWR). BENEDICT et al. (1940) proposed an EOS, which is an extension of the virial EOS, which was applied successfully in oil engineering. LEE and KESLER (1975) modified the BWR and gave the following equation:

$$(MBWR): P_r v_r / T_r = 1 + B/v_r + C/v_r^2 + D/v_r^3 + \{c_4/[T_r v_r^2]\} \cdot \{\beta + \gamma/v_r\} \cdot \exp(-\gamma/v_r^2), \quad (27)$$

$$\text{with } v_r = P_c \cdot v / (RT_c), \quad P_r = P/P_{c_m}^*, \quad T_r = T/T_{c_m}^*,$$

$$B = b_1 - b_2/T_r - b_3/T_r^2 - b_4/T_r^3,$$

$$C = c_1 - c_2/T_r + c_3/T_r^2,$$

$$D = d_1 + d_2/T_r.$$

The values of the parameters used for the modified BWR EOS are given in Table 5. It is a priori possible to use the LK EOS for calculating directly the pressure of liquid-vapour equilibria and the molar volumes of both phases at equilibrium. However, calculations are much more complicated to perform than for cubic EOS due to the formula of the MBWR EOS; in addition, the accuracy of the pressure and molar volume calculations are no better than the accuracy obtained using a cubic EOS for the calculation of pressure (AL-SAHHAH et al., 1983).

The quality of the Lee-Kesler correlation for predicting molar volumes of saturated vapour and liquid of pure CO₂,

Table 4 : experimental data on the ternary system. #: number of data points.

T (K)	P (bar)	#	Source
220.00	20.000	9	Trappehl and Knapp (1989)
220.00	40.000	22	Trappehl and Knapp (1989)
220.00	60.800	8	Al-Sahhaf et al. (1983)
220.00	80.000	15	Trappehl and Knapp (1989)
220.00	91.190	8	Al-Sahhaf et al. (1983)
220.00	120.000	10	Trappehl and Knapp (1989)
220.00	121.590	7	Al-Sahhaf et al. (1983)
230.00	62.050	8	Al-Sahhaf (1990)
230.00	86.190	12	Al-Sahhaf (1990)
230.00	96.520	5	Al-Sahhaf (1990)
233.15	60.795	5	Sarashina et al. (1971)
233.15	81.060	8	Sarashina et al. (1971)
233.15	81.060	7	Al-Sahhaf et al. (1983)
233.15	101.325	5	Sarashina et al. (1971)
240.00	70.930	6	Al-Sahhaf et al. (1983)
240.00	91.190	11	Al-Sahhaf et al. (1983)
240.00	121.590	7	Al-Sahhaf et al. (1983)
250.00	89.630	7	Al-Sahhaf (1990)
250.00	103.420	5	Al-Sahhaf (1990)
253.15	60.795	3	Sarashina et al. (1971)
253.15	81.060	10	Sarashina et al. (1971)
253.15	101.325	4	Sarashina et al. (1971)
270.00	45.956	4	Somait and Kidnay (1978)
270.00	60.795	8	Somait and Kidnay (1978)
270.00	86.126	12	Somait and Kidnay (1978)
270.00	111.547	5	Somait and Kidnay (1978)
273.15	60.795	4	Sarashina et al. (1971)
273.15	81.060	9	Sarashina et al. (1971)
273.15	101.325	5	Sarashina et al. (1971)

Table 5. Coefficients of the modified BWR EOS used for the calculation of the molar volumes.

	Spherical fluid	Non-spherical fluid		Spherical fluid	Non-spherical fluid
b_1	0.1181193	0.2026579	c_3	0.0	0.016901
b_2	0.265728	0.331511	c_4	0.042724	0.041577
b_3	0.154790	0.027655	$10^4 d_1$	0.155488	0.48736
b_4	0.030323	0.203488	$10^4 d_2$	0.623689	0.0740336
c_1	0.0236744	0.0313385	β	0.65392	1.226
c_2	0.0186984	0.0503618	γ	0.060167	0.03754

CH₄, and N₂ is illustrated by the relative errors never exceeding 2%, except very near the critical point (Fig. 4). Two-parameter cubic SRK and PR EOS fail for calculating the molar volume of saturated liquids. Three-parameter cubic EOS show improved results, as is explained in the first section, but some accuracy is lost in the estimation of the saturated vapour (Fig. 4). The Heyen EOS is the most accurate of the cubic EOS for predicting the molar volume of saturated pure liquid but systematically underestimates the molar volumes of saturated vapours (Fig. 4).

Binary Mixtures

As the L-K correlation is the most accurate for calculating molar volumes of saturated liquids and vapours of pure CO₂, CH₄ and N₂, only this equation is tested on its ability to predict molar volumes of mixtures. The only available data are those of ARAI et al. (1971) on the CO₂-CH₄ and CO₂-N₂ systems. Relative deviations are smaller than 5%, except in the critical and the retrograde condensation regions, where relative errors can reach 10–20% (Fig. 5).

APPLICATION TO FLUID INCLUSIONS

v-X Diagrams of Binary Systems

Projections of liquid-vapour isotherms for the three binary N₂-CH₄, CO₂-CH₄, and CO₂-N₂ systems are given in Figs. 6, 7, and 8. The 300 K isotherm of the CO₂-CH₄ and CO₂-N₂ systems exhibits an irregular curvature in the liquid part near the critical point. This is due to some inconsistencies

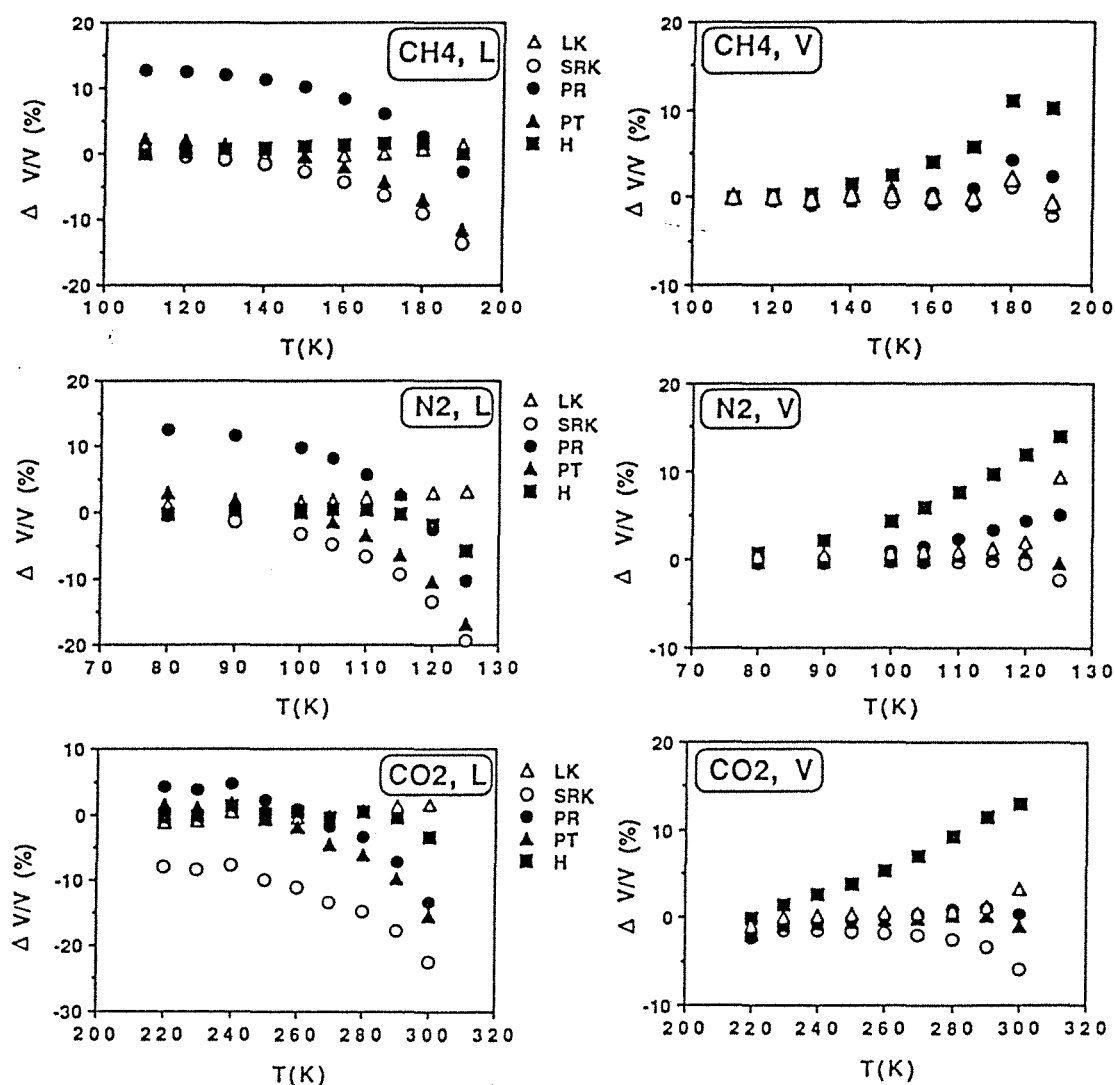


FIG. 4. Relative deviations of the molar volume of vapour and liquid phases along the saturation curve of pure components calculated using the LK, SRK, PR, PT, and H equations of state and the data of IUPAC tables (CH₄: ANGUS et al., 1978; CO₂: ANGUS et al., 1973, 1979); N₂: ANGUS et al., 1979).

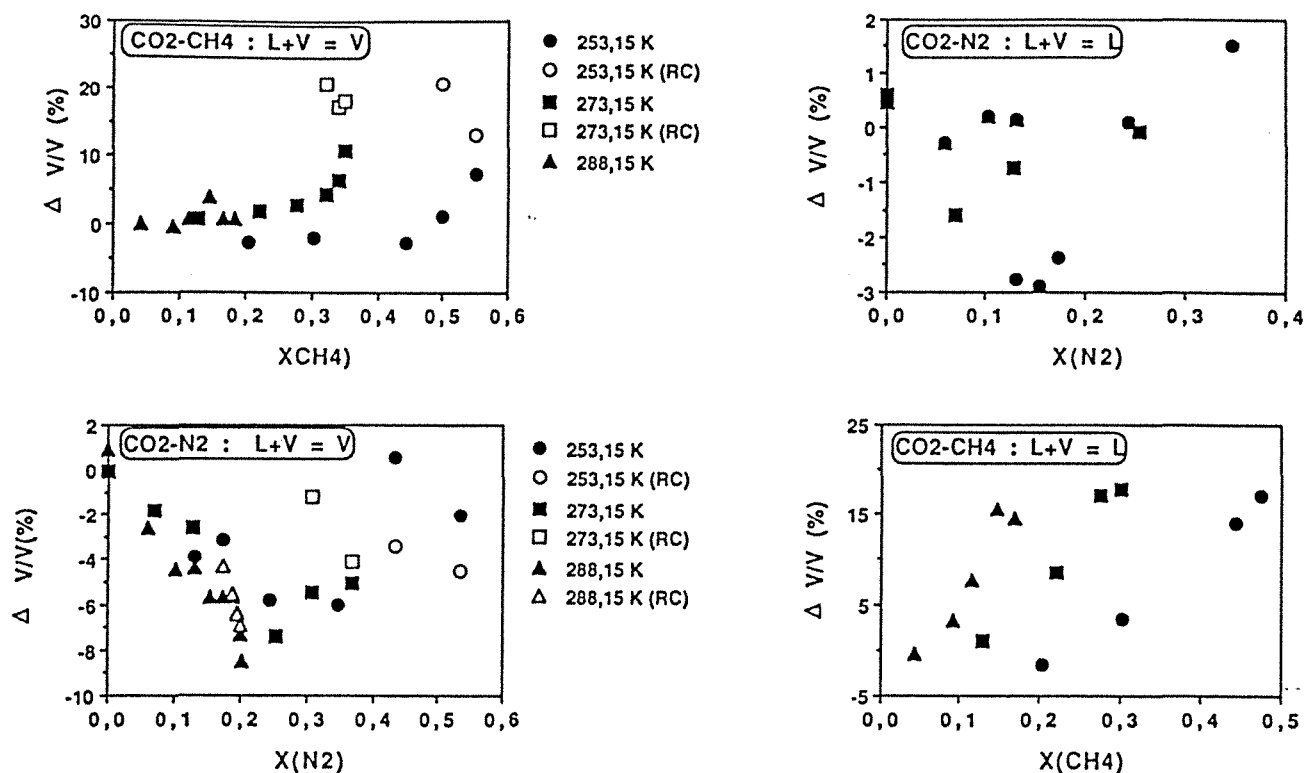


FIG. 5. Relative deviations of the molar volume of the vapour and liquid phases of CO₂-CH₄ and CO₂-N₂ mixtures calculated using the Lee and Kesler correlation (1975) and the experimental data of ARAI et al. (1971). RC: retrograde condensation.

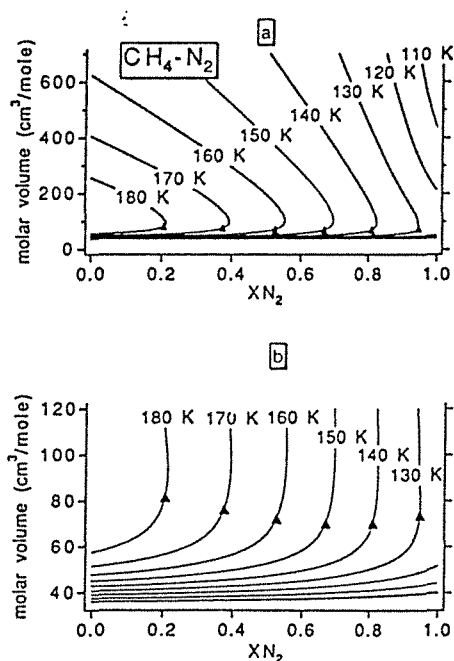


FIG. 6. Polybaric projections of liquid-vapour isotherms in the v - X plane for the CH₄-N₂ system. The triangles are the calculated critical points. The pressure of the saturation curve was calculated using the SRK EOS and the molar volume was modeled with the L-K EOS and modified BWR EOS. For homogenisation to the vapour phase ($L + V \rightarrow V$ transition), molar volumes are above the critical curve: use diagram *a*. For homogenisation to the liquid phase ($L + V \rightarrow L$ transition), molar volumes are below the critical curve: use diagram *b*, which is an expansion of diagram *a* for liquids.

introduced by the application of two different EOS in the critical region.

Comparison with v - X diagrams calculated using the Heyen EOS (HEYEN et al., 1982; DARIMONT and HEYEN, 1988) shows that our model significantly improves the accuracy of the molar volume of the vapour phase which was systematically underestimated by the Heyen EOS. This means that the internal pressure of a CO₂-CH₄ or CO₂-N₂ vapour phase and the concentration of these gases contained in water-bearing complex fluid inclusions was systematically overestimated using the v - X diagrams of HEYEN et al. (1982) and DARIMONT and HEYEN (1988).

Each isotherm is composed of two parts: (1) the first part corresponds to $L + V \rightarrow L$ transitions for molar volumes lower than the critical volume of the mixture; (2) the second part corresponds to $L + V \rightarrow V$ transitions for molar volumes above the critical volume of the mixture (RAMBOZ, 1980; KERKHOF, 1988). The v - X projections for the CO₂-CH₄ system given in this work do not apply to fluids with densities greater than the density of the liquid along the univariant $S_{\text{CO}_2} + L + V$ curve. For the CO₂-N₂ system, the v - X projection does not apply to fluids with high concentration ($X_{\text{N}_2} > 0.6-0.7$), since the critical curve is intersected by the univariant $S_{\text{CO}_2} + L + V$ curve (KERKHOF, 1988).

Application of the binary diagrams to fluid inclusion studies for the purpose of determining the molar volumes requires one to know (1) the chemical composition in one binary system, determined for instance by micro-Raman spectrometry; (2) the temperature (T_h) of the phase transition, measured by microthermometric techniques, which permits the

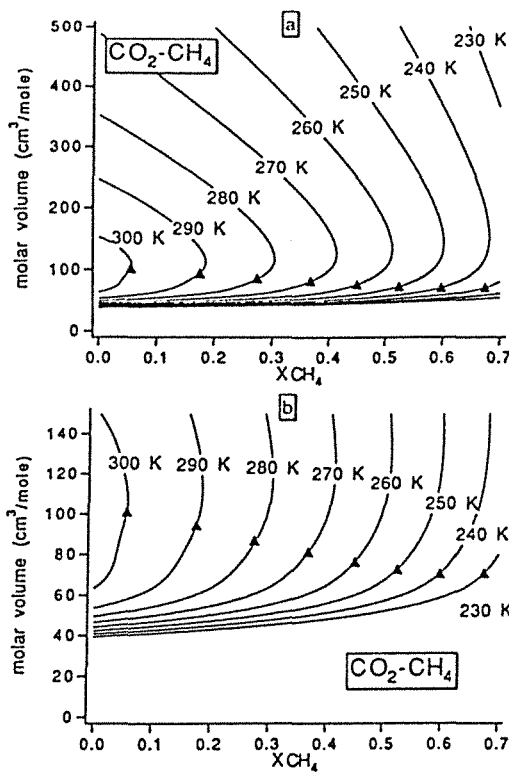


FIG. 7. Polybaric projections of liquid-vapour isotherms in the v - X plane for the CO_2 - CH_4 system. The pressure of the saturation curve was calculated using the SRK EOS and the molar volume was modelled with the L-K EOS and modified BWR EOS. The triangles are the calculated critical points. For homogenisation to the vapour phase ($L + V \rightarrow V$ transition), molar volumes are above the critical curve: use diagram *a*. For homogenisation to the liquid phase ($L + V \rightarrow L$ transition), molar volumes are below the critical curve: use diagram *b*, which is an expansion of diagram *a* for liquids.

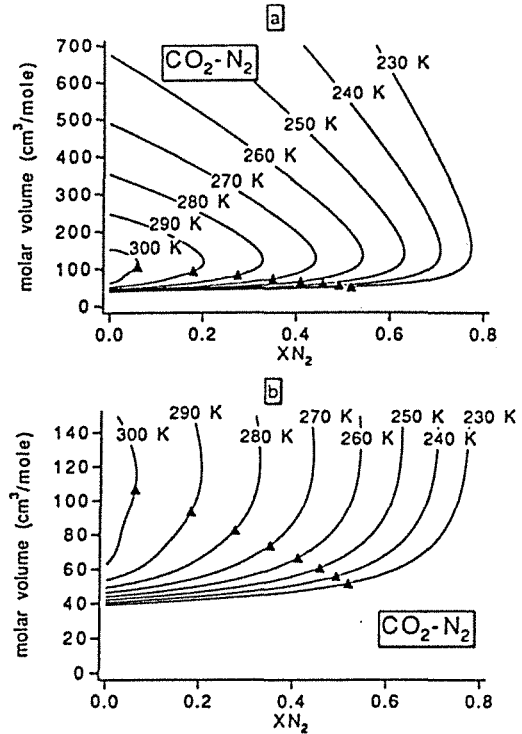


FIG. 8. Polybaric projections of liquid-vapour isotherms in the v - X plane for the CO_2 - N_2 system. The pressure of the saturation curve was calculated using the SRK EOS and the molar volume was modelled with the L-K EOS and modified BWR EOS. The triangles are the calculated critical points. For homogenisation to the vapour phase ($L + V \rightarrow V$ transition), molar volumes are above the critical curve: use diagram *a*. For homogenisation to the liquid phase ($L + V \rightarrow L$ transition), molar volumes are below the critical curve: use diagram *b*, which is an expansion of diagram *a* for liquids.

selection of the isotherm; and (3) the type of phase transition ($L + V \rightarrow L$ or $L + V \rightarrow V$) to choose the proper part of the isotherm (RAMBOZ, 1980). The molar volume of the fluid is located at the intersection of the straight line defined by the molar fraction of one component, with the proper part of the isotherm defined by T_h and the type of phase transition. This method is exemplified in Table 6. As it was already emphasized by RAMBOZ (1980) and HEYEN et al. (1982), this procedure cannot be used if a clathrate is present at T_h since the v - X properties of the volatile part of the inclusion are affected by the presence of clathrates.

The Ternary System: Its Calculation and a Simplified Projection

It is not possible to construct v - X diagrams for the ternary system for the temperature range of interest. Consequently, it will be useful to know if the molar volume of the common CO_2 -rich fluids in the ternary system could be estimated using the v - X diagrams established for the CO_2 - CH_4 and CO_2 - N_2 binary systems. For CO_2 -rich fluids ($X_{\text{CO}_2} > 0.6$), isochores calculated by the model for the liquid and the vapour along the L - V curve form almost straight and parallel lines on a composition diagram (Fig. 9). Therefore, it is possible to use

Table 6. Comparison of the molar volume of CO_2 -rich fluids, derived from calculations in the ternary system, with estimations obtained using empirical equations (28-31) and v - X projections in the CH_4 - CO_2 and N_2 - CO_2 systems.

T_h	ϕ	X_{CO_2}	X_{CH_4}	X_{N_2}	v	$X_{\text{CO}_2}^*$	$X_{\text{CH}_4}^*$	v^*	$X_{\text{CO}_2}^*$	$X_{\text{N}_2}^*$	v^*
0	L	.80	.10	.10	58.7	.78	.22	58.0	.82	.18	58.4
-20	L	.80	.10	.10	48.4	.78	.22	48.6	.82	.18	48.0
-40	L	.80	.10	.10	43.5	.78	.22	43.9	.82	.18	43.1
-20	L	.60	.20	.20	61.0	.56	.44	61.8	.64	.36	58.1
-40	L	.60	.20	.20	49.6	.56	.44	50.4	.64	.36	48.1
0	V	.80	.20	.20	320	.82	.18	324	.78	.22	316
-20	V	.80	.20	.20	646	.82	.18	658	.78	.22	635

T_h : homogenization temperature; ϕ : phase to which the homogenization occurs (L: liquid; V: vapour); X_i : mole fraction of component i in the ternary system; X_i^* : pseudo-mole fraction of component i calculated from one of the empirical equations (28-31) in one of the binary systems; v^* : molar volume calculated from a v - X projection in a binary system using the corresponding X_i^*

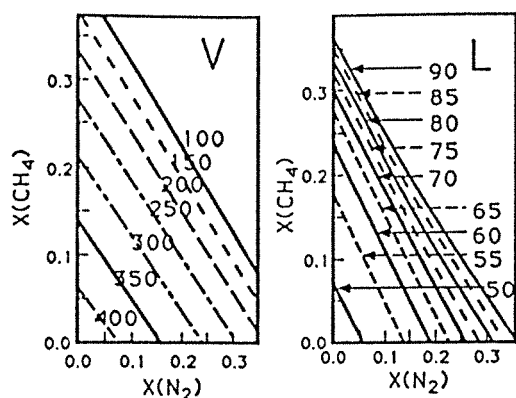


FIG. 9. Projection of isochores ($\text{cm}^3 \cdot \text{mol}^{-1}$) of the saturated liquid (L) and vapour (V) in the composition plane X_{CO_2} - X_{N_2} and X_{CO_2} - X_{CH_4} at 0°C . The origins of the diagrams correspond to pure CO_2 .

the v - X projections for the CO_2 - CH_4 and CO_2 - N_2 system by calculating a pseudo-composition (X_i^*) in these binary systems.

Projection in the CO_2 - CH_4 System

$$X_{\text{CH}_4}^* = 1.1(X_{\text{CH}_4} + X_{\text{N}_2})$$

for an homogenisation to the liquid. (28)

$$X_{\text{CH}_4}^* = 0.9(X_{\text{CH}_4} + X_{\text{N}_2})$$

for an homogenisation to the vapour. (29)

Projection in the CO_2 - N_2 system

$$X_{\text{N}_2}^* = 0.9(X_{\text{CH}_4} + X_{\text{N}_2})$$

for an homogenisation to the liquid. (30)

$$X_{\text{N}_2}^* = 1.1(X_{\text{CH}_4} + X_{\text{N}_2})$$

for an homogenisation to the vapour. (31)

The pseudo-compositions, calculated from appropriate previous equations, are then combined with the temperature of phase transition to estimate the molar volume using the appropriate v - X diagram of the CO_2 - CH_4 or CO_2 - N_2 system. The validity of this method has been verified for several temperatures and compositions (Table 6). Therefore, fluid inclusionists need only the v - X projections of the CO_2 - CH_4 and CO_2 - N_2 systems to estimate the molar volume of CO_2 -rich fluids in the ternary system.

CONCLUSION

The use of two kinds of EOS, one for calculating the saturation pressure (PR or SRK) and the other for calculating the molar volume (the Lee-Kesler correlation), is key to obtaining the best accuracy in the calculation of the molar volume of the nonaqueous phase. The v - X projections given in this paper can be used in fluid inclusion studies for determining the molar volume of fluids in the CO_2 - CH_4 , CO_2 - N_2 , and N_2 - CH_4 binary systems. In addition, it has been

demonstrated that the determination of the molar volume of CO_2 -rich fluids ($X_{\text{CO}_2} > 0.6$) within the ternary CO_2 - CH_4 - N_2 system can be carried out using the v - X projections of the CO_2 - CH_4 and CO_2 - N_2 systems after modification of the ternary composition by empirical formulae. Further studies will attempt to improve the calculation in the critical region and to model the $S_{\text{CO}_2} + L + V$ solubility curve.

Acknowledgments—We have appreciated very much the careful reviews by Z. Duan, A. M. Kerkhof, and J. C. Seitz. We thank also M. McKibben and D. Hall for all their constructive comments.

Editorial handling: M. A. McKibben

REFERENCES

- AL-SAHHAFF T. A. (1990) Vapor-liquid equilibria for the ternary $\text{N}_2 + \text{CO}_2 + \text{CH}_4$ system at 230 and 250 K. *Fluid Phase Equilibria* 55, 159-172.
- AL-SAHHAFF T. A., KIDNAY A. J., and SLOAN E. D. (1983) Liquid-vapor equilibria in the $\text{N}_2 + \text{CO}_2 + \text{CH}_4$ system. *Ind. Eng. Chem. Fundam.* 22, 372-380.
- ANGUS S., ARMSTRONG B., and DE RENCK K. M., eds (1976) *International Thermodynamic Tables of Fluid State-3, Carbon dioxide*. Pergamon Press.
- ANGUS S., ARMSTRONG B., and DE RENCK K. M., eds (1978) *International Thermodynamic Tables of Fluid State-5, Methane*. Pergamon Press.
- ANGUS S., ARMSTRONG B., and DE RENCK K. M., eds (1979) *International Thermodynamic Tables of Fluid State-6, Nitrogen*. Pergamon Press.
- ARAI Y., KAMINISHI G., and SAITO S. (1971) The experimental determination of the P-V-T-X relations for the carbon dioxide-nitrogen and carbon dioxide-methane systems. *J. Chem. Eng. Japan* 4, 113-122.
- ASSELIN L., BOGDANIC G., and VIDAL J. (1979) A versatile algorithm for calculating vapour-liquid equilibria. *Fluid Phase Equilibria* 3, 273-290.
- BENEDICT M., WEBB G. B., and RUBIN L. C. (1940) An empirical equation for thermodynamic properties of light hydrocarbons and their mixtures. *J. Chem. Phys.* 8, 334-345.
- BURRUS R. C. (1981) Analysis of fluid inclusions: phase equilibria at constant volume. *Amer. J. Sci.* 281, 1104-1126.
- BLOOMER O. T., EAKIN B. E., ELLINGTON R. T., and GAMI D. C. (1955). Thermodynamic properties of methane-nitrogen mixtures. *Inst. Gas. Techn. Res. Bull.* 21
- CHANG S. D. and LU B. C. Y. (1967) Vapor-liquid equilibria in the nitrogen-methane ethane system. *Chem. Eng. Progr. Symp. Ser.* 63
- CINES M. R., ROACH J. T., HOGAN R. J., and ROLAND C. H. (1953) Nitrogen-methane vapor-liquid equilibria. *Chem. Eng. Progr. Ser.* 49, 1-100.
- DARIMONT A. and HEYEN G. (1988) Simulation des équilibres de phase dans le système CO_2 - N_2 . Applications aux inclusions fluides. *Bull. Mineral* 111, 179-182.
- DAVALOS J., ANDERSON W. R., PHELPS R. E., and KIDNAY A. J. (1976) Liquid-vapor equilibria at 250 K for systems containing CH_4 , C_2H_6 and CO_2 . *J. Chem. Eng. Data* 21, 81-84.
- DUBESSY J., THIERY R., and CANALS M. (1992) Modelling of phase equilibria involving mixed gas clathrates. Application to the determination of molar volume of the vapour phase and of the salinity of the aqueous solution in fluid inclusions. *Eur. Mineral.* 4, 873-884.
- HERSKOWITZ M. and KISCH H. J. (1984) An algorithm for finding composition, molar volume and isochors of CO_2 - CH_4 fluid inclusions from T_h and T_{im} (for $T_h < T_{im}$). *Geochim. Cosmochim. Acta* 48, 1581-1587.
- HEYEN G. (1981) A cubic equation of state with extended range of application, Second World of Congress of Chemical Engineering, Montreal, 4-9 October 1981. In *Chemical Engineering Thermodynamics* (ed. by S. A. NEWMAN), p. 175. Ann Arbor Sci.

- HEYEN G., RAMBOZ C., and DUBESSY J. (1982) Simulation des équilibres de phases dans le système $\text{CO}_2\text{-CH}_4$ en dessous de 50°C et de 100 bar. Application aux inclusions fluides. *C. R. Acad. Sc. Paris* 294, 203-206.
- KERKHOF A. M. VAN DEN (1988) The system $\text{CO}_2\text{-CH}_4\text{-N}_2$ in fluid inclusions: theoretical modelling and geochemical applications. PhD dissertation, Free Univ.
- KIDNAY A. J., MILLER R. C., PARRISH W. R., and HIZA M. J. (1975) Liquid-vapour phase in the $\text{N}_2\text{-CH}_4$ system from 130 to 180K. *Cryogenics* 15, 531-540.
- LEE B. I. and KESLER M. G. (1975) A generalized thermodynamic correlation based on three-parameter corresponding states. *AIChE J.* 21, 510-527.
- LERMITE Ch. and VIDAL J. (1988) Les règles de mélange appliquées aux équations d'état. *Rev. Inst. Français Pétr.* 43, 73-94.
- MRAW S. C., HWANG S. C., and KOBAYASHI R. (1978) Vapor-liquid equilibrium of the $\text{CO}_2\text{-CH}_4$ system at low temperatures. *J. Chem. Eng. Data* 23, 135-139.
- MUIRBROOK N. K. and PRAUSNITZ J. M. (1965) Multicomponent vapor-liquid equilibria at high pressures. Part I: experimental study of the nitrogen-oxygen-carbon dioxide system at 0°C . *AIChE J.* 11, 1092-1096.
- NEUMANN P. N. A. and WALCH W. (1968) Dampf/Flüssigkeits-Gleichgewicht $\text{CH}_4\text{-CO}_2$ in Bereich tiefer Temperaturen und kleiner CO_2 -Molenbrüche. *Chem. Ing. Techn.* 40, 241-244.
- PARRISH W. R. and HIZA M. J. (1974) Liquid-vapor equilibria in the nitrogen-methane system between 95 and 120 K. *Adv. Cryogen. Eng.* 19, 300-308.
- PATEL N. C. and TEJA A. S. (1982) A new cubic equation of state for fluids and fluid mixtures. *Chem. Eng. Sci.* 37, 463-473.
- PENELOUX A., RAUZY E., and FREZE R. (1982) A consistent volume correction for Redlich-Kwong-Soave volumes. *Fluid Phase Equilibria* 8, 7-23.
- PENG D. Y. and ROBINSON D. B. (1976) A new two constants equation of state. *Ind. Eng. Chem. Fundam.* 15, 59-64.
- PRAUSNITZ J. M., LICHTENHALER R. N., and DE AZEVEDO E. G. (1986) *Molecular Thermodynamics of Fluid-phase Equilibria*, 2nd ed. Prentice-Hall.
- RAMBOZ C. (1980) Problèmes posés par la détermination de la composition des fluides carboniques complexes à l'aide des techniques microthermométriques. *C. R. Acad. Sci.* 290, 499-502.
- REID R. C., PRAUSNITZ J. M., and SHERWOOD T. K. (1977) *The Properties of Gases and Liquids*, 3rd ed. McGrawHill.
- SARASHINA E., ARAI Y., and SAITO S. (1971) Vapor-liquid equilibria for the nitroge-methane-carbon dioxide system. *J. Chem. Eng. Japan* 4, 377-378.
- SKRIPKA V. G., NIKITINA I. E., ZHDANOVITCH I. A., SIROTNIN A. G., and BEN'JAMINOVICH O. A. (1972) Equilibres liquide-vapeur aux basses températures dans les systèmes binaires formes par les composants du gaz naturel. *Gazov. Pro.* 15, 35-46.
- SOAVE G. (1972) Equilibrium constants from a modified Redlich-Kwong equation of state. *Chem. Eng. Sci.* 27, 1197-1203.
- SOMAIT F. A. and KIDNAY A. J. (1978) Liquid-vapor equilibria for systems containing N_2 , CH_4 and CO_2 . *J. Chem. Eng. Data* 23, 301-305.
- STRYJEK R., CHAPELEAR P. S., and KOBAYASHI R. (1974) Low-temperature vapor-liquid equilibria of nitrogen-methane system. *J. Chem. Eng. Data* 19, 334-339.
- TRAPPEHL G. and KNAPP H. (1989) Vapour-liquid equilibria in the ternary mixture $\text{N}_2 + \text{CH}_4 + \text{CO}_2$ and the quaternary mixture $\text{N}_2 + \text{CH}_4 + \text{C}_2\text{H}_6 + \text{C}_3\text{H}_8$. *Cryogen.* 29, 42-50.
- VIDAL J. (1978) Mixing rules and excess properties in cubic equations of state. *Chem. Eng. Sci.* 33, 787-791.
- VIDAL J. (1983) Equations of state—Reworking the old forms. *Fluid Phase Equilibria* 13, 15-33.
- YORIZANE M., YOSHIMURA S., MASUOKA H., MIYANO Y., and KAKIMOTO Y. (1971) New procedure for vapor-liquid equilibria. Nitrogen + carbon dioxide, methane + freon 22, and methane + freon 12. *J. Chem. Eng. Data* 30, 174-176.
- ZENNER G. H. and DANA L. I. (1963) Liquid-vapor equilibrium compositions of carbon dioxide-oxygen-nitrogen-mixtures. *Chem. Eng. Progr. Ser.* 59, 36-61.

Improved modelling of vapour–liquid equilibria up to the critical region. Application to the CO₂–CH₄–N₂ system

R. Thiéry^{*}, J. Dubessy

*CREGU, Centre de Recherche sur la Géologie des Matières Minérales et Énergétiques, BP 23,
54501-Vandoeuvre-les-Nancy Cedex, France*

Received 30 June 1995; accepted 30 January 1996

Abstract

A new procedure for extending the applicability of cubic EOS to critical conditions is described. This method requires to determine two sets of optimum binary interaction parameters for the non-critical and critical parts of *PTx* experimental data of binary systems. The effective binary interaction parameters are calculated by interpolation between these two sets of binary interaction parameters. The interpolation factor is a function of a distance from critical conditions, which is evaluated from an *a priori* calculation of the molar volumes of coexistent liquid and vapour. The algorithm is shown to improve the prediction of the Soave–Redlich–Kwong equation of state in the ternary CO₂–CH₄–N₂ system. Application conditions of this approach to other systems are discussed.

Keywords: Theory; Equation of state; Cubic; Critical; CO₂–CH₄–N₂ mixtures

1. Introduction

Cubic equations of state (EOS) are successful for predicting fluid phase equilibria of nonpolar mixtures with a few number of parameters. However, they cannot be used for critical conditions, as they overestimate the extent of the liquid–vapour immiscibility. Any calculated liquid–gas isotherm of a binary system deviates largely from the experimental data in the critical region on a *Px* diagram. This is a serious problem when an accurate modelling of phase equilibria is required, e.g. for fluid inclusion studies in the CO₂–CH₄–N₂ system [1,2]. Several attempts have been proposed for improving the predictions for the CO₂–CH₄–N₂ system. A first solution is to use other mixing and combining rules [3], or to incorporate more parameters to the equation [3,4]. These methods generally improve the predictions of volumetric properties of fluids, but significant deviations are still observed

^{*} Corresponding author.

for the critical conditions. Kreglewski and Hall [5] proposed a non-cubic EOS for the binary $\text{CO}_2\text{-CH}_4$ and $\text{CO}_2\text{-N}_2$ system, and they applied a semi-empirical correction in the critical regions. However, as it can be seen on their published figures (Figs. 1 and 5, their article), their model introduces unrealistic discontinuity and dissymmetry in the critical part of isothermal P_x curves.

It is well known that the theoretical basis of a cubic EOS is not adequate for predicting the properties of a system near its critical state. Indeed, cubic EOS are based on the assumption of the "mean molecular field", which assumes that the potential energy field exerted around a molecule is practically the same for each molecule of a phase. This simplification is clearly not valid for critical conditions, which are characterized by large density fluctuations at the molecular scale. Surprisingly, it remains possible to correlate experimental critical points of a binary system with a simple cubic EOS [6,7]. However, this requires the use of binary interaction parameters (BIP), whose values are

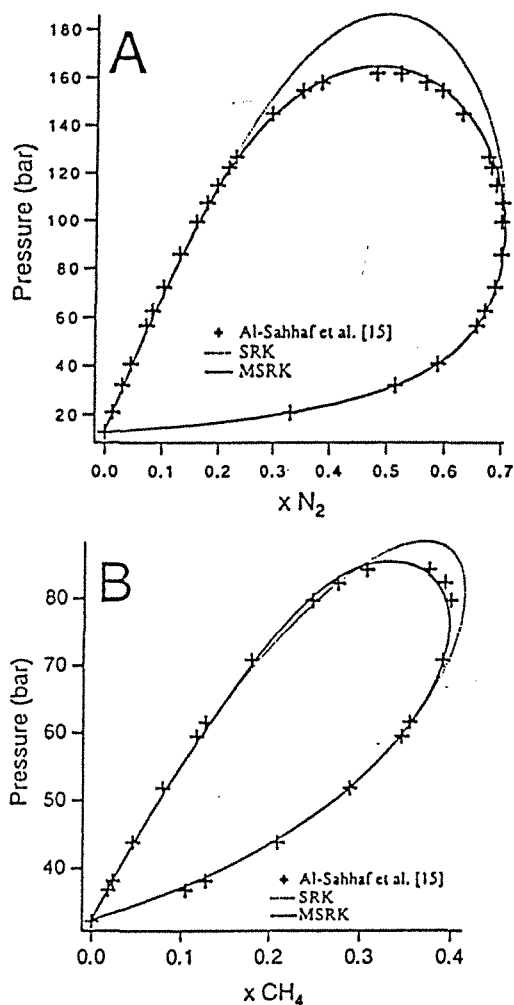


Fig. 1. Isothermal P_x projections of the liquid-vapour immiscibility region. A, at -33.15°C for the $\text{CO}_2\text{-N}_2$ system; B, at -3.15°C for the $\text{CO}_2\text{-CH}_4$ system. The experimental data are those of Al-Sahhaf et al. [15]. The dotted curve is for the SRK EOS, whereas the solid curve is for the MSRK EOS, with variable BIP.

largely different from those used for liquid–vapour equilibria, and therefore, are not suitable outside the critical region. The aim of this paper is to show that cubic EOS are capable of representing vapour–liquid equilibria, both for critical and non-critical conditions, by building a model whose BIP are allowed to vary as a function of the distance from critical conditions [8–10]. An interpolation parameter is used in order to join the two areas of applicability of cubic EOS without discontinuity. First, the definition of the interpolation factor is given. Two sets of optimum BIP are determined from experimental data. Then, the improvements on the prediction of phase equilibria are reported.

2. The algorithm

The Soave–Redlich–Kwong (SRK) EOS [11] has been chosen as a basis for modelling liquid–gas equilibria of the $\text{CO}_2\text{--CH}_4\text{--N}_2$ system. The usual quadratic and combining rules are used for both a and b parameters of the SRK EOS [12]:

$$a = \sum_i \sum_j x_i x_j a_{ij} (1 - k_{a,ij}) \quad (1)$$

$$b = \sum_i \sum_j x_i x_j b_{ij} (1 - k_{b,ij}) \quad (2)$$

$$a_{ij} = \sqrt{a_i a_j} \quad (3)$$

$$b_{ij} = (b_i + b_j) / 2 \quad (4)$$

where $k_{a,ij}$ and $k_{b,ij}$ are the binary interaction parameters (BIP) respectively on the a and b parameters, which are specific to the interactions between species i and j .

The SRK EOS has been successfully applied to the $\text{CO}_2\text{--CH}_4\text{--N}_2$ system with only one BIP on the a parameter [1,2], except in the critical and retrograde condensation regions. The pressure is strongly overestimated in the critical region. Pressure discrepancies may be as large as 25 bar for the $\text{CO}_2\text{--N}_2$ system at -30°C (Fig. 1) and the CO_2 content of the critical point is always underestimated (up to 10%) for the $\text{CO}_2\text{--N}_2$ and the $\text{CO}_2\text{--CH}_4$ system (Fig. 1(A) and 1(B)). Therefore, an improvement of the EOS is necessary for quantitative use. However, the $\text{CH}_4\text{--N}_2$ system is well predicted by the SRK EOS [1]. Discrepancies near critical points are not important enough and do not justify a modification of the model for the $\text{CH}_4\text{--N}_2$ system.

As stated above, a new interpolation parameter, denoted as ξ , is introduced for calculating effective BIP, as follows

$$k_{a,ij} = \xi k_{a,ij}^c + (1 - \xi) k_{a,ij}^{nc} \quad (5a)$$

$$k_{b,ij} = \xi k_{b,ij}^c + (1 - \xi) k_{b,ij}^{nc} \quad (5b)$$

where superscripts nc and c denote non-critical and critical conditions respectively. ξ takes values ranging between 0 (non-critical state) and 1 (critical state); $k_{a,ij}^{nc}$, $k_{b,ij}^{nc}$, $k_{a,ij}^c$, and $k_{b,ij}^c$ are BIP, determined independently by fitting the EOS with experimental data. ξ should represent a function of the distance of the state of the fluid with respect to critical conditions. We can make use of the fact that molar volumes of the gas and liquid phases become almost equal for near-critical conditions. Accordingly, ξ is expressed as a function of ν_r , the ratio of the molar volume of the gas (ν_G) to the

molar volume of the coexistent liquid (ν_L):

Table 1
Binary interaction parameters

Systems	Non-critical part		Critical part	
	k_a^{nc}	k_b^{nc}	k_a^c	k_b^c
CO ₂ -N ₂	-0.035	0.0	-0.116	-0.071
CO ₂ -CH ₄	0.1	0.0	0.074	-0.051
CH ₄ -N ₂	0.03	0.0	0.03	0.0

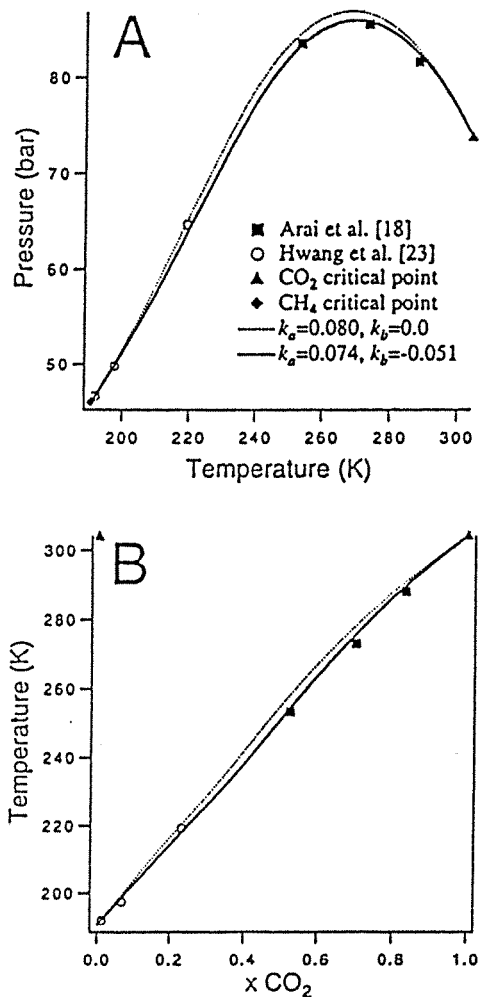


Fig. 2. The critical curve of the CO₂-CH₄ system. A, *PT* projection. B, *Tx* CO₂ projection. Experimental data are those of Arai et al. [18] and Hwang et al. [23]. The dotted curve is the critical line calculated by the SRK EOS with one BIP on the *a* parameter ($k_a^c = 0.08$). A more satisfactory agreement with experimental data is obtained by considering two BIP on the *a* and *b* parameters (solid curve, $k_a^c = 0.074$, $k_b^c = -0.051$).

$$\nu_r = \frac{\nu_G}{\nu_L} \quad (6)$$

where ν_G and ν_L are calculated with the classical SRK EOS ($\xi = 0$). The following threshold function is used to describe the dependence of the ξ parameter to ν_r :

$$\xi = \exp(-A(s - \nu_r)^2) \text{ for } \nu_r > s \quad (7a)$$

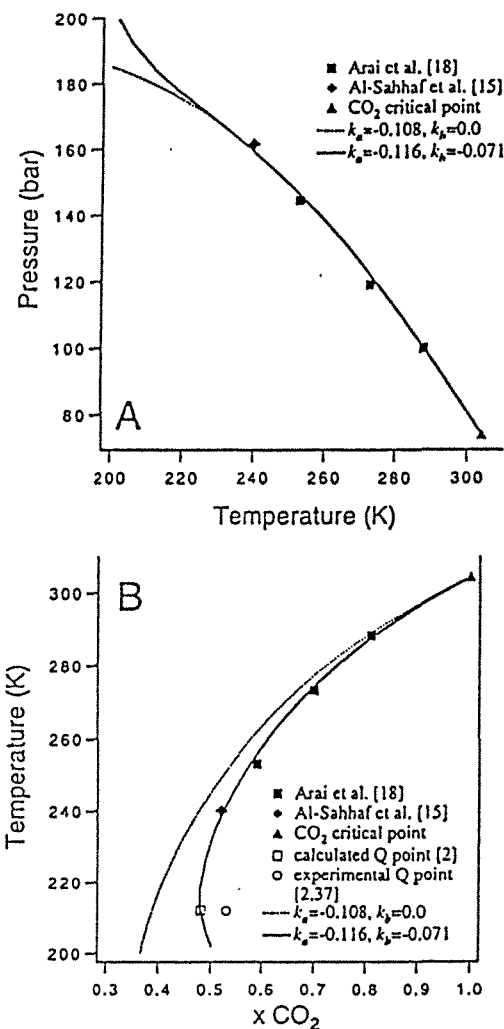


Fig. 3. The critical curve of the CO₂-N₂ system. A, *PT* projection, B, *Tx* projection. Experimental data used for fitting BIP are those of Arai et al. [18] and Al-Sahhaf et al. [15]. The dotted curve is calculated by the SRK EOS by using only one BIP on the *a* parameter ($k_a^c = -0.108$). Closer agreement with experimental data is obtained with two BIP on the *a* and *b* parameters (solid curve, $k_a^c = -0.116, k_b^c = -0.071$). The intersection of the CO₂-N₂ critical curve with the CO₂ solid-liquid-gas curve has been calculated with the MSRK EOS at $T = -61.1^\circ\text{C}$ and $x_{N_2} = 0.53$ (empty square, [2]). This calculated Q point is in fair agreement with the estimation of Kerkhof [37], using synthetic fluid inclusions ($T = -61.2^\circ\text{C}$ and $x_{N_2} = 0.47$).

$$\xi = 1.0 \text{ for } \nu_r < s \quad (7b)$$

As required, this function is equal to 1 for critical states and to 0 for non-critical conditions. A function, that mimics a half gaussian bell curve, has been used for the transition region between the critical and non-critical fields. This function has been found to give the best results, whereas other tested functions, such a linear or a parabolic ramp, fail to reproduce adequately the shape of the isothermal Px isotherms. Two parameters are involved for the gaussian transition (Eq. (7)). The first parameter, denoted as s , influences the position of the ramp with respect to ν_r values of reduced molar volumes (Eq. (6)). The second parameter, denoted as A , has an influence on the slope of the ramp between critical and non-critical conditions. Values of A and s parameters have been estimated crudely for the $\text{CO}_2\text{-CH}_4\text{-N}_2$ system from experimental data of the binary subsystems ($A = 0.5$ and $s = 1.05$).

In short, two steps are required for calculating a liquid–vapour equilibrium point. The first one is the calculation of a point with the usual BIP that are suitable in the non-critical part.

$$k_{a,ij} = k_{a,ij}^{nc} \quad (8a)$$

$$k_{b,ij} = k_{b,ij}^{nc} \quad (8b)$$

The molar volumes of the coexistent liquid (ν_L) and vapour (ν_V) phases are calculated. The interpolation factor ξ is estimated from Eqs. (7a) and (7b). Then, new BIP are calculated from Eqs. (5a) and (5b). These effective BIP are used for calculating the correct liquid–vapour equilibria point. This algorithm has been implemented with thermodynamic calculations packages for calculating Px isotherms, PT isopleths and other projections of the liquid–vapour immiscibility regions [13,14]. Contrary to the empirical correction proposed by Kreglewski and Hall [5] in the critical region, it is not necessary here to iterate until consistent values of the ξ interpolation factor and the ν_r ratio of molar volumes are obtained. Such iterations would increase a lot the complexity of calculations, and

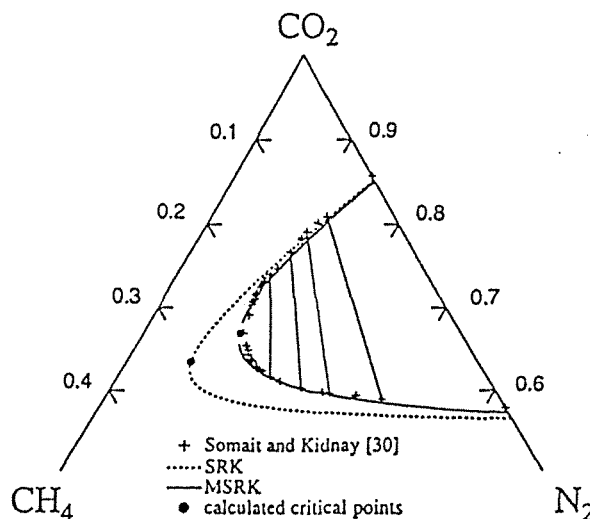


Fig. 4. Isothermal and isobaric liquid–vapour immiscibility region on a ternary $\text{CO}_2\text{-CH}_4\text{-N}_2$ diagram. The experimental data are those of Somait and Kidnay [30] at -3.15°C and 96.3 bar. The dotted curve is for the SRK EOS, whereas the solid curve is for the MSRK EOS with variable BIP. Calculated critical points and some experimental tie-lines are drawn too.

the accuracy of results could not be improved significantly.

3. The fitting of binary interaction parameters in the CO₂–CH₄–N₂ system

Best-fitting k_{ij}^{nc} BIP have been determined in a previous study in the non-critical region [1] from experimental data of the binary systems CH₄–N₂, CO₂–N₂ and CO₂–CH₄ [15–36]. The $k_{b,ij}^{nc}$ values have been set to zero, and the $k_{a,ij}^{nc}$ values are temperature independent (Table 1).

Optimum k_{ij}^c BIP have been determined along the critical locus curve for the CO₂–N₂ and the CO₂–CH₄ systems from available experimental data [15,18,23] (see Fig. 2). For this purpose, the minimum of an objective S function has been searched by using a minimization routine.

$$S = \sum_{i=1}^N \left[\left(\frac{P_i^{exp} - P_i^{calc}}{P_i^{exp}} \right)^2 + (y_i^{exp} - y_i^{calc})^2 \right] \quad (9)$$

where y_i^{exp} and y_i^{calc} are the experimental and calculated mole fraction of CO₂ respectively, and P_i^{exp} and P_i^{calc} are the respective experimental and calculated pressures for each experiments i . A first attempt, where only the $k_{a,ij}^c$ BIP was fitted, did not result to a sufficient agreement with experimental data, as it can be seen on PT and Tx projections of the critical curve (dotted curve on Figs. 3 and 4). For our purposes, a close agreement between the model and experimental data is important. Otherwise, unrealistic variations of the isothermal Px immiscibility loops may be produced (as in the work of Kreglewski and Hall [5]). Incorporation of the BIP on the b parameter (Eq. (4)) into the model results in a better agreement (Figs. 3 and 4).

4. Results

Improvements of the prediction of the model on the binary CO₂–CH₄ and CO₂–N₂ systems are shown in Fig. 1(A) and 1(B). As expected, the critical and the retrograde condensation regions are

Table 2
Accuracies of bubble pressure calculations for the CO₂–N₂ system

References	Temperature (K)	Number of points N	AADP ^a		AADy ^b	
			SRK	MSRK	SRK	MSRK
[15]	240.00	4	5.58	0.63	3.02	0.96
[30]	270.00	6	1.88	1.08	2.63	1.06
[32]	273.15	3	4.88	1.29	2.78	0.54
[33]	273.15	3	1.65	1.27	1.10	0.54
[33]	232.85	3	2.44	1.39	1.59	1.65
[17]	223.15	3	3.31	1.95	0.70	0.30
[17]	273.15	2	1.80	1.04	1.14	0.68
All data		24	3.08	1.20	2.03	0.86

$${}^a \text{AADP} = \left[\frac{1}{N} \sum_{i=1}^N |P_i^{exp} - P_i^{calc}| / P_i^{exp} \right] \times 100; \quad {}^b \text{AADy} = \left[\frac{1}{N} \sum_{i=1}^N |y_i^{exp} - y_i^{calc}| \right] \times 100.$$

Table 3
Accuracies of bubble pressure calculations for the CO₂–CH₄ system

References	Temperature (K)	Number of points <i>N</i>	AAD <i>P</i> ^a		AAD <i>y</i> ^b	
			SRK	MSRK	SRK	MSRK
[22]	271.48	3	4.35	3.42	0.96	1.16
[24]	253.15	2	1.10	0.26	1.54	0.53
[15]	240.00	7	1.95	1.42	1.0	1.23
[21]	230.00	5	0.91	0.75	0.80	0.85
[21]	250.00	3	1.75	0.70	1.99	1.98
All data		20	1.93	1.33	1.15	1.17

$${}^a \text{AAD}P = \left[\frac{1}{N} \sum_{i=1}^N |P_i^{\text{calc}} - P_i^{\text{exp}}| / P_i^{\text{exp}} \right] \times 100; \quad {}^b \text{AAD}y = \left[\frac{1}{N} \sum_{i=1}^N |y_i^{\text{calc}} - y_i^{\text{exp}}| \right] \times 100$$

reproduced better. For example, in Fig. 1(A), the critical pressure is overpredicted by more than 25 bar with the SRK EOS, whereas the pressure deviation ($\Delta P = P_{\text{calc}} - P_{\text{exp}}$) is below 3 bar with our modified Soave–Redlich–Kwong (MSRK) EOS. Comparisons between the SRK and our MSRK EOS are reported in Table 2 for the CO₂–N₂ system and in Table 3 for the CO₂–CH₄ system. Liquid–vapour phase equilibria have been calculated for all available experimental data. For a given temperature and liquid composition, the pressure and the vapour composition were calculated. Results in Tables 2 and 3 have been reported only for the retrograde condensation region and the critical region, i.e. in the fields where the MSRK EOS produces strongly different values from the SRK EOS. The use of our improved model allows the reproduction of experimental data with a better accuracy. Pressure and vapour composition are reproduced with a relative error around the percent for the binary CO₂–CH₄ and CO₂–N₂ systems in the critical region. The method has been tested also for the CO₂–CH₄–N₂ ternary system. An isothermal and isobaric projection of the liquid–gas immiscibility is given in Fig. 4. Whereas the CH₄ mole fraction of the critical point is predicted with a deviation of 0.07 by the SRK EOS, the deviation is below 0.01 with the MSRK EOS. Numerical comparisons between the SRK and the MSRK EOS are reported in Table 4 for the ternary system in the critical region. Relative errors on the pressure and vapour composition are below 1.5%. Thus, our model improves significantly too the predictions in the ternary system and no ternary interaction parameters are required.

5. Application to other systems

This method improves the prediction of liquid–vapour equilibria of the CO₂–CH₄–N₂ system with a cubic EOS up to the critical conditions. Such a method could be used for other systems and with other EOS. However, it is important to point out the potential problems and to show how to solve them.

First of all, a successful EOS should be available for modelling the liquid–vapour properties for non-critical conditions. One set of BIP must be fitted firstly for best agreement of the EOS with experimental data outside the critical and retrograde condensation region. Then, another set of BIP should be obtained for reproducing accurately the critical curves of binary subsystems.

If this work of fitting has been done with success, the experimental immiscibility curves must be

Table 4
Accuracies of bubble pressure calculations for the CO₂-CH₄-N₂ system

References	Temperature (K)	Pressure (bar)	Number of points N	AAD P_a		AAD y^b (N ₂)		AAD y^b (CH ₄)	
				SRK	MSRK	SRK	MSRK	SRK	MSRK
[15]	220.00	91.19	2	5.01	3.94	0.97	1.03	0.83	0.85
[15]	220.00	121.59	5	3.91	2.86	0.96	0.92	0.73	0.73
[15]	233.15	81.06	3	2.27	1.96	0.12	0.15	0.72	0.77
[15]	240.00	91.19	6	2.30	0.97	0.32	0.33	1.00	0.77
[15]	240.00	121.59	7	2.62	0.45	1.49	0.92	0.55	0.34
[16]	230.00	96.52	2	4.31	3.04	2.53	2.45	2.12	1.92
[16]	250.00	86.19	7	2.39	1.28	2.05	1.96	1.33	1.43
[16]	250.00	103.42	4	1.93	1.01	5.04	4.51	3.18	3.41
[30]	270.00	96.26	4	2.21	0.88	2.52	0.30	3.13	0.34
[30]	270.00	111.46	5	2.50	1.44	5.34	0.35	0.84	0.36
All data			45	2.73	1.48	2.02	1.22	1.12	0.90

$${}^a \text{AAD}P = \left[\frac{1}{N} \sum_{i=1}^N |p_i^{\text{exp}} - p_i^{\text{cal}}| / p_i^{\text{exp}} \right] \times 100; \quad {}^b \text{AAD}y = \left[\frac{1}{N} \sum_{i=1}^N |y_i^{\text{exp}} - y_i^{\text{cal}}| \right] \times 100$$

compared with the immiscibility curves calculated by the EOS with non-critical BIP. Fig. 5 illustrates the possible problems that may arise for binary systems. Isothermal bubble and dew curves are plotted in pressure-composition diagrams. The dotted line represents the curves calculated by the EOS with non-critical BIP, whereas the solid line represents the experimental immiscibility curves. The three main types of vapour–liquid equilibria (VLE) calculations are considered here (bubble pressure, flash and dew pressure calculations). In Fig. 5(A), the temperature (T^*) and the mole fraction of the volatile component (x^*) are given for a bubble pressure calculation. A VLE solution, shown by an empty circle, does exist. However, this VLE point cannot be reached with our method. Indeed, the x^* composition is located outside the range of composition predicted by the EOS with non-critical BIP for the bubble curve. Thus, the ξ parameter cannot be estimated. In Fig. 5(B), the T^* temperature and the P^* pressure are fixed for a flash calculation. But, the P^* pressure exceeds the critical pressure calculated by the EOS with non-critical BIP. As a consequence, the solution cannot be found by a flash calculation. Fortunately, in this case, the solution can be approximated by performing several bubble pressure calculations. Another type of problem occurs when a bad ξ interpolation parameter has been obtained after a VLE calculation with non-critical BIP. This problem arises, for example, in Fig. 5(C), where the T^* temperature and the y^* composition of the vapour are fixed for a dew pressure calculation. The VLE solution lies in the retrograde condensation region, near the critical point. But, the VLE calculation with non-critical BIP leads to a point on the dew curve (filled circle) far outside the critical region. Thus, a value close to zero for the ξ interpolation parameter is found by using Eqs. (6) and (7a), whereas a value close to one would be expected. This problem can be bypassed too by doing bubble pressure or flash calculations instead of dew pressure calculations.

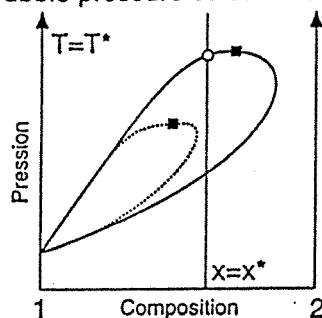
Such problems are expected to be rare. The liquid–vapour immiscibility region calculated by an EOS with non-critical BIP extends very often over the experimental immiscibility field. Thus, in most cases, there is no problem for estimating the ξ parameter from a VLE calculation with non-critical BIP. In the $\text{CO}_2\text{--CH}_4\text{--N}_2$ system, no serious problem was met. Only, dew pressure calculations could fail in the retrograde condensation region, as illustrated in Fig. 5(C). Indeed, the calculated critical points of the $\text{CO}_2\text{--CH}_4$ and $\text{CO}_2\text{--N}_2$ system are always shifted to CO_2 -poorer concentrations with respect to experimental critical points. But, as explained above, VLE points in the retrograde condensation region can be calculated by a bubble pressure calculation.

In summary, our approach can be applied to any system that fulfills the following conditions: (1) an EOS can reproduce the experimental data points of VLE by using non-critical BIP; (2) the critical curve can be reproduced with a good accuracy with the same EOS, but with a different set of BIP; (3) the immiscibility region predicted with non-critical BIP includes the experimental immiscibility region. After these conditions have been checked for the system under investigation, it remains to define an interpolation function between non-critical and critical BIP. For the $\text{CO}_2\text{--CH}_4\text{--N}_2$ mixture, the ξ interpolation function, as defined by Eq. (7), has been used. The following values for s and A , 1.05 and 0.5, have been estimated for the $\text{CO}_2\text{--CH}_4\text{--N}_2$ system, and they are found to give satisfactory results. But another values could be required for modelling the VLE in the transition region between non-critical and critical conditions of other systems.

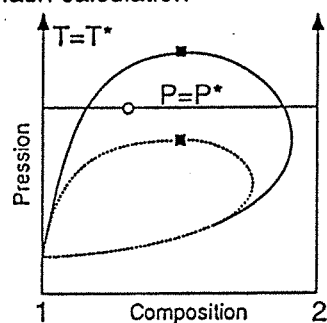
6. Conclusion

It is shown that cubic EOS provide a convenient framework for modelling liquid–vapour equilibria

A. Bubble pressure calculation



B. Flash calculation



C. Dew pressure calculation

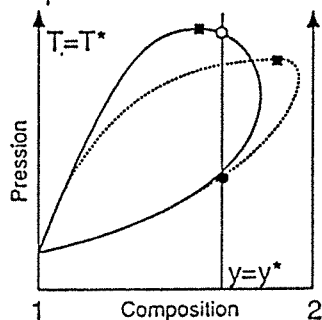


Fig. 5. Illustration of possible mismatches of our system. Fictive isothermal Px projections of the liquid-vapour immiscibility field are given here for a binary system (1–2). The solid line represents the experimental biphasic liquid-vapour region, that should be reproduced as closely as possible with our method. The dashed line delimits the immiscibility field calculated by an EOS with noncritical BIP. This dashed curve indicates the range of possible pressure-composition values that are obtained after a VLE calculation with noncritical BIP. Critical points on these immiscibility curves are indicated by full squares. The empty circle on the solid curve is an example of VLE point that cannot be calculated with our approach. A, A bubble pressure calculation cannot be done here with the given T^* temperature and x^* liquid composition. Indeed, the EOS with noncritical BIP fails to predict a VLE state, and thus no ξ distance can be determined. B, A flash calculation cannot be performed here with the given T^* temperature and P^* pressure. The P^* pressure is greater than the critical pressure (P_c) calculated by the EOS with noncritical BIP. Thus, no VLE state can be calculated with a flash calculation at the first step of our algorithm. C, A dew pressure calculation can be carried out with the given T^* temperature and y^* vapour composition, but leads to an incorrect solution (represented by a filled circle), as it is characterized by a ξ value close to zero (noncritical conditions).

for non-critical and critical conditions. Two best-fitting sets of BIP have been determined from experimental data in and outside the critical region for the binary $\text{CO}_2\text{-N}_2$ and the $\text{CO}_2\text{-CH}_4$ system. One BIP on the a is sufficient for predicting liquid–vapour equilibria outside the critical region. On the contrary, two BIP on the a and b parameters are necessary for representing the critical curve of binary systems with sufficient accuracy. Effective BIP applied to the system are allowed to vary between both non-critical and critical sets of BIP. The continuity is ensured by an interpolation parameter, which is a function of the distance from the critical state. The interpolation parameter is obtained by an *a priori* liquid–vapour calculation, which provides an estimate of the ratio of the molar volumes of coexistent liquid and vapour. Our modified SRK EOS allows one to represent liquid–vapour equilibria with a good accuracy. Prediction of liquid–vapour equilibria are significantly improved in the ternary $\text{CO}_2\text{-CH}_4\text{-N}_2$ system, in particular for near-critical conditions. It is believed that this method could be applicable to other mixtures of nonpolar molecules.

7. List of symbols

P	pressure
T	temperature
a	attractive parameter of the SRK EOS
b	covolume of the SRK EOS
x_i	mole fraction of the i component
S	objective function used for fitting BIP
k_a^{nc}	BIP for the a parameter for non-critical conditions
k_a^{c}	BIP for the a parameter for critical conditions
k_b^{nc}	BIP for the b parameter for non-critical conditions
k_b^{c}	BIP for the b parameter for critical conditions
ξ	interpolation function
ν_r	ratio of molar volumes of coexistent liquid and gas
ν_L	molar volume of the liquid
ν_G	molar volume of the gas
N	number of experimental data
A	parameter of the ξ function
s	parameter of the ξ function
P^*	a fixed pressure
T^*	a fixed temperature
x^*	a fixed liquid mole fraction
y^*	a fixed vapour mole fraction

Acknowledgements

This work has been funded by Elf Aquitaine and CNRS, and has been carried out through the HCM network (CEE-DG XII-G) "Hydrothermal-metamorphic water-rock interactions in crystalline rocks: a multidisciplinary approach based on paleofluid analysis". The article has greatly benefited

from a careful review of earlier drafts with Dr A.M. van den Kerkhof. Professor H. Renon, Dr H. Zhou and two anonymous reviewers who are thanked for their comments and suggestions for improving the manuscript.

References

- [1] Thiéry, R., Vidal, J. and Dubessy, J. (1994) *Geochim Cosmochim. Acta*, (Vol. 58), 1073–1082.
- [2] Thiéry, R., van den Kerkhof, A.M. and Dubessy, J. (1994) *Eur. J. Mineral.*, (Vol. 6), 753–771.
- [3] G. Heyen, 2nd World Congr. of Chemical Engineering, In: S.A. Newmann (Editor), Montreal, Que., 1981, p 175.
- [4] Ferroiu, V. and Geana, D. (1990) *Fluid Phase Equilibria*, (Vol. 55), 263–270.
- [5] Kreglewski, A. and Hall, K.R. (1983) *Fluid Phase Equilibria*, (Vol. 15), 11–32.
- [6] Huron, M.J., Dufour, G.N. and Vidal, J. (1977) *Fluid Phase Equilibria*, (Vol. 1), 247–265.
- [7] Peng, D.Y. and Robinson, D.B. (1977) *A.I.Ch.E J.*, (Vol. 23), 137–144.
- [8] R. Thiéry and J. Dubessy, Proc. 4th Int. Symp. on Hydrothermal Reactions, Nancy, France, August 31–September 3, 1993, Institut Lorrain des Geosciences, Nancy, p. 259.
- [9] R. Thiéry and J. Dubessy, 13th IUPAC Conf. on Chemical Thermodynamics, Clermont-Ferrand, July 17–22, 1994, p 296.
- [10] Firozabadi, A. (1994) *Can. J. Chem. Eng.*, (Vol. 72), 134–141.
- [11] Soave, G. (1972) *Chem. Eng. Sci.*, (Vol. 27), 1197–1203.
- [12] Vidal, J. (1978) *Chem. Eng. Sci.*, (Vol. 33), 787–791.
- [13] Asselineau, L., Bogdanic, G. and Vidal, J. (1979) *Fluid Phase Equilibria*, (Vol. 3), 273–290.
- [14] R. Thiéry, *Computers & Geosciences*, 1996, in press.
- [15] Al-Sahhaf, T.A., Kidnay, A.J. and Sloan, E.D. (1983) *Ind. Eng. Chem. Fundam.*, (Vol. 22), 372–380.
- [16] Al-Sahhaf, T.A. (1990) *Fluid Phase Equilibria*, (Vol. 55), 159–172.
- [17] Al-Wakeel, 1976. Diss. TU Berlin.
- [18] Arai, Y., Kaminishi, G. and Saito, S. (1971) *J. Chem. Eng. Jap.*, (Vol. 4), 113–122.
- [19] Chang, S.D. and Lu, B.C.Y. (1967) *Chem. Eng. Prog. Symp. Ser.*, (Vol. 63), 18–27.
- [20] Cines, M.R., Roach, J.T., Hogan, R.J. and Roland, C.H. (1953) *Chem. Eng. Prog. Symp. Ser.*, (Vol. 49), 1–100.
- [21] Davalos, J., Anderson, W.R., Phelps, R.E. and Kidnay, A.J. (1976) *J. Chem. Eng. Data*, (Vol. 21), 81–84.
- [22] Donnelly, H.G. and Katz, D.L. (1954) *Ind. Eng. Chem.*, (Vol. 46), 511–517.
- [23] Hwang, S.C., Lin, H.M., Chappellear, P.S. and Kobayashi, R. (1976) *J. Chem. Eng. Data*, (Vol. 21), 493–497.
- [24] Kaminishi, G.I., Arai, Y., Saito, S. and Maeda, S. (1968) *J. Chem. Eng. Jap.*, (Vol. 1), 109–116.
- [25] Kidnay, A.J., Miller, R.C., Sloan, E.D. and Hiza, M.J. (1985) *J. Phys. Chem. Ref. Data*, (Vol. 14), 681–694.
- [26] Mraw, S.C., Hwang, S.C. and Kobayashi, R. (1978) *J. Chem. Eng. Data*, (Vol. 23), 135–139.
- [27] Muirbrook, N.K. and Prausnitz, J.M. (1965) *AIChE J.*, (Vol. 11), 1092–1097.
- [28] Neumann, P.N.A. and Walch, W. (1968) *Chem. Eng. Tech.*, (Vol. 40), 241–244.
- [29] Parrish, W.R. and Hiza, M.J. (1974) *Adv. Cryog. Eng.*, (Vol. 19), 300–308.
- [30] Somait, F.A. and Kidnay, A.J. (1978) *J. Chem. Eng. Data*, (Vol. 23), 301–305.
- [31] Stryjek, R., Chappellear, P.S. and Kobayashi, R. (1974) *J. Chem. Eng. Data*, (Vol. 19), 334–339.
- [32] Yorzane, M., Yoshimura, S., Masuoka, H., Myano, Y. and Kakimoto, Y. (1971) *J. Chem. Eng. Jap.*, (Vol. 30), 174–176.
- [33] Zenner, G.H. and Dana, L.I. (1963) *Chem. Eng. Prog. Symp. Ser.*, (Vol. 59), 36–41.
- [34] Xu, N. (1992) *Fluid Phase Equilibria*, (Vol. 81), 175–180.
- [35] Bian, B., Wang, Y., Shi, J., Zhao, E. and Lu, B.C.Y. (1993) *Fluid Phase Equilibria*, (Vol. 90), 177–185.
- [36] Wei, M.S.W., Brown, T.S., Kidnay, A.J. and Sloan, E.D. (1996) *J. Chem. Eng. Data*, (Vol. 40), 726–740.
- [37] van den Kerkhof, A.M. (1990) *Geochim. Cosmochim. Acta*, (Vol. 54), 621–629.

vX properties of CH₄-CO₂ and CO₂-N₂ fluid inclusions : modelling for $T < 31^{\circ}\text{C}$ and $P < 400$ bars

RÉGIS THIÉRY*, ALFONSUS MARTINUS VAN DEN KERKHOFF**
and JEAN DUBESSY*

* CREGU, Centre de Recherche sur la Géologie des Matières Minérales et Energétiques,
BP 23, 54501-Vandœuvre-lès-Nancy Cedex, France

** Institute of Geology and Dynamics of the Lithosphere, University of Göttingen,
Goldschmidtstraße 3, D-37077 Göttingen, Germany

Abstract: vX properties of the binary systems CO₂-CH₄ and CO₂-N₂ are described with improved accuracy and for the full ranges of composition and molar volume. PTX conditions of phase transitions including liquid, gas and solid are modelled by the Soave-Redlich-Kwong equation of state, and molar volumes by the Lee-Kesler correlation. The Soave-Redlich-Kwong equation of state has been improved for critical fluids. vX diagrams are presented, which describe phase transitions involving liquid, gas and CO₂ solid phases for CO₂-CH₄ and CO₂-N₂ fluid inclusions. Also discussed are the conditions of the metastable liquid-liquid-gas phase assemblage.

Key-words: fluid inclusions, CO₂-CH₄-N₂ system, phase equilibria, vX properties, equations of state.

Introduction

The determination of fluid compositions (X) and molar volumes (v) is an essential step for any quantitative study of paleo-fluids, presently found as relicts in fluid inclusions. Temperature measurements of phase transitions observed by microthermometry and combined with Raman spectrometry allow fairly accurate determinations of the vX properties of the non-aqueous volatile parts of fluid inclusions. As popularized by Burruss (1981), vX diagrams are most appropriate for quantitative interpretations of phase transitions in fluid inclusions. In many cases, non-aqueous

volatile portions of fluid inclusions can be described in the CO₂-CH₄-N₂ system. Unfortunately, experimental data are not numerous enough for an accurate interpretation of phase equilibria, and molar volumes of CO₂-CH₄-N₂ fluids are poorly known. Thus, the accuracy of vX determinations mainly relies on the applied equations of state (EOS) and the derived phase diagrams. The large amounts of microthermometric and Raman data, produced during the last decade, have demonstrated that available phase diagrams for the CO₂-CH₄ system (Herskowitz & Kisch, 1984; Heyen *et al.*, 1982) and for the CO₂-N₂ system (Darimont & Heyen, 1988) have limited ranges of application and are

0935-1221/94/0006-0753 \$ 4.75

© 1994 E. Schweizerbart'sche Verlagsbuchhandlung, D-70176 Stuttgart

inaccurate in some parts. Therefore, it was felt that more reliable thermodynamic models, with larger ranges of application and higher accuracy, are required in order to be in better agreement with fluid-inclusion data.

Earlier vX diagrams for the two binary systems were constructed by means of single models like cubic equations of state (Heyen, 1981; Peng & Robinson, 1976; Soave, 1972). However, it is not possible to build one cubic equation of state (EOS), that reproduces all thermodynamic properties of a fluid (Vidal, 1983). Therefore, instead of using only one EOS, two different thermodynamic models are successively applied as described by Thiéry *et al.* (1994). The first step is the calculation of the saturation pressure of a mixture of given composition and temperature from a cubic EOS. Subsequently, the molar volume is calculated from the calculated pressure with a model based on the corresponding-states principle (Prausnitz, 1969), the correlation developed by Lee & Kesler (1975). This method results in more accurate calculation of all parameters. Indeed, cubic EOS are efficient in modelling the PTX properties of phase equilibria in mixtures of non-polar molecules. On the other hand, the Lee-Kesler method is most successful when applied to the calculation of bulk properties such as the molar volume. In this way, vX diagrams have been published for the systems $\text{CO}_2\text{-CH}_4$ and $\text{CO}_2\text{-N}_2$ (Thiéry *et al.*, 1994). However, the results obtained for near-critical fluids are still poor as compositions in this range are inaccurate and the pressure is overestimated. Consequently, molar volumes in the critical and retrograde condensation regions are badly reproduced. This makes an improvement of the model for critical fluids necessary. Moreover, phase transitions involving a CO_2 solid phase (initial and final melting, partial homogenization and sublimation) are also indicative of vX properties of fluid inclusions (Van den Kerkhof, 1988). Modelling of these phase transitions is also addressed in the present paper. The previous models used by Heyen *et al.* (1982), Herskowitz & Kisch (1984), Darimont & Heyen (1988) are highly inaccurate in parts of the vX diagrams and the stability conditions of the univariant three-phase solid-liquid-gas assemblage are not well estimated. Modelling of the metastable liquid-liquid-gas assemblage, which has been recently described in fluid inclusions (Berdnikov, 1987; Van den Kerkhof *et al.*, 1993) has also been done with the same combined EOS.

Symbols

S	the CO_2 solid phase
F	the fluid phase
L	the liquid phase
L_1	the CH_4 -rich liquid phase
L_2	the CO_2 -rich liquid phase
G	the gas phase
S(LG)	the CO_2 solid phase in equilibrium with liquid and gas
L(SG)	the liquid phase in equilibrium with CO_2 solid and gas
G(SL)	the gas phase in equilibrium with CO_2 solid and liquid
LG(S)	the tie-line joining L(SG) and G(SL)
SG(L)	the tie-line joining S(LG) and G(SL)
SL(G)	the tie-line joining S(LG) and L(SG)
EOS	equation of state
SRK	the Soave-Redlich-Kwong equation of state
LK	the Lec-Kesler correlation
X	composition (mole fraction)
P	pressure (bar)
v	molar volume (cm^3/mol)
T	temperature (K)
k_{ij}	binary interaction parameter characteristic of components i and j used in the SRK EOS
δ_{ij}	binary interaction parameter in the LK correlation
ξ	a distance between non-critical conditions and critical conditions.

The topology of the $\text{CO}_2\text{-CH}_4$ and $\text{CO}_2\text{-N}_2$ systems

The main difference between the systems $\text{CO}_2\text{-CH}_4$ and $\text{CO}_2\text{-N}_2$ is due to the relative positions of the liquid-gas ($L = G$) critical and the univariant solid-liquid-gas (SLG) curves (Fig. 1). The critical curve is continuous between the two critical points of the pure components for the system $\text{CO}_2\text{-CH}_4$ (Fig. 1a), whereas it is discontinuous for the system $\text{CO}_2\text{-N}_2$ (Fig. 1b). In the latter system, the critical curve is intersected twice by the univariant three-phase SLG curve, where solid phase is in equilibrium with critical fluid ($SL = G$). One of the intersection points (P point) is very close to the critical point of N_2 , whereas the

intersection point at the high temperature side (Q point) has been located at $X_{N_2} = 0.47$ and $T = -61^\circ\text{C}$ (Van den Kerkhof, 1990). At temperatures not below -183°C , the solid phase is always pure CO₂. Solid solution between CO₂ and CH₄/N₂ does not occur. However, solid phases forming at lower temperatures involve solid solutions between CH₄ and N₂ (Omar, 1962). These solids are not considered here, since the purpose of this work is to model phase equilibria observed using liquid N₂ as cooling agent at temperatures above -182°C .

Recently, immiscibility of the metastable undercooled liquid has been observed in the CO₂-CH₄-N₂ system below -90°C (Berdnikov, 1987; Van den Kerkhof *et al.*, 1993, see below) and suggests that phase transitions in the systems CO₂-CH₄ and CO₂-N₂ may be more complex than first assumed (Kreglewski & Hall, 1983; Van Konynenburg & Scott, 1980). Based on a theoretical analysis of the van der Waals EOS,

binary (*i* - *j*) systems show different topology in relation to the strength of molecular interactions (Van Konynenburg & Scott, 1980). In the case of strong attractive interactions between molecules *i* and *j*, mixing of the end-member fluids at low temperatures produces heat and, consequently, liquid-liquid immiscibility does not occur. Examples of such systems are CO₂ + ethanol and CO₂ + nitrobenzene, and have been classified by Van Konynenburg & Scott (1980) as type I. On the other hand, if interactions between *i* and *j* molecules are not very strong, heat must be furnished to mix the pure components, attractive forces are not strong enough to counteract the repulsive part of molecular interactions, and liquid-liquid immiscibility occurs at low temperatures. Moreover, if the critical temperature of one end-member component is much higher than the critical temperature of the other one (*i.e.*, $T_{c,j} > 2 T_{c,i}$ for molecules of similar size), the attractive forces (*j* - *j*) are much stronger than attractive forces (*i* - *i*). As shown by Van Konynenburg & Scott (1980), this must have also implications for the position of the liquid-gas critical curve relative to the liquid-liquid critical curve. If the difference between the critical temperatures of the end-members is not large, the liquid-gas critical curve does not intersect the liquid-liquid critical curve. These systems are classified as type II by Van Konynenburg & Scott (1980), *e.g.* the systems of CO₂-*n*-alkanes. If the difference between the critical temperatures of the end-member components is large, there is

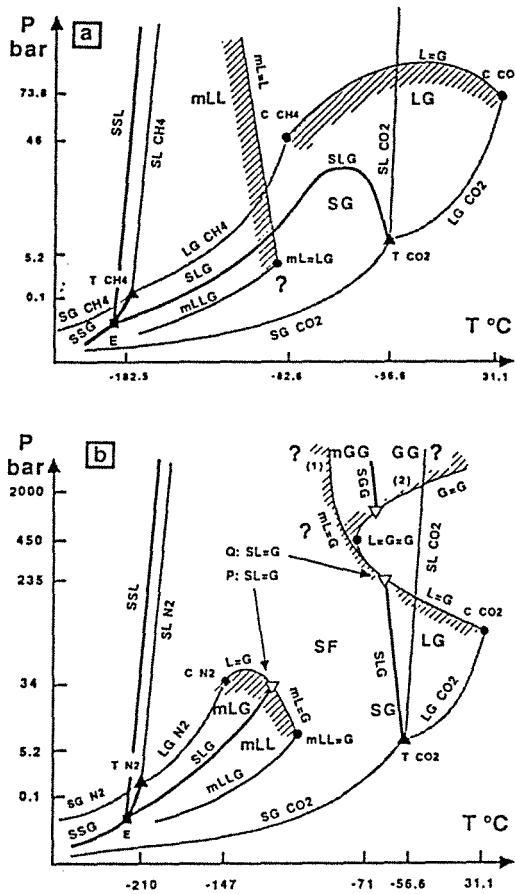


Fig. 1. Topology of the binary systems CO₂-CH₄ (Fig. 1a) and CO₂-N₂ (Fig. 1b) in *PT* diagrams. The pressure and temperature scales are arbitrary. Invariant points: eutectic point $S_{CH_4/N_2}CO_2LG$ (E, filled square), triple points (T, filled triangles), L = G critical points for pure fluids (C, filled circles), three-phase critical end-points (empty circles), intersection points of a critical curve with the SLG curve (empty triangles). Univariant lines: two-phase assemblage for the pure end-members (gray lines), three-phase assemblage for the binary systems (thick solid lines), and critical curves (thin solid lines). The prefix "m" denotes metastable parts. Regions around the triple points T CH₄ and T N₂ have been considerably enlarged. The critical curves (L = L and L = G) delimit LL and LG immiscibility (shaded areas). Also indicated are the stability fields of liquid-liquid (LL), solid-gas (SG) and solid-fluid (SF) assemblages. The metastable L = G critical curves (mL = G) predicted by the SRK EOS and the Kreglewski & Hall model (1983) are sketched.

no continuous liquid-gas critical curve, metastable or not, joining the critical points of the pure components. Such systems are classified as type III, e.g. the system H₂O-CO₂. Kreglewski & Hall (1983) suggested from calculations with their EOS that the CO₂-CH₄ system would be type II and the CO₂-N₂ system type III. According to their calculations, liquid-liquid immiscibility for the CO₂-CH₄ system would occur below -80°C in the stability field of solid CO₂. Furthermore, for the CO₂-N₂ system, the metastable branch of the critical curve starting from the Q point would exhibit a temperature minimum and then, would run with increasing temperatures to very high pressures and delimit the field of so-called gas-gas immiscibility (Schneider, 1978). The temperature minimum of the critical curve is referred to as a "double critical" point (L = G = G), where the liquid-gas and gas-gas critical loci meet. Kreglewski & Hall (1983) estimated the temperature of the double critical point at -71°C, 450 bars, and approximately 40 cm³/mole. Thus, gas-gas equilibria may occur in fluid inclusions of lowest molar volume and above -71°C, but they are assumed to be indistinguishable from "normal" LG equilibria. Moreover, gas-gas immiscibility would occur partly in the stability field of solid CO₂ (denoted mGG field in Fig. 1b). In this case, a second intersection point with the SLG curve should exist and the G = G critical curve should become stable again at higher temperatures and pressures. However, gas-gas immiscibility is not predicted with the SRK EOS. The L = G critical curve calculated by the SRK EOS steeply rises to high pressures with cooling and shows no double critical point. The reality of gas-gas immiscibility can be proved by experiment only. A series of high-pressure experiments has been started at the van der Waals Laboratory, Amsterdam (Schouten *et al.*, in prep.). The low temperature side of the L = G critical curve starts from the critical point of N₂, intersects the three-phase SLG curve at the P point, and should go on metastably up to an intersection point (mLL = G point in Fig. 1b) with the three-phase metastable LLG curve. The metastable extension of the L = G critical curve at low temperature (mL = G in Fig. 1b) has never been observed, but is important to consider in order to understand the transition from the type-II system CO₂-CH₄ to the type-III system CO₂-N₂. When N₂ is added to the CO₂-CH₄ system, the LL stability field extends progressively to higher tempera-

tures. Then, the L = L critical curve intersects the L = G critical curve. From this step on, the system becomes a type-III system, as illustrated in Fig. 1b: the L = G curve splits into a low-temperature and a high-temperature parts. The low-temperature side ends at a critical end-point (LL = G) on the LLG curve; and the high-temperature part starts from the CO₂ critical point and rises to high pressures as an extension of the previous L = L curve.

The larger difference between the critical temperatures of pure components for the system CO₂-N₂ compared to CO₂-CH₄ has also implications for the partitioning of the components in liquid and gas, and for the phenomena of retrograde condensation. The partitioning of N₂ is much higher in the gas phase and much lower in the liquid phase than CH₄. The phenomenon of retrograde condensation is important for the understanding of the binary systems and for a proper interpretation of fluid inclusions. Retrograde condensation is a remarkable fluid phase behaviour in mixtures: by compressing a gas mixture at constant temperature, as expected, liquid condensates, but again it may disappear during further compression. In pure systems, the critical point is the highest temperature of liquid-gas coexistence, and therefore the highest possible homogenization temperature. The implication of retrograde condensation for fluid inclusions is that, contrary to pure fluids, mixtures of given composition may homogenize to gas at a higher temperature than the critical temperature of the mixture with the same composition. Retrograde condensation is very common for CO₂-N₂ fluid inclusions.

Phase equilibria modelling

Modelling of liquid-gas phase equilibria

Modelling of liquid-gas equilibria is carried out using the Soave-Redlich-Kwong (SRK) EOS (Soave, 1972), associated with the quadratic mixing rules (Vidal, 1978). As shown by Thiéry *et al.* (1994), such an EOS could be successfully applied to CH₄-CO₂-N₂ fluids except in the critical and retrograde condensation regions. The pressure is strongly overestimated in the critical region (up to 50 bars for the CO₂-N₂ system, at -30°C) and the CO₂ content at the critical point

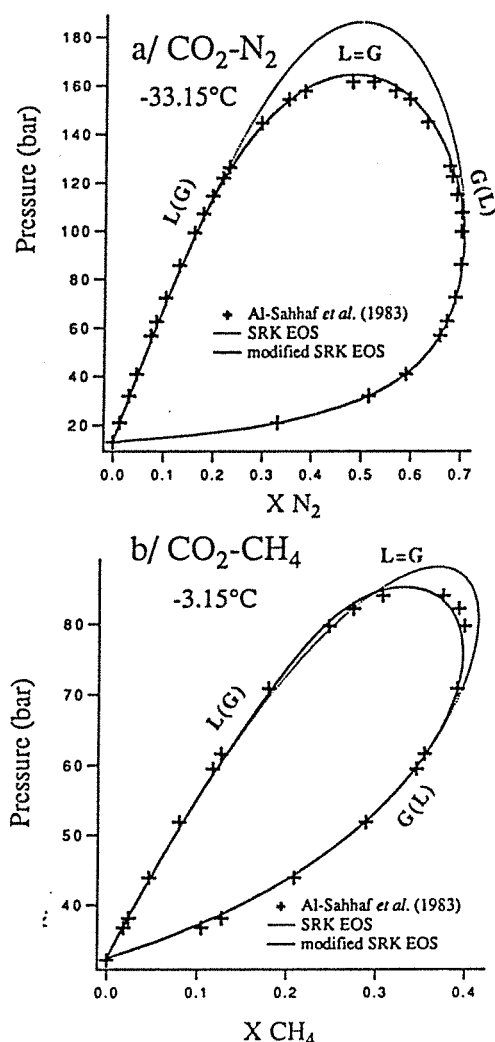


Fig. 2. PX isothermal LG immiscibility curves of the binary systems. (a) CO₂-N₂, (b) CO₂-CH₄. Experimental data of Al-Sahhaf *et al.* (1983).

is always underestimated (up to 10 percent), as shown in Fig. 2. Therefore, an improvement of the EOS is necessary for any quantitative use.

As shown by Huron *et al.* (1978), the SRK EOS is able to predict liquid-gas equilibria in the critical region for binary mixtures of CO₂ and *n*-alkanes, if binary interaction parameters (BIP) are determined from experimental data along the critical lines. However, these critical BIP are not suitable outside the critical region. Therefore, BIP should be expressed as a function of some

characteristic distance between non critical and critical conditions for using the SRK EOS over the whole range of conditions.

$$k_{a,ij} = \xi k_{a,ij}^c + (1 - \xi) k_{a,ij}^{nc} \quad (1a)$$

$$k_{b,ij} = \xi k_{b,ij}^c + (1 - \xi) k_{b,ij}^{nc} \quad (1b)$$

where superscripts *nc* and *c* denote non-critical and critical conditions respectively. ξ is an interpolation parameter ranging between 0 (non-critical state) and 1 (critical state); $k_{a,ij}^{nc}$, $k_{b,ij}^{nc}$, $k_{a,ij}^c$, and $k_{b,ij}^c$ are BIP, determined independently by fitting the EOS with experimental data. Determination of ξ can be done by making use of the fact that molar volumes of the gas and liquid phases become almost equal for the critical conditions. Accordingly, ξ is expressed as function of v_r , the ratio of the molar volume of the gas (v_G) the molar volume of the coexistent liquid (v_L):

$$v_r = \frac{v_G}{v_L} \quad (2)$$

where v_G and v_L are calculated with the classical SRK EOS ($\xi = 0$).

A threshold function has been used to describe the dependence of the ξ parameter to v_r :

$$\xi = \exp\left(-\frac{1}{2}(1.05 - v_r)^2\right) \text{ for } v_r > 1.05 \quad (3a)$$

$$\xi = 1.0 \text{ for } v_r < 1.05 \quad (3b)$$

Best-fitting k_{ij}^{nc} BIP have been determined in a previous study in the non-critical region (Thiéry *et al.*, 1994) from experimental data of the binary systems CH₄-N₂, CO₂-N₂ and CO₂-CH₄ (Al-Sahhaf *et al.*, 1983; Arai *et al.*, 1971; Chang & Lu, 1967; Cines *et al.*, 1953; Davalos *et al.*, 1976; Hwang *et al.*, 1976; Kidnay *et al.*, 1985; Mraw *et al.*, 1978; Muirbrook & Prausnitz, 1965; Neumann & Walch, 1968; Parrish & Hiza, 1974; Somait & Kidnay, 1978; Stryjek *et al.*, 1974; Zenner & Dana, 1963). The $k_{b,ij}^c$ values have been set to zero, and the $k_{a,ij}^{nc}$ values are temperature independent (Table 1).

Optimum k_{ij}^c BIP have been determined along the critical locus curve for the CO₂-N₂ and the CO₂-CH₄ systems from available experimental data (Al-Sahhaf *et al.*, 1983; Arai *et al.*, 1971; Davalos *et al.*, 1976; Krichevskii *et al.*, 1962; Mraw *et al.*, 1978; Muirbrook & Prausnitz, 1965; Zenner & Dana, 1963). Slight discrepancies have been recognized between the data of Arai *et al.* (1971) and other data (Krichevskii *et al.*, 1962; Zenner & Dana, 1963). The CO₂ mole fraction of the critical points given by Arai *et al.* (1971) is overestimated by 2-3 percent. Arai's experimental data of critical points were obtained by

Table 1 : parameters used for the calculations of BIP.

i-j	CO ₂ -CH ₄	CO ₂ -N ₂	CH ₄ -N ₂
$k_{a,ij}^{nc}$	0.1	-0.035	0.03
$k_{b,ij}^{nc}$	0.0	0.0	0.0
$k_{a,ij}^{cc}$	0.06	-0.13	0.03
$k_{b,ij}^{cc}$	-0.10	-0.08	0.0
$T_{a,ij}$ (K)	255	235	-
$\sigma_{a,ij}$ (K)	15	15	-
$T_{b,ij}$ (K)	255	235	-
$\sigma_{b,ij}$ (K)	5	15	-

extrapolation of their bubble and dew points measurements, but as explained below, their method is not accurate enough for measuring dew points. Consequently, the CO₂ contents of their dew point data are overestimated when compared to other published experimental data. For this reason Arai's experimental data of critical points have not been taken into account for the fitting of k_{ij}^c BIP along the critical curve. Critical data obtained from fluid inclusion data could be a help for the construction of the critical curve, but most data are not accurate enough for the present calculations. Diamond (1986) noticed

similar discrepancies by comparing Arai's data of critical points with his data from CO₂-N₂ fluid inclusions, showing critical homogenization, for which both Raman-spectroscopic and microthermometric analyses are available. However, microthermometry and revised Raman data of Van den Kerkhof (1988) for experimentally produced fluid inclusions give two additional critical loci at 2°C ($X_{N_2} = 0.25$) and at -57°C ($X_{N_2} = 0.44$). These data show somewhat higher CO₂ contents compared to Arai *et al.* (1971).

Better agreement of the model with experimental data of critical loci is achieved when non-zero values for the $k_{b,ij}^c$ parameters are taken. Moreover, $k_{a,ij}^c$ and $k_{b,ij}^c$ BIP are temperature-dependent and strongly correlated. At low temperatures, $k_{a,ij}^c$ and $k_{b,ij}^c$ values tend to converge to the values of $k_{a,ij}^{nc}$ and $k_{b,ij}^{nc}$. Towards the critical temperature of CO₂, $k_{a,ij}^c$ and $k_{b,ij}^c$ BIP become constant, denoted as $k_{a,ij}^{cc}$ and $k_{b,ij}^{cc}$ respectively. By taking into account these considerations, the following empirical relations for $k_{a,ij}^c$ and $k_{b,ij}^c$ BIP are proposed:

$$k_{a,ij}^c = \frac{k_{a,ij}^{cc} + k_{a,ij}^{nc}}{2} + \frac{k_{a,ij}^{cc} - k_{a,ij}^{nc}}{2} \tanh\left(\frac{T - T_{a,ij}}{\sigma_{a,ij}}\right) \quad (4a)$$

$$k_{b,ij}^c = \frac{k_{b,ij}^{cc} + k_{b,ij}^{nc}}{2} + \frac{k_{b,ij}^{cc} - k_{b,ij}^{nc}}{2} \tanh\left(\frac{T - T_{b,ij}}{\sigma_{b,ij}}\right) \quad (4b)$$

Values of parameters of these relations are given in Table 1.

This model has been used for gas-liquid equilibria calculations with the Asselineau *et al.*

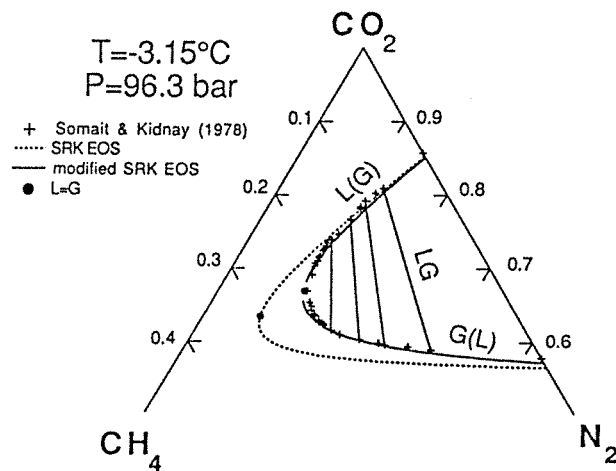


Fig. 3. Isothermal and isobaric LG immiscibility curve in the ternary CO₂-CH₄-N₂ system: comparison of the models with experimental data.

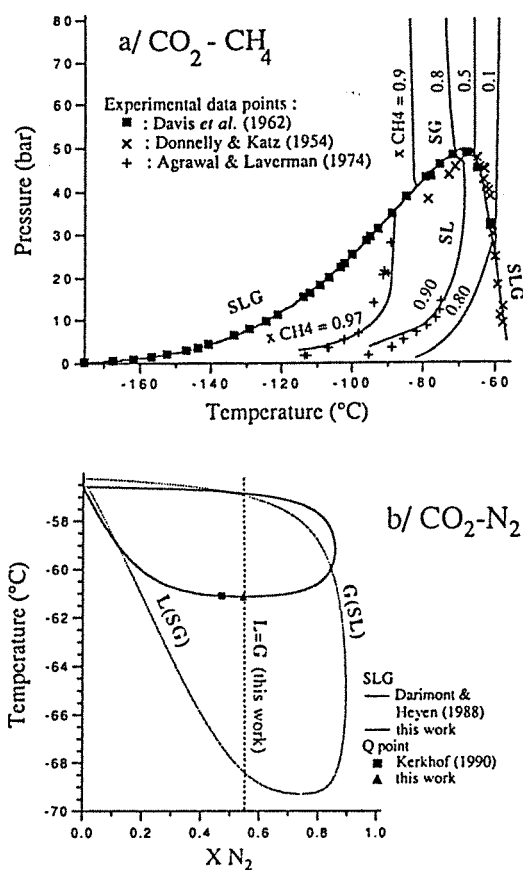


Fig. 4. SLG stability curve calculated with the modified SRK EOS

(a) *PT* diagram in the CO₂-CH₄ system. The SLG curve delimits the SL stability field from the SG stability region. SL isopleths and SG isopleths have been calculated for different methane compositions.

(b) *TX* diagram in the CO₂-N₂ system. The SLG stability area is calculated with the Heyen EOS (dotted line) and with our model (solid line). The L = G critical curve calculated by our model is represented by the dashed line. The Q point obtained with our model is in fair agreement with the estimation of Van den Kerkhof (1990), using synthetic fluid inclusions.

(1979) algorithm. The improvements for the CO₂-N₂ and the CO₂-CH₄ systems are shown in Fig. 2. In contrast to the classical SRK EOS, the pressure is no more overestimated and the compositions in the critical and retrograde condensation regions are reproduced better. Cubic EOS can be used for liquid-liquid and liquid-liquid-

gas immiscibility calculations in "simple" cases (for example, methane-*n*-hexane mixture, Vidal, 1984) and have also been used for the systems investigated in this work. The model has been also applied to the ternary system. A comparison between the predicted values and the experimental data of Somait *et al.* (1978) shows fairly good agreement (Fig. 3).

Modelling of phase equilibria involving a CO₂ solid phase

In order to apply the SRK EOS to SLG, SL and SG equilibria, an expression of the fugacity of CO₂ in the CO₂ solid phase must be derived as a function of pressure and temperature. Smoothed pressure-temperature data of the sublimation curve of the CO₂ system, reported by Angus *et al.* (1976) have been converted in fugacity values with the SRK EOS. Obtained fugacity $f_{CO_2}^s$ values have been fitted by the following expression :

$$\ln f_{CO_2}^s = 13.08053 - 0.0047478 (T - 216.58) - 3250.44 \left(\frac{1}{T} - \frac{1}{216.58} \right) + \frac{Pv_s}{RT} \quad (5)$$

where v_s denotes the molar volume of CO₂ solid phase ($v_s = 28.7552$ cm³/mole, Angus *et al.*, 1976). Contrary to the model developed by Heyen (Darimont & Heyen, 1988; Heyen *et al.*, 1982), the pressure dependence of $f_{CO_2}^s$ is taken into account as high pressures can be reached (up to 200 bars) for the CO₂-N₂ system.

The SRK EOS predicts the saturation curve of pure CO₂ with 1-2 % accuracy (Thiéry *et al.*, 1994); but in the vicinity of the CO₂ triple point ($T = 216.58$ K = -56.57°C, $P = 5.185$ bars), higher accuracy of the SRK EOS is required. Otherwise, like the Heyen EOS, the temperature of the triple point would be overestimated by a few tenths of a degree. Therefore, the dependence of the a_{CO_2} parameter with temperature has been modified as follows :

$$\text{for } T > 216.58 \text{ K} \\ a_{CO_2}(T) = 0.999404 a_{CO_2}^{Soave}(T) \exp \left(-10 \frac{T-216.58}{216.58} \right) \quad (6a)$$

$$\text{for } T < 216.58 \text{ K} \\ a_{CO_2}(T) = 0.999404 a_{CO_2}^{Soave}(T) \quad (6b)$$

where $a_{CO_2}^{Soave}(T)$ is the a_{CO_2} parameter calculated by the relation given by Soave (1972).

The modification does not alter the quality of the model for predicting liquid-gas equilibria.

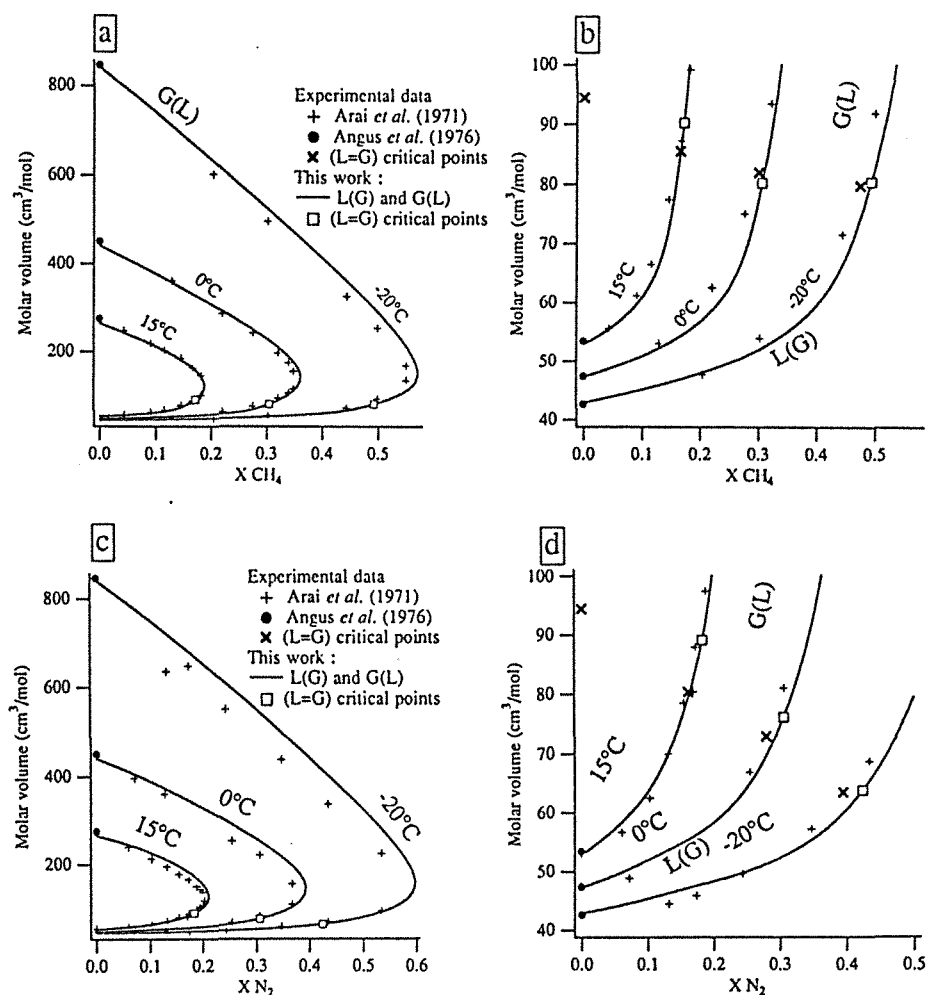


Fig. 5. Projections of the LG isotherms in vX diagrams, calculated at -20°C, 0°C and 15°C including the experimental data (Angus *et al.*, 1976; Arai *et al.*, 1971). (a and b) CO₂-CH₄ system; (c and d) CO₂-N₂ system.

Results given by our model for SLG and SG are in good agreement with experimental data (Agrawal & Laverman, 1974; Davis *et al.*, 1962; Donnelly & Katz, 1954) for the CO₂-CH₄ system (Fig. 4a). For the CO₂-N₂ system, experimental SLG data are not available. However, Van den Kerkhof (1990) determined the intersection point of the critical and solid-liquid-gas curves (SL = G) at a temperature of -61.2°C and $X \text{ N}_2$ around 0.47, using synthetic fluid inclusions. These values are in good agreement with our model (-61.1°C, $X \text{ N}_2 = 0.55$) as shown in a TX diagram (Fig. 4b). This temperature must also correspond to the lowest possible CO₂ melting temperature in the system

CO₂-N₂ and could be confirmed by the evaluation of microthermometry data. In comparison, the Heyen EOS (Darimont & Heyen, 1988) produces a lower minimum CO₂ melting temperature of -70°C.

Molar volume modelling

The Lee-Kesler (LK) correlation (Lee & Kesler, 1975) has been used for calculating the molar volume of fluids from their PTX properties. However, the original Lee-Kesler mixing

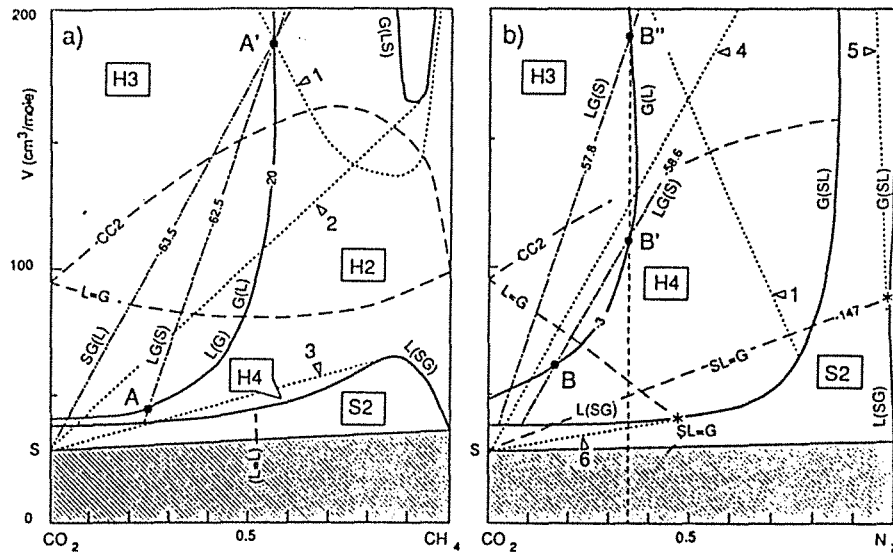


Fig. 6. The use of vX diagrams for the determination of molar volume and composition from microthermometric data. (a) the system CO₂-CH₄, (b) the system CO₂-N₂.

Thick solid line : L(SG) and G(SL) curves. Inclusions plotting in the shaded area are classified as "S-type" (mostly S2) and may show metastable LG homogenization below melting. Inclusions plotting outside the shaded area are classified as "H-type". Inclusions plotting below the critical curve (L = G) homogenize to liquid, above the critical curve to gas. Inclusions between the curve denoted as CC2 (second-order critical curve) and L = G show (LG → G) homogenization to gas at higher temperature than critical for given composition as a consequence of retrograde condensation. Most common phase transition sequences are indicated by H2, H3, H4 and S2 (see text). The type boundaries are given by line 2 (H2-H3), line 3 (H2-H4), and line 4 (H3-H4). Line 1 (in both diagrams) indicates fill degrees of 10 % liquid: the liquid phase in inclusions plotting above these lines can normally not be observed in fluid inclusions due to optical restrictions. Similarly, line 5 indicates fill degrees of 1 % for SG equilibria: the solid phase cannot be observed above this line. Inclusions plotting left of line 6 show complex "S-type" behaviour (S1, S2 and S3). Line signatures for the phase transitions are the following: thin solid lines = homogenization (LG → L or G); dashed-dotted lines = final melting (SLG → LG); dashed-double dotted lines = initial melting (SG → SLG), bubble nucleation (SL → SLG) or partial homogenization (SLG → SG or SLG → SL).

Following inclusions are given as an example for the system CO₂-CH₄: (A) Type H2: $T_m = -62.5^\circ\text{C}$, $Th(L) = -20^\circ\text{C}$; (A') Type H3: the same Th and T_m as inclusion A, but LG homogenization to the gas phase and initial melting can be observed at -63.5°C . In the system CO₂-N₂: (B) Type H4: $T_m = -58.6^\circ\text{C}$ and $Th(L) = -3^\circ\text{C}$. As B plots above the SL = G line, partial homogenization will be to the gas phase (SLG → SG) and expected around -153°C (line not shown). Temperature difference between initial and final melting is very small and lines for T_i are omitted here; (B') Type H4: Inclusion showing the same Th and T_m as inclusion B, but homogenization to the gas phase; (B'') Type H3: inclusion showing homogenization to gas phase at the same temperature as for inclusion B', but melting temperature is higher (-57.8°C).

rules have been slightly modified by introducing a new interaction parameter δ_{ij} in the calculation of the pseudo-critical temperature of the mixture (Thiéry *et al.*, 1994). This modification was suggested in order to improve the accuracy of molar volumes calculations in the critical region. Values of δ_{ij} are the following : $\delta_{\text{CO}_2 - \text{N}_2} = -0.08$, $\delta_{\text{CO}_2 - \text{CH}_4} = 0.02$. As shown by Thiéry *et al.* (1994), the Lee-Kesler correlation gives accurate results for the molar volumes of saturated liquids

and vapours of pure CO₂, CH₄ and N₂ (Angus *et al.*, 1976, 1978, 1979), except for conditions very near the critical point. For the binary CO₂-CH₄ and CO₂-N₂ systems, the only available $PvTX$ data are those of Arai *et al.* (1971). Fair agreement is obtained between the present model and the experimental data (Arai *et al.*, 1971) of molar volumes of saturated liquids (Fig. 5a, 5b, 5c and 5d), but the model seems to overestimate the molar volumes of saturated vapour. As it is not

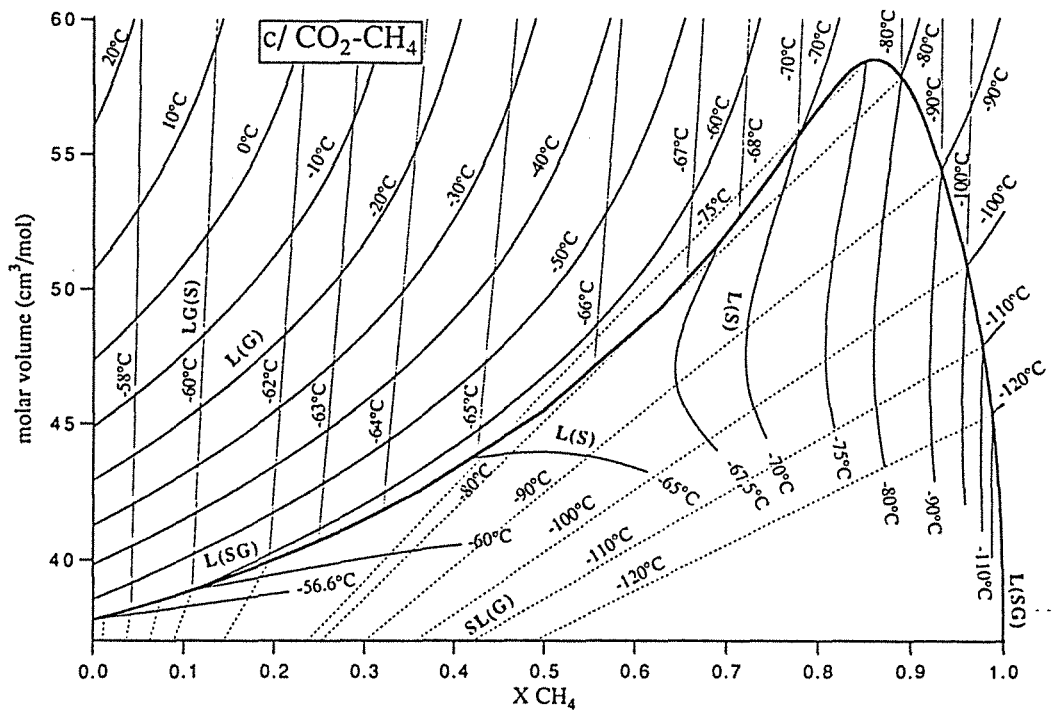


Fig. 7 (continued)

possible to compare with other experimental data, it is useful to look in more detail at the experimental method. Arai *et al.* (1971) used the dew and bubble point apparatus with a glass equilibrium cell, in which a gaseous mixture of known composition was compressed through the dew point and the bubble point by adding mercury to a fixed volume. Dew and bubble points were observed visually and also determined by discontinuities of pressure and volume data. This method is accurate for determining bubble points, as the disappearance of the last bubble in the cell is visible and marked by a rapid change of the pressure-volume slope. However, for the dew points, the change of the slope is much less evident, and it is difficult to observe the disappearance of the thin film of liquid on the surface of the equilibrium cell. Therefore, at the time the dew point measurements were done, a small amount of liquid may still have been present. This must be the reason why measurements of the CO₂ composition of the dew points of Arai *et al.* (1971) are systematically overestimated by 2-4 %, when compared to other experimental data (Al-Sahhaf *et al.*, 1983; Davalos *et al.*, 1976; Muirbrook & Prausnitz, 1965; Somait & Kidnay,

1978; Zenner & Dana, 1963). Consequently, molar volumes of the gas phase given by Arai *et al.* (1971) are assumed to be underestimated by up to 30 cm³/mole.

Application to fluid inclusions

The vX diagrams

The determination of molar volume and composition is one of the principal steps in fluid-inclusion studies. vX phase diagrams are most useful for the interpretation of microthermometry and Raman analysis of binary fluid inclusions. The use of vX diagrams for the determination of molar volume and composition is illustrated in Fig. 6. Calculated vX diagrams are given for the CO₂-CH₄ system in Fig. 7 and for the CO₂-N₂ system in Fig. 8. Fluid inclusions behave as constant molar volume and composition systems. Consequently, a fluid inclusion is represented as a fixed point in the relevant vX diagram.

The stability curve of a SLG phase assemblage

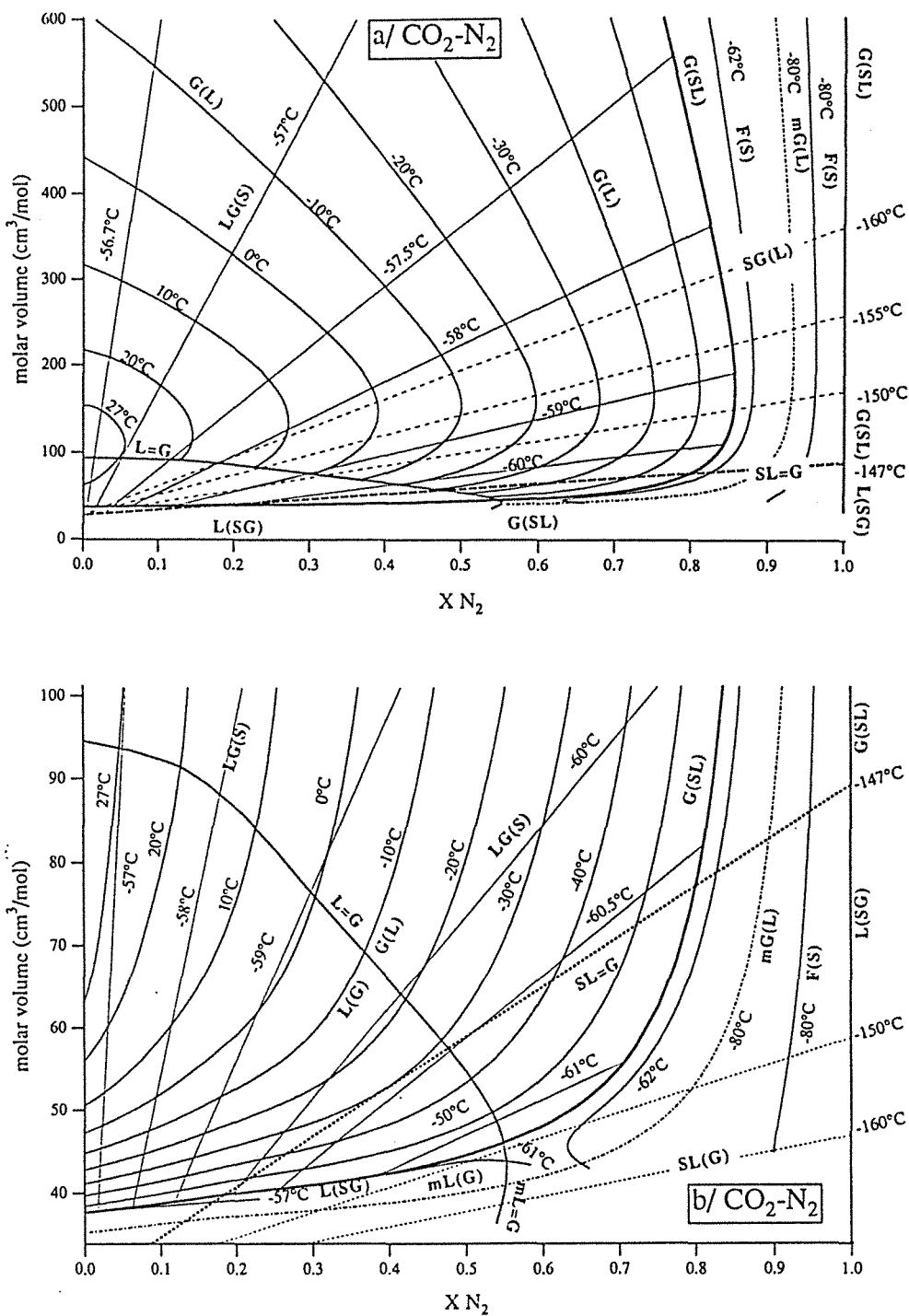


Fig. 8. v - x diagrams calculated for the CO_2 - N_2 system, (a) for high molar volumes ($v < 600\text{cm}^3/\text{mole}$), (b) for low molar volumes ($v < 100\text{cm}^3/\text{mole}$).

(*cf.* Fig. 1 and 4) splits into three parts in a vX diagram: the L(SG) curve, the G(SL) curve and the S point. As shown by the phase rule, a three-phase association in a binary system is invariant for a given temperature, *i.e.*, all intensive properties (and, thus vX properties) of the coexisting phases are fixed. Hence, a fluid inclusion containing a SLG assemblage is defined in a vX diagram by a point located inside the triangle shaped by the three apices describing the vX properties of the liquid, gas and solid phases. The relative position of the fluid inclusion point inside this triangle is a function of the volume percentages of the coexisting phases. When one of the three phases disappears on changing temperature, the fluid inclusion point must be located on the tie-line connecting the two remaining phases. For example, if we observe a phase transition like SLG \rightarrow LG (final melting) at temperature T_m , the fluid inclusion point must plot on the tie-line joining the points, which define the vX properties of the liquid and gas phases, *i.e.* L(SG, $T = T_m$) and G(SL, $T = T_m$) respectively, at the disappearance of the last CO₂ crystal. The same rule can be similarly applied for other phase transition types like initial melting (SG \rightarrow SLG, SL \rightarrow SLG) and partial homogenization (SLG \rightarrow SG, SLG \rightarrow SL).

The variance of a two-phase assemblage for a given temperature is equal to one. The intensive properties of both phases are not defined, unless one extra parameter is given. In other words, the vX properties of each of the coexisting phases are represented by a curve at a given temperature in a vX diagram. This is the case for LG assemblages, which are described for any temperature by a set of tie-lines connecting two vX points on L(G) and G(L) curves. For SL and SG assemblages, one isothermal curve degenerates into a point, as the vX properties of the CO₂ solid phase are fixed. When one of the two coexisting phases disappears, the fluid inclusion point must be situated on the curve describing the vX properties of the remaining phase at that temperature. For example, for the phase transition LG \rightarrow L at temperature T_h , the fluid inclusion point necessarily plots on the isothermal L(G, $T = T_h$) curve, for LG \rightarrow G on the isothermal G(L, $T = T_h$) curve. G(L) isotherms exhibit a minimum in CO₂ concentration; this point is called "critical point of the second order" (Van den Kerkhof, 1988) or "cricodontherm" (Asselineau *et al.*, 1979; King, 1969). LG assemblages with gas homogenizations between the critical point and the "critical

point of the second order" are typified by "retrograde condensation". The implication of retrograde condensation for fluid inclusions is that for given compositions, homogenizations (to gas) are observed at higher temperatures than the critical temperature of the same isopleth (Fig. 6). For example, CO₂-N₂ inclusions with 25% N₂, homogenize critically at around 7°C, but homogenizations to gas can be found as high as about 12°C (Van den Kerkhof, 1988). This effect is particularly valid for the system CO₂-N₂, where the field of retrograde condensation extends to lower molar volumes. Two fluid inclusions of the same composition and the same homogenization temperature to gas may have different molar volumes and can be distinguished by different melting temperatures. For example, CO₂-N₂ fluid inclusion with 25 % N₂ and homogenizing at 10°C in the retrograde condensation field would show melting of CO₂ at -58.4°C, whereas CO₂ solid would melt at -57.6°C for fluid inclusions homogenizing outside the retrograde condensation field.

The molar volume and compositions of fluid inclusions entirely determines the sequence of phase transitions observed during cooling runs. Van den Kerkhof (1988, 1990) proposed to distinguish between two main types of phase behaviour in CO₂-CH₄-N₂ inclusions, namely inclusions showing LG-homogenization ("H-type") and inclusions showing SG or SL-homogenization ("S-type", sublimation) as the final phase transition. The number of possible phase transitions may vary from 1 to 4 for both types, but the order of phase transitions is always the same *i.e.* SLG \rightarrow (SL or SG) \rightarrow SLG \rightarrow LG \rightarrow (L or G) for "H-type" inclusions and SLG \rightarrow SL \rightarrow SLG \rightarrow (SL or SG) \rightarrow (L or G) for "S-type" inclusions. Type and number of phase transitions are indicative for vX properties of fluid inclusions. All phase transitions can be read from the present diagrams. For example for a "H-type" inclusion showing four phase transitions (H4) the tie-lines for partial homogenization (SL \rightarrow SLG), initial melting (SLG \rightarrow SL), final melting (SLG \rightarrow LG) and the homogenization-temperature L(G) isotherm should intersect in one point in the vX diagram. The vX properties of fluid inclusions can be obtained from two phase transitions, which are not necessarily homogenization and final melting only. Partial homogenization (SLG \rightarrow SL or SLG \rightarrow SG) may give more accurate interpretations *e.g.* if melting temperatures are difficult to measure like in CO₂-N₂ mixtures.

Contrary to the system CO₂-CH₄, the range of CO₂ melting temperatures for the system CO₂-N₂ (between -56.6 and -61°C) is small and the difference between initial (SLG → SG or SLG → SL) and final melting (SLG → LG) is only on the order of tenth of a degree. Therefore highest accuracy of melting temperature measurements is required in order to determine vX properties from microthermometry data only (without additional Raman analysis). For inclusions containing additional water this will be difficult and sometimes impossible as the gas phase will be enriched in CH₄ and N₂ by the formation of clathrate hydrates at low temperatures (Seitz *et al.*, 1987). On the other hand, clathrate hydrates in fluid inclusions may show a stability maximum during cooling (Murphy & Roberts, in press) and decompose on cooling to very low temperatures (and at low pressures).

The evolution of degree of fill of fluid inclusions homogenizing at the same temperature

Our model has been applied to simulate the variation of the degree of fill of CO₂-CH₄ fluid inclusions. An example is given for fluid inclusions homogenizing either to liquid or to gas at -3.15°C and with compositions ranging from pure CO₂ up to critical CO₂-CH₄ mixture (Fig. 9). It can be seen that the variation of the degree of fill is small at temperatures well below the homogenization point. Retrograde condensation behaviour can be diagnosed for fluid inclusions with significant higher degrees of liquid fill than fluid inclusions of the same composition with much lower degrees of fill. For example, two CO₂-CH₄ fluid inclusions with the same composition of 34% CH₄ and the same $T_h(G)$ at -3.15°C have strongly different fill degrees (around the melting point) of 0.43 and 0.11 volume percent of liquid. In practice, homogenization to gas can be observed only when degrees of fill are higher than 0.1. That means that observed gas homogenizations normally present fluids typified by "retrograde condensation", as gas homogenizations of "normal" fluids can only be observed with difficulty.

The liquid-liquid-gas immiscibility

In the system CO₂-CH₄-N₂ immiscibility of the liquid phase in fluid inclusions has been recently observed for the metastable, undercooled

liquid and shows evidence for the existence of a liquid immiscibility gap (L₁L₂) besides LG immiscibility (G = CH₄-N₂-rich gas; L₂ = CO₂-rich liquid; L₁ = CH₄-rich liquid) (Berdnikov, 1987; Van den Kerkhof *et al.*, 1993). Metastable phase transitions in fluid inclusions (Fig. 10) occur on cooling below melting, but at higher temperatures than solid nucleation, normally between -110 and -80°C. Just before the freezing point, but always below -92°C, liquid immiscibility is evident from the L₁L₂G or L₁L₂ phase assemblages. In the case of no liquid immiscibility, L₁G persists down to the freezing point. Subsequent warming results in a combination of the following metastable phase transitions (Fig. 10a): (1) liquid homogenization at $-95 \pm 2^\circ\text{C}$ by the disappearance of the outer meniscus (L₁L₂G → L₁G); (2) simple liquid homogenization (L₁L₂ → L); (3) rare L₁G-homogenization by first disappearance of the inner meniscus (L₁L₂G → L₁L₂) and (4) liquid-gas homogenization (L₁G → L₁). Van den Kerkhof *et al.* (1993) observed combined phase transitions (1) + (4), (2), and (3) + (2) for inclusions of about the same composition and re-

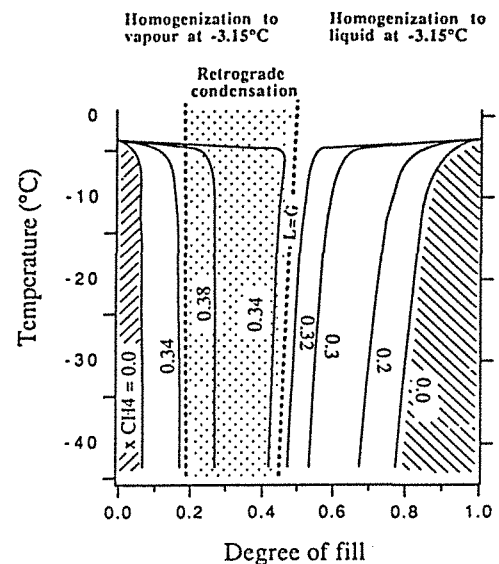


Fig. 9. Evolution of the volume fraction of the liquid upon cooling, for CO₂-CH₄ fluid inclusions homogenizing at -3.15°C either to liquid or to gas, and for composition ranging from pure CO₂ up to critical CO₂-CH₄ composition. Note difference in degree of fill for two fluids homogenizing to gas at -3.15°C with the same composition, but different molar volume.

spective lower molar volume. Simple liquid homogenization is optically similar to LG → G homogenization. The L₁L₂G phase assemblage can be calculated for the binary system CO₂-CH₄ with our EOS. However, as liquid-liquid-gas phase assemblages have never been observed in binary CO₂-CH₄ fluid inclusions, this phenomenon was believed to be more common for ternary CO₂-CH₄-N₂ fluids. Therefore, our model has been applied in order to investigate the vTx conditions of the liquid-liquid-gas phase assemblages also for ternary mixtures. Fluid inclusion data and calculated liquid-liquid-gas isotherms at -103°C, -93°C and -83°C are shown in a ternary CO₂-CH₄-N₂ diagram (Fig. 11). It can be seen

that metastable liquid-liquid-gas immiscibility occurs below -83°C. The immiscibility area strongly expands to lower temperatures and also covers the CO₂-CH₄ system below -90°C. Moreover, at a given temperature and with increasing N₂ content, the CH₄-rich liquid (L₁) curve meets the gas curve at a critical point (L₂L₁ = G), and a continuous line joins the (L₁ = L₂) critical point to the (L = G) critical point of the CO₂-N₂ mixture.

Discussion

The present phase diagrams show differences with the existing diagrams which not only affect

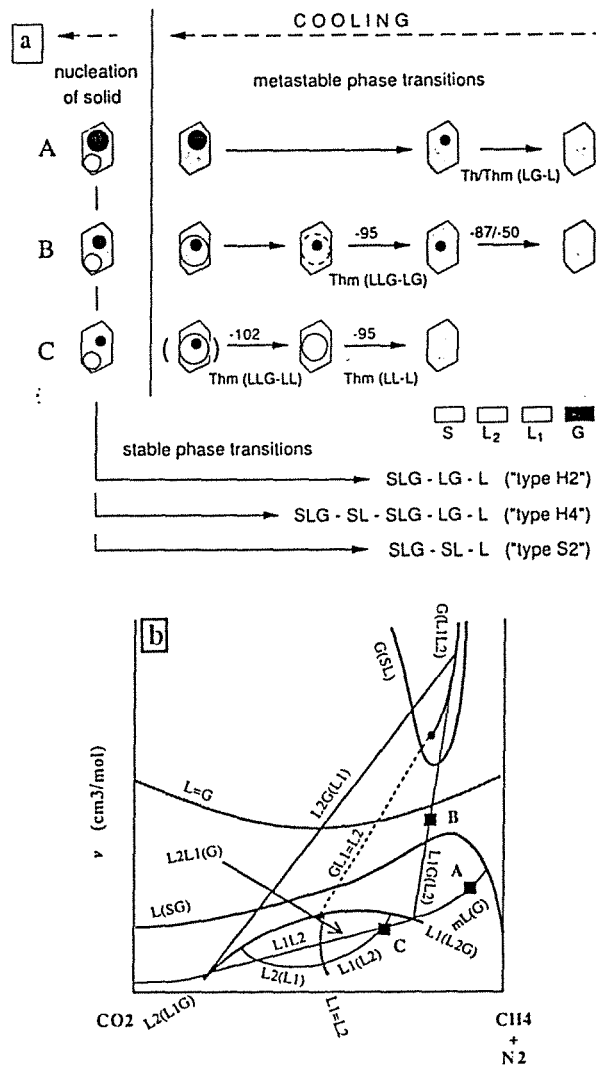


Fig. 10. (a) Phase transitions with liquid immiscibility observed in CO₂-CH₄-N₂ fluid inclusions (Van den Kerkhof *et al.*, 1993). Immiscibilities of the undercooled liquid (at higher temperature than solid nucleation) results in (A) L₁G, (B) L₁L₂G or (C) L₁L₂ phase assemblages. On subsequent warming, LL homogenization is observed around -95°C, before LG homogenization, or more rarely (v < 42 cm³/mole) LG homogenization before LL homogenization. Phase transition sequences observed on warming the "frozen" inclusions (SLG) are typified as H2, H4, or S2 (see text). (b) Interpretations of metastable phase transitions in a vX diagram for a pseudo-binary mixture CO₂-(CH₄ ± N₂). Thick solid lines : univariant three-phase curves : L(SG), G(SL), L₁(L₂G), L₂(L₁G) and G(L₁L₂). Thick gray lines : critical curves L₁ = L₂ and L = G. Thin solid lines : metastable isotherm mL(G) at -102°C, isotherms L₂(L₁) and L₁(L₂) at -95°C. Thin solid lines : tie-lines L₂G(L₁), L₁G(L₂) and L₁L₂(G) at -102°C. Dotted line : the tie-line GL₁ = L₂ connecting the gas and the liquid (filled circles) at the critical end-point GL₁ = L₂. Filled squares : relative positions of fluids inclusions A, B and C.

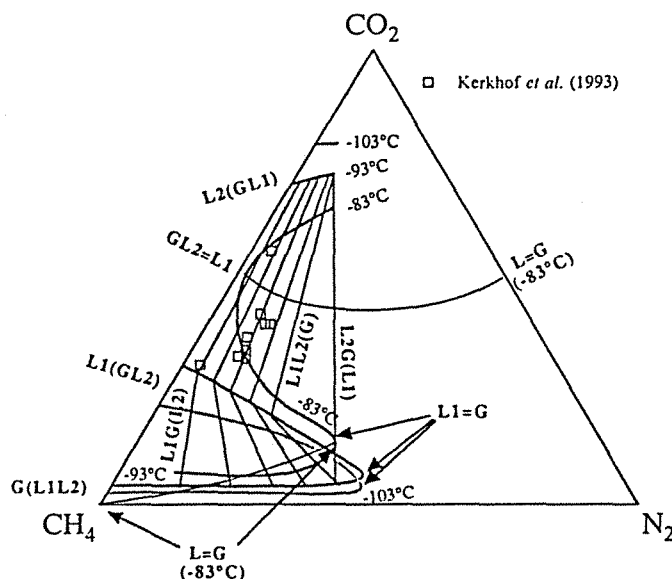


Fig. 11. Projection of the liquid-liquid-gas isotherms at -83.15°C , -93.15°C , -103.15°C and plotted measurement data from Van den Kerkhof *et al.* (1993) in the ternary $\text{CO}_2\text{-CH}_4\text{-N}_2$ polybaric diagram. Tie-lines for different compositions in the ternary system have been calculated by graphical determination of the intersection of L_1L_2 isotherms with L_1G isotherms calculated by the SRK EOS. Only the $\text{L}_1\text{L}_2(\text{G})$ and $\text{L}_1\text{G}(\text{L}_2)$ tie-lines calculated at -93.15°C are shown here. Liquid-liquid-gas isotherms have been drawn by hand. $\text{L}_1(\text{L}_2\text{G})$ isotherms meet the $\text{G}(\text{L}_1\text{L}_2)$ isotherms with increasing N_2 content. The calculated $\text{L} = \text{G}$ critical curve at -83.15°C joins the $\text{L} = \text{G}$ critical point of the $\text{CO}_2\text{-N}_2$ mixture to the $\text{GL}_1 = \text{L}_2$ critical point of the $\text{CO}_2\text{-CH}_4\text{-N}_2$ mixture.

the accuracy, but also the topology in some parts. Comparison with vX diagrams calculated by using the Heyen EOS (Darimont & Heyen, 1988; Heyen *et al.*, 1982) shows that our model significantly improves the accuracy of molar volume of the gas phase which was systematically underestimated by the Heyen EOS. This means that the internal pressure of a $\text{CO}_2\text{-CH}_4$ or $\text{CO}_2\text{-N}_2$ gas phase is overestimated using the vX diagrams of Heyen *et al.* (1982) and Darimont & Heyen (1988). Comparison with the diagram given by Herskowitz & Kisch (1984) as calculated with the Peng-Robinson EOS (Peng & Robinson, 1976) shows major differences in the $0.6 < X_{\text{CH}_4} < 0.7$ and $44 \text{ cm}^3/\text{mole} < v < 50 \text{ cm}^3/\text{mole}$ regions. Contrary to our diagram, the $\text{L}(\text{S})$ isotherms in the vX diagram given by Herskowitz & Kisch (1984) are partly metastable and run above the $\text{L}(\text{SG})$ curve *e.g.* for the -70°C isotherm. This behaviour is not possible from a topological point of view and is not predicted by our model. According to our calculations, the $\text{L}(\text{S})$ isotherms must always end on the three-

phase curve. Furthermore, $\text{L}(\text{S})$ isotherms for temperatures below -65°C are highly indicative for molar volume. The vX diagram of Herskowitz & Kisch (1984) also shows a higher molar volume maximum of the $\text{L}(\text{SG})$ than our diagram (64 instead of $58.5 \text{ cm}^3/\text{mole}$). This must have consequences for the interpretation of microthermometry data, notably for some of the "S2-type": our diagram gives systematically higher molar volumes, for partial homogenization temperatures above -100°C and lower molar volumes ($v < 50 \text{ cm}^3/\text{mole}$) below -100°C . On the other hand, compositions obtained from microthermometry data are in good agreement for the CH_4 -rich part in both diagrams and also with Raman analysis. By using the diagram of Herskowitz & Kisch (1984), Kisch & Van den Kerkhof (1991) found somewhat too high trapping pressures for the highest-density inclusions by isochore extrapolation. Our diagram would have given somewhat lower trapping pressures for these inclusions. The $\text{SL}(\text{G})$ tie-lines connecting solid and liquid at the three-phase equilibria partly run

above the L(SG) for the system CO₂-CH₄. These lines in part coincide for different temperatures and fluid inclusions points plotting on these tie-lines present both partial homogenization (SLG → SL) and "initial melting" by appearance of a gas bubble (SL → SLG). This phase behaviour is typical for CH₄-rich inclusions of "type H4" and has been frequently observed in fluid inclusions, notably in retrograde granulite rocks (Van den Kerkhof *et al.*, 1991, 1993). For binary CO₂-CH₄ mixtures, this type of phase behaviour is limited to compositions of 24-85 mole% CH₄ and molar volumes of 38-63 cm³/mole, according to Herskowitz & Kisch (1984). The present model predicts much more limited ranges: 44-81 % CH₄ and 44-56 cm³/mole. On the other hand, both observations and the model show that the H4 behaviour is strongly favoured with increasing N₂ contents.

Conclusion

vX properties of CO₂-CH₄ and CO₂-N₂ fluids for the complete ranges of composition and molar volumes have been calculated. The model shows good agreement with experimental data. The result has been obtained by using two thermodynamic models, namely the SRK and the LK EOS. In particular, better accuracies in the ranges of near-critical fluids have been obtained. Different projections of phase diagrams were constructed and appeared to predict well the complex phase behaviour as observed in fluid inclusions in the absence of water. We believe that, by using our model, molar volumes and compositions can be obtained with good accuracy from microthermometry and Raman data.

It is also possible to apply our model to ternary mixtures of the system CO₂-CH₄-N₂. Calculations on vX properties of this system will be done in the future. However, the results cannot be presented in simple phase diagrams. The conditions of the occurrence of the liquid-liquid-gas immiscibility at low temperatures have been discussed and calculated with our model; but it is felt that more basic experimental data are needed. The model presented here in this work will also be coupled with the model of mixed gas clathrates (Dubessy *et al.*, 1992) for the calculation of all phase transitions in the CO₂-CH₄-N₂-H₂O-NaCl system.

Acknowledgements : We have appreciated very much the careful reviews by Dr Grevel, Dr Vapnik and Kisch. We thank also C. Chopin and E.A.J. Burke for all their constructive comments. This work has been funded partially by Elf Aquitaine and CNRS.

References

- Agrawal, G.M. & Laverman, R.J. (1974): Phase behavior of the methane-carbon dioxide system in the solid-vapor region. *Adv. Cryog. Eng.*, 19, 327-338.
- Al-Sahhaf, T.A., Kidnay, A.J., Sloan, E.D. (1983): Liquid-vapor equilibria in the N₂ + CO₂ + CH₄ system. *Ind. Eng. Chem. Fundam.*, 22(4), 372-380.
- Angus, S., Armstrong, B., De Reuck, K.M. (1976): Carbon dioxide. Vol. 3 of *International Thermodynamic Tables of the Fluid State*. Pergamon Press.
- , —, — (1978): Methane. Vol. 5 of *International Thermodynamic Tables of the Fluid State*. Pergamon Press.
- , —, — (1979): Nitrogen. Vol. 6 of *International Thermodynamic Tables of the Fluid State*. Pergamon Press.
- Arai, Y., Kaminishi, G., Saito, S. (1971): The experimental determination of the P-V-T-X relations for the carbon dioxide-nitrogen and carbon dioxide-methane systems. *J. Chem. Eng. Jap.*, 4(2), 113-122.
- Asselineau, L., Bogdanic, G., Vidal, J. (1979): A versatile algorithm for calculating vapour-liquid equilibria. *Fluid Phase Equilibria*, 3, 273-290.
- Berdnikov, N.V. (1987): Thermobarogeochemistry: Precambrian metamorphic complexes of the Far East (Russia). Ph.D. Thesis, Institute of Tectonics and Geophysics, Khabarovsk, 115 p (in Russian).
- Burruss, R.C. (1981): Analysis of fluid inclusions: phase equilibria at constant volume. *Amer. Jour. Sci.*, 281, 1104-1126.
- Chang, S.D. & Lu, B.C.Y. (1967): Vapor-liquid equilibria in the nitrogen-methane-ethane system. *Chem. Eng. Prog. Symp. Ser.*, 63(81), 18-27.
- Cines, M.R., Roach, J.T., Hogan, R.J., Roland, C.H. (1953): Nitrogen-methane vapor-liquid equilibria. *Chem. Eng. Prog. Symp. Ser.*, 49(6), 1-100.
- Darimont, A. & Heyen, G. (1988): Simulation des équilibres de phases dans le système CO₂-N₂. Applications aux inclusions fluides. *Bull. Minéral.*, 111, 179-182.
- Davalos, J., Anderson, W.R., Phelps, R.E., Kidnay, A.J. (1976): Liquid-vapor equilibria at 250 K for systems containing CH₄, C₂H₆ and CO₂. *J. Chem. Eng. Data*, 21(1), 81-84.
- Davis, J.A., Rodewald, N., Kurata, F. (1962): Solid-liquid-

- vapor phase behavior of the methane-carbon dioxide system. *A.I.Ch.E. Journal*, 8(4), 537-539.
- Diamond, L. (1986): Hydrothermal geochemistry of late-metamorphic gold-quartz veins at Brusson, Val d'Ayas, Pennine Alps, NW. Italy. Unpubl. Ph.D. thesis, ETH-Zürich, 226 p.
- Donnelly, H.G. & Katz, D.L. (1954): Phase equilibria in the carbon dioxide-methane system. *Ind. Eng. Chem.*, 46(3), 511-517.
- Dubessy, J., Thiéry, R., Canals, M. (1992): Modelling of phase equilibria involving mixed gas clathrates. Application to the determination of molar volume of the vapour phase and of the salinity of the aqueous solution in fluid inclusions. *Eur. J. Mineral.*, 4, 873-884.
- Herskowitz, M. & Kisch, H.J. (1984): An algorithm for finding composition, molar volume and isochores of CO₂-CH₄ fluid inclusions from Th and Tfm (for Th < Tfm). *Geochim. Cosmochim. Acta*, 48, 1581-1587.
- Heyen, G. (1981): A cubic equation of state with extended range of application. Second World Congress of Chemical Engineering. Ed. S.A. Newmann. Montreal: Ann Arbor Science, 1981. 175-185.
- Heyen, G., Ramboz, C., Dubessy, J. (1982): Simulation des équilibres de phases dans le système CO₂-CH₄ en dessous de 50°C et de 100 bar. Application aux inclusions fluides. *C.R. Acad. Sci. Paris*, 294, 203-206.
- Huron, M.-J., Dufour, G.-N., Vidal, J. (1978): Vapour-liquid equilibrium and critical locus curve calculations with the Soave equation for hydrocarbons systems with carbon dioxide and hydrogen sulphide. *Fluid Phase Equilibria*, 1, 247-265.
- Hwang, S.-C., Lin, H.-M., Chappellear, P.S., Kobayashi, R. (1976): Dew point study in the vapor-liquid region of the methane + carbon dioxide system. *J. Chem. Eng. Data*, 21(4), 493-497.
- Kidnay, A.J., Miller, R.C., Sloan, E.D., Hiza, M.J. (1985): A review and evaluation of the phase equilibria, liquid-phase heats of mixing and excess volumes, and gas-phase PVT measurements for nitrogen + methane. *J. Phys. Chem. Ref. Data*, 14(3), 681-694.
- King, M.B. (1969): Phase equilibrium in mixtures. Pergamon Press, 585 p.
- Kisch, H.J. & Van den Kerkhof, A.M. (1991): CH₄-rich inclusions from quartz veins in the Valley-and-Ridge province and the anthracite fields of the Pennsylvania Appalachians. *Am. Mineral.*, 76, 230-240.
- Kreglewski, A. & Hall, K.R. (1983): Phase equilibria calculated for the systems N₂ + CO₂, CH₄ + CO₂ and CH₄ + H₂S. *Fluid Phase Equilibria*, 15, 11-32.
- Krichevskii, I.R., Khazanova, N.E., Lesnevskaya, L.C., Sandalova, L. (1962): Liquid-gas equilibria in the nitrogen + carbon dioxide system at high pressures. *Khem. Prom.*, 3, 169-171.
- Lee, B.I. & Kesler, M.G. (1975): A generalized thermodynamic correlation based on three-parameter corresponding states. *A.I.Ch.E. J.*, 21, 510-527.
- Mraw, S.C., Hwang, S.C., Kobayashi, R. (1978): Vapor-liquid equilibrium of the CO₂-CH₄ system at low temperatures. *J. Chem. Eng. Data*, 23(2), 135-139.
- Muirbrook, N.K. & Prausnitz, J.M. (1965): Multicomponent vapor-liquid equilibria at high pressures. Part I: experimental study of the nitrogen-oxygen-carbon dioxide system at 0°C. *A.I.Ch.E. J.*, 11(6), 1092-1097.
- Murphy, P.J. & Roberts, S. (1994): Laser Raman spectroscopy of differential partitioning in mixed-gas clathrates in H₂O-CO₂-N₂-CH₄ fluid inclusions: implications in microthermometry. *Geochim. Cosmochim. Acta*, in press.
- Neumann, P.N.A. & Walch, W. (1968): Dampf / Flüssigkeits-Gleichgewicht CH₄-CO₂ im Bereich tiefer Temperaturen und kleiner CO₂ Molenbrüche. *Chem. Ing. Techn.*, 40(5), 241-244.
- Omar, H.O. (1962): Phase equilibria of some binary systems at low temperatures. Ph.D. Thesis. Univ. Leiden.
- Parrish, W.R. & Hiza, M.J. (1974): Liquid-vapor equilibria in the nitrogen-methane system between 95 and 120 K. *Adv. Cryog. Eng.*, 19, 300-308.
- Peng, D.Y. & Robinson, D.B. (1976): A new two constants equation of state. *Ind. Eng. Chem. Fundam.*, 15, 59-64.
- Prausnitz, J.M. (1969): Molecular thermodynamics of fluid-phase equilibria. Prentice-Hall, Inc.
- Schneider, G.M. (1978): High-pressure phase diagrams and critical properties of fluid mixtures. *Chem. Therm.*, 2, 105-146.
- Seitz, J.C., Pasteris, J.D., Wopenka, B. (1987): Characterization of CO₂-CH₄-H₂O fluid inclusions by microthermometry and laser Raman microprobe spectroscopy: inferences for clathrate equilibria. *Geochim. Cosmochim. Acta*, 51, 1651-1664.
- Soave, G. (1972): Equilibrium constants from a modified Redlich-Kwong equation of state. *Chem. Eng. Sci.*, 27, 1197-1203.
- Somait, F.A. & Kidnay, A.J. (1978): Liquid-vapor equilibria for systems containing N₂, CH₄ and CO₂. *J. Chem. Eng. Data*, 23(4), 301-305.
- Stryjek, R., Chappellear, P.S., Kobayashi, R. (1974): Low-temperature vapor-liquid equilibria of nitrogen-methane system. *J. Chem. Eng. Data*, 19(4), 334-339.
- Thiéry, R., Vidal, J., Dubessy, J. (1994): Phase equilibria modelling applied to fluid inclusions. Liquid-vapour equilibria and calculation of the molar

- volume in the CO₂-CH₄-N₂ system. *Geochim. Cosmochim. Acta*, 58, 1073-1082.
- Van den Kerkhof, A.M. (1988): The system CO₂-CH₄-N₂ in fluid inclusions : theoretical modelling and geochemical applications. Ph.D. Thesis. Amsterdam (Free University), 206 p.
- (1990): Isochoric phase diagrams in the systems CO₂-CH₄ and CO₂-N₂: Application to fluid inclusions. *Geochim. Cosmochim. Acta*, 54, 621-629.
- Van den Kerkhof, A.M., Touret, J.L.R., Maijer, C., Jansen, J.B.H. (1991): Retrograde methane-dominated fluid inclusions from high-temperatures granulites of Rogaland, southwestern Norway. *Geochim. Cosmochim. Acta*, 55(9), 2533-2543.
- Van den Kerkhof, A.M., Frezzoti, M.-L., Talarico, F., Berdnikov, N.V. (1993): Metastable phase transitions in the system CO₂-CH₄-N₂ including immiscibility of the undercooled liquid (L₁L₂G): an example from granulites of the Wilson terrane, North Victoria Land (Antartica). European Current Research on Fluid Inclusions XII. *Archivum Mineralogiscae*. Warsaw: 1993. XLIX: 227-229.
- Van Konynenburg, P.H. & Scott, R.L. (1980): Critical lines and phase equilibria in binary Van der Waals mixtures. *Phil. Trans. R. Soc., A*, 298, 495-540.
- Vidal, J. (1978): Mixing rules and excess properties in cubic equations of state. *Chem. Eng. Sci.*, 33, 787-791.
- (1983): Equations of state- Reworking the old forms. *Fluid Phase Equilibria*, 13, 15-33.
- (1984): Phase equilibria and density calculations for mixtures in the critical range with simple equation of state. *Ber. Bunsenges. Phys. Chem.*, 88, 784-791.
- Zenner, G.H. & Dana, L.I. (1963): Liquid-vapor equilibrium compositions of carbon dioxide-oxygen-nitrogen mixtures. *Chem. Eng. Prog. Symp. Ser.*, 59, 36-41.

Received 27 October 1993

Accepted 16 June 1994

Note added in proofs :

In Fig. 7b, read -63°C instead of -62°C for one of the LG(S) tie-line.

CHAPITRE 3

**Les équilibres
de phases fluides
du système ion-dipôle
par un modèle MSA.**

Le diagramme de phase global.

Résumé

Dans les solutions aqueuses salées, les interactions ion-ion, ion-dipôle et dipôle-dipôle jouent certainement un rôle prédominant par rapport aux autres types d'interactions moléculaires (forces de dispersion, d'induction, ...). De cette constatation provient notre intérêt porté pour les modèles thermodynamiques des fluides théoriques composés d'ions et de dipôles. Les calculs des propriétés thermodynamiques des fluides ion-dipôle ont déjà fait l'objet de nombreux travaux en mécanique statistique. C'est un de ces modèles, le modèle ion-dipôle développé sur la base de la "Mean Spherical Approximation" (MSA), qui est décrit dans ce chapitre. La "Mean Spherical Approximation" (ou "Approximation en champ sphérique moyen") est en effet une théorie, permettant de calculer les propriétés thermodynamiques d'un fluide à partir de ses potentiels moléculaires. L'équation d'état MSA du système ion-dipôle est donc seulement fonction de paramètres, qui ont tous une signification physique. Ces paramètres sont le moment dipolaire, la taille des ions, la taille des dipôles, la valence et la charge des ions. Le but de ce chapitre est l'étude de l'influence de ces paramètres sur la topologie des diagrammes de phases. Plusieurs diagrammes de phases caractéristiques sont calculés. La synthèse des résultats est représentée sous la forme d'un diagramme de phase global. Cette étude nous servira dans le chapitre suivant pour le choix des paramètres à utiliser pour une équation d'état dans le système H₂O-NaCl.

Référence.

Thiéry, R., Lvov, S.N., et Dubessy, J. (soumis à J. Chem. Phys.) A global phase diagram for the Ion-Dipole model in the Mean Spherical Approximation.

A global phase diagram for the Ion-Dipole Model in the Mean Spherical Approximation.

R. Thiéry*, S.N. Lvov**, J. Dubessy*

* CREGU, BP 23, 54 501, Vandoeuvre-les-Nancy, FRANCE

** Center for Advanced Materials, The Pennsylvania State University, 517 Deike
Building, University Park, PA, 16 802, USA.

(submitted to J. Chem. Phys.)

ABSTRACT

This work is a theoretical study of electrolyte solutions by using the mean spherical approximation of the ion-dipole mixture. Binary dipolar solvent-salt mixtures are modelled as mixtures of hard spheres, that interact between each other by means of Coulombic and dipolar forces. The topology of phase diagrams, including saturation curves, critical lines, liquid-liquid-gas curves, and azeotropic lines have been determined and classified according to the nomenclature of van Konynenburg and Scott, as a function of physical parameters, such as the dipolar moment, the ionic valence and the size of dipolar and ionic spheres. The different system types have been mapped accurately onto a two-dimensional global phase diagram in the space of two dimensionless parameters, called respectively α_1 and α_2 . The α_1 parameter is related to the ratio of the intensity of the dipolar field to the electrostatic field produced by the ions, whereas the α_2 parameter is the ratio of the dipole diameter to the ion diameter. For mixtures of equal-sized ions and dipoles, the following sequence of phase diagrams has been recognized with increasing α_1 parameter: type III, type III_m, type IV, type II, type II with double azeotropy, type IV with double azeotropy and type III-HA. The α_2 parameter is shown to have a major influence on the topology of

phase diagrams. For low α_1 values (below 0.1), the decrease of the α_2 parameter enhances the miscibility of both components and leads to the stretching of the critical curve between the critical points of both components, whereas for high α_1 values (above 0.3), a decrease of the α_2 parameter reduces the miscibility of both components and leads to the development of gas-gas equilibria, double azeotropy and heteroazeotropy.

INTRODUCTION

Theoretical studies about the topology of fluid phase equilibria have proven to be very useful for deciphering the complex fluid phase relations observed in multicomponent systems¹. Indeed, whereas the phase diagram of a one-component system is very simple, at least eight different types of phase diagrams have already been observed for binary systems¹. Mixtures containing three or more components appear to be incredibly much more complex^{1,2}. Many studies have established that equations of state (EOS) are able to generate the different kinds of fluid phase equilibria (liquid-vapour, liquid-liquid, gas-gas and liquid-liquid-gas). The first pioneering work of this type was the study of van Konynenburg and Scott^{3,4}, who have shown that a simple EOS as the van der Waals EOS can reproduce qualitatively the major types of phase diagrams of binary fluids. A classification was proposed and is now currently used as a basis for describing the different kinds of phase diagrams in binary systems. The influence of the two parameters of the van der Waals EOS on the phase topology could be conveniently visualized on a diagram, called a global phase diagram. Such a diagram shows the different fields of occurrence of the kinds of phase diagrams as a function of the van der Waals a and b parameters. Moreover, such a study showed how a type of phase diagram can be generated from another type by a continuous variation of one of the model parameter. Since the work of van Konynenburg and Scott^{3,4}, numerous studies have been carried out on other more realistic equations of state⁵⁻¹³. But, up to now, these studies have been focused on equations of state, that are only appropriate for mixtures of nonelectrolytes. Obviously, the modelling of mixtures containing electrolytes is by far a much more difficult problem. Despite the overwhelming role of these fluids into biological, geochemical and industrial processes, theoretical thermodynamic models have not been investigated far enough for electrolyte solutions. A solution to a problem can only be approached after using some simplifications. One of the first widely used simplification leads to the so-called "primitive" models of electrolyte solutions. In these models, the solutions are represented by a system of charged spheres (the ions) embedded in a continuous dielectric continuum (the solvent). However, the ion-solvent and solvent-

solvent interactions are not specifically taken into account, and the dependence of the dielectric constant with the ionic concentration is neglected. Thus, the deficiencies of the primitive models can only be treated on an empirical way. For this reason, primitive models cannot be applied over large range of pressure, temperature and composition. On the contrary, in "non-primitive" models, the solvent is represented by spheres with a permanent point dipole. Such an approach is clearly more difficult, but recent advances in statistical mechanics and computer simulation have provided the tools for estimating the thermodynamic properties, dielectric constant and pair correlation functions of the ion-dipole mixture. Thus, several theoretical non-primitive models have been recently developed. One of these theories is the Mean Spherical Approximation (MSA), that has been developed in a series of papers¹⁴⁻²⁴. During the past years, the MSA has gained renewed interests, as it provides an analytical solution for the thermodynamic properties of ion-dipole mixtures. Contrary to other approximations, such as the hypernetted chain correlation, the MSA can be calculated analytically and this is a great advantage for the very demanding calculations of fluid phase equilibria. Furthermore, the MSA model is theoretically sound, as it is consistent with the Debye-Hückel theory and satisfies to the large-charge and large-density Onsager's limits.

Therefore, the aim of this work is to study the global phase diagram of an EOS, based on the MSA. The investigated EOS combines a hard-sphere repulsion term with a MSA term taking into account the electrostatic ion-ion, ion-dipole and dipole-dipole interactions. The MSA solution used in this work is the one obtained for a ion-dipole mixture with dissimilar size for ions and dipoles¹⁹. The case of different size for the anions and the cations have been recently solved²⁵⁻²⁹, but its analytical solution is more complex. The study of ion-dipole mixtures has already been sketched by Harvey²³ in the case of the MSA solution with equal-sized dipoles and ions. This paper is thus a new development of the work of Harvey. A brief outline of the MSA model is given in the first section. Most featured phase diagrams are presented in the second part. Attention is given to the influence of the dipole moment, ionic valence and the diameters of ionic and dipolar spheres on the topology of fluid phase equilibria. The global phase diagram is described in

the third part. A discussion and comparison with water-salt systems is made in the last and fourth part.

THEORY.

The Mean Spherical Approximation.

A binary fluid mixture composed of ions and dipoles is considered in this study. Ions are produced by the dissolution of a salt, composed of v_m anions of charge z_m and v_p cations of charge z_p . The dipolar moment of dipoles is μ . All ions have the same diameter σ_i , but the ionic σ_i diameter can be different from the σ_d diameter of the dipoles.

Four types of intermolecular forces are considered between two particles i and j separated by a distance r :

- hard sphere repulsion between two particles i and j :

$$u_{ij}(r) = 0 \text{ for } r > \sigma, \quad (1a)$$

$$\text{and } u_{ij}(r) = \infty \text{ for } r < \sigma, \quad (1b)$$

$$\text{where } \sigma = (\sigma_i + \sigma_j) / 2, \quad (1c)$$

- coulombic interaction between two ions i and j :

$$u_{ij}(r) = z_i z_j e^2 / \epsilon_0 r, \quad (2)$$

where e is the elementary charge, and ϵ_0 is the vacuum permittivity;

- electrostatic interaction between an ion i and a dipole j :

$$u_{ij}(r) = z_i \mu_j e \cos \theta / \epsilon_0 r^2, \quad (3)$$

where θ is the angle between the dipole moment and the line joining i and j ;

- electrostatic interaction between two dipoles i and j :

$$u_{ij}(r) = - \mu_i \mu_j (2 \cos \theta_i \cos \theta_j - \sin \theta_i \sin \theta_j \cos (\phi_i - \phi_j)) / \epsilon_0 r^3, \quad (4)$$

where θ_i , θ_j , ϕ_i and ϕ_j are angles describing the orientation of the dipoles i and j ³⁰.

Statistical mechanics provides several methods for estimating the thermodynamic properties of a fluid mixture from the knowledge of the u_{ij} pair potentials (PP) of the system. The MSA is one of these methods. The MSA can be decomposed in two main steps. At first, the g_{ij} radial distribution function (RDF) between two particles i and j is

derived from the knowledge of pair potentials u_{ij} . Then, the thermodynamic properties of the mixture are calculated from the g_{ij} RDF.

The derivation of the g_{ij} RDF from the u_{ij} PP is one of the basic and difficult problem of the statistical mechanical theory of fluids, and approximations must be used. The MSA theory uses a method, based on the so-called "integral equations" for deriving the g_{ij} RDF from the u_{ij} PP. This method is here briefly described by considering successively the cases of the perfect gas, a dilute fluid and finally a dense fluid.

In the absence of intermolecular forces, the g_{ij} RDF is simply equal to 1.

$$g_{ij}(r) = 1. \quad (5)$$

In a dilute fluid, a remarkable simple relation between the RDF and the PP between two particles i and j can be derived³¹:

$$g_{ij}(r) = \exp(-\beta u_{ij}(r)), \quad (6a)$$

$$\text{where } \beta = 1/kT. \quad (6b)$$

This approximation is effectively valid in very dilute electrolyte solutions, where an ion is surrounded by a cloud of counterions. The same relation is indeed developed in the Debye-Hückel theory. When $u_{ij}(r)$ is small when compared to the product kT (i.e. when the molecules are far away), Eq. (6a) can be further simplified by linearizing the exponential function :

$$g_{ij}(r) = 1 - \beta u_{ij}(r). \quad (7)$$

Eq. (6a) is no more valid in dense fluids, and the influence of neighbouring particles to a pair (i - j) must be taken into account. A way of achieving this is to decompose the g_{ij} RDF into three contributions :

$$g_{ij}(r) = 1 + c_{ij}(r) + g_{ind}. \quad (8)$$

The first term, equal to one, is simply the contribution of a mixture of non-interacting molecules (Eq. (5)). The second term, given by the c_{ij} function, describes the direct influence of the u_{ij} PP on the g_{ij} RDF. c_{ij} is called the direct correlation function (DCF). The third term, denoted g_{ind} , describes the indirect influence of the u_{ij} PP to the g_{ij} RDF through all neighboring particles. It is worth to note that in a dilute fluid, g_{ind} is

neglectable. The *gind* contribution can be further explicated, as it is done in the exact Ornstein and Zernike³² (OZ) equation :

$$g_{ij}(r) = 1 + c_{ij}(r) + \sum \rho_k \int [g_{ik}(r,r') - 1] c_{kj}(r,r') dr', \quad (9)$$

where the *gind* term is calculated by a convolution of the c_{kj} DCF with the g_{ik} RDF minus one. The summation is made over all kinds of k particules surrounding the i - j pair with the density ρ_k (in this study, k is either an ion or a dipole). The OZ equation is an integral equation, which contains two unknowns (the g_{ij} RDF and the c_{ij} DCF). Thus, additional relations are required for solving the OZ equation and calculating the g_{ij} RDF. The most evident relation is the following :

$$g_{ij}(r) = 0 \text{ for } r < \sigma_{ij}. \quad (10)$$

This condition is simply a consequence of the impenetrability of hard spheres representing the particules. For the case $r > \sigma_{ij}$, another assumption must be stated. One possibility is to assume that the c_{ij} DCF is a function of the u_{ij} PP in the same way for a dense fluid than for a dilute fluid. Therefore, by identifying the corresponding terms in Eq. (7) for a dilute fluid and Eq. (8) for a dense fluid, the following relation is obtained:

$$c_{ij}(r) = -\beta u_{ij}(r) \text{ for } r > \sigma_{ij}. \quad (11)$$

This approximation strictly holds for $r \rightarrow \infty$ and is most questionable in the intermediate region, where $u_{ij}(r)$ reaches its potential depth. But, the great advantage of this approximation over other approximations is that it gives expressions that can be solved analytically. For this reason, this approximation, commonly referred to as the Mean Spherical Approximation (MSA)³³, looks attractive. Analytical expressions for the g_{ij} RDF have been derived respectively for the ion-ion, ion-dipole and dipole-dipole pairs³⁴.

Any thermodynamic property of the mixture can be calculated from the g_{ij} RDF. The equation relating the excess internal energy to the RDF is usually used³⁵:

$$U^{ex} = 1/2V \sum N_i N_j \int u_{ij}(r) g_{ij}(r) dr. \quad (12)$$

Other thermodynamic properties are then calculated by adequate differentiation or integration of U^{ex} .

The equation of state

The equation of state for the ion-dipole mixture is formulated by means of an analytical expression of the Helmholtz free energy (HFE) and is split into two contributions :

$$A = A^{\text{hs}} + A^{\text{MSA}}. \quad (13)$$

The first term takes into account the repulsive forces between hard spheres, whereas the second one describes the influence of ion-ion, ion-dipole and dipole-dipole interactions. The A^{hs} HFE of a mixture of hard spheres is given by the Boublik equation of state³⁶. The A^{MSA} HFE is given in the Appendix. All thermodynamic properties have been obtained by analytical differentiations of HFE with respect to the temperature, molar volume and composition. Derivatives up to the fourth order are calculated analytically by using a software package³⁷ for differentiation and thermodynamic calculations. This was necessary because of the length and complexity of the mathematical expressions.

Scaling relations.

The HFE of the ion-dipole mixture is a function of three variables (the temperature T , the molar volume V and the mole fraction x_I of dipoles) and seven model parameters ($v_p, v_m, z_p, z_m, \mu, \sigma_d$ and σ_i). Note here that in all what follows x_I is defined as the number of dipoles divided by the total number of ion molecules and dipoles, and molar quantities are expressed on the basis of the total number of ion molecules and dipoles. Fortunately, the parameters are not independent and there is no need to study separately the influence of each parameter. First of all, the condition of the electroneutrality of the solution requires that:

$$v_p z_p + v_m z_m = 0. \quad (14)$$

Other relations do exist and can be revealed by dimensional analysis of the underlying equations of the MSA. These scaling relations are important to consider, as they allow us to generalize quickly a given result to other cases. The particular cases of a pure dipolar fluid and pure ionic fluid will be first considered before the general case of the ion-dipole mixture.

For dipolar fluids, the HFE depends on two variables (T and V) and two model parameters (μ and σ_d).

$$A = A(T, V, \mu, \sigma_d). \quad (15a)$$

Dimensional analysis shows that the HFE can be written as follows :

$$A = kT A_r(T_r, V_r), \quad (15b)$$

where T_r and V_r are reduced temperature and molar volume, defined by :

$$T_r = kT/(\mu^2/\sigma_d^3) K, \quad (15c)$$

$$V_r = V/(N_a \sigma_d^3). \quad (15d)$$

K is a convenient conversion factor used when the dipolar moment is expressed in Debye ($K= 10^{49}$), and N_a is the Avogadro's number.

For an ionic fluid, the HFE depends on two variables (T and V) and five model parameters ($z_m, z_p, v_p, v_m,$ and σ_i):

$$A = A(z_m, z_p, v_p, v_m, \sigma_i, T, V). \quad (16a)$$

The HFE can be written :

$$A = kT A_r(T_r, V_r), \quad (16b)$$

where

$$T_r = K' kT / (v_p z_p^2 + v_m z_m^2) e^2 / (v_p + v_m) \sigma_i, \quad (16c)$$

$$V_r = V / (N_a \sigma_i^3), \quad (16d)$$

where K' is a constant equal to 10^9 .

For the ion-dipole mixture, the HFE of the ion-dipole mixture depends on three variables and seven model parameters :

$$A = A(z_m, z_p, v_p, v_m, \sigma_i, \sigma_d, \mu, T, V, x_I), \quad (17a)$$

where x_I is the mole fraction of the dipolar component.

Dimensional analysis yields that the HFE can be written as

$$A = kT A_r(T_{r1}, T_{r2}, V_{r1}, V_{r2}, x_I), \quad (17b)$$

where the subscripts 1 and 2 refer respectively to the dipolar and the ionic component. T_{r1} and V_{r1} are given by Eqs (15c) and (15d), T_{r2} and V_{r2} by Eqs (16c) and (16d).

An equivalent formulation can be given :

$$A = kT A_r(T_{r1}, V_{r1}, \alpha_1, \alpha_2, x_I), \quad (17c)$$

where α_1 and α_2 are defined by :

$$\alpha_1 = [\mu^2/\sigma_d^3] [(v_p+v_m)/(v_pz_p^2 + v_mz_m^2)] [\sigma_i / e^2 K/K], \quad (17d)$$

and

$$\alpha_2 = \sigma_d/\sigma_i. \quad (17e)$$

α_1 can be seen as a parameter measuring the force of the polar component or the weakness of the salt.

It can be noted that :

$$\alpha_1 = T_{r1}/T_{r2} \quad (18a)$$

$$\alpha_2 = (V_{r1}/V_{r2})^{1/3} \quad (18b)$$

Thus, only two parameters (α_1 and α_2) are required for an entire study of the ion-dipole model.

PHASE DIAGRAMS

The first objective of this study is to understand the influence of simple physical parameters such as the dipole moment, the charges of ions and the diameters of molecules on the fluid phase equilibria. For this purpose, the phase diagrams for various sets of (α_1 - α_2) parameters have been determined.

Pure fluids

Before considering the phase diagrams of the binary ion-dipole mixture, it is necessary to characterize the phase equilibria of both pure components. First, the critical point of a pure fluid has been calculated by solving the following set of equations:

$$A_{VV}=0, \quad (19a)$$

$$\text{and } A_{VVV} = 0, \quad (19b)$$

with the critical temperature (T_c) and molar volume (V_c) as unknowns. In the notation above, subscripts indicate the differentiation variables. For the polar fluid, the following reduced coordinates (Eqs (15c)-(15d)) of the critical point were calculated:

$T_r = 0.2250463$, $V_r = 9.41149074$ and $P_r = 0.031270$. These results agree with those obtained by Harvey²³. For the pure ionic fluid, the critical point in reduced coordinates (Eqs. (16c)-(16d)) are $T_r = 0.07857696$, $V_r = 69.032985$ and $P_r = 0.00122855$. Again, these results are in good agreement with the values obtained by Harvey²³. The saturation curve has been obtained by solving the equations for a given temperature T and with the molar volume of the liquid (V_l) and gas (V_g) as unknowns :

$$P(T, V_l) = P(T, V_g), \quad (20a)$$

$$\mu(T, V_l) = \mu(T, V_g), \quad (20b)$$

where μ designates here the chemical potential of one component in a phase.

The scaling relations allow us to estimate easily the influence of model parameters on the position of the saturation curve and critical point. For the polar fluid, differentiation of the HFE (Eq. (15b)) with respect to the molar volume leads to :

$$P = T_r / K \mu^2 / \sigma_d^6 P_r(T_r, V_r), \quad (21)$$

where T_r and V_r are given by Eqs. (15c)-(15d), and P_r is an universal function for polar fluids, which is independent of the dipole moment μ and the σ_d diameter. Combined use of Eqs. (15c) and (21) gives us the coordinates of the critical point as a function of μ and σ_d :

$$T_{cd} = 0.2250463 / kK \mu^2 / \sigma_d^3, \quad (22a)$$

$$P_{cd} = 0.0070372 / K \mu^2 / \sigma_d^6. \quad (22b)$$

For the ionic fluid, differentiation of the HFE (Eq. (16b)) with respect to the molar volume gives:

$$P = T_r / K' (v_p z_p^2 + v_m z_m^2) / (v_p + v_m) e^2 / \sigma_i^4 P_r(T_r, V_r), \quad (23)$$

where T_r and V_r are given by Eqs (16c)-(16d), and P_r is an universal function for ionic fluids which does not depend on the valence of the salt, the charge of the ions and the ionic diameter. Combined use of Eqs. (16c) and (23) give us the coordinates of the critical point as a function of v_p , v_m , z_p , z_m and σ_i :

$$T_{ci} = 0.07857696 (v_p z_p^2 + v_m z_m^2) / (v_p + v_m) e^2 / \sigma_i / kK', \quad (24a)$$

$$P_{ci} = 9.65357e-05 / K' (v_p z_p^2 + v_m z_m^2) / (v_p + v_m) e^2 / \sigma_i^4. \quad (24b)$$

Binary mixtures.

The phase diagram of any binary mixture is at first conditioned by the volatility difference² between both constituent pure components, i.e. by the ratios T_{ci}/T_{cd} and P_{ci}/P_{cd} for the ion-dipole mixture. Combination of Eqs. (22a)-(24a) and (22b)-(24b) yields us these simple results :

$$T_{ci}/T_{cd} = 0.349159 / \alpha_1, \text{ and} \quad (25a)$$

$$P_{ci}/P_{cd} = 72.8974 \alpha_1 / (\alpha_2)^3. \quad (25b)$$

Thus, for low α_1 values ($\alpha_1 < 0.349159$), the polar component is more volatile than the ionic component. Conversely, for high α_1 values ($\alpha_1 > 0.349159$), the ionic component is more volatile than the the polar component. The α_2 parameter has no influence on the T_{ci}/T_{cd} ratio, but exerts a strong effect on the P_{ci}/P_{cd} ratio. Thus, the more the α_2 parameter is large, the more the P_{ci}/P_{cd} ratio is small for a given α_1 parameter.

Critical points (CP) of the binary mixture have been found by solving the relations:

$$(G_{2x})_{T,P=0}, \text{ and} \quad (26a)$$

$$(G_{3x})_{T,P=0}. \quad (26b)$$

Two critical lines are in general found for any (α_1, α_2) parameters (see below). The stability of any calculated critical point was checked by checking that the fourth differentiate of the Gibbs energy with respect to the composition at constant pressure and temperature is positive:

$$(G_{4x})_{T,P} > 0. \quad (27)$$

Several isothermal sections of liquid-gas and liquid-liquid phase equilibria have been calculated for locating roughly the three-phase liquid-liquid-gas curves and azeotropic lines. Three-phase liquid-liquid-gas (LLG) curves have been calculated by solving the equations of equality of the pressure and chemicals potentials between three coexisting phases (labelled by the a , b , and c subscripts) :

$$P(x_I, V_a) = P(y_I, V_b), \quad (28a)$$

$$P(x_I, V_a) = P(z_I, V_c), \quad (28b)$$

$$\mu_1(x_I, V_a) = \mu_1(y_I, V_b), \quad (28c)$$

$$\mu_2(x_I, V_a) = \mu_2(y_I, V_b), \quad (28d)$$

$$\mu_1(x_I, V_a) = \mu_1(z_I, V_c), \quad (28e)$$

$$\mu_2(x_1, V_a) = \mu_2(z_1, V_c). \quad (28f)$$

At a given temperature, the five unknowns are the molar volumes of the three phases (V_a , V_b and V_c), and the mole fractions of the first component in each phase (x_1 , y_1 and z_1).

Liquid-liquid-gas immiscibility was located too by searching critical end-points (CEP). A CEP occurs when a critical phase is in equilibrium with another phase. Thus, in a P - T diagram, CEP are at the intersection of a LLG curve with a critical curve. In other words, CEP are points that terminate LLG curves in a P - T diagram. The conditions for a CEP are given by the equations:

$$G_{2x}(T, V_c, x_c) = 0, \quad (29a)$$

$$G_{3x}(T, V_c, x_c) = 0, \quad (29b)$$

$$P(T, V_c, x_c) = P(T, V_a, x_a), \quad (29c)$$

$$\mu_1(T, x_c, V_c) = \mu_1(T, x_a, V_a), \quad (29d)$$

$$\mu_2(T, x_c, V_c) = \mu_2(T, x_a, V_a). \quad (29e)$$

The five unknowns are the temperature T , the molar volume V_c and the composition x_c of the critical phase, the molar volume V_a and the composition x_a of the coexisting phase.

Azeotropic points occur when two distinct phases are in equilibrium and have the same composition. Conditions for an azeotropic point are thus :

$$P(T, V_a, x) = P(T, V_b, x), \quad (30a)$$

$$\mu_1(T, V_a, x) = \mu_1(T, V_b, x), \quad (30b)$$

$$\mu_2(T, V_a, x) = \mu_2(T, V_b, x). \quad (30c)$$

The set of nonlinear equations for calculating critical points, liquid-gas points, liquid-liquid-gas points, critical end-points and azeotropic points was solved by the Newton-Raphson algorithm. Whole critical curves, LLG curves and azeotropic curves were calculated with the help of a technique using the Jacobian matrix calculated in the last iteration of the Newton-Raphson algorithm^{37,38}.

Several phase diagrams are shown here for different sets of the (α_1, α_2) parameters. They illustrate the major characteristics of fluid phase relations in the ion-dipole mixture. First, the case of equal-size dipole and ions, which has already been briefly described by Harvey²³, will be completed and reviewed. For convenience, P - T phase diagrams have

been plotted in the same reduced coordinates chosen by Harvey²³, i.e. in the (P_{r1}, T_{r1}) scale as defined by Eqs. (21) and (15c). For very small values of α_1 (Fig. 1, $\alpha_1 = 0.065$), the critical point of the ionic component (referred to as CPi) lies at a much higher temperature than the critical point of the polar component (referred to as CPd). The critical line starting from CPi runs to very high pressures. A three-phase LLG curve is present at pressures slightly below saturation pressures of the polar component. The critical curve starting from CPd meets the LLG curve at an upper critical end-point (UCEP), which is very close to CPd. The UCEP and the LLG curve cannot be distinguished from the saturation curve of the polar component at the scale of Fig. 1. The CPi-CPm critical curve (where CPm is a fictive critical point introduced for convenience for designating the high-pressure part of a critical curve) exhibits in Fig. 1 a pressure maximum and a pressure minimum. Such a phase topology has been classified by van Konynenburg and Scott^{3,4} as a type-III_m system. At still lower values of α_1 ($\alpha_1 < 0.0538$), the pressure minimum and maximum disappear, and the system becomes a simple type-III system. For extremely low values of α_1 (α_1 below 10^{-4}), the critical curve CPi-CPm goes to higher temperatures than T_{ci} , thus showing the so-called "gas-gas" equilibria. In Fig. 2, P - T phase diagrams are shown for the case $\alpha_1=0.072$. When compared to the previous case $\alpha_1=0.0645$, the temperature gap between CPi and CPd has been slightly reduced, but a major topological modification occurs. The LLG immiscibility field is separated in two parts, one at lower temperatures and the other at higher temperatures just below T_{cd} . The critical curve starting from CPi does not join CPm, but a lower-critical end-point (LCEP) at the low extremity of the high-temperature LLG curve. A critical line connects CPd to the UCEP of this LLG curve. The critical curve starting from CPm joins the UCEP of the low-temperature LLG curve. Such a phase diagram is classified as a type-IV system. Fig. 3 shows the P - T diagrams for the case $\alpha_1=0.085$. This is still a type-IV system, but the low-temperature LLG field lies now at temperatures very close to zero and is not visible on Fig. 3. Moreover, the high-temperature LLG curve near CPd has shrunk a lot, when compared to the case $\alpha_1=0.072$, and cannot be seen at

the scale of Fig. 3A. An enlarged view is given in Fig. 3B, which should be compared with Fig. 4 of the paper of Harvey²³, where slightly different values have been found for the position of the LLG curve. Our results should be more reliable, as more accurate algorithms (see above) have been used for solving the occurrence conditions of LLG equilibria. The P - T diagram for the case $\alpha_1=0.1$ is shown in Fig. 4. The LLG curve near CPd has disappeared, and a continuous critical curve connects now CPi and CPd. LL immiscibility is present at very low temperatures (not shown in Fig. 4). Thus, this is a type-II system.

The P - T phase diagram for the case $\alpha_1=0.45$ is shown in Fig. 5. Now, CPd is located at higher temperatures than CPi. The continuous CPi-CPd critical curve is concave towards high temperatures, and a LL immiscibility field arises at quite high temperatures (T_{rI} around 0.11). This is a type-II system. The case $\alpha_1=0.504$ is shown in Fig. 6 and is characterized by several new features. The CPi-CPd critical curve intersects the saturation curve of the polar component. In the region around the intersection point, two azeotropic curves appear. A negative azeotropic line lies below the saturation curve of the polar component (barely visible on Fig. 6) for compositions of x_{salt} between 0 and 0.05. A positive azeotropic curve connects an UCEP ($T_{rI} = 0.142712$, $P_{rI} = 0.001306$) to an azeotropic end-point (AEP). An AEP occurs at the intersection of the CPi-CPd critical curve and the positive azeotropic line ($T_{rI} = 0.16496$, $P_{rI} = 0.00527$). This azeotropic line lies in the continuity of the LLG curve. The LLG curve is at higher pressures than the saturation pressures of both ionic and polar components. Such a topological feature is referred to as "heteroazeotropy"²⁻⁴. Moreover, for values of T_{rI} between 0.1668 and 0.1678, a small part of the CPi-CPd critical curve becomes unstable ($G_{4x} < 0$). This indicates the presence of a small LLG curve³⁹. This is a type-IV system, but presenting features not described in the classification of van Konynenburg and Scott^{3,4}. The P - T phase diagram for $\alpha_1=0.6$ is shown in Fig. 7. This figure corrects also Fig. 1 shown in the paper of Harvey²³. Indeed, the LLG curve lies at higher (and not lower) pressures than the saturation curve for the ionic component, thus producing heteroazeotropy. Thus, this is a type III-HA system^{3,4}.

In summary, the following sequence of type of phase diagrams is observed for low to high values of α_1 in the case $\alpha_2 = 1$: III -> III_m -> IV -> II -> IV -> III-HA. Phenomena of double azeotropy occur for some of the type-II and type-IV at high values of α_1 . Some phase diagrams have been investigated too for fluids with different ionic and polar sizes. As shown by Eqs. (25a) and (25b), the α_2 parameter has no influence on the ratio T_{ci}/T_{cd} , but exerts a strong influence on the P_{ci}/P_{cd} . The smaller is the α_2 parameter, the larger is the P_{ci}/P_{cd} ratio. In the range of investigated α_1 and α_2 values (α_1 between 0 and 1, α_2 between 0.1 and 2), the P_{ci}/P_{cd} ratio is generally below 1 (except for α_1 values lower than 0.0-0.12). Thus, in other words, CP_i and CP_d get closer when the α_2 parameter is increased. Therefore, the α_2 parameter is not expected to change a lot the topology of phase diagrams described in the case $\alpha_2=1$, except for low values of α_2 . This has been confirmed by preliminary calculations. The case $\alpha_1=0.757$ and $\alpha_2=1.5$ is shown in Fig. 8. This is a type-III_m system. The LLG curve is located at pressures just below the saturation pressures of the ionic component. Therefore, this system does not exhibit heretoazeotropy. The case $\alpha_1=0.5$ and $\alpha_2=0.5$ is given in Fig. 9. This a type-III system showing gas-gas equilibria and heteroazeotropy. When reducing the α_2 parameter ($\alpha_1=0.5$ and $\alpha_2=0.2$) at constant α_1 value, the heteroazeotropy disappears (Fig. 10), and a new LLG curve occurs near CP_d. This LLG curve has not been calculated because of numerical problems, but is revealed by the presence of unstable points ($G_{4x}<0$) along the CP_d-CP_m critical curve. This is a type-IV* system. The case $\alpha_1=0.5$ and $\alpha_2=0.1$ is shown in Fig. 11. The connectivity of the critical curves has changed. The critical curve starting from CP_d stops now at an UCEP very close to CP_d, and CP_i is connected to CP_m. Gas-gas equilibria is still present, and the LLG curve is located at pressures just below the saturation pressures of the polar component. Therefore, this is a type-III system.

THE GLOBAL PHASE DIAGRAM

The influence of the parameters of the model on phase diagrams is best visualized with the help of a global phase diagram. The different types of phase diagrams have been classified by using the nomenclature of van Konynenburg and Scott^{3,4}. Since the

pioneering work of van Konynenburg and Scott^{3,4}, several mathematical criteria have been developed in order to calculate accurately a global phase diagram^{11,12,39,40}. These criteria allow one to draw the boundaries between the different types and are briefly summarized before the description of the global phase diagram.

The calculation method

One of the most important boundary is given by systems that exhibit tricritical points (TCP). This boundary delimits the fields of classes I and V, II and IV, or III and IV*. Classes V, IV and IV* are all characterized by the presence of liquid-liquid-gas (LLG) immiscibility. The tricritical state is a state where the field of the LLG immiscibility shrinks to one point, which is the TCP. In other words, three phases become identical at a TCP. A TCP occurs when the differentiates of the Gibbs free energy at constant pressure and temperature with respect to the mole fraction of one of both components are equal to zero :

$$G_{2x} = 0, \quad (31a)$$

$$G_{3x} = 0, \quad (31b)$$

$$G_{4x} = 0, \quad (31c)$$

$$G_{5x} = 0. \quad (31d)$$

The coordinates (T , V , x , and α_1) of a tricritical point are determined by solving this set of nonlinear equations. An additional condition ($G_{6x} \geq 0$) ensures that the tricritical point is stable.

Another important boundary in a global phase diagrams is the locus of double critical endpoints (DCEP). This boundary delimits classes III and IV, or II and IV*. Class IV is characterized by two LLG curves. One is at high temperatures and is delimited by two CEP (a LCEP and an UCEP). The other LLG curve lies at lower temperatures and ends at another UCEP. A DCEP occurs in a class IV system when the LCEP of the high-temperature LLG (HT-LLG) field joins the UCEP of the low-temperature LLG (LT-LLG) field. Conversely, a DCEP is produced in a class III system when the critical curve cuts tangentially the three-phase LLG in a pressure-temperature diagram. As a consequence, the criteria for locating a DCEP are :

$$G_{2x}(c) = 0, \quad (32a)$$

$$G_{3x}(c) = 0, \quad (32b)$$

$$\mu_1(c) = \mu_1(a), \quad (32c)$$

$$\mu_2(c) = \mu_2(a), \quad (32d)$$

$$(dP/dT)_c = (dP/dT)_a \quad (32e)$$

where $(dP/dT)_c$ and $(dP/dT)_a$ designate respectively the slope of the critical curve and the slope of the three-phase LLG curve at the DCEP. Symbols "c" and "a" refer to the two phases (the first one is critical, and the other is non-critical) that coexist at a CEP.

A third boundary delimits classes I and II, or IV and V. Classes II and IV are characterized by the existence of a liquid-liquid (LL) immiscibility field at low temperatures. The low-temperature LL (LT-LL) immiscibility field can be shifted to lower temperatures and disappear. This produces respectively classes I and V, which are characterized by the absence of LT-LL phase equilibria. A mathematical criterion has been proposed¹¹ for locating points on the global phase diagram at which the LT-LL immiscibility field disappears at 0 K (zero-temperature endpoints). However, ZTEP are not as important as TCP and DCEP. Even if a LT-LL immiscibility field is predicted by an EOS, LT-LL phase equilibria are often not observed because of the crystallization of a solid phase. Thus, in this work, zero-temperature endpoints (ZTEP) have not been considered. LT-LL immiscibility have always been detected up to very low temperatures with the MSA EOS. No class I and V have been found in this study, but their presence cannot be excluded.

Other additional criteria have been taken into account for the construction of the global phase diagram. One of these criteria is used for locating mathematical double points³⁹ (MDP). MDP are useful as they allow us to do a first classification of phase diagrams with respect to the topology of the critical curves. A MDP is a point of intersection between two critical curves, where an exchange of the different branches of the critical curves occurs. Therefore, MDP gives us a first indication of the boundary limit between class III and IV systems. MDP are much easier to calculate than DCEP and give

us some clues for the construction of the global phase diagram (in particular, for localizing the point of van Laar, see below). The criterion of the MDP is the following³⁹ :

$$G_{2x}=0, \quad (33a)$$

$$G_{3x}=0, \quad (33b)$$

$$G_{2xV} G_{3xT} - G_{2xT} G_{3xV} = 0, \quad (33c)$$

$$G_{2xT} G_{3xx} - G_{2xx} G_{3xT} = 0. \quad (33d)$$

Another additional criterion used for the construction of the global phase diagram is given by the so-called critical pressure step points (CPSP). These are the points associated with an inflexion change on a pressure-temperature diagram⁴⁰. The locus of CPSP separates two subclasses of the class III system. The first subclass is called class III_m. In this subclass, the critical curve starts from the critical point of the more volatile component, runs first to higher pressures, then exhibits a pressure minimum, and eventually runs to C_{Pm}. The second subclass is simply called class III. In this subclass, the critical curve starting from the critical point of the more volatile component runs monotonously to higher pressures, without showing successively a pressure maximum and minimum. Like MDP, CPSP help to locate DCEP, as the class III_m is often closely associated with the class IV system. The criterion for calculating a CPSP is given by the following equations :

$$G_{2x}=0, \quad (34a)$$

$$G_{3x}=0, \quad (34b)$$

$$G_{2xT} = 0, \quad (34c)$$

$$G_{4x} G_{2x2T} - G_{3xT} G_{3xT} = 0. \quad (34d)$$

The global phase diagram

Figure 12 shows the global phase diagram for mixtures of ions and dipoles, plotted in the two-dimensional (α_1 - α_2) space.

The relative position of the CP of the pure fluids is the first key parameter to consider when studying the topologies of the phase diagrams. For low- α_1 values, the dipolar fluid is more volatile than the ionic fluid, i.e., the critical temperature of the dipolar fluid is lower than the critical temperature of the ionic fluid ($T_{cd} < T_{ci}$). Conversely, for high α_1

values, the dipolar fluid is less volatile than the ionic fluid ($T_{cd} > T_{ci}$). Three vertical thin vertical lines have been drawn on the global phase diagram: the first one at $\alpha_1=0.349159$ marks the limit $T_{ci}=T_{cd}$, whereas the two others mark the limits $T_{ci}=2T_{cd}$ and $T_{ci}=T_{cd}/2$ at $\alpha_1= 0.17458$ and $\alpha_1= 0.698318$. These limits have been calculated by using Eq. (25a). In a similar way, the ratio of the critical pressures is given by using Equations (25b). Several thin curves have been drawn on the global phase diagram for representing the iso- P_{ci}/P_{cd} ratios.

There are four tricritical curves (TC) in Figure 12: one roughly parallel to the α_2 axis and at low α_1 -values (α_1 between 0.065 and 0.4), one at higher α_1 -values, and the two others roughly parallel to the α_1 axis and located at low α_2 -values. These TC have been called respectively TC1, TC2, TC3 and TC4. The TC1 curve intersects itself at the point ($\alpha_1 = 0.10259$, $\alpha_2 = 1.2753$). At this point, the calculated critical curve exhibits two TCP. The TC1 curve shows moreover two cusps, one at ($\alpha_1= 0.10477$ and $\alpha_2 = 1.3981$), and the other at ($\alpha_1 = 0.089259$ and $\alpha_2 = 1.1286$). The intersection point and both cusp points delimit a region where phase diagrams are more complex (Fig. 13). This region of the global phase diagram will be detailed below. For low α_1 value ($\alpha_1 < 0.1$), TCP belonging to the TC1 curve are situated on the critical curve connecting CPd to CPi, and they are close to the CPd. At $\alpha_1 = 0.113$, the TC1 goes through a particular point, called the van Laar point (VLP)³⁹. The VLP sets the limit of a connectivity change of the critical curves. Indeed, at higher α_1 ($\alpha_1 > 0.113$), TCP of the TC1 curve are located on the CPi-CPm branch. With increasing α_1 and α_2 values, TCP of the TC1 curve get closer to the CPi. The TC2 curve is related to TCP which are closer to the CPi. It was not possible to calculate the extension of the TC2 curve beyond the point ($\alpha_1=0.31081$, $\alpha_2=0.59379$), as the tricritical curve gets asymptotically closer to a MDP curve (see below). Two other tricritical curves (TC3 and TC4) were detected for low α_2 values. The TC3 and TC4 curves intersect the TC1 curve at points ($\alpha_1=0.0662$ and $\alpha_2= 0.2991$) and ($\alpha_1= 0.0654$ and $\alpha_2= 0.29117$). The TC3 curve is associated to TCP, which are very close to CPd (Tr_I between 0.211 and 0.226, and x_{salt} between 0.001 and 0.0045). TCP of the TC4 curve are slightly richer in ions (x_{salt} between 0.002 and 0.008), and can reach lower

temperatures (Tr_I between 0.06 and 0.22). Both TC3 and TC4 curves indicate the occurrence of LLG phase equilibria. Systems located between the TC3 and TC4 curves (α_1 between 0.05 and 1.0, α_2 between 0.2 and 0.3) are characterized by a LLG curve which appears near the CPd. An illustration of this is given by the type-IV* system ($\alpha_1=0.5$ and $\alpha_2=0.2$) of Fig. 10. Systems below the TC4 curve possess a second LLG, but whose extension is probably smaller. No phase diagram has been calculated in this region of the global phase diagram because of numerical problems. These systems exhibit complex phase diagrams, that have not been reported by van Konynenburg and Scott. But, they have not been studied in this work, as they correspond to quite extreme values of the α_1 and α_2 parameters.

Three MDP curves have been calculated by solving the set of Eqs. (33): one near the TC1, one close to the TC2, and the other below the TC4. These curves have been called respectively MDP1, MDP2 and MDP3 (Figure 12). They delimit three large fields of the global phase diagram, characterized by a different connectivity of the critical branches. In the region between MDP1 and MDP2, a continuous critical curve connects CPi and CPd. However, some points along the critical curve may be unstable. In this case, the critical curve is interrupted by a LLG field immiscibility. For low values of α_1 (α_1 roughly below 0.1), at the left of the MDP1 curve, CPi is connected to CPm, whereas for high values of α_1 , at the right of the MDP2 curve, CPd is connected to CPm. The MDP3 curve is roughly parallel to the α_1 -axis and below the TC4 curve. Above the MDP3 curve, a critical branch connects CPd and CPm, and the critical curve starting from CPi stops at an UCEP. Below the MDP3 curve, the situation is inverse: the critical branch starting from CPd stops at an UCEP, whereas CPi and CPm are connected. Illustration of this connectivity change is given on Figs. (10) and (11).

Two CPSP curves have been found. These boundary curves delimit the fields of type III (sensu stricto) and III_m. A first CPSP curve, referred to as CPSP1, is located in the region of low α_1 values (α_1 below 0.2), and the second one (called CPSP2) is in the

region of high α_1 and α_2 values. The CPSP2 curve stops at the point ($\alpha_1 = 0.71387$ and $\alpha_2 = 1.328$).

Contrary to the TCP, MDP, and CPSP curves, DCEP could not be determined exactly by solving the set of Eqs (33) because of numerical problems. However, by calculating the phase diagrams along a grid of (α_1, α_2) values, it was possible to locate quite accurately the locus of DCEP with an accuracy of ± 0.0005 in α_1 for a given α_2 value. A first curve, called DCEP1, was found between CPSP1 and TC1. The second one, called DCEP2, lies on the left of the TC2 curve. As expected, DCEP1 intersects the MDP1 and TC1 curves at the van Laar point³⁹. To the contrary, no van Laar point has been found on the α_1 -high side of the global phase diagram. The TC2, MDP2 and DCEP2 curves seem to meet asymptotically, but no intersection point could be detected.

An enlarged view of the global phase diagram is given in Figure 13 for α_1 between 0.09 and 0.12, and α_2 between 1.1 and 1.5. The systems inside the region delimited by the two cusp points (($\alpha_1 = 0.10477$ and $\alpha_2 = 1.3981$) and ($\alpha_1 = 0.089259$ and $\alpha_2 = 1.1286$)) and the intersection point ($\alpha_1 = 0.10259$, $\alpha_2 = 1.2753$) are characterized by two instability zones along the critical branch starting from CPd. This indicates the presence of two distinct LLG curves near CPd. Thus, the phase diagrams in this region of the global phase diagram are complex. They have not been studied in detail because of numerical difficulties. However, such a region is quite similar to the so-called "shield" region, as described for van der Waals^{41,42} and Lennard-Jones fluids⁷.

DISCUSSION

As already noticed by Harvey²³, an important question which can be addressed by the ion-dipole fluid in the MSA, is related to the stretching of the critical curve between the polar and ionic critical points. Indeed, a continuous critical curve connects the critical points of water and NaCl, although the ratio of their critical temperatures $T_c(\text{NaCl})/T_c(\text{H}_2\text{O})$ is as high as 6. For comparison, in mixture of non-electrolytes, a ratio T_{c2}/T_{c1} higher than 2 is generally sufficient (for example, $\text{H}_2\text{O}-\text{CO}_2$) for breaking the critical curve between the critical points of both components 1 and 2. In this respect, it is

interesting to look at the limiting values of the T_{ci}/T_{cd} ratio for breaking a continuous critical curve in the ion-dipole mixture. For this, the T_{ci}/T_{cd} ratio along the DCEP curves has been calculated by using Eq. (25a). Results are plotted on a $(\alpha_2, T_{ci}/T_{cd})$ plot in Figure 14. For equal-sized dipoles and ions ($\alpha_2=1$), the T_{ci}/T_{cd} ratio for a continuous critical curve must lie between 0.69 and 4.80. This latter value is yet much higher than the value of 3, which is obtained when considering a van der Waals EOS for equal-sized components ($b_1=b_2$) associated with a geometric combining rule for the unlike interactions ($a_{12}=(a_1 a_2)^{1/2}$). This first result confirms the fact that molecular interactions in ion-dipole mixtures favour this stretching of the critical curve. Moreover, it can be seen on Fig. 14 that the α_2 parameter can strongly favor the continuity of the critical curve. For low α_2 -values (α_2 between 0.7 and 1.0) and low α_1 values ($\alpha_1 < 0.1$), a continuous critical curve is maintained up to very high T_{ci}/T_{cd} ratios (greater than 15 for α_2 equal to 0.7). Such a result agrees with the observation of a long continuous critical curve between both critical points of water and salt in water-salt systems.

For equal-sized dipoles and ions ($\alpha_2=1$) and when increasing the α_1 parameter, the following sequence of types is observed : type III -> type III_m -> type IV -> type II -> type II with double azeotropy -> type IV with double azeotropy -> type III-HA. When the α_2 parameter is increased above one (i.e. when the size of the dipole is increased), the strength of the dipole is reduced and the saturation curve of the polar component is shifted to lower pressures. In the region of high α_1 values ($\alpha_1 > 0.4$), this leads to an enhancement of the miscibility of both ionic and polar components. As a consequence, an extension of type-II field is observed on the global phase diagram, and phenomena such as double azeotropy and heteroazeotropy disappear. Conversely, in the region of low α_1 values ($\alpha_1 < 0.1$), an increase of the α_2 parameter leads to a decrease of the miscibility of ionic and polar components, and an extension of the type-III field over the type-II field is observed. To the contrary, when lowering the α_2 parameter below one (i.e. when the size of the dipole is reduced), the force field of the dipole becomes higher and the saturation curve of the polar component is shifted to higher pressures. The miscibility of both ionic

and polar components is reduced in the region of high α_1 values and enhanced in the region of low α_1 values. Thus, this part of the global phase diagram is predominantly characterized by the extension of type-III field for high α_1 and of type-II field for low α_1 . Moreover, phenomena such as azeotropy, heteroazeotropy and gas-gas equilibria appear for low α_2 values and high α_1 values. All these new features indicate that the interactions between unlike particules are significantly less favoured than the interactions between like particules.

A brief comparison with real electrolyte systems can be made. Phase diagrams for binary real water-salts systems have been summarized⁴³. Published experimental phase diagrams include phase transitions involving salts, but these types of phase transitions are out of the scope of our study. Three main types of phase topologies have been recognized in binary water-electrolyte systems. These are type-III, type-II and type-IV phase diagrams. An example of type-III water-salt system is believed to be given by the H₂O-HCl system²³, but the high-pressure part of the phase diagram of this system is not known. Hydrogen chloride is more volatile than water ($T_c(\text{HCl})=51.5^\circ\text{C}$) and a negative azeotropic line is present for water-rich compositions ($x_{\text{H}_2\text{O}}$ around 0.9) at pressures below saturation pressures of water⁴⁴ and LLG immiscibility occurs below $T_c(\text{HCl})$ at pressures near the saturation pressures of HCl. Although an accurate thermodynamic model for such a system should take into account the extensive association between H⁺ and Cl⁻ ions, features such as negative azeotropy near the dipolar saturation curve and LLG immiscibility near the ionic saturation curve are predicted by the MSA for high α_1 values (see Figs. 5 and 6). Examples of type-II phase diagrams are H₂O-NaCl, H₂O-NaOH, ... and such phase diagrams look similar too with type-II phase diagrams calculated by the MSA (see Fig. 2, for $\alpha_1 = 0.1$ and $\alpha_2 = 1.0$). As noticed by Harvey²³ in a P - T diagram of water-salt systems, the critical curve runs from the critical point of water in colinearity with the saturation curve of water, and such a feature is indeed reproduced on some phase diagrams calculated with the MSA. Examples of type-IV phase diagrams are H₂O-Na₂WO₄, H₂O-K₂SO₄, H₂O-KLiSO₄, H₂O-Na₂SO₄, H₂O-UO₂SO₄, ... The

LLG immiscibility of these type-IV systems is observed in the vicinity of the critical point of pure water, and this feature is effectively reproduced on some of the type-IV phase diagrams calculated by the MSA (see Fig. 3, $\alpha_1=0.085$ and $\alpha_2=1.0$). Moreover, it can be noticed that most of the type-IV water-salt systems are encountered for large ions (WO_4^{2-} , SO_4^{2-} , UO_2^{2+} , ...) and for salts of valence 1-2, 2-1 or 2-2, i.e. in the case of low- α_1 and low- α_2 values. Such an observation is effectively predicted by the MSA, as the type-IV field is predicted in this region of the global phase diagram for low α_2 values (see Fig.12 for α_1 between 0.05 and 0.10, and α_2 between 0.5 and 1.0).

As a consequence, comparison between real and calculated phase diagrams shows that the MSA is able to reproduce the main features of fluid phase equilibria in water-salt systems.

CONCLUSION

This study is one of the first application of an EOS based on statistical thermodynamics for extensive fluid phase equilibria calculations in the ion-dipole mixture. The model is based on the Ornstein-Zernike equation, which allows one to take explicitly into account the influence of neighboring molecules on two interacting particles. The association of the Ornstein-Zernike equation with the assumptions contained in the MSA leads to an integral equation, which is analytically solvable. The solution for the ion-dipole mixture in the case of unequal-sized ions and dipoles has been used here. The influence of the different parameters of the model (dipole moment, valence and charge of the ions, size of the dipoles and ions) on fluid phase topology has been investigated. The phase diagrams have been classified according to the nomenclature of van Konynenburg and Scott^{3,4}, and the results have been mapped onto a two-dimensional global phase diagram as a function of two reduced parameters α_1 and α_2 . The α_1 parameter can be described as a measure of the force of the dipole, or inversely, as a measure of the weakness of the ions. The α_2 parameter is the ratio of the dipole diameter and ionic diameter. In the case equal-sized dipoles and ions, the following sequence of types has been found when increasing the α_1 parameter : type III -> type III_m -> type IV -> type II -> type II with

double azeotropy -> type IV with double azeotropy -> type III-HA. The influence of the α_2 parameter on fluid phase topologies depends on the α_1 parameter. For low α_1 values (α_1 roughly below 0.1), a decrease of the α_2 parameter favours ion-dipole interactions, thus leading to the development of type-II and type-IV phase diagrams and the stretching of the critical curve between both components. To the contrary, for high α_1 values (α_1 roughly below 0.4), a decrease of the α_2 value enhances the immiscibility of both components, as revealed by the occurrence of gas-gas equilibria, double azeotropy and heteroazeotropy. This model compares favorably with known phase diagrams of water-salts mixtures. Therefore, the mean spherical approximation provides a solid theoretical foundation for building new predictive equations of state for electrolyte mixtures.

APPENDIX

The electrostatic contribution of the molar Helmholtz free energy for the ion-dipole mixture, as given by the MSA, is :

$$\frac{A^{MSA}}{kT} = \left(x_1 + \frac{x_2}{\alpha_2} \right) \left(\begin{array}{l} 2\chi^2 + b_0\alpha_2^2 - 2\chi\sqrt{3y}b_1\alpha_2^2 \\ -\alpha_2^3 Q_{00}^2 - (1 + \alpha_2)\alpha_2 Q_{01}^2 \\ -Q_{11}^2 - 2b_2^2 \frac{\beta_{24}^2}{\beta_{14}^4} \end{array} \right) / (72\eta) \quad (A1)$$

where x_1 and x_2 are respectively the mole fractions of the dipolar and ionic components in the mixture (i.e. x_1 is the number of dipoles divided by the number of ion molecules and dipoles, and $x_2 = 1 - x_1$).

η is a reduced density :

$$\eta = \pi N_a \frac{(x_1\sigma_s^3 + x_2\sigma_i^3)}{6V} \quad (A2)$$

$$y = \frac{4\pi}{9} \beta \frac{\mu^2}{\sigma_s^3} \rho_s \quad (A3)$$

$$\chi^2 = 4\pi\beta \frac{e^2}{\sigma_i^2} \rho_i \quad (A4)$$

$$\beta_3 = 1 + \frac{b_2}{3} \quad (A5)$$

$$\beta_6 = 1 - \frac{b_2}{6} \quad (A6)$$

$$\beta_{12} = 1 + \frac{b_2}{12} \quad (A7)$$

$$\beta_{24} = 1 - \frac{b_2}{24} \quad (A8)$$

$$D = (1 + b_0)\beta_6 - \alpha_2^2 \frac{b_1^2}{12} \quad (A9)$$

$$\Delta = \beta_6^2 + \frac{b_1^2}{4} \quad (A10)$$

$$\Lambda = \frac{(1 + b_0 + \alpha\beta_6 / 3)}{2} \quad (A11)$$

$$a_1 = \left(-\frac{(b_1^2(3 + \alpha_2\beta_6))}{6} + 2b_0\beta_6^2 \right) / D^2 \quad (A12)$$

$$a_2 = -b_1 \left(\beta_6 + \frac{b_1^2}{6} + \beta_3 \frac{1 + b_0}{\alpha_2} \right) / D^2 \quad (A13)$$

$$Q_{00} = 2 - a_1 - 2 \frac{\beta_6}{D} \quad (\text{A14})$$

$$Q_{01} = b_1 \frac{\beta_3 - a_1(3\Lambda - D)}{\Delta} \quad (\text{A15})$$

$$Q_{11} = \frac{2\beta_3^2 - b_1 a_2 \alpha_2 (3\Lambda - D)}{\Delta} - 2 \quad (\text{A16})$$

The calculation of the Helmholtz free energy requires to solve a set of three nonlinear equations for determining the three b_0 , b_1 and b_2 parameters.

$$\begin{cases} f_0(b_0, b_1, b_2) = 0 \\ f_1(b_0, b_1, b_2) = 0 \\ f_2(b_0, b_1, b_2) = 0 \end{cases} \quad (\text{A17})$$

where f_0 , f_1 and f_2 are given by :

$$f_0 = a_1^2 + a_2^2 - \chi^2 \quad (\text{A18})$$

$$f_1 = a_1 K_{10} - a_2 (1 - K_{11}) - \chi \sqrt{3y} \quad (\text{A19})$$

$$f_2 = K_{10}^2 + (1 - K_{11})^2 - \left(\frac{\beta_6}{\beta_{12}^2} \right)^2 - 3y \quad (\text{A20})$$

where :

$$K_{10} = -b_1 \alpha_1^2 \frac{(1 - a_1 \Lambda)}{2\Delta} \quad (\text{A21})$$

$$K_{11} = 1 - \frac{\beta_3 - b_1 \alpha_1 a_2 \Lambda / 2}{\Delta} \quad (\text{A22})$$

REFERENCES

- ¹ R.J Sadus, *High Pressure Behaviour of Multicomponent Fluid Mixtures* (Elsevier, Amsterdam, 1992).
- ² J.S. Rowlinson and F.L. Swinton, *Liquids and liquid mixtures* 3rd ed. (Butterworths, London, 1982).
- ³ P.H. van Konynenburg and R.L. Scott, *Philos. Trans. R. Soc. London Ser. A* **298**, 495 (1980).
- ⁴ R.L. Scott and P.H. van Konynenburg, *Discuss. Faraday Soc.* **49**, 87 (1970).
- ⁵ P. Clancy, K.E. Gubbins, and C.G. Gray, *Discuss. Faraday Soc.* **66**, 116 (1978).
- ⁶ G. Jackson, J.S. Rowlinson, and C.A. Lang, *J. Chem. Soc. Faraday Trans. I* **82**, 3461 (1986).
- ⁷ V.A. Mazur, L.Z. Boshkov, and V.G. Murakhovsky, *Phys. Lett.* **104**, 8 (1984).
- ⁸ V.A. Mazur, L.Z. Boshkov and V.B. Fedorov, *Dokl. Akad. Nauk. SSSR* **282(1)**, 137 (1985).
- ⁹ L.Z. Boshkov and V.A. Mazur, *Russ. J. Phys. Chem.* **60**, 16 (1986).
- ¹⁰ L.Z. Boshkov, *Dokl. Akad. Nauk. SSSR* **294(4)**, 901 (1987).
- ¹¹ U.K. Deiters and I.L. Pegg, *J. Chem. Phys.* **90**, 6632 (1989).
- ¹² Th. Kraska and U.K. Deiters, *J. Chem. Phys.* **96**, 539 (1992).
- ¹³ D.G Green and G. Jackson, *J. Chem. Soc. Faraday Trans.* **88**, 10 (1992).
- ¹⁴ A. Adelman and J.M. Deutch, *J. Chem. Phys.* **60**, 3935 (1974).
- ¹⁵ L. Blum, *Chem. Phys. Lett.* **26**, 200 (1974).
- ¹⁶ L. Blum, *J. Chem. Phys.* **61**, 2129 (1974).
- ¹⁷ F. Vericat and L. Blum, *J. Chem. Phys.* **87**, 2999 (1987).
- ¹⁸ F. Garisto, P.G. Kusalik and G.N. Patey, *J. Chem. Phys.* **79**, 6294 (1983).
- ¹⁹ S.N. Lvov and R.H. Wood, *Fluid Phase Equilib.* **60**, 273 (1990).
- ²⁰ J.S. Hoye and E. Lomba, *J. Chem. Phys.* **88**, 5790 (1988).
- ²¹ J.S. Hoye, E. Lomba and G. Stell, *J. Chem. Phys.* **89**, 7462 (1988).
- ²² L. Blum and W.R. Fawcett, *J. Chem. Phys.* **96**, 3039 (1992).

- 23 A.H. Harvey, J. Chem. Phys. **95**, 479 (1991).
- 24 L. Blum, F. Vericat and W.R. Fawcett, J. Chem. Phys. **96**, 4 (1992).
- 25 L. Blum, J. Stat. Phys. **18**, 451 (1978).
- 26 L. Blum and D.Q. Wei, J. Chem. Phys. **87**, 555 (1987).
- 28 D.Q. Wei and L. Blum, J. Chem. Phys. **87**, 2999 (1988).
- 29 D.Q. Wei and L. Blum, J. Chem. Phys. **89**, 1091 (1991).
- 30 J. Wu, J. Lu and Y. Li, Fluid Phase Equilib. **101**, 121 (1994).
- 31 D.L. Goodstein, *States of matter* (Dover Publications, Inc, New York, 1975).
- 32 L.S. Ornstein and F. Zernike, Proc. Akad. Sci. (Amsterdam) **17**, 793 (1914).
- 33 J.L. Lebowitz and J.K. Percus, Phys. Rev. **144**, 251 (1966).
- 34 O.A. Pizio, M.F. Holovko and A.D. Trokhimchuck, Acta Chim. Hung. **125(3)**, 385 (1988).
- 35 see R. Fernandez-Prini, *High temperature aqueous solutions: Thermodynamic properties* (CRC Press, Boca Raton, 1992), Appendix A.
- 36 T. Boublik, J. Chem. Phys. **51**, 472 (1970).
- 37 R. Thiéry, Computer & Geosci., under press (1996).
- 38 L. Asselineau, G. Bogdanic and J. Vidal, Fluid Phase Equilib. **3**, 273 (1979).
- 39 A. van Pelt and Th. W. de Loos, J. Chem. Phys. **97**, 1271 (1992).
- 40 L.Z. Boshkov, Ber. Bunsenges. Phys. Chem. **96**, 940 (1992).
- 41 D. Furman, S. Dattagupta, and R.B. Griffiths, Phys. Rev. B **15**, 441 (1977).
- 42 D. Furman and R.B. Griffiths, Phys. Rev. A **17**, 1139 (1978).
- 43 V.M. Valyashko, Ber. Bunsenges. Phys. Chem. **81**, 338 (1977).
- 44 T. Sako, T. Hakuta and H. Yoshitome, J. Chem. Eng. Data **30**, 224 (1985).

FIGURES

Figure 1.

P-T plot for $\alpha_1 = 0.0645$ and $\alpha_2 = 1.0$. The filled circles represent the critical points of both components. The solid lines are the saturation curves. The critical curves are represented by the dotted curves.

Figure 2.

A/ *P-T* plot for $\alpha_1 = 0.072$ and $\alpha_2 = 1.0$. B/ Enlarged view of the region around CPd. The LLG curve is represented by a dashed line. CEP are represented by triangles. See Fig. 1 for an explanation of other symbols.

Figure 3.

A/ *P-T* plot for $\alpha_1 = 0.085$ and $\alpha_2 = 1.0$. B/ Enlarged view of the region around CPd. For an explanation of symbols, see Fig. 1 and 2.

Figure 4.

P-T plot for $\alpha_1 = 0.1$ and $\alpha_2 = 1.0$. For an explanation of symbols, see Fig. 1 and 2.

Figure 5.

P-T plot for $\alpha_1 = 0.45$ and $\alpha_2 = 1.0$. For an explanation of symbols, see Fig. 1 and 2.

Figure 6.

P-T plot for $\alpha_1 = 0.504$ and $\alpha_2 = 1.0$. The azeotropic curves are represented by dotted-dashed lines. The azeotropic end point (AEP) is represented by a small diamond. For an explanation of other symbols, see Fig. 1 and 2.

Figure 7.

P-T plot for $\alpha_1 = 0.6$ and $\alpha_2 = 1.0$. For an explanation of symbols, see Fig. 1 and 2.

Figure 8.

P-T plot for $\alpha_1 = 0.757$ and $\alpha_2 = 1.5$. For an explanation of symbols, see Fig. 1 and 2.

Figure 9.

P-T plot for $\alpha_1 = 0.5$ and $\alpha_2 = 0.5$. For an explanation of symbols, see Fig. 1 and 2.

Figure 10.

P - T plot for $\alpha_1 = 0.5$ and $\alpha_2 = 0.2$. For an explanation of symbols, see Fig. 1 and 2.

Figure 11.

P - T plot for $\alpha_1 = 0.5$ and $\alpha_2 = 0.1$. For an explanation of symbols, see Fig. 1 and 2.

Figure 12.

The (α_1, α_2) global phase diagram. For an explanation of symbols, see Fig. 1 and 2.

Figure 13.

Enlarged view of the global phase diagram. Solid lines are tricritical points. Thick dashed lines are double critical end-point curves. Dotted lines are mathematical double points. Thin dashed lines are critical pressure step points. Vertical dotted-dashed lines are curves of iso- T_{cd}/T_{ci} . Thin solid lines are curves of iso- P_{cd}/P_{ci} .

Figure 14.

$(\alpha_2, T_{ci}/T_{cd})$ plot. The central field between both curves is related to systems, for which CPd and CPi is connected by a continuous critical curve (type IV and type II). Other fields are related to systems characterized by a discontinuous critical curve (type III).

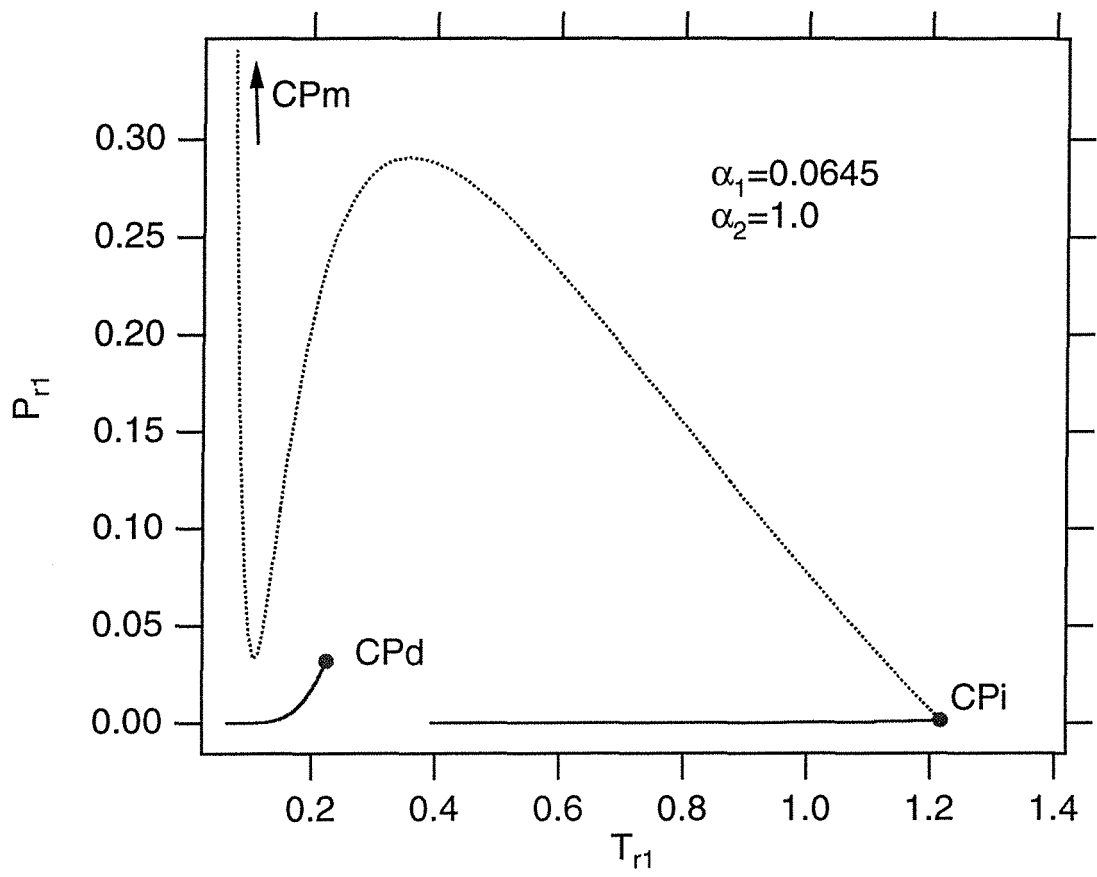


Figure 1

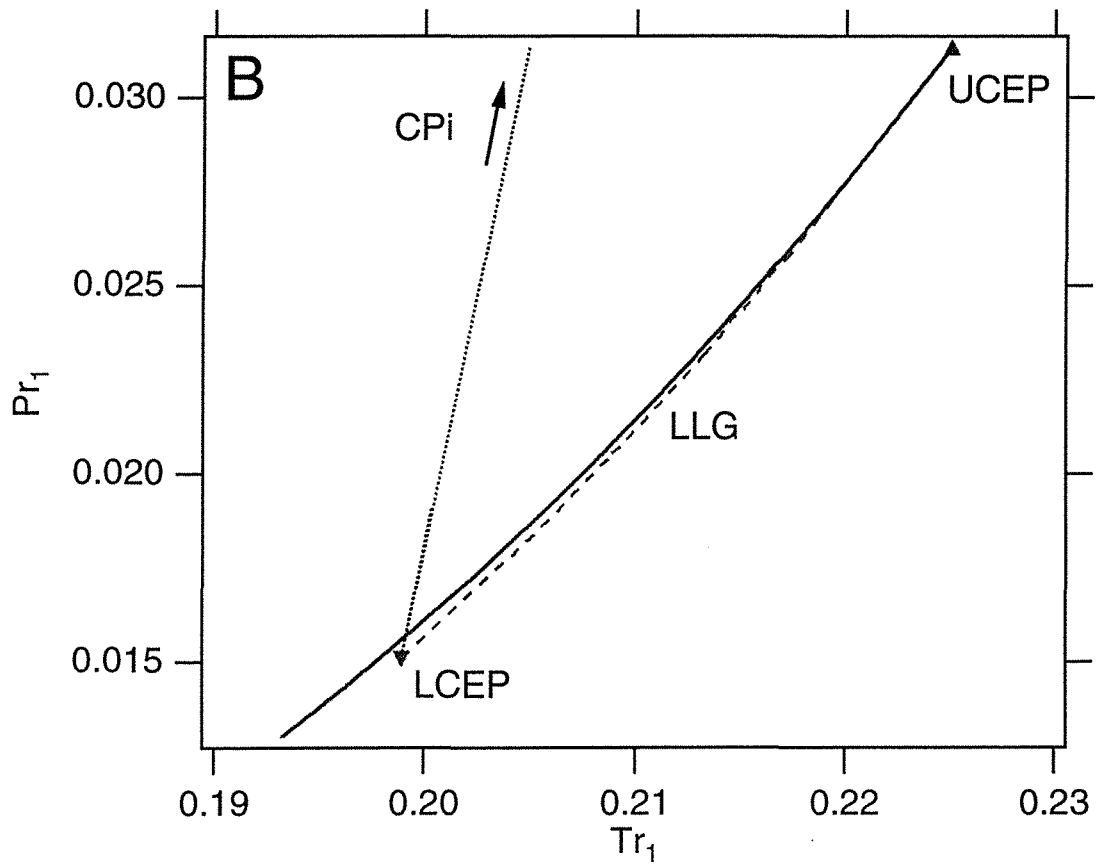
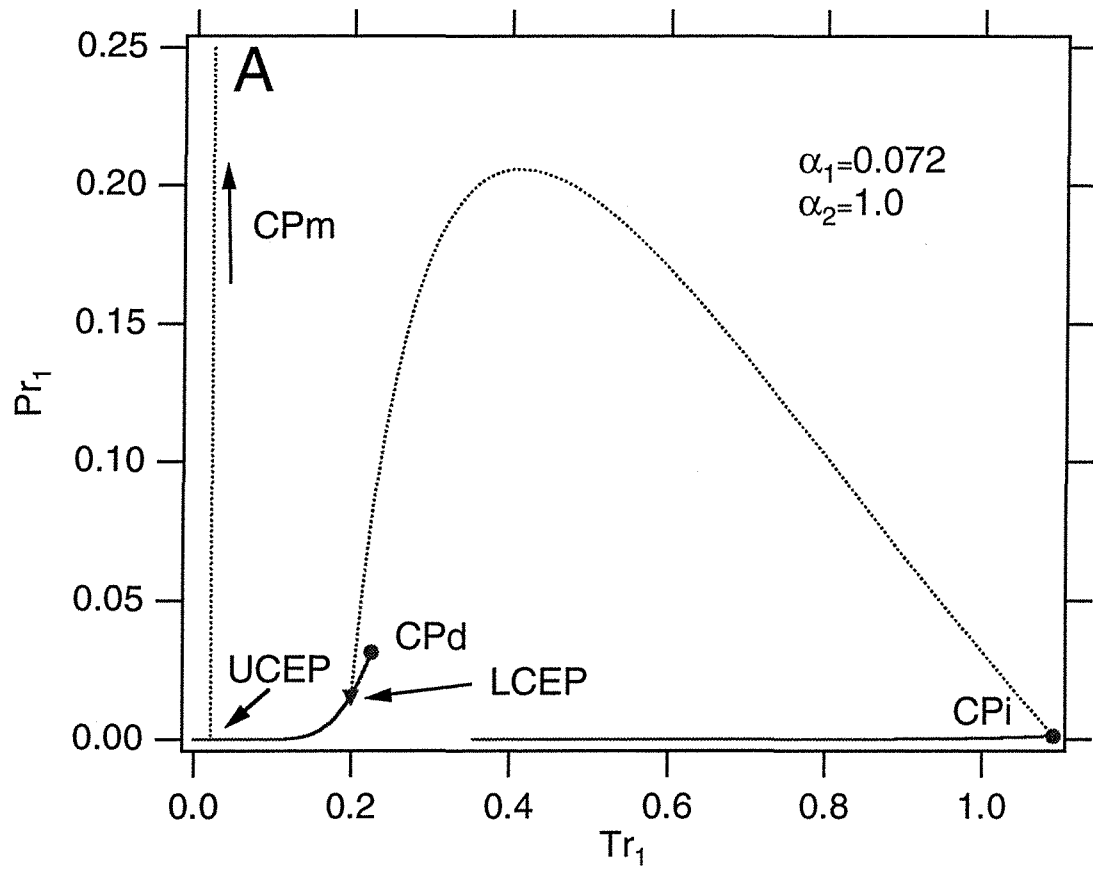


Figure 2

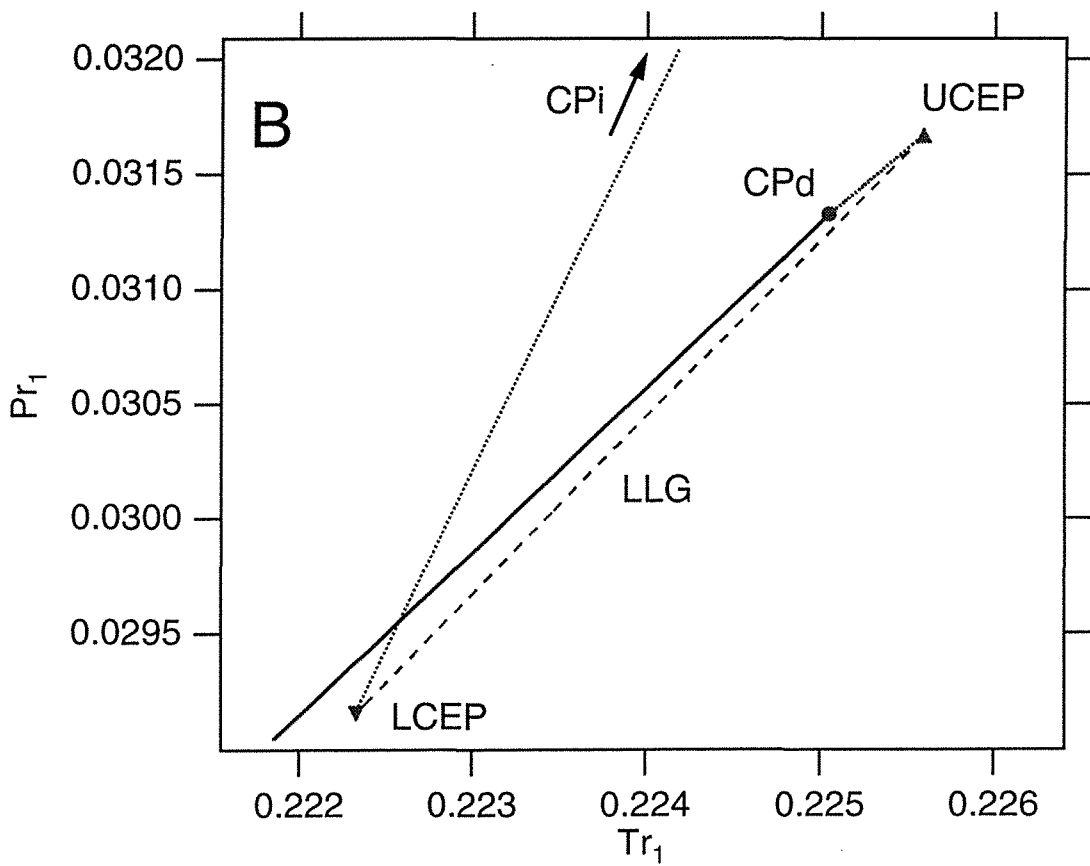
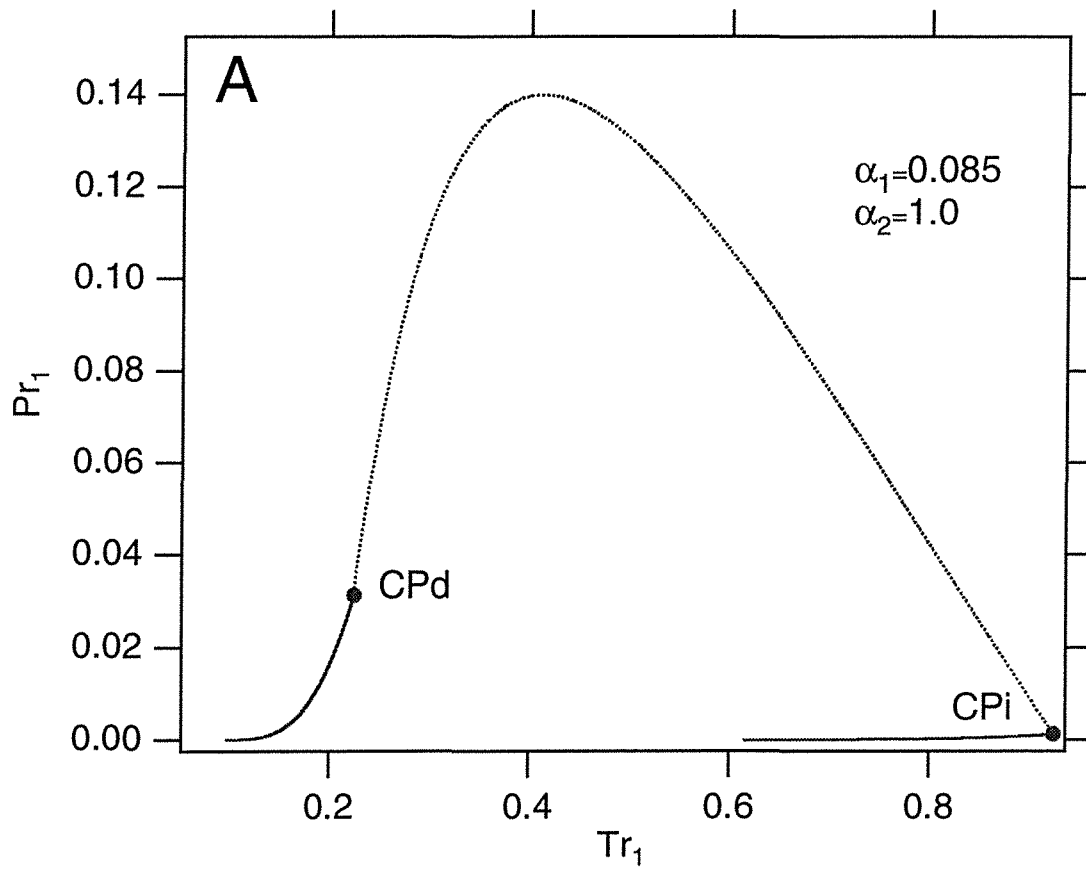


Figure 3

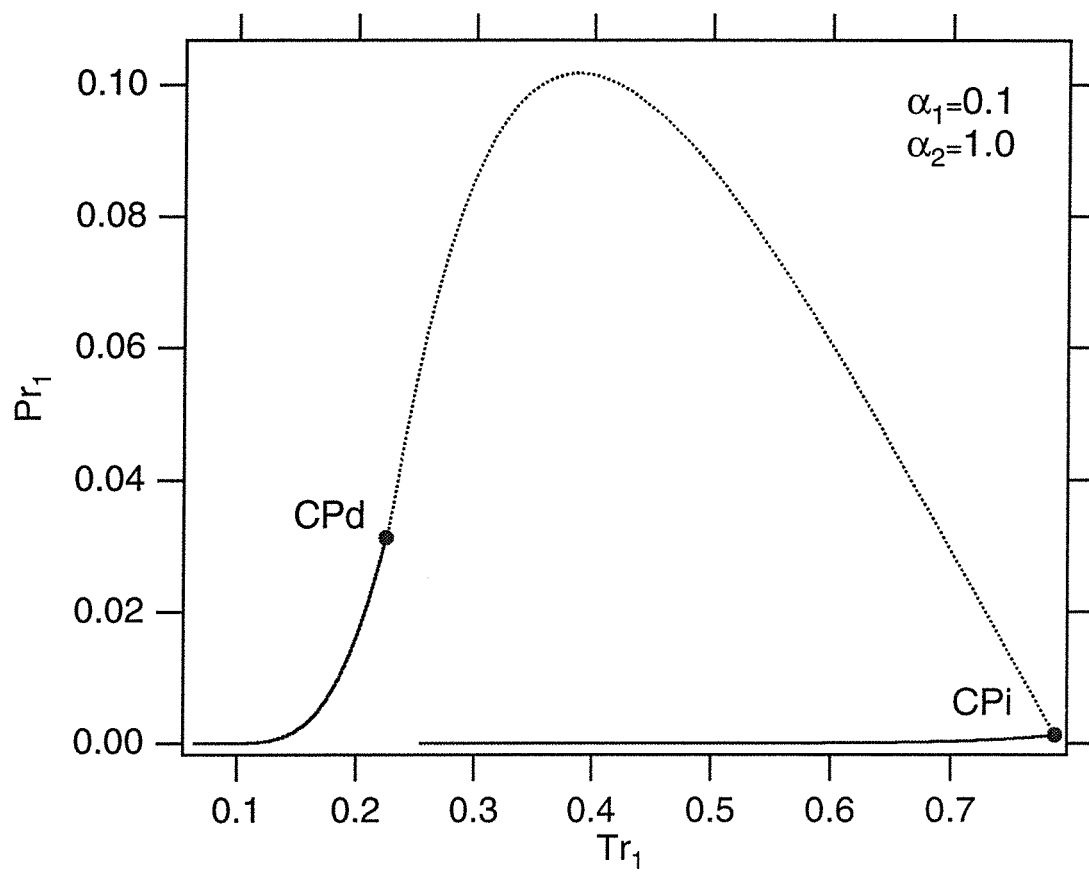


Figure 4

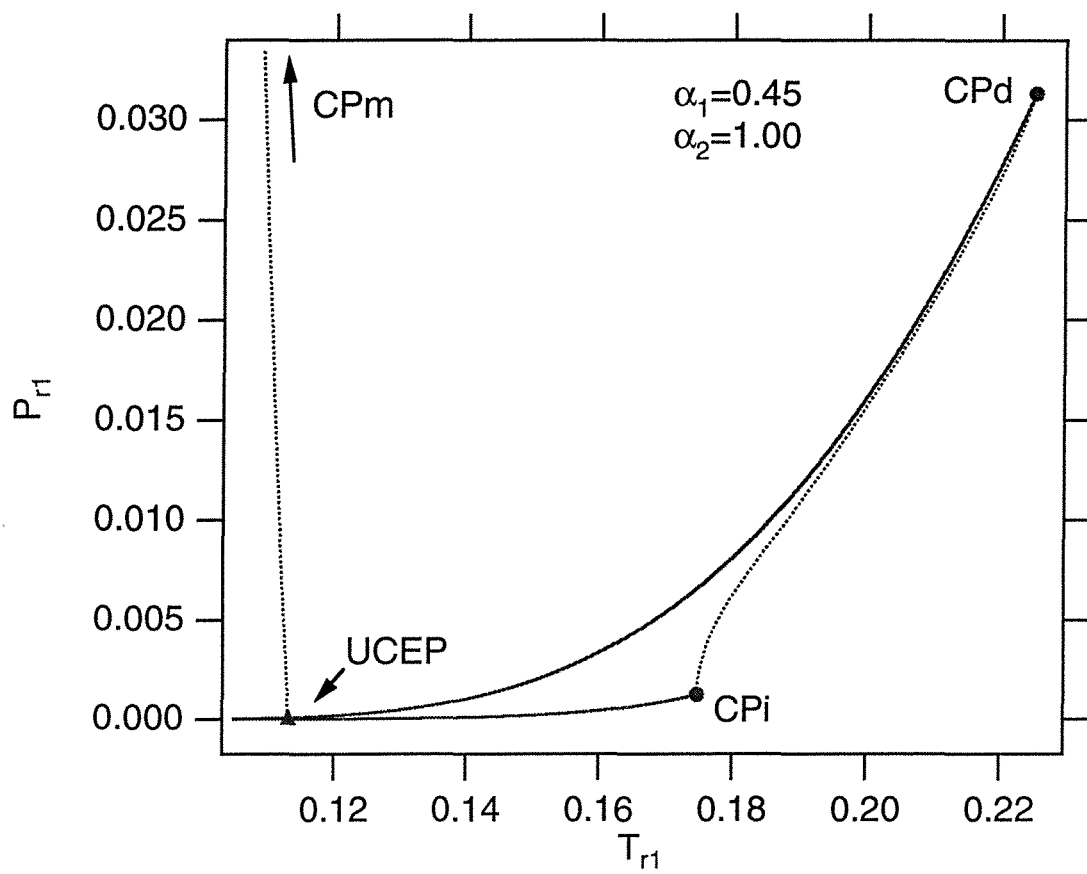


Figure 5

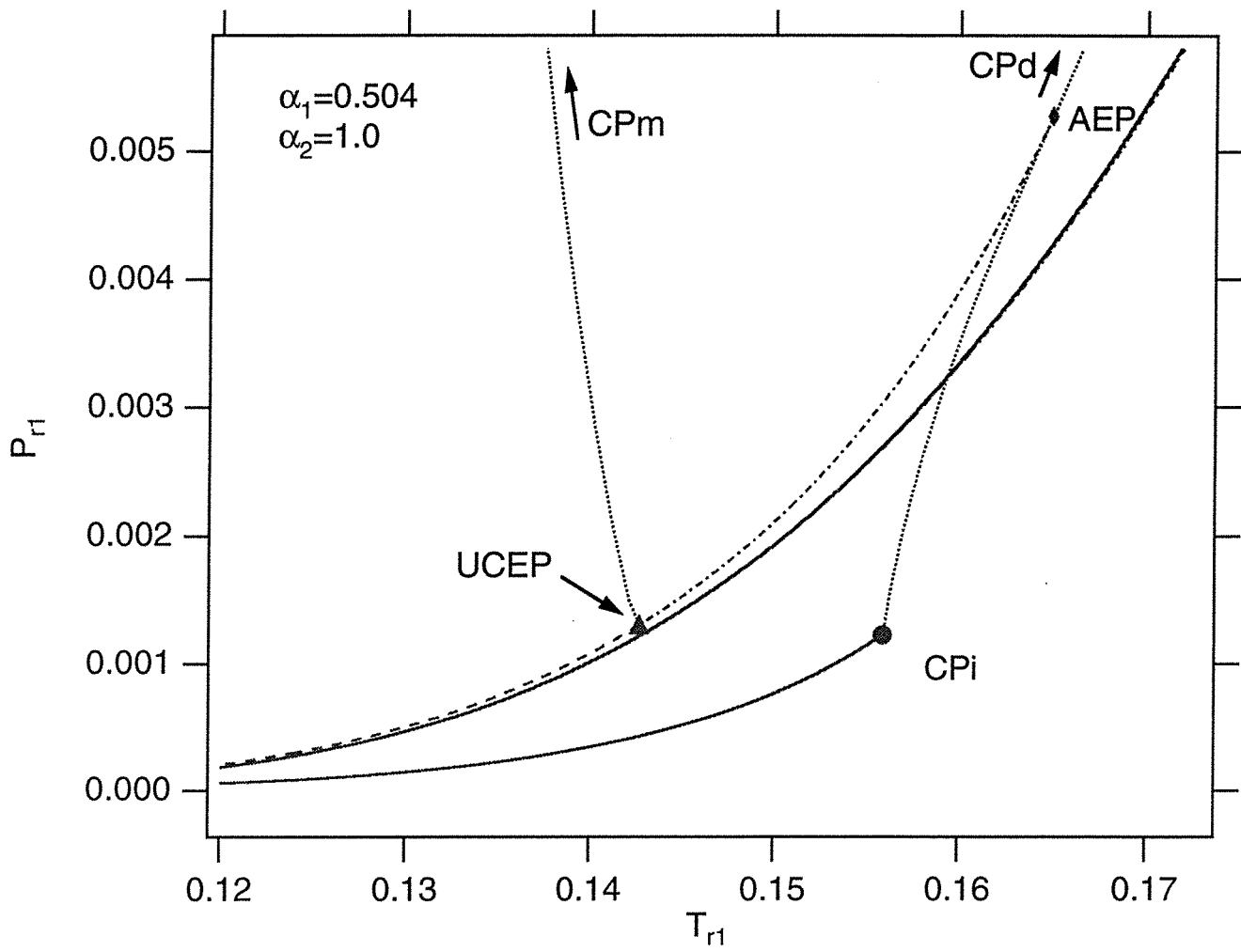


Figure 6

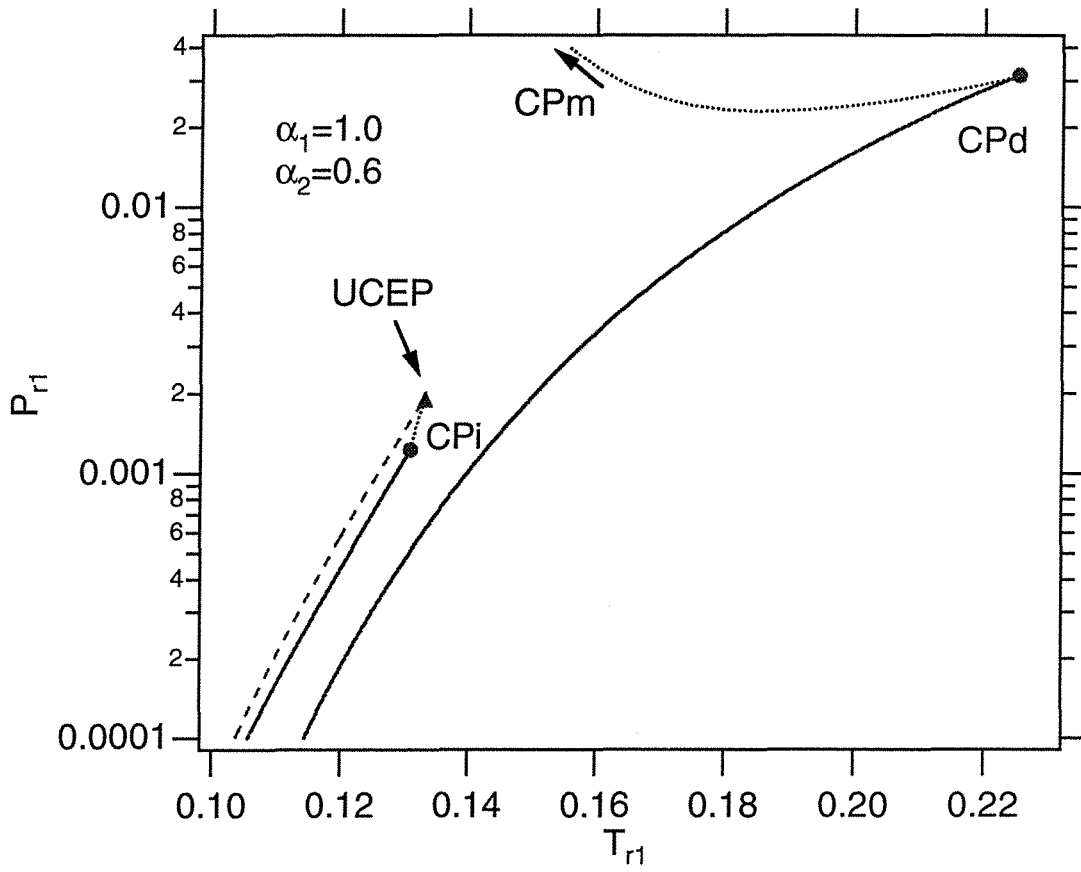


Figure 7

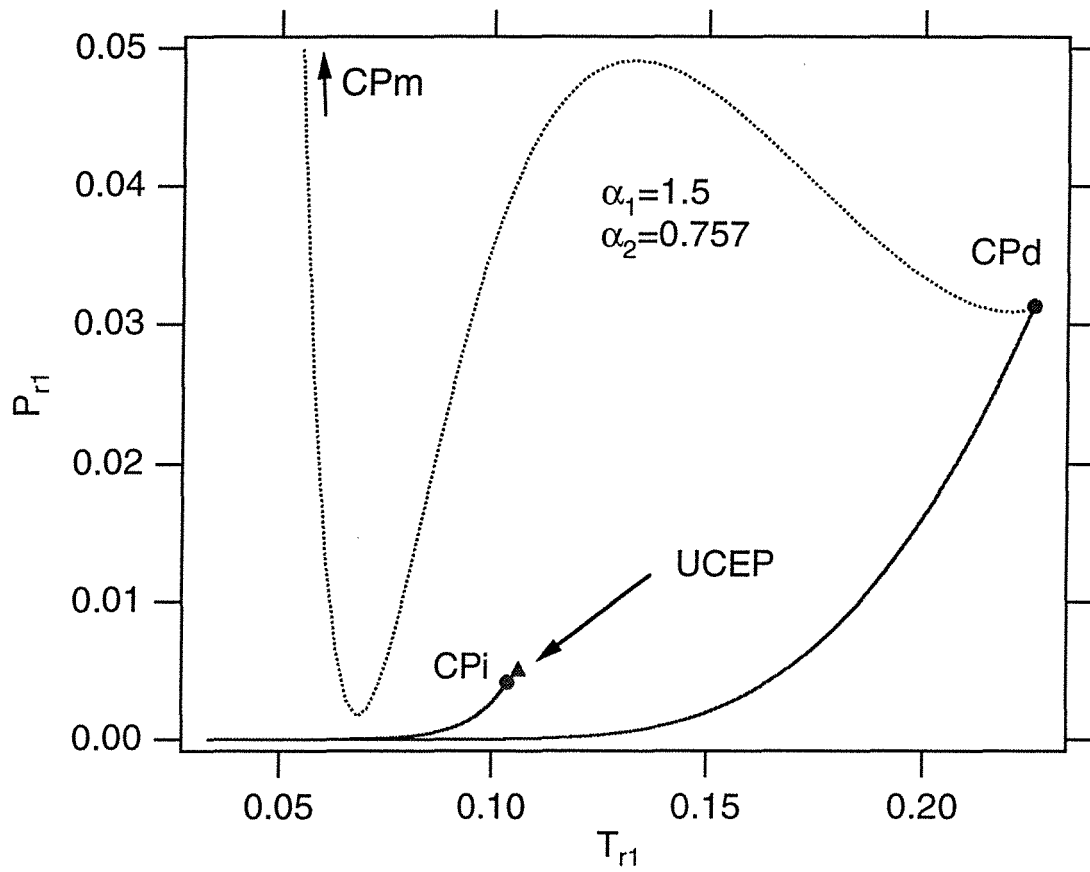


Figure 8

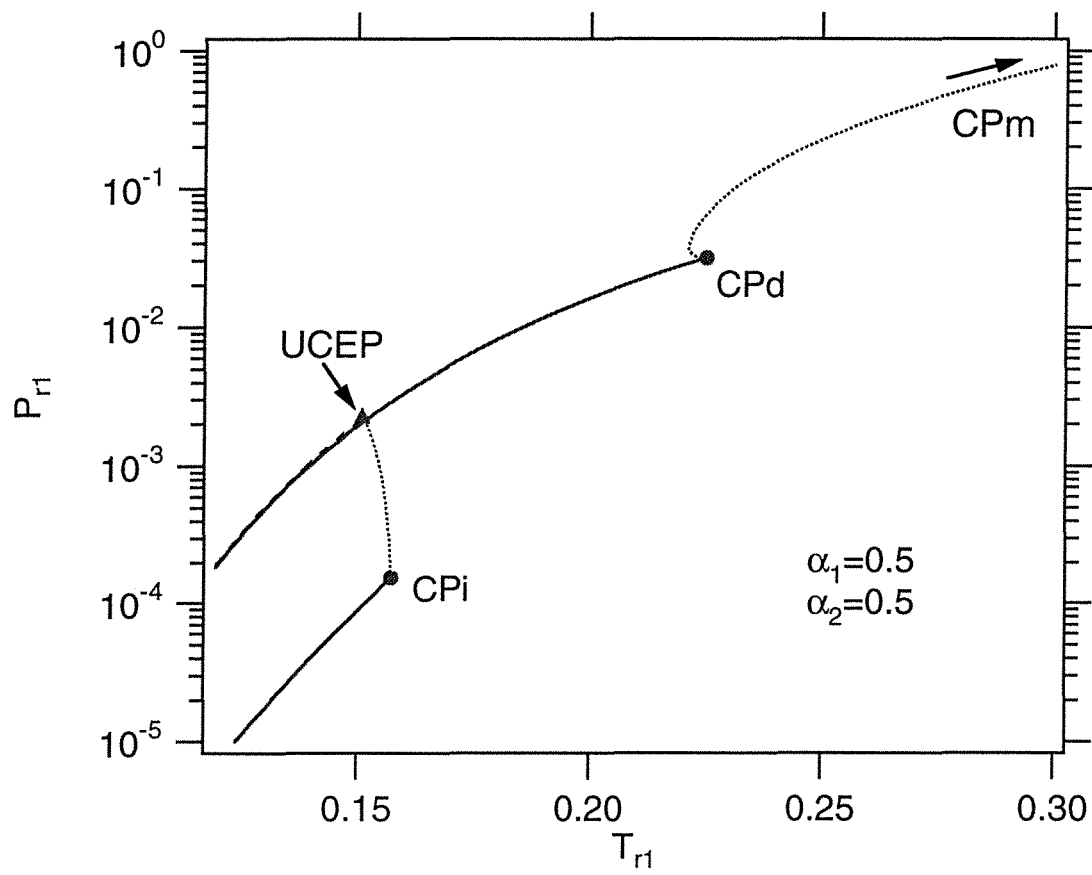


Figure 9

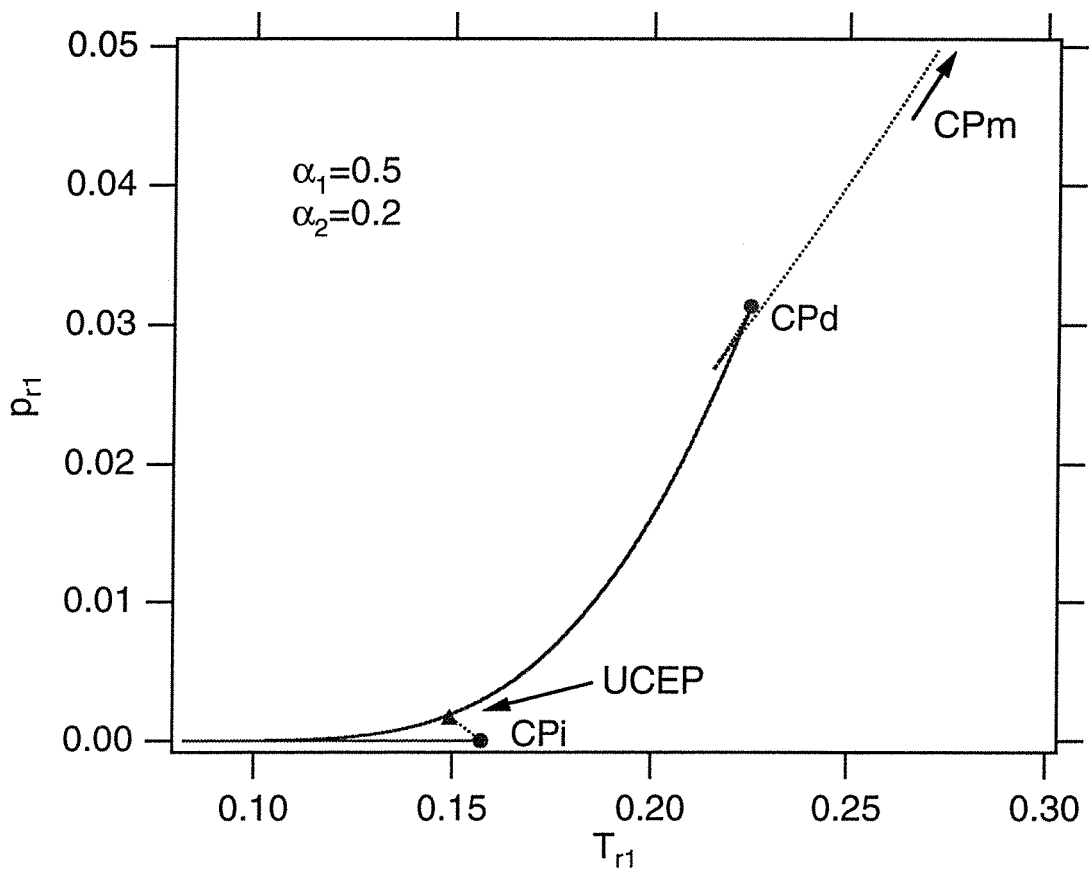


Figure 10

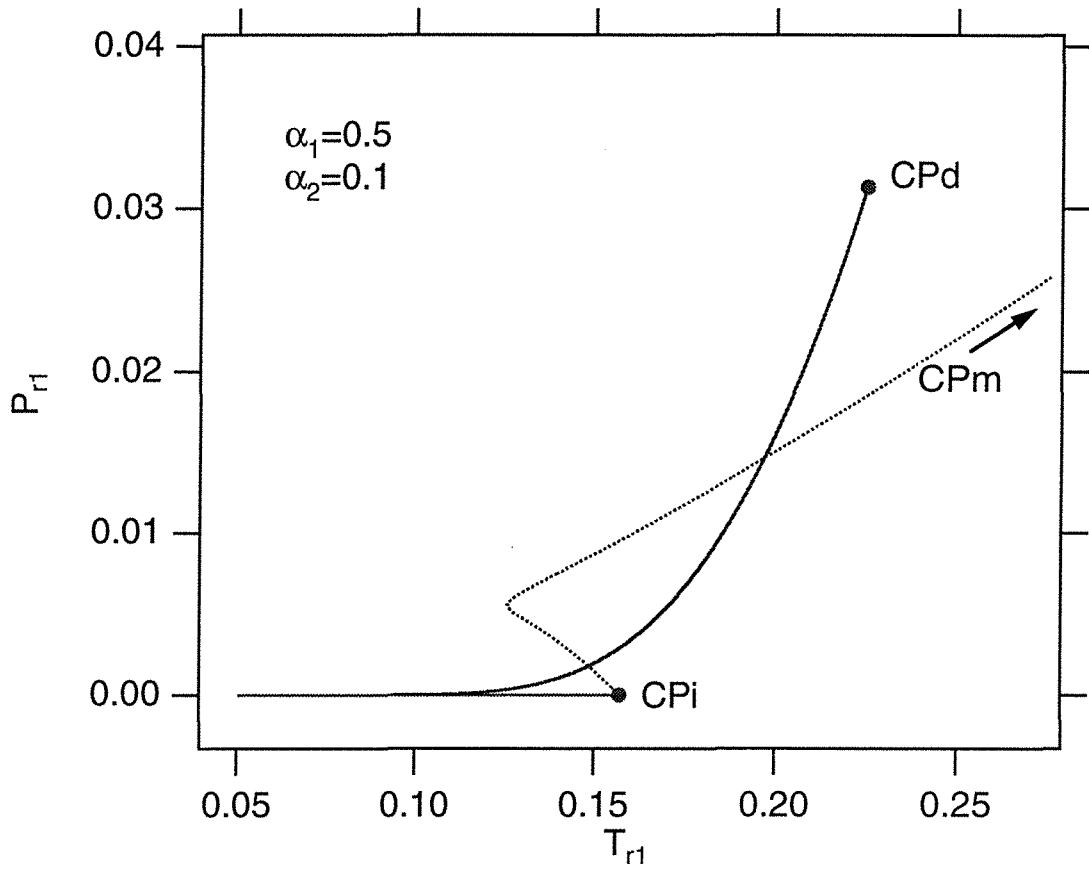
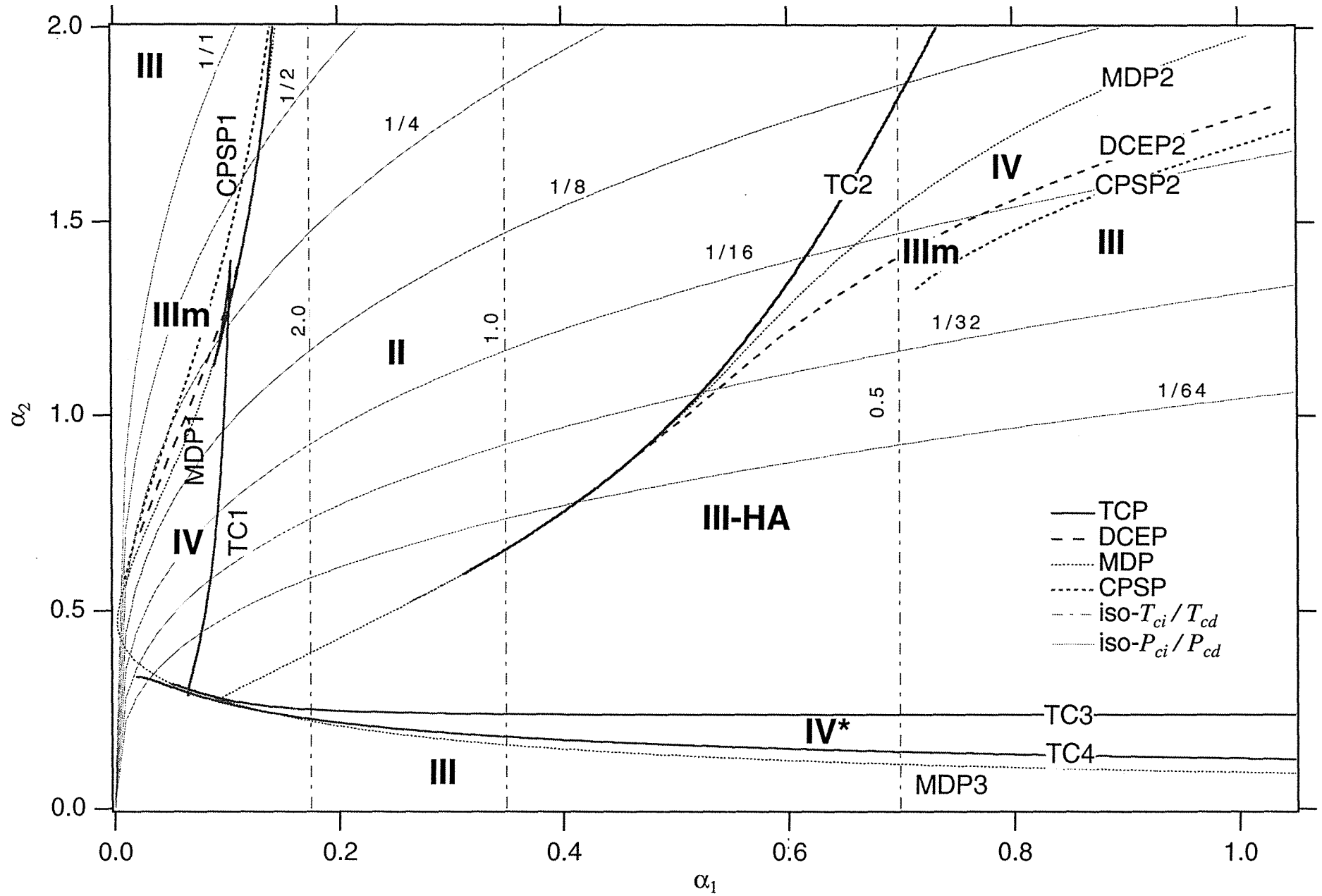


Figure 11

Figure 12



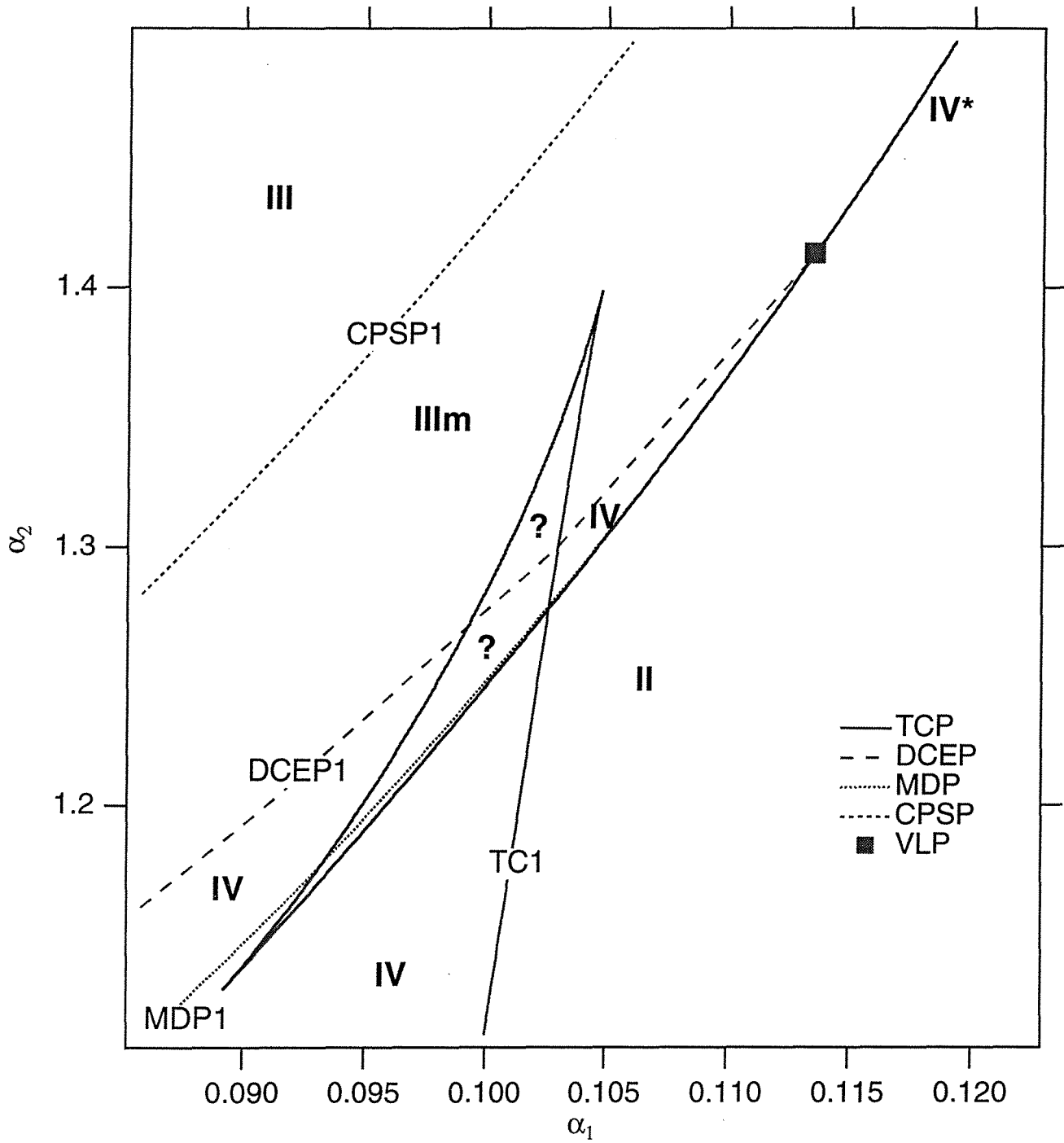


Figure 13

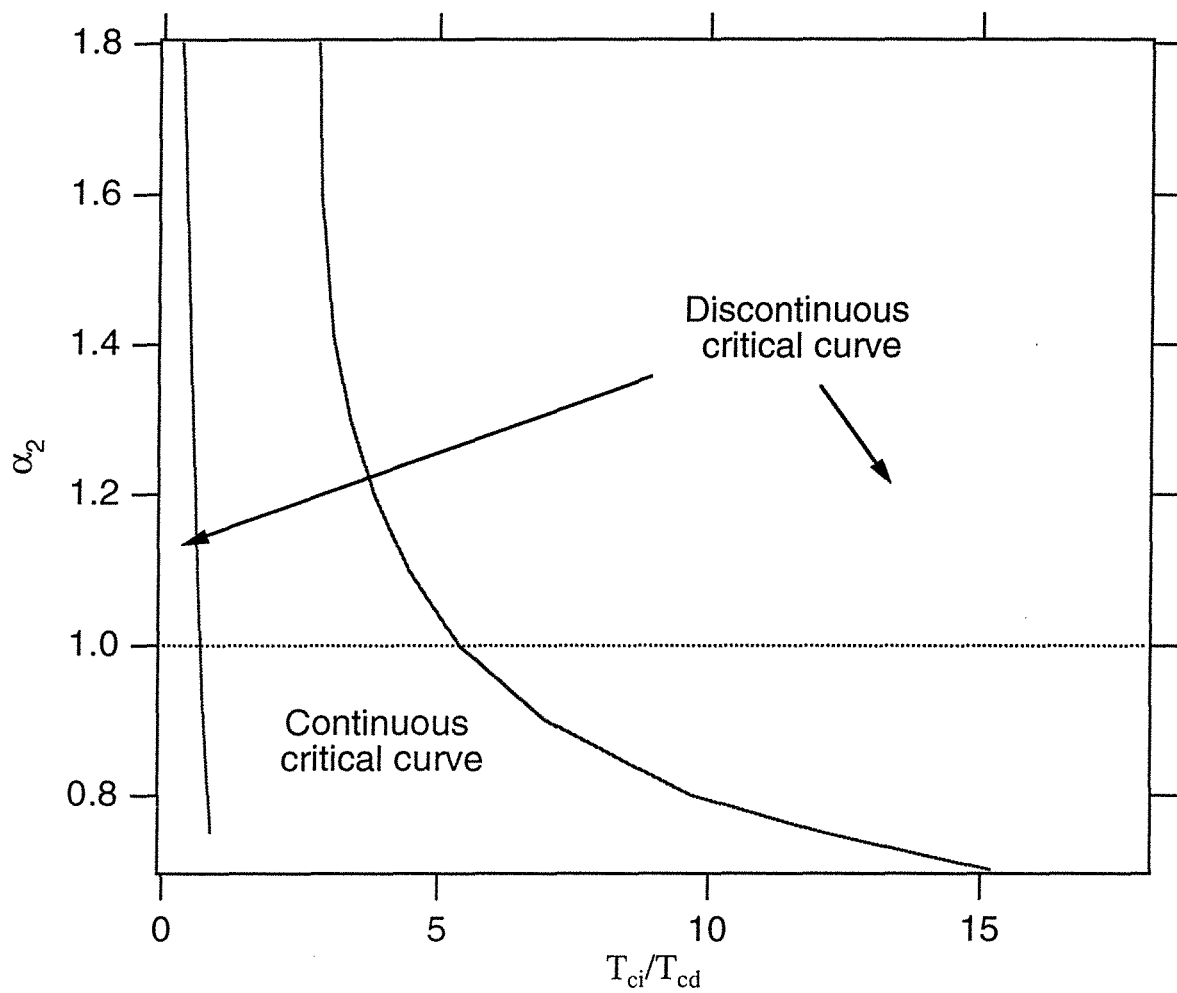


Figure 14

CHAPITRE 4

**La modélisation
des équilibres liquide-vapeur
dans le système H₂O-NaCl
à l'aide du modèle MSA ion-dipôle.**

Résumé

Ce chapitre aborde la question de l'application de l'équation d'état MSA pour le système ion-dipôle au système $\text{H}_2\text{O}-\text{NaCl}$. Dans un premier temps, les paramètres du modèle (moment dipolaire, diamètres de l'ion et du dipôle) sont déterminés à partir du diagramme de phase global et en utilisant les données (pression-température) de la courbe de saturation de l'eau et de la courbe critique du système $\text{H}_2\text{O}-\text{NaCl}$. Cependant, les premiers calculs d'équilibre liquide-vapeur montrent clairement que le système $\text{H}_2\text{O}-\text{NaCl}$ ne peut pas être décrit par un modèle basé uniquement sur le système théorique ion-dipôle. Ainsi, les fractions molaires en NaCl dans la phase gaz ou dans les liquides à forte température (au dessus de 400°C) sont fortement sous-estimées par le modèle ion-dipôle. En-dessous de 390°C , la situation inverse se produit et le modèle ion-dipôle surestime les fractions molaires de NaCl dans les phases liquides. Des modifications au modèle doivent donc être apportées. Les écarts dans les liquides à haute température ($T > 400^\circ\text{C}$) ou dans les phases vapeur ont été significativement réduits en adoptant une simple loi d'association (ion+ion=dipole). Cette hypothèse permet de rendre compte de la formation des paires d'ions NaCl , sans avoir à rajouter de constituant supplémentaire dans le système (en fait, les paires d'ions NaCl devraient être traitées comme des dipôles de moment dipolaire beaucoup plus élevé que celui de la molécule H_2O). Bien que des écarts jusqu'à deux ordres de grandeur soient parfois constatés entre les constantes d'association déterminées dans cette étude et les valeurs déterminées par conductimétrie (Quist et Marshall, 1968), deux arguments militent en la faveur de cette simplification. Premièrement, les constantes d'association suivent les mêmes tendances en fonction de la température que celles mesurées par conductimétrie (au dessus de 400°C). Deuxièmement, l'analyse de la variation des constantes d'association à dilution infinie en fonction de la densité permet d'estimer le nombre de molécules d'eau libérées hors des sphères d'hydratation des ions (nombre d'hydratation) lors de la formation de paires d'ions; et les nombres d'hydratation déterminés à partir des équilibres liquide-vapeur de

H₂O-NaCl sont en assez bon accord avec les valeurs estimées par d'autres méthodes (Wood et al., 1984). En dessous de 390°C, l'incorporation d'un terme de van der Waals avec le modèle ion-dipôle améliore nettement les prédictions. Mais, ce terme de van der Waals n'a pas de signification physique évidente. En conclusion, le modèle MSA ion-dipôle combiné avec une loi d'association des paires d'ions et un terme de van der Waals permet de décrire de manière satisfaisante les équilibres liquide-vapeur du système H₂O-NaCl avec relativement peu de paramètres d'ajustement.

Ce premier travail (Thiéry et al., soumis à *Geochim. et Cosmochim. Acta*) démontre la puissance d'une équation d'état basée sur la physique des interactions. Cela exige aussi de connaître parfaitement la chimie du fluide, c'est-à-dire les compositions des espèces associées, puisque celles-ci contrôlent la physique des interactions.

Références

- Quist, A.S et Marshall, W.L. (1968) Electrical conductances of aqueous sodium chloride solutions from 0°C to 800°C and at pressures to 4000 bars. *J. Phys. Chem.* **72**, 684-703.
- Thiéry, R. et Dubessy, J. (soumis à *Geochim. et Cosmochim. Acta*) Description of vapor-liquid phase equilibria of the H₂O-NaCl system with a thermodynamic model based on the MSA.
- Wood, S.A., Crerar, D.A., Brantley, S.L., et Borcsik, M. (1984) Mean molal stoichiometric activity coefficients of alkali halides and related electrolytes in hydrothermal solutions. *Am. J. of Science* **284**, 668-705.

Description of vapor-liquid phase equilibria of the H₂O-NaCl system with a thermodynamic model based on the MSA.

R. THIÉRY and J. DUBESSY

CREGU, Centre de Recherche sur la Géologie des Matières Minérales et Energétiques,
BP 23, 54 501, Vandoeuvre-les-Nancy Cedex (FRANCE)

(submitted to *Geochim. & Cosmochim. Acta*)

Abstract:

The Mean Spherical Approximation (MSA) developed for the ion-dipole mixture has been used as a reference fluid for describing the vapor-liquid equilibria of the H₂O-NaCl system. Comparison with experimental data reveals that the H₂O-NaCl mixture cannot be modelled solely by the MSA ion-dipole model. Discrepancies have been significantly reduced by taking into account NaCl ion pair formation in vapors at all temperatures and in high-temperature liquids ($T > 387^{\circ}\text{C}$). Furthermore, a van der Waals interaction term must be included at low temperatures ($T < 387^{\circ}\text{C}$) for correcting the predicted NaCl mole fraction in aqueous solutions by the MSA, which are too high when compared to experimental data. The model has been fitted in the 100°-500°C temperature range, and is shown to be partly valid at higher temperatures for NaCl mole fractions below 0.3. This model provides insights on the relative effects of electrostatic interactions (ion-ion, ion-dipole, dipole-dipole) and NaCl ion pair formation on the vapor-liquid equilibria of the H₂O-NaCl system.

INTRODUCTION

The H₂O-NaCl system plays an important role in geological processes. Of major importance is the liquid-vapor immiscibility of saline fluids at high pressures and temperatures, that occurs in geothermal systems. In particular, the formation of ore deposits is controlled to a large part by the large solubility difference between a saline liquid and steam (the formation of porphyry copper deposits, for instance). However, the H₂O-NaCl system represents one of the most difficult system to tackle, as it is characterized by complex intermolecular and interionic interactions. A solution to such a complex problem can only be approached by using simplifications. The first one is to treat electrolyte solutions as a system of electric charges (the ions) embedded in a continuous dielectric continuum (the solvent). This approximation is the starting point of the numerous excess Gibbs energy models, that have been developed for electrolyte solutions. These models include a Debye-Hückel term, which describes the ionic effects at infinite dilution. But, more or less empirical correcting terms must be incorporated for extending the application range to higher salinities (PITZER et al., 1984). Such a model is based on a virial-type expansion and is successful up to 300°C and for NaCl molalities below 6 molal. Attempts have been done to extend the PITZER model to higher temperatures (450°C) and more saline compositions (PITZER and SIMONSON, 1986; PABALAN and PITZER, 1990), but models based on the continuum approximation clearly show their limits for the wide range of conditions encountered in geological processes. The other possibility is to treat the solvent and electrolytes in a more symmetrical way, i.e. as a mixture of interacting spheres. First attempts are based on the van der Waals and other cubic equations of state (BOWERS and HELGESON, 1983; SØREIDE and WHITSON, 1992). Most of these studies leads to rather complex empirical relations containing a high number of fitting parameters. The most difficult step is clearly the description of long-range electrostatic interactions. As a result, equations of state, that are developed for electrolyte solutions, are most successful for conditions where ions are absent. An illustration of this is given by the equation of state of PITZER and PABALAN (1986) for modelling the NaCl solubility in steam up to 300°C. It is

simply based on an equation of state for a two-component imperfect gas, adapted for describing the successive hydration of the NaCl ion pair in the steam. Another example is provided by the equation of state of ANDERKO and PITZER (1993), where the H₂O-NaCl system is modelled by a mixture of dipolar hard spheres for temperatures above 300°C. Such an approach is indeed valid, as the larger part of Na⁺ and Cl⁻ ions associates to form ion pairs at these high temperatures. This equation of state agrees well with experimental data, but cannot be extended below 300°C. In this paper, a new equation of state is proposed for the H₂O-NaCl system, that considers explicitly the presence of ions in the system. Recent advances in statistical mechanics and computer simulation provide the tools for reaching this goal. Two main ways have emerged. The first one is based on the "perturbation theory", whereas the second one uses "integral equations". In the perturbation theory, a well-known idealized theoretical fluid is chosen as the reference fluid, and departures between the real system and the reference fluid are described by a series of terms calculated with the help of the perturbation theory (PRAUSNITZ et al., 1986). Such an approach has been used for describing the thermodynamic properties of a mixture of dipolar hard spheres (STELL et al., 1972, 1974; RUSHBROOKE et al., 1973). The reference fluid is a mixture of hard spheres (BOUBLIK, 1970), and perturbation terms are calculated by considering two-body and three-body interactions. Such a model has been used in the equation of state of ANDERKO and PITZER (1993) cited above. The second way is based on integral equations. These are equations that describe exactly the influence of all surrounding particules on two interacting particules (FERNANDEZ-PRINI, 1992). Approximations must be used for solving integral equations. The Mean Spherical Approximation (MSA) is one of these approximations. The great advantage of this approximation over other approximations is that it yields analytical expressions. Other approximations, which are more realistic, are only solvable by numerical procedures (such as the HyperNetted Chain Correlation). The MSA solution for the ion-dipole mixture has been developped in a series of papers (ADELMAN and DEUTCH, 1974; BLUM and WEI, 1987; HOLOVKO and PROTSYKEVICH, 1987; HOYE and LOMBA, 1988; HOYE et al., 1988; PIZIO et al., 1988; VERICAT and

BLUM, 1980; WEI and BLUM, 1987). Up to now, there is only one quantitative application of the MSA model to the H₂O-NaCl system. This is the equation of state of LVOV and WOOD (1990) for calculating the density of aqueous, liquid-phase NaCl solutions. It can be applied at temperatures from 0°C to 700°C and at pressures between 1 bar and 10 kbar. The interest of such an equation of state is its ability to reproduce accurately experimental data with a few number of empirical parameters. The same theoretical equation is proposed here for describing liquid-vapour phase equilibria of the H₂O-NaCl over a wide range of conditions (100°C < T < 700°C, and for NaCl composition up to the halite saturation).

THEORY.

The Mean Spherical Approximation.

An ideal fluid composed of ionic and dipolar hard-spheres is considered as the reference fluid for describing the thermodynamic properties of the H₂O-NaCl system. The diameter (σ_d) of the dipoles is different from that of the ions, but anions and cations are assumed to have the same size ($\sigma_+ = \sigma_-$). The more realistic MSA solution for different sizes of cations and anions has been recently developed, but the equations are more complex (BLUM and WEI, 1987; WEI and BLUM 1987; HOLOVKO and PROTSYKEVICH, 1987). Thus, the present model is a compromise between simplicity and reality.

In this idealized mixture, only four types of intermolecular forces are considered between two particles i and j separated by a distance r :

- hard sphere repulsion between two particles i and j :

$$u_{ij}(r) = 0 \text{ for } r > \sigma, \quad (1a)$$

$$\text{and } u_{ij}(r) = \infty \text{ for } r < \sigma, \quad (1b)$$

$$\text{where } \sigma = (\sigma_i + \sigma_j) / 2, \quad (1c)$$

- coulombic interaction between two ions i and j :

$$u_{ij}(r) = e^2 / \epsilon_0 r, \quad (2)$$

where e is the elementary charge, and ϵ_0 is the vacuum permittivity;

- electrostatic interaction between an ion i and a dipole j :

$$u_{ij}(r) = \mu_j e \cos \theta / \epsilon_0 r^2, \quad (3)$$

where θ is the angle between the dipole moment and the line joining i and j ; and μ_j is the dipole moment of the dipolar hard sphere;

- electrostatic interaction between two dipoles i and j :

$$u_{ij}(r) = - \mu_i \mu_j (2 \cos \theta_i \cos \theta_j - \sin \theta_i \sin \theta_j \cos (\varphi_i - \varphi_j)) / \epsilon_0 r^3, \quad (4)$$

where θ_i , θ_j , φ_i and φ_j are angles describing the orientation of the dipoles i and j (WU et al., 1994).

Statistical mechanics provides several methods for estimating the thermodynamic properties of a fluid mixture from the knowledge of the u_{ij} pair potentials (PP) of the system. The MSA is one of these methods. The MSA can be decomposed in two main steps. At first, the g_{ij} radial distribution function (RDF) between two particles i and j is derived from the knowledge of pair potentials u_{ij} . Then, the thermodynamic properties of the mixture are calculated from the g_{ij} RDF.

The derivation of the g_{ij} RDF from the u_{ij} PP is one of the basic and difficult problem of the statistical mechanical theory of fluids, and approximations must be used. The MSA theory uses a method, based on the so-called "integral equations" for deriving the g_{ij} RDF from the u_{ij} PP. This method is here briefly described by considering successively the cases of the perfect gas, a dilute fluid and finally a dense fluid.

In the absence of intermolecular forces, the g_{ij} RDF is simply equal to 1.

$$g_{ij}(r) = 1. \quad (5)$$

In a dilute fluid, a remarkable simple relation between the RDF and the PP between two particles i and j can be derived (GOODSTEIN, 1975):

$$g_{ij}(r) = \exp(-\beta u_{ij}(r)), \quad (6a)$$

$$\text{where } \beta = 1/kT, \quad (6b)$$

and k is the Boltzmann constant.

This approximation is effectively valid in very dilute electrolyte solutions, where an ion is surrounded by a cloud of counterions. The same relation is indeed developed in the Debye-

Hückel theory. When $u_{ij}(r)$ is small when compared to the product kT (i.e. when the molecules are far away), Eq. (6a) can be further simplified by linearizing the exponential function :

$$g_{ij}(r) = 1 - \beta u_{ij}(r). \quad (7)$$

Eq. (6a) is no more valid in dense fluids, and the influence of neighbouring particles to a pair (i - j) must be taken into account. A way of achieving this is to decompose the g_{ij} RDF into three contributions :

$$g_{ij}(r) = 1 + c_{ij}(r) + g_{ind}. \quad (8)$$

The first term, equal to one, is simply the contribution of a mixture of non-interacting molecules (Eq. (5)). The second term, given by the c_{ij} function, describes the direct influence of the u_{ij} PP on the g_{ij} RDF. c_{ij} is called the direct correlation function (DCF). The third term, denoted g_{ind} , describes the indirect influence of the u_{ij} PP to the g_{ij} RDF through all neighboring particles. It is worth to note that in a dilute fluid, g_{ind} is neglectable. The g_{ind} contribution can be further explicited, as it is done in the exact Ornstein and Zernike (OZ) equation :

$$g_{ij}(r) = 1 + c_{ij}(r) + \sum \rho_k \int [g_{ik}(r,r') - 1] c_{kj}(r,r') dr', \quad (9)$$

where the g_{ind} term is calculated by a convolution of the c_{kj} DCF with the g_{ik} RDF minus one. The summation is made over all kinds of k particles surrounding the i - j pair with the density ρ_k (in this study, k is either an ion or a dipole). The OZ equation is an integral equation, which contains two unknowns (the g_{ij} RDF and the c_{ij} DCF). Thus, additional relations are required for solving the OZ equation and calculating the g_{ij} RDF. The most evident relation is the following :

$$g_{ij}(r) = 0 \text{ for } r < \sigma_{ij}. \quad (10)$$

This condition is simply a consequence of the impenetrability of hard spheres representing the particles. For the case $r > \sigma_{ij}$, another assumption must be stated. One possibility is to assume that the c_{ij} DCF is a function of the u_{ij} PP in the same way for a dense fluid than for a dilute fluid. Therefore, by identifying the corresponding terms in Eq. (7) for a dilute fluid and Eq. (8) for a dense fluid, the following relation is obtained:

$$c_{ij}(r) = -\beta u_{ij}(r) \text{ for } r > \sigma_{ij}. \quad (11)$$

This approximation strictly holds for $r \rightarrow \infty$ and is most questionable in the intermediate region, where $u_{ij}(r)$ reaches its potential depth. But, the great advantage of this approximation over other approximations is that it gives expressions that can be solved analytically. For this reason, this approximation, commonly referred to as the Mean Spherical Approximation (MSA), looks attractive. Analytical expressions for the g_{ij} RDF have been derived respectively for the ion-ion, ion-dipole and dipole-dipole pairs (PIZIO et al., 1988).

Any thermodynamic property of the mixture can be calculated from the g_{ij} RDF. The equation relating the excess internal energy to the RDF is usually used (FERNANDEZ-PRINI, 1992):

$$U^{ex} = 1/2V \sum N_i N_j \int u_{ij}(r) g_{ij}(r) dr. \quad (12)$$

Other thermodynamic properties are then calculated by adequate differentiation or integration of U^{ex} .

The equation of state

The equation of state for the ion-dipole mixture is formulated by means of an analytical expression of the Helmholtz Free Energy (HFE) and is split into two contributions :

$$A = A^{hs} + A^{MSA}. \quad (14)$$

The first term (A^{hs}) takes into account the repulsive forces between hard spheres, whereas the second one describes the influence of ion-ion, ion-dipole and dipole-dipole interactions. The A^{hs} HFE of a mixture of hard spheres is given by the BOUBLIK equation of state (1970). The complete equations for calculating A^{MSA} are given in LVOV and WOOD (1990), and in THIÉRY et al. (submitted). All thermodynamic properties have been obtained by analytical differentiations of the Helmholtz free energy with respect to the temperature, molar volume and composition. Derivatives up to the fourth order are calculated analytically by using a software package (THIÉRY, under press) for differentiation and thermodynamic calculations. This was necessary because of the length and complexity of the mathematical expressions. The MSA for the ion-dipole mixture is characterized by a few number of physical parameters (the dipole moment, the

diameter of the dipole and the ion, and the valence of the salt) that must be fitted in order to get a good agreement with experimental data.

PROCEDURE FOR THE DETERMINATION OF THE PARAMETERS.

The first step is the evaluation of the parameters for the water. Only two parameters can be adjusted. These are the dipole moment and size. The same procedure usually used for the van der Waals equation of state can be applied. Values of the dipole moment (μ) and size (σ_d) have been obtained by solving the conditions for a critical point at $T = 374.1^\circ\text{C}$ and $P = 221$ bar.

$$A_{VV} = 0, \text{ and} \tag{15a}$$

$$A_{VVV} = 0. \tag{15b}$$

where A_{VV} and A_{VVV} are respectively the second-order and the third-order of the Helmholtz free energy with respect to the molar volume V . Solving of this nonlinear set of equations yields the following values: $\mu = 2.243$ Debye and $\sigma_d = 2.331$ Å. These values are in good agreement with values obtained experimentally. The dipole moment for the H_2O molecule is 1.85 Debye, but the formation of hydrogen bonds modifies the dielectric properties of water (HASTED, 1972). A value of 2.45 Debye is commonly cited at 0°C (HASTED, 1972). A good reproduction of the saturation properties of pure water is required. There is the choice to fit either the dipole moment (μ), either the diameter of the dipole (σ_d), or both. The dipole moment and the dipole diameter have an antagonist influence. An increase of the saturation pressure for a given temperature is obtained when the dipole moment is decreased or when the dipole diameter is increased. In this study, we have chosen to keep the dipole diameter to the constant value of 2.331 Å and to fit the dipole moment. This choice is partly justified by the fact that the dipole moment does decrease with the temperature, as more and more hydrogen bonds are broken when heating the system (HASTED, 1972). The third parameter to adjust is the diameter of the ion. But contrary to the the water, there is no solid criterion for estimating a value for the ionic diameter. The first idea would be to adopt a mean value for the crystallographic radii of the Na^+ and Cl^- ions. Values for the diameter of Na^+ and Cl^- are respectively 0.9 and

1.81 Å, giving a mean value of 1.35 Å. Another way would be to consider the thermodynamic properties of pure NaCl, although they are not well known. LVOV and WOOD (1990) followed this way. They used an ionic diameter between 2.6 and 3.0 Å, as the MSA equation of state for pure salt was found to reproduce well the volumetric data for molten NaCl when a value of 2.6 Å was used (LVOV and WOOD, 1990). Another possibility is to estimate the ionic diameter from the critical temperature of NaCl. The ratio of the critical temperatures of the salt (T_{ci}) and dipolar component (T_{cd}) is inversely proportional to the size of the ion (THIÉRY et al., submitted). With the values cited above ($\mu = 2.243$ Debye and $\sigma_d = 2.331$ Å), this yields :

$$T_{ci} / T_{cd} = 20.280 / \sigma_i \quad (\sigma_i \text{ in } \text{Å}). \quad (16)$$

Actual estimations of the ratio of the critical temperatures of NaCl and H₂O are about 6 (HARVEY, 1991), thus leading to an ionic diameter of 3.38 Å. A systematic study of the influence of dipole moment, sizes of the dipoles and ions on fluid phase equilibria for the ion-dipole mixture has been made (THIÉRY et al., submitted). For a fixed dipole moment and size ($\mu = 2.243$ Debye and $\sigma_d = 2.331$ Å), different types of phase diagrams are obtained when the ionic diameter is modified. This can be best visualized on a global phase diagram, where an excerpt is given in Figure 1 in the space of the (α_1, α_2) parameters. The α_1 parameter is a dimensionless quantity related to the strength of the dipole. For a salt of valence 1-1, α_1 is defined by :

$$\alpha_1 = 0.0365384 \mu^2 \sigma_i / \sigma_d^3, \quad (17a)$$

where μ is in Debye, σ_i and σ_d are in Å,

and α_2 is the ratio of the diameter of the dipoles and ions:

$$\alpha_2 = \sigma_d / \sigma_i. \quad (17b)$$

The α_1 parameter is related to the ratio of the critical temperatures of ionic and polar components (Thiéry et al., submitted) by :

$$T_{ci} / T_{cd} = 0.349159 / \alpha_1. \quad (18)$$

The dotted curves in Figure 1 separate the different types of phase diagrams following the nomenclature of VAN KONYNENBURG and SCOTT (1980). Type II systems are characterized by a continuous critical curve connecting the critical points of dipolar and

ionic components. Liquid-liquid immiscibility occurs at lower temperatures, but is most often metastable because of the solidification of a salt. Conversely, type III systems are characterized by a discontinuous critical curve. The critical curve starting from the ionic component runs to high pressures, whereas the critical branch starting from the polar component terminates on a liquid-liquid-gas curve. Type IV systems are similar to type II systems, except that the critical curve is interrupted by a three-phase liquid-liquid-gas curve. Type III_m is a variant of type III systems, that is characterized by a pressure maximum and minimum on the critical curve. The solid curve in Figure 1 represents the possible different values for the ionic diameter, when the dipolar moment is set to 2.243 Debye and the dipole diameter is set to 2.331 Å. As it can be seen on Figure 1, very different types of phases diagrams are obtained for different values of the ionic diameter. For low ionic diameters (σ_i below 4.5 Å), type III, type III_m and type IV are observed. Such types of phase diagrams are very different from the H₂O-NaCl, which is a type II system. Type II systems are obtained for ionic diameter between 4.7 and 7 Å. However, the corresponding ratios of the critical temperatures are between 3 and 4. Such ratios are too low, and it would lead to problems for fitting the critical curve of H₂O-NaCl. The critical pressure maxima would indeed occur around 800°C. A decrease of the critical pressure would be calculated for temperatures above 800°C, and this decrease occurs probably at much higher temperatures. Thus, a compromise must be made, and a constant value of 4.5 Å has been chosen. The ion-dipole mixture is then of type IV, but the liquid-liquid-gas curve is limited to only a few tenths of degrees near the critical point of water. Therefore, it is barely distinctable on the calculated phase diagrams. The ratio of critical temperatures is above 4.5, which is a reasonable value. LVOV and WOOD (1990) have used an ionic diameter which is a complex function of the temperature, the density and the composition. This alternative is not pushed away, but will be discussed later.

A first comparison with the MSA equation of state with P - T - x - y experimental data of liquid-vapor equilibria is shown in Figure 2. These first attempts reveal clearly that the sole use of the MSA is not appropriate for reproducing the experimental data. At low temperatures (for example, at 200°C), the MSA model overestimates significantly the

NaCl mole fraction of the liquid, whatever the diameter of the ion. Moreover, liquid-liquid-gas immiscibility occurs if the ionic diameter is too low ($\sigma_i = 2.5 \text{ \AA}$, for example) or too large ($\sigma_i = 5 \text{ \AA}$). The situation is more problematic at high temperatures (at 500°C , for example). Significant discrepancies appear between the calculated NaCl mole fractions with experimental data, both in the liquid and the vapour. The MSA model predicts a very low amount of ions in the vapour (y_{NaCl} below 10^{-5}) and in the liquid. A better agreement with liquid composition can be obtained ($\sigma_i = 4.0 \text{ \AA}$), but in this case, the pressure is strongly overestimated in the critical region. Moreover, Figure 2 shows too that the use of variable ionic diameter as done by LVOV and WOOD (1990) would not be sufficient for obtaining a good agreement with the experimental data. All of these observations suggest that some essential features of the H_2O -NaCl system do lack in the present model. At the present stage of the development of the system, the most questionable point is the absence of ion pair and larger clusters. At supercritical temperatures, NaCl behaves as a weak electrolyte, as it has been demonstrated by conductometric measurements (FRANCK, 1956; QUIST and MARSHALL, 1968; MARSHALL, 1990). The dielectric constant of the fluid decreases dramatically when the molar volume or temperature are increased. This decrease of the dielectric constant favors the formation of ion pairs (HELGESON et al., 1981). Thus, for liquids above 300°C and for vapors at all temperatures, NaCl ion pair becomes the dominant species over Na^+ and Cl^- ionic species. Thus, the discrepancies observed at high temperatures are not surprising and can be only reduced by taking into account the formation of ion pairs. This could explain why the liquid and vapour phases are more enriched in NaCl than predicted by the MSA theory. The NaCl ion pair is a strong dipole, and therefore, this new species should be added in the ion-dipole mixture. At lower temperatures, the situation is different. Below 387°C , the MSA theory predicts indeed a larger solubility of NaCl in the aqueous liquid phase than experimental data. Below 300°C , NaCl dissociates in a large part to give free Na^+ and Cl^- ions in the solution. For saturating liquids at infinite dilution, the association constant is 0.15 at 300°C and -1.0 at 200°C (QUIST and MARSHALL, 1968). Therefore, it is clear that hydrogen bonds and dispersion forces play an important role at low temperatures; but,

their influence on the NaCl solubility is difficult to estimate. The solvation of ions by water molecules and the dispersion forces would enhance certainly the solubility of ions in the aqueous solution. In the other way, the network of water molecules formed by the hydrogen bonds should probably hinder the transfer of NaCl in aqueous solutions. All of these phenomena should be taken into account in the model for obtaining a satisfactory agreement with experimental data.

The consideration of ion pairs in our model is not a simple work. First, a second dipolar component must be added into the binary ion-dipole system, and a chemical equilibrium must be considered at each step of the iterative liquid-vapour phase equilibria calculations. This complicates a lot the calculations. Secondly, the solution for a mixture of two types of dipoles and ions has not been developed in the MSA and would probably lead to more complex equations. All of these reasons push us to try to search a simpler solution. This can be achieved by assuming that the NaCl ion pair can be described by a dipole of 2.243 Debye like the H₂O molecule. Obviously, this is wrong as a value of 9 Debye has been estimated for the dipole moment of the NaCl ion pair (McCLELLAN, 1963-1989). However, water molecules solvate the ion pair (PITZER and PABALAN, 1986), and this hydration decreases probably the strength of the electrostatic field around the NaCl ion pair. But, the greater advantage of our assumption is that calculation of chemical equilibria can be avoided. The complex problem of a liquid-vapour equilibria calculation in the ternary system (H₂O, NaCl ion pair, and dissociated NaCl) is replaced by a simpler problem in the ion-dipole mixture. The association of Na⁺ and Cl⁻ ions is treated a posteriori. Once a liquid-vapour equilibria has been solved for the ion-dipole mixture, the "true" compositions of H₂O, dissociated NaCl and ion pairs can be calculated from the mole fractions of the dipole and ionic components by using the relations :

$$z(\text{H}_2\text{O}) = 1 - z_i - 4 K z_i^2, \quad (19a)$$

$$z(\text{NaCl, undissociated}) = 4 K z_i^2, \quad (19b)$$

$$z(\text{NaCl, dissociated}) = z_i, \quad (19c)$$

$$z(\text{NaCl, total}) = z_i (1 + 4 K z_i). \quad (19d)$$

where K is the association constant, expressed on a mole fraction basis, and z_i denotes the mole fraction of ions ($z_{\text{Na}^+} = z_{\text{Cl}^-} = z_i/2$).

As described above, the MSA equation predicts below 387°C a larger NaCl solubility in saturated liquids than measured for H₂O-NaCl fluids. This discrepancy between the model and experimental data is certainly due to hydrogen bonds and dispersion forces. As there is no firm guideline for describing these types of molecular interactions, a simple van der Waals attraction (A^{vdW}) term has been chosen. Thus, Eqn. (14) for the Helmholtz free energy must be modified as follows:

$$A = A^{hs} + A^{MSA} + A^{vdW}, \quad (20a)$$

$$\text{where } A^{vdW} = -a / V. \quad (20b)$$

The van der Waals parameter (a) is a function of the fluid composition:

$$a = x_{dipole}^2 a_{dipole} + 2 x_{dipole} x_{ion} a_{ion-dipole} + x_{ion}^2 a_{ion}, \quad (21)$$

where x_{ion} and x_{dipole} are the mole fractions of ions (Na⁺ and Cl⁻) and dipoles.

As the properties of water are modelled by the MSA equation for a pure dipolar fluid, the van der Waals attraction term for the dipolar component must be set to zero:

$$a_{dipole} = 0. \quad (22a)$$

As a consequence, the mixing term for ion-dipole interactions is equal to zero too :

$$a_{ion-dipole} = 0. \quad (22b)$$

Thus, there remains only one fitting parameter, which is the van der Waals parameter for the ionic component (a_{ion}).

EVALUATION OF THE PARAMETERS.

In the last paragraph, it has been shown that additional equations are necessary with the MSA equation in order to describe the liquid-vapor equilibria of the H₂O-NaCl system. Now, it is possible to evaluate the fitting parameters, which are the dipole moment (μ), the ion association constant (K) and the van der Waals attraction term (a_{ion}).

Two different temperature ranges have been considered for the adjustment of the dipole moment. For temperatures below 374°C, the dipole moment has been obtained by fitting the calculated saturation pressure to experimental data (HAAR et al., 1984) :

$$\mu/\mu_c = 1 - 0.1204 \delta - 0.26051 \delta^2 - 0.44201 \delta^3 - 0.3454 \delta^4, \quad (23a)$$

$$\text{where } \delta = (T - T_c)/T_c. \quad (23b)$$

For supercritical temperatures ($T > 374^\circ\text{C}$), the dipole moment has been obtained by fitting the calculated critical pressure with experimental data of BISCHOFF (1991) and extrapolated values from TANGER and PITZER (1989). The following relation has been obtained :

$$\mu/\mu_c = 1 + 0.11679 \delta - 1.1123 \delta^2 + 1.3661 \delta^3. \quad (24)$$

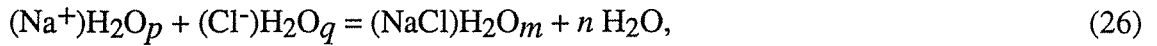
The dependence of the dipole moment as a function of the temperature is given in Figure 3. The dipole moment increases slightly for temperatures between 374°C and 380°C , and then decreases. A linear dependence with the temperature is observed at higher temperatures. As shown in Figure 3, our approach is not entirely satisfactory. A discontinuity is observed at the critical point of water, and the increase of the dipole moment just above the critical point is problematic. It is worth to note that the model is very sensitive to the value of the dipole moment, and the use of a smoother function would lead to a significant degradation of the model. The calculated and experimental H_2O - NaCl critical curve is shown in Figure 4. As expected, good agreement is obtained on the pressure-temperature plot, but the predicted critical NaCl mole fraction is strongly underestimated. This discrepancy increases with the temperature and is due to the non-use of association constants describing the ion pair formation at the present stage of the model.

The P - T - x - y experimental data for H_2O - NaCl , that have been compiled by BISCHOFF and PITZER (1989) and HAAS (1976), have been used for the adjustments of the association constants and van der Waals term. First, association constants have been estimated by considering discrepancies between the calculated and experimental NaCl mole fractions at high temperatures ($T > 387^\circ\text{C}$):

$$K = (z(\text{NaCl}, \text{total}) / z(\text{NaCl}, \text{diss.}) - 1) / (4 z(\text{NaCl}, \text{diss.})), \quad (25)$$

where $z(\text{NaCl}, \text{total})$ is given by the experimentally measured NaCl mole fraction, and $z(\text{NaCl}, \text{diss.})$ is calculated by the MSA for the ion-dipole mixture. Association constants depend on the temperature, density and composition of the solutions, and the problem is

to find a suitable formulation. Ion pair formation occurs when the constant dielectric decreases (HELGESON et al., 1981). Thus, association is expected to increase dramatically with the temperature and to decrease with the density of the fluid phase. As shown by FRANCK (1956), and by MARSHALL and QUIST (1967), ion pair formation in aqueous solutions is accompanied by a net release of water molecules, as ion pairs are less hydrated than both ions:



where p , q , and m are the hydration numbers of Na^+ , Cl^- and ion pair NaCl , and n is the number of water molecules released during ion pair formation.

Thus, an association constant K° should be used :

$$K^\circ = a_{\text{NaCl}} (a_{\text{H}_2\text{O}})^n / (a_{\text{Na}^+} a_{\text{Cl}^-}), \quad (27)$$

where a_{NaCl} , $a_{\text{H}_2\text{O}}$, a_{Na^+} and a_{Cl^-} refer to the activities of the different species.

After some transformation, Eqn. (27) can be written as (MARSHALL and QUIST, 1967):

$$\log K' = \log K^\circ - n \log a_{\text{H}_2\text{O}}, \quad (28)$$

where K' is the association constant at infinite dilution of electrolyte.

When the association constant is expressed on the molarity unit basis as suggested by MARSHALL and QUIST (1967), the H_2O activity can be replaced by the H_2O molarity ($C_{\text{H}_2\text{O}}$):

$$\log K' = \log K^\circ - n \log (C_{\text{H}_2\text{O}}). \quad (29a)$$

When K' and K° are expressed on the molality basis, Eqn. (29a) becomes to :

$$\log K' = \log K^\circ - (n-1) \log (C_{\text{H}_2\text{O}}) + \log (M_{\text{H}_2\text{O}}), \quad (29b)$$

where $M_{\text{H}_2\text{O}}$ is the molar weight of H_2O ($M_{\text{H}_2\text{O}}=18 \text{ g/mol}$).

Conductometric measurements of aqueous solutions of QUIST and MARSHALL (1968) reveal that association constants at infinite dilution for temperatures between 0°C to 800°C and for densities below 0.80 g/cm^3 could be fitted by Eqn. (29b) with a K° constant, that is independent of the density and of the dielectric constant. Thus, the availability of water molecules in the system has a large influence on the value of the association constant. A plot of the logarithm of the fitted association constant (on the molality basis) for the vapor as a function of the logarithm of the H_2O molarity is given at 500°C in Figure 5B. A

straight line is obtained with a slope of -11.7, which corresponds to an hydration number of 12.7. This latter number agrees quite well with the value of 10.2 given by QUIST and MARSHALL (1968), or with the value of 12 estimated by WOOD et al. (1984) at 300°C. However, as seen in Figure 5B, large errors between the association constants at infinite dilution determined by MARSHALL and QUIST (1967) and in this study occur at densities below 0.1 g/cm³ and above 0.3 g/cm³ (up to a factor 2 at 1 g/cm³). Although our model is based on some physical reality, discrepancies are still large. As a consequence, it would be possible to use directly the association constants of MARSHALL and QUIST (1968) with our model, but this would lead to a poor agreement with the experimental data. Moreover, an activity coefficient model should be used for NaCl-containing fluids in order to calculate the proportion of ion pairs from the mass action law, and the calculation of activity coefficients in electrolyte solutions is not a simple problem too. For all these reasons, it has been preferred to treat the association constants as a fitting parameter. It is worth noting that our K association constants are not true reaction constants, as they incorporate the effects of activity coefficients. For a given temperature, it was found that the K constant could be represented by a function like:

$$\log K = A + B \log (\eta), \quad (30a)$$

where η is a reduced density:

$$\eta = (x_d b_d + x_i b_i) / (4V), \quad (30b)$$

b_d and b_i are the covolumes of the dipolar and ionic components in the system:

$$b_d = 2/3 \pi N_a \sigma_d^3, \text{ and} \quad (30c)$$

$$b_i = 2/3 \pi N_a \sigma_i^3. \quad (30d)$$

where N_a is the Avogadro number, and V is calculated by the MSA equation of state for the ion-dipole mixture.

A plot of the logarithm of the K association constants (on the mole fraction basis) with respect to the logarithm of η is given in Figure 5C. Two distinct lines are obtained for the liquid and the vapor.

For the vapour phase, association constants K_G (on the mole fraction basis) have been regressed as follows :

$T < 387^{\circ}\text{C}$,

$$\log K_G = 91.536 - 0.1638 T + (32.051 - 0.07384 T) \log \eta, \quad (31a)$$

$T > 387^{\circ}\text{C}$,

$$\log K_G = -29.548 + 0.019683 T + (-29.063 + 0.018585 T) \log \eta, \quad (31b)$$

Following relations have been found for the association constants K_L in the liquid phase:

$T < 387^{\circ}\text{C}$,

$$\log K_L = -\infty, \quad (31c)$$

$T > 387^{\circ}\text{C}$,

$$\log K_L = -14.9541 - 15.261 / (T-660) + 0.012944 T \\ + (-17.3808 - 12.417 / (T-660) + 0.014786 T) \log \eta. \quad (31d)$$

For temperatures above 387°C , an interpolation function has been used in order to ensure a smooth transition in the critical region between the vapor and liquid.

$$\alpha = 1 + (\tanh (10 (\log(\eta) - \log(\eta_c)))) / 2, \quad (32)$$

where $\log(\eta_c)$ is equal to -1.095.

α takes a value between 0 (for a liquid-like phase) and 1 (for a vapour-like phase).

Once an association constant has been calculated, the "true" NaCl mole fraction is calculated by :

$$z (\text{NaCl, total}) = z (\text{NaCl diss.}) (1 + 4 K z (\text{NaCl diss.})). \quad (33)$$

where z denotes either the NaCl mole fraction in the liquid or in the gas and K is calculated by Eqns (31 a,b) for a vapor or by Eqns (31 c,d) for a liquid.

Ionization fraction F can be estimated by using the relation :

$$F = z (\text{NaCl diss.}) / z (\text{NaCl, total}), \text{ i.e.} \quad (34a)$$

$$F = 1 / (1 + 4 K z (\text{NaCl diss.})). \quad (34b)$$

A comparison of our association constants at infinite dilution with those of QUIST and MARSHALL (1968) is given in Figure 6. At temperatures above 400°C , our model underestimates the K° association constants in solutions at infinite dilution and for a density of 1 g/cm^3 by a factor of two when compared to the constants of QUIST and MARSHALL (1968). But both association constants follow the same trend as a function of the temperature. The predicted hydration number n decreases with the temperature from

15.4 at 400°C to 12.7 at 500°C. These values are larger than the value of 10.2 estimated by QUIST and MARSHALL (1968). Our association constants are in good agreement with values of QUIST and MARSHALL (1968) for densities between 0.2 and 0.3 g/cm³ (see Figure 5B). Below 400°C, major discrepancies are observed between our model and association constants of QUIST and MARSHALL (1968). The values of $\log(K^\circ)$ increase strongly when the temperature is lowered. Overestimation of dissociation constants at infinite dilution up to a factor of 15 is observed for all densities. This alteration of the model is probably due to our approximation to neglect association in NaCl-rich saturated liquids below 387°C.

Below 387°C, discrepancies between the MSA for the ion-dipole mixture and the H₂O-NaCl system have been reduced by considering a van der Waals term (a_{ion}). Experimental data of HAAS (1976) for saturated liquids have been used for calculating the a_{ion} parameter at different temperatures. The dependence of the a_{ion} parameter is given in Figure 7. As expected, a_{ion} tends to zero when the temperature approaches 387°C, but the sign of the a_{ion} term is negative. This is very different from usual mixtures of non-polar components, where the van der Waals parameters are always of positive sign. Thus, the van der Waals term cannot represent the effects of dispersion forces. Clearly, it is a correcting contribution to some deficiency of the model. The first explanation is that the MSA model does not represent the thermodynamic properties of the ion-dipole mixture with sufficient accuracy. Such an hypothesis can only be tested by testing more elaborate models for the ion-dipole mixture. Another explanation would be that other molecular interactions, that are not taken into account explicitly in the ion-dipole model, do play an important role at low temperatures ($T < 390^\circ\text{C}$). This is the case of hydrogen bonds. Hydrogen bonds represent indeed an important part of molecular interactions in aqueous electrolyte solutions. They are considered in our model, but on a false basis. Indeed, hydrogen bonding in pure water is treated like dipole-dipole interactions. As a consequence, the values of the dipolar moment given by Eqn. (23a) include the effects of hydrogen bonds. The van der Waals term would thus represent a correcting term to our present way of treating hydrogen bonding. The extent of hydrogen bonding diminishes

with increasing temperatures, and this is effectively observed in Figure 7, where the absolute value of a_{ion} decreases with the temperature. Such an hypothesis could be tested by including a more realistic term for hydrogen bonding in our model for pure water as proposed by JACKSON et al. (1988) and GREEN and JACKSON (1992). In Figure 7, it can be seen that the a_{ion} parameter cannot be represented by a simple function of the temperature. Following expressions have been obtained for the a_{ion} parameter:

for $T > 387^{\circ}\text{C}$,

$$a_{ion} = 0, \quad (35a)$$

for T between 300°C and 390°C ,

$$a_{ion} = -1382.3 + 6.7191 T - 0.010909 T^2 + 5.912e-3 T^3, \quad (35b)$$

for T between 100°C and 300°C ,

$$a_{ion} = 12.32 - 0.069712 T + 7.8335e-5 T^2. \quad (35c)$$

RESULTS.

Comparison of vapor-liquid equilibria calculated by our model with the smoothed experimental data reported by HAAS (1976) and BISCHOFF (1991) is given in Figures 8, 9, 10, 11 and 12. In general, a good agreement is obtained with experimental data between 100°C and 500°C , although the equation of state is slightly less accurate than the equation of ANDERKO and PITZER (1991). Figure 13 shows vapor-liquid equilibria calculated by the model at temperatures above 500°C . The equation of state is extrapolated over the temperature range (100°C - 500°), where the equation has been fitted. At these high temperatures, the only available experimental data are those of BODNAR (1985), that have been reviewed by CHOU (1987). First, it can be seen on Figure 13 that the equation of state is not extrapolable at 700°C and 800°C for pressures above 1000 bar. Extrapolated association constants yield indeed unrealistic NaCl mole fractions for saturated liquids, that are above 1. However, errors are limited to ± 0.1 in NaCl mole fraction for x_{NaCl} below 0.5 above 1000 bars. The model underestimates salinities at high pressures ($P > 1000\text{bar}$) and overestimates them at lower pressures ($P < 1000\text{bar}$). The equation of state of ANDERKO and PITZER (1991) gives better results, when it is extrapolated

above 500°C. This comparison reveals the limit of our model at these extreme conditions. Above 500°C, ionic species are almost absent, and therefore, the ANDERKO and PITZER equation of state is more appropriate. Moreover, other chemical reactions may become important in the H₂O-NaCl system above 500°C.

CONCLUSION.

This study is the application of a heavy theoretically-sound equation of state for modelling the liquid-vapor equilibria of the H₂O-NaCl system. This equation of state is derived from the MSA theory for the ion-dipole mixture. First comparison of the MSA model with experimental data reveals clearly that the ion-dipole mixture cannot be used solely for reproducing the properties of the H₂O-NaCl system. Large discrepancies occur between the calculated and measured NaCl compositions for saturated vapours at all temperatures and for saturated liquids at high temperatures ($T > 387^\circ\text{C}$). These discrepancies can be eliminated by using an association constant for describing ion association. Association constants determined in this study have been compared with the association constants of QUIST and MARSHALL (1968). On the other side, at lower temperatures ($T < 387^\circ\text{C}$), the MSA equation predicts higher salinities in saturated liquids than measured in the H₂O-NaCl system. The incorporation of a simple van der Waals term in the Helmholtz free energy of the model allows one to reproduce the experimental data within experimental error. However, this van der Waals parameter is of negative sign, and this means means that this term does not represent the effects of dispersion forces, but is rather a correction to the deficiency of the ion-dipole model for representing vapor-liquid equilibria at low temperatures ($T < 387^\circ\text{C}$).

The equation of state reproduces experimental data with a good accuracy. However, it gives poor results, when it is extrapolated above 500°C. Ionic species are practically absent at these high temperatures. As a result, it is not surprising that the MSA equation for the ion-dipole mixture is not appropriate in such cases.

The equation of state is based on two simplifying assumptions, that are discutable. The first one is that anions have the same size than cations; the second one is that the dipole

moment of ions pairs is the same than the dipole moment of water. Moreover, an arbitrary limit has been set arbitrarily at 387°C for the simplicity. Above this temperature, the van der Waals term has been set to zero; and below this temperature, no association reaction is taken into account in liquids. Refinements of the equation of state would certainly improve the results. However, at the present stage of development, this model provides already useful information on the thermodynamics of electrolyte solutions at the molecular scale.

REFERENCES

- ADELMAN S.A. and DEUTCH J.M. (1974) Exact solution of the mean spherical model for strong electrolytes in polar solvent. *J. Chem. Phys.* **60**, 3935-3940.
- ANDERKO A. and PITZER K.S. (1993) Equation-of-state representation of phase equilibria and volumetric properties of the system NaCl-H₂O above 573 K. *Geochim. Cosmochim. Acta* **57**, 1657-1660.
- BISCHOFF J.L. (1991) Densities of liquids and vapors in boiling NaCl-H₂O solutions: a PVTX summary from 300°C to 500°C. *Amer. J. Sci.* **291**, 309-338.
- BISCHOFF J.L. and PITZER K.S. (1989) Liquid-vapor relations for the system NaCl-H₂O: Summary of the P-T-x surface from 300 to 500°C. *Am. J. Sci.* **289**, 217-248.
- BLUM L. and WEI D. (1987) Analytical solution of the mean spherical approximation for an arbitrary mixture of ions in a dipolar solvent. *J. Chem. Phys.* **87**, 555-565.
- BODNAR R. J. (1985) Pressure-volume-temperature-composition (PVTX) properties of the system H₂O-NaCl at elevated temperatures and pressures. Ph.D. dissertation, Pennsylvania State University.
- BOUBLIK T. (1970) Hard sphere equation of state. *J. Chem. Phys.* **53**, 471-472.
- BOWERS T.S. and HELGESON H.C. (1983) Calculation of the thermodynamic properties and geochemical consequences of nonideal mixing in the system H₂O-CO₂-NaCl fluids at high pressures and temperatures. *Geochim. Cosmochim. Acta* **47**, 1247-1275.

CHOU I.M. (1987) Phase relations in the system NaCl-KCl-H₂O. III. Solubilities of halite in vapor-saturated liquids above 445°C and redetermination of phase equilibrium properties in the system NaCl-H₂O to 1000°C and 1500 bar. *Geochim. Cosmochim. Acta* **51**, 1965-1975.

FERNANDEZ-PRINI, R.J. (1992) Statistical mechanical tools *In* High-temperature aqueous solutions: thermodynamic properties. CRC Press, pp 189-201.

FRANCK, E.U. (1956) *Z. Physik. Chem.*, **8** (107), 192.

GOODSTEIN D.L. (1975) States of matter. Dover Publications Inc.

GREEN D.G. and JACKSON G. (1992) Theory of phase equilibria for model aqueous solutions of chain molecules: water + alkane mixtures. *J. Chem. Soc. Faraday Trans.* **88**, 1395-1409.

HAAR L., GALLAGHER T.S., and KELL G.S. (1984) NBS/NRS Steam Tables: Thermodynamic and transport properties and computer programs for vapor and liquid states in SI units. Hemisphere, Washington, DC.

HAAS J.L. Jr. (1976) Thermodynamic properties of the coexisting phases and thermochemical properties of the NaCl component in boiling NaCl solutions. Preliminary steam tables for NaCl solutions. *Geol. Surv. Bull.* **1421-B**, 1-71.

HARVEY A.H. (1991) Phase equilibria and critical lines in model water/salt mixtures. *J. Chem. Phys.* **95**, 479-484.

HASTED J.B. (1972) Liquid Water: Dielectric properties *In* *Water, a comprehensive treatise* (ed. F. Franks), vol. 1, Chap. 7, pp 255-309, Plenum Press.

HELGESON H.C., KIRKHAM D.H. and FLOWERS G.C. (1981) Theoretical prediction of the thermodynamic behavior of aqueous electrolytes at high pressures and temperatures. IV. Calculation of activity coefficients, osmotic coefficients and apparent molal and standard and relative partial molal properties to 600°C and 5 kbar. *Am. J. Sci.* **287**, 1249-1516.

HOLOVKO M.F. and PROTSYKEVICH I. (1987) Pair correlation functions for the asymmetric ion-dipole model in the mean spherical approximation. *Chem. Phys. Lett.* **142**, 463-468.

HOYE J.S. and LOMBA E. (1988) Mean Spherical Approximation (MSA) for a simple model of electrolytes. I. Theoretical foundation and thermodynamics. *J. Chem. Phys.* **99**, 5790-5797.

HOYE J.S., LOMBA E. and STELL G. (1988) Mean spherical approximation for a simple model of electrolytes. II. Correlation functions and thermodynamics: numerical results. *J. Chem. Phys.*, **89**, 7462-7470.

JACKSON G., CHAPMAN W.G. and GUBBINS K.E. (1988) Phase equilibria of associating fluids Spherical molecules with multiple bonding sites. *Molecular Physics* **65**, 1, 1-31.

LVOV S.N. and WOOD R.H. (1990) Equation of state of aqueous NaCl solutions over a wide range of temperatures, pressures and concentrations. *Fluid Phase Equilibria* **60**, 273-287.

MARSHALL W.L. (1990) Critical curves of aqueous electrolytes related to ionization behaviour: New temperatures for sodium chloride solutions. *J. Chem. Soc. Faraday Trans.* **86**, 1807-1814.

MARSHALL W.L. and QUIST A.S. (1967) A representation of isothermal ion-ion-pair-solvent equilibria independent of changes in dielectric constant. *Proc. Nation. Acad. Sci.* **58**, 901-908.

McCLELLAN A.L. (1963-1989) Tables of Experimental Dipole Moments, Freeman.

MESMER R.E., PALMER D.A., and SIMONSON J.M. (1991) Ion association at high temperatures and pressures. In *Activity coefficients in Electrolyte Solutions*, 2d ed. (ed. K.S. Pitzer), Chap. 8, pp 491-529, CRC Press.

PABALAN R.T. and PITZER K.S. (1990) Models for aqueous electrolyte mixtures for systems extending from dilute solutions to fused salts. *ACS Symp. Series* **416**, 44-57.

PITZER K.S. and PABALAN R.T. (1986) Thermodynamics of NaCl in steam. *Geochim. Cosmochim. Acta* **50**, 1445-1454.

PITZER K.S., PEIPER J.C. and BUSEY R.H. (1984) Thermodynamic properties of aqueous sodium chloride solutions. *J. Phys. Chem. Ref. Data* **13**, 1-102.

PITZER K.S. and SIMONSON J.M. (1986) Thermodynamics of multicomponent, miscible, ionic systems: Theory and equations. *J. Phys. Chem.* **90**, 3005-3009.

PIZIO O.A., HOLOVKO M.F. and TROKHIMCHUK A.D. (1988) The pair distribution functions and thermodynamic properties of the ion-dipole model of electrolyte solutions. *Acta Chim. Hung.* **125**, 385-402.

- PRAUSNITZ J.M., LICHTENTHALER R.N., and GOMES de AZEVEDO E. (1986) Molecular thermodynamics of fluid-phase equilibria. 2nd Ed., Prentice-Hall Inc., 600 p.
- QUIST A.S. and MARSHALL W.L. (1968) Electrical conductances of aqueous sodium chloride solutions from 0°C to 800°C and at pressures to 4000 bars. *J. Phys. Chem.* **72**, 684-703.
- RUSHBROOKE G.S., STELL G. and HØYE J.S. (1973) Theory of polar fluids. I. Dipolar hard spheres. *J. Mol. Phys.* **26**, 1199-1215.
- SØREIDE I. and WHITSON C.H. (1992) Peng-Robinson predictions for hydrocarbons, CO₂, N₂, and H₂S with pure water and NaCl brine. *Fluid Phase Equilibria* **77**, 217-240.
- STELL G., RASAIHAH J.C., and NARANG H. (1972) Thermodynamic perturbation theory for simple polar fluids. *J. Mol. Phys.* **23**, 393-406.
- STELL G., RASAIHAH J.C., and NARANG H. (1974) Thermodynamic perturbation theory for simple polar fluids, II. *J. Mol. Phys.* **27**, 1393-1414.
- TANGER J.C. IV and PITZER K.S. (1989) Thermodynamics of NaCl-H₂O: A new equation of state for the near-critical region and comparisons with other equations for adjoining regions. *Geochim. Cosmochim. Acta* **53**, 973-987.
- THIÉRY R. (1996) A new library for calculating analytically high-order multivariable derivatives and thermodynamic properties of fluids with equations of state. *Computer & Geosciences* (under press).

THIÉRY R., LVOV S.N. and DUBESSY J. (submitted to *J. Chem. Phys.*) A global phase diagram for the ion-dipole model in the mean spherical approximation.

VAN KONYNENBURG P.H. and SCOTT R.L. (1980) Critical lines and phase equilibria in binary van der Waals mixtures. *Philos. Trans. R. Soc. London Ser. A* **298**, 495-540.

VERICAT F. and BLUM L. (1980) Mean spherical model for hard ions and dipoles: thermodynamic and correlation functions. *J. Stat. Phys.* **22**, 593-604.

WEI D. and BLUM L. (1987) The mean spherical approximation for an arbitrary mixture of ions in a dipolar solvent. Approximate solution, pair correlation functions, and thermodynamics. *J. Chem. Phys.* **87**, 2999-3007.

WOOD S.A., CRERAR D.A., BRANTLEY S.L., and BORCSIK M. (1984) Mean molal stoichiometric activity coefficients of alkali halides and related electrolytes in hydrothermal solutions. *Am. J. of Science* **284**, 668-705.

WU J., LU J., and LI Y. (1994) A new perturbation method for electrolyte solutions based on MSA. *Fluid Phase Equilibria* **101**, 121-136.

LIST OF FIGURES

Figure 1. A part view of the global phase diagram for the ion-dipole mixture in the MSA (THIERY et al., submitted) used for choosing a value for the ionic diameter. Parameters α_1 and α_2 are explicited in the text. The different types of phase diagrams are delimited by the dotted lines. The solid line is the curve corresponding to the different possible choices for the ionic diameter, when a dipolar moment of 2.243 Debye and a dipole diameter of 2.331 Å are adopted for modelling the properties of water. Ratios of the critical temperatures and ionic diameter, which correspond to the α_1 and α_2 values, are indicating on the top and right axis. The solid square corresponds to the the ionic diameter ($\sigma_i = 4.5$ Å) chosen in this study.

Figure 2. A/ (Pressure - NaCl mole fraction) diagram representing the saturation curves of aqueous NaCl solutions at 200°C. Isotherms are calculated for different ionic diameters (2.5 Å, 3.5 Å, 4.5 Å and 5 Å). Solid squares are smoothed experimental data reported by HAAS (1976). B/ (Pressure - NaCl mole fraction) diagram for immiscible liquids and gas in equilibria at 500°C. Crosses are smoothed experimental data given by BISCHOFF (1991). The isotherms are calculated at 4.0 Å, 4.5 Å and 5.0 Å for the ionic diameter and with a dipole moment μ of 2.22 Å and a dipole diameter σ_d of 2.331Å.

Figure 3. The variation of the dipole moment as a function of the temperature. Solid circles and squares are values of the dipole moment determined respectively by fitting the (pressure-temperature) data for the H₂O saturation curve and the H₂O-NaCl critical curve.

Figure 4. A/ The critical curve calculated by the MSA model (dotted line) in a (pressure - temperature) diagram. Solid squares and filled circles are respectively experimental data reported by BISCHOFF (1991) and extrapolated values of TANGER and PITZER (1989). B/ idem in a (temperature - NaCl mole fraction) diagram.

Figure 5. A/ Liquid-vapour equilibria isotherm at 500°C in a (pressure - NaCl mole fraction). Crosses are smoothed experimental data of BISCHOFF (1991). The dotted line is the liquid-vapor immiscibility curve calculated by the MSA equation for the ion-dipole mixture. The solid line is the immiscibility curve obtained when the NaCl ion pair formation is taken into account. B/ Log-log plot of the association constants (on the molality scale) against the H₂O molarity. Crosses are the association constants determined along the vapor branch by using Eqn. (25). The points are aligned along a straight line. The dotted line is given by MARSHALL and QUIST (1967) and is plotted for comparison. C/ A log-log plot of the K constants (on the mole fraction scale) against the reduced density η . Crosses are calculated by using Eqn. (25) and the smoothed experimental data of BISCHOFF (1991). Points are aligned along two different lines, one for the vapor and the other for the liquid.

Figure 6. Evolution of the parameters describing ion association as a function of the temperature. Filled squares are the logarithmic values of the K° association constants (on the molality scale) at infinite dilution and for a density of 1 g/cm³, that have been estimated from the data reported by BISCHOFF (1991). Empty circles are the hydration numbers. The straight line represent the smoothed K° values given by QUIST and MARSHALL (1968).

Figure 7. The dependence of the a_{ion} parameter on the temperature, estimated by fitting the smoothed data reported by HAAS (1976) and BISCHOFF (1991).

Figure 8. Comparison of the liquid-vapor immiscibility curve calculated from the equation of state with the smoothed data reported by HAAS (1976) in a pressure-NaCl mole fraction diagram at 100°C, 150°C, 200°C and 250°C.

Figure 9. Comparison of the liquid-vapor immiscibility curve calculated from the equation of state with the smoothed data reported by BISCHOFF (1991) in a pressure-NaCl mole fraction diagram at 300°C, 310°C, 320°C, 330°C, 340°C and 350°C.

Figure 10. Comparison of the liquid-vapor immiscibility curve calculated from the equation of state with the smoothed data reported by BISCHOFF (1991) in a pressure-NaCl mole fraction diagram at 360°C, 370°C, 380°C and 390°C.

Figure 11. Comparison of the liquid-vapor immiscibility curve calculated from the equation of state with the smoothed data reported by BISCHOFF (1991) in a pressure-NaCl mole fraction diagram at 400°C, 410°C, 420°C, 430°C and 440°C.

Figure 12. Comparison of the liquid-vapor immiscibility curve calculated from the equation of state with the smoothed data reported by BISCHOFF (1991) in a pressure-NaCl mole fraction diagram at 450°C and 500°C.

Figure 13. Extrapolation of the equation of state at temperatures above 500°C and comparison with the data of BODNAR (1985) recalculated by CHOU (1987) in a pressure-NaCl mole fraction diagram. A/ Solid line and empty squares refer to the 550°C temperature, dotted curve and filled triangles to the 600°C temperature, long-dashed curve and empty circles to the 650°C temperature, and the short-dashed line and filled squares to the 700°C temperature. Horizontal lines represent uncertainties of the experimental composition of liquids. B/ Solid line and filled circles refer to the 700°C temperature, and the dotted and empty squares to the 800°C temperature.

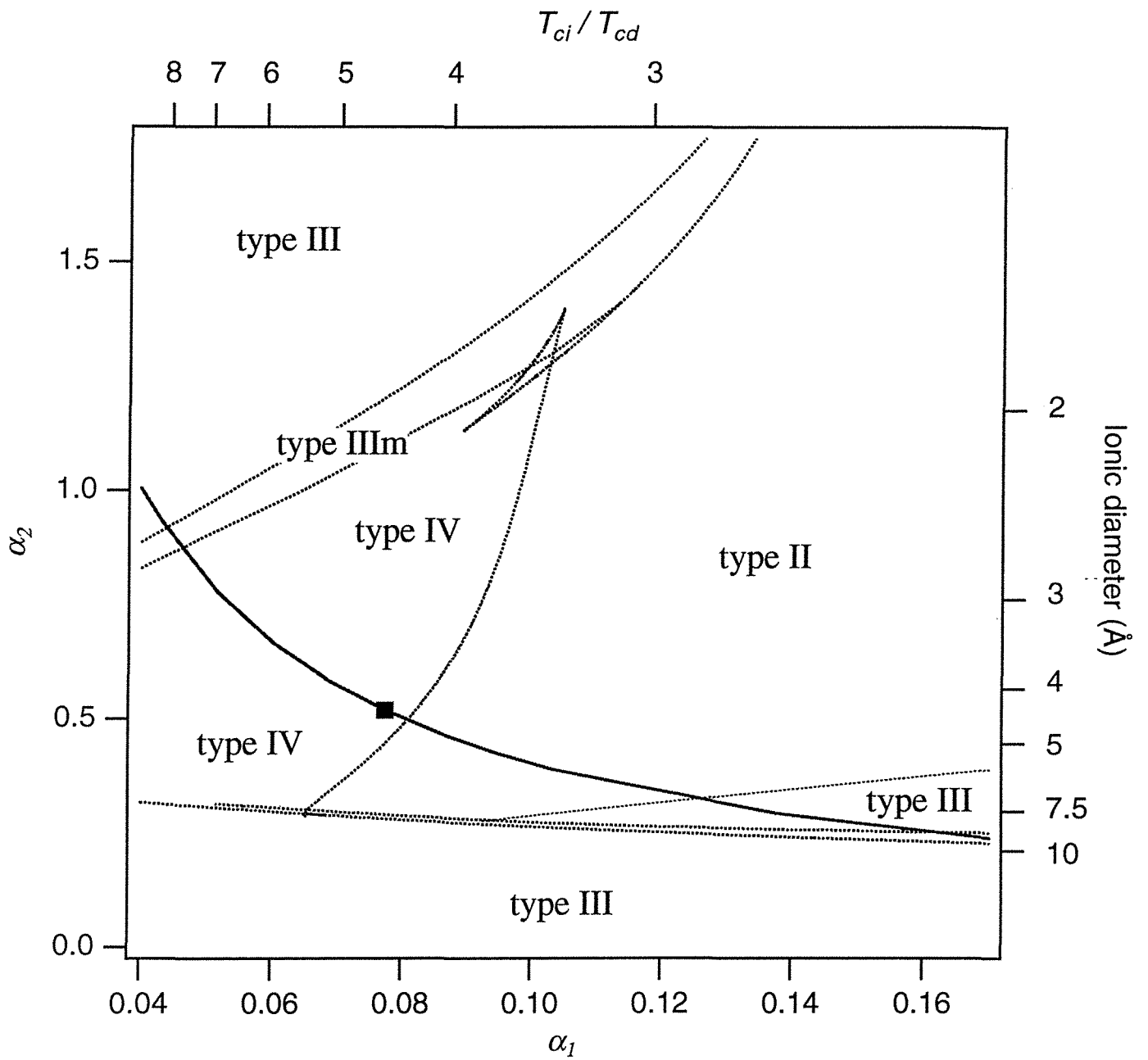


FIGURE 1

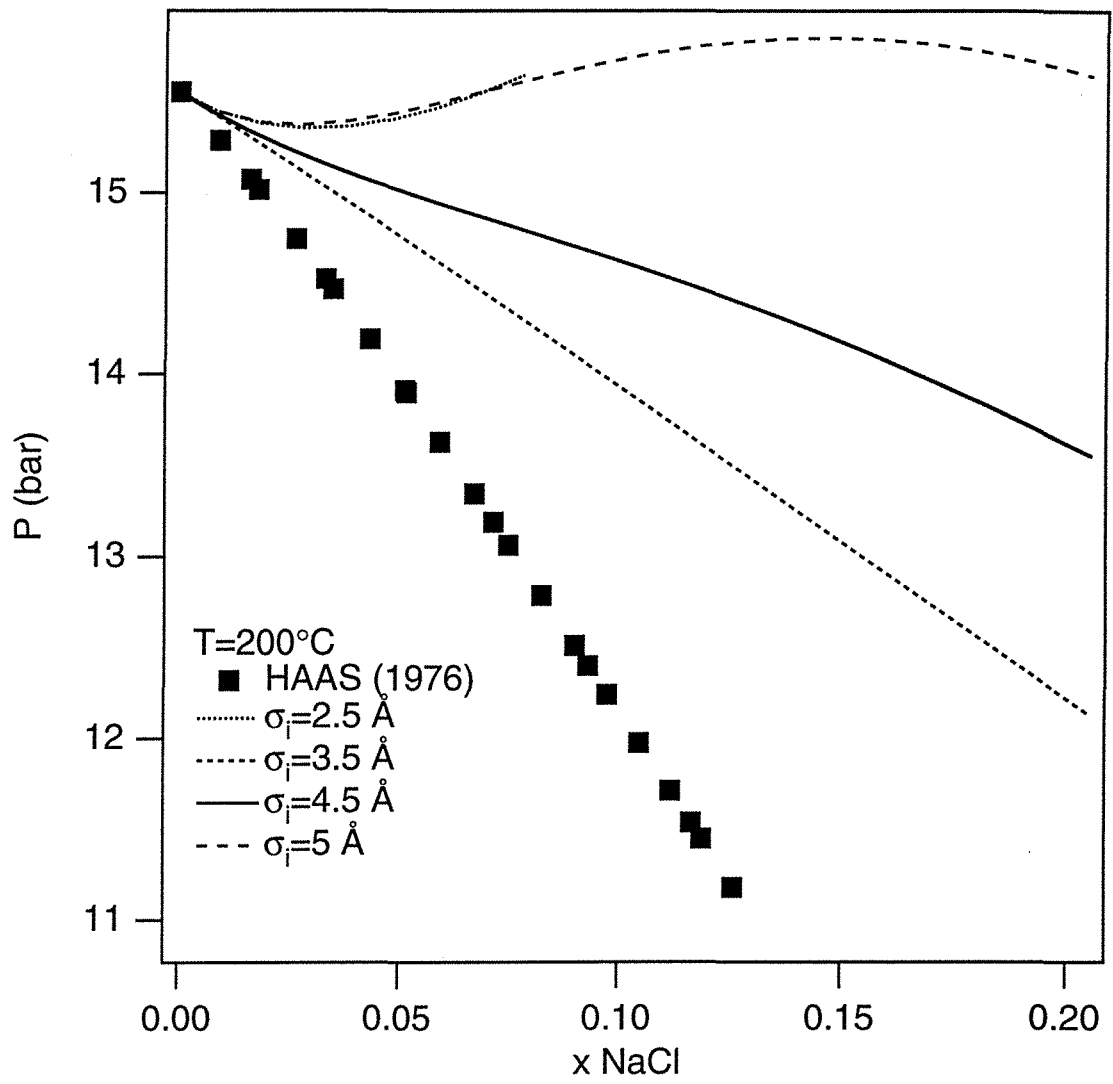


FIGURE 2A

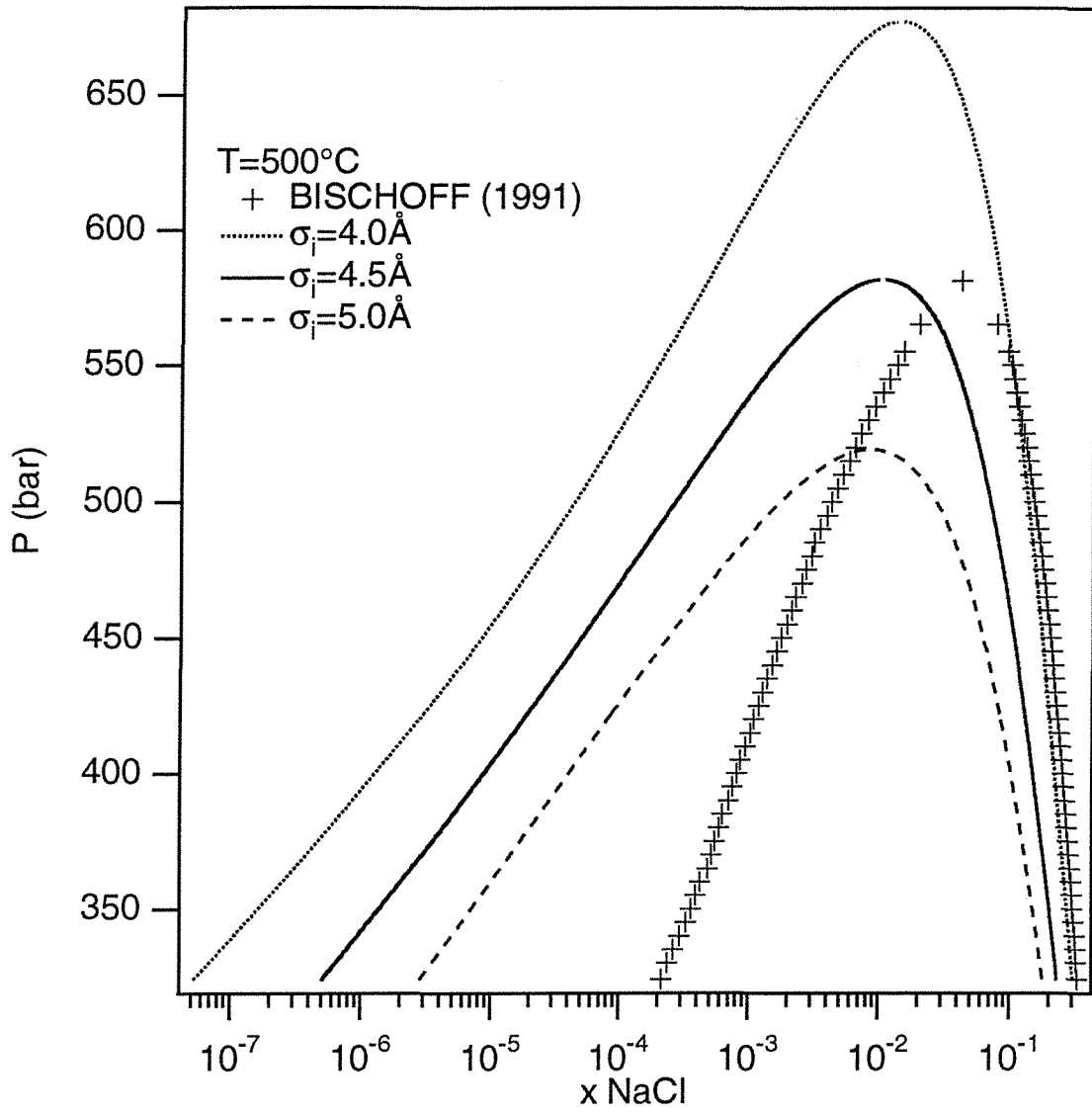


FIGURE 2B

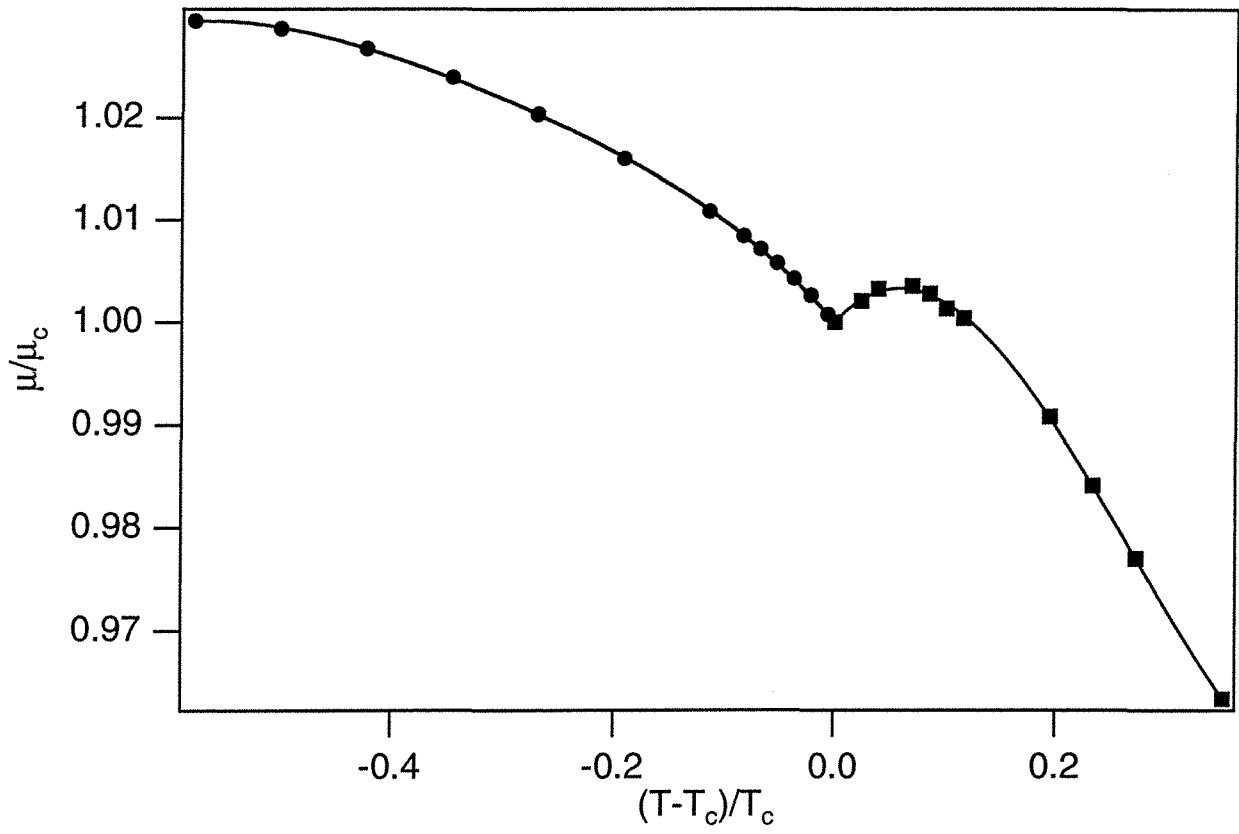


FIGURE 3

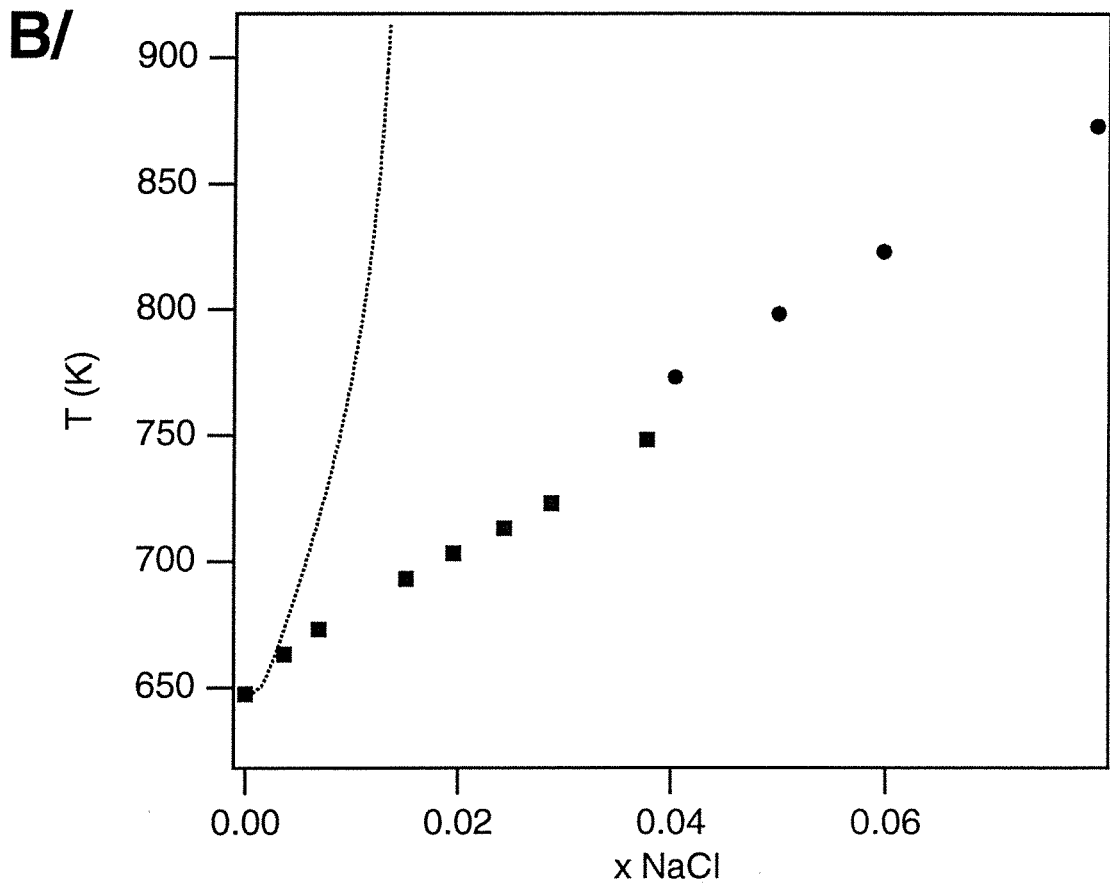
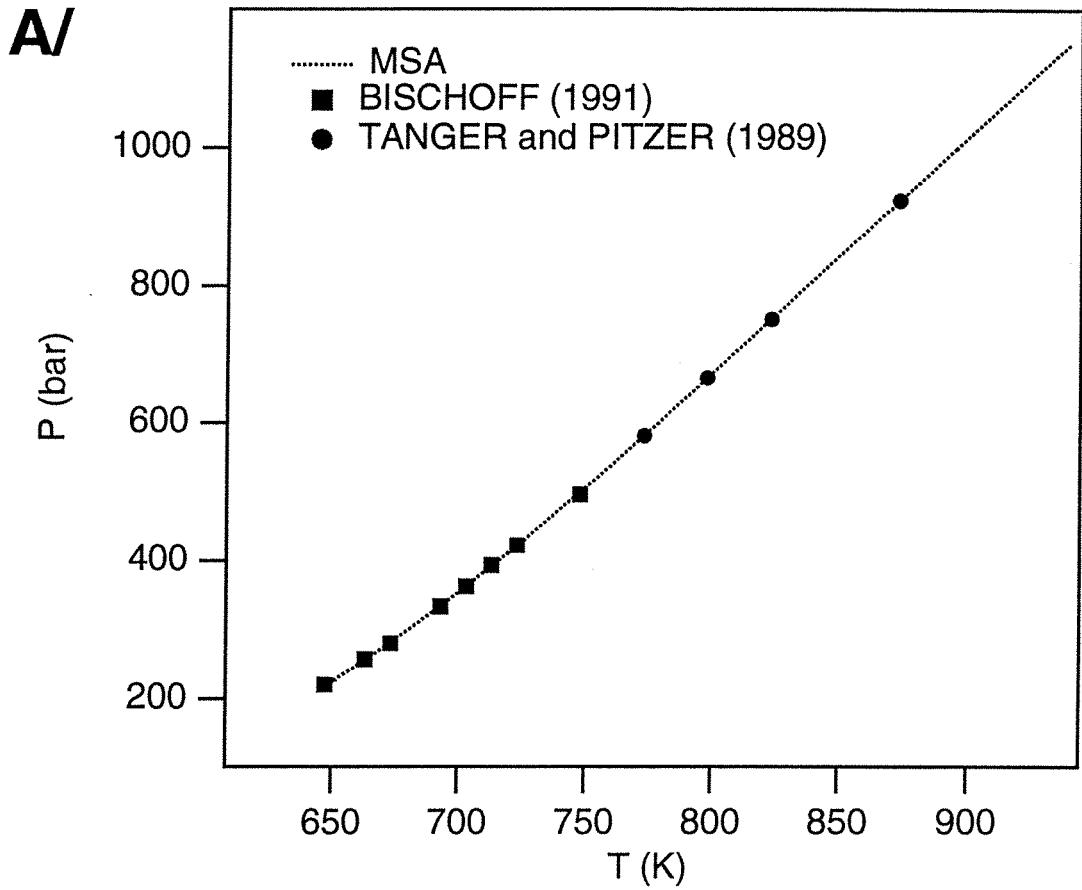


FIGURE 4

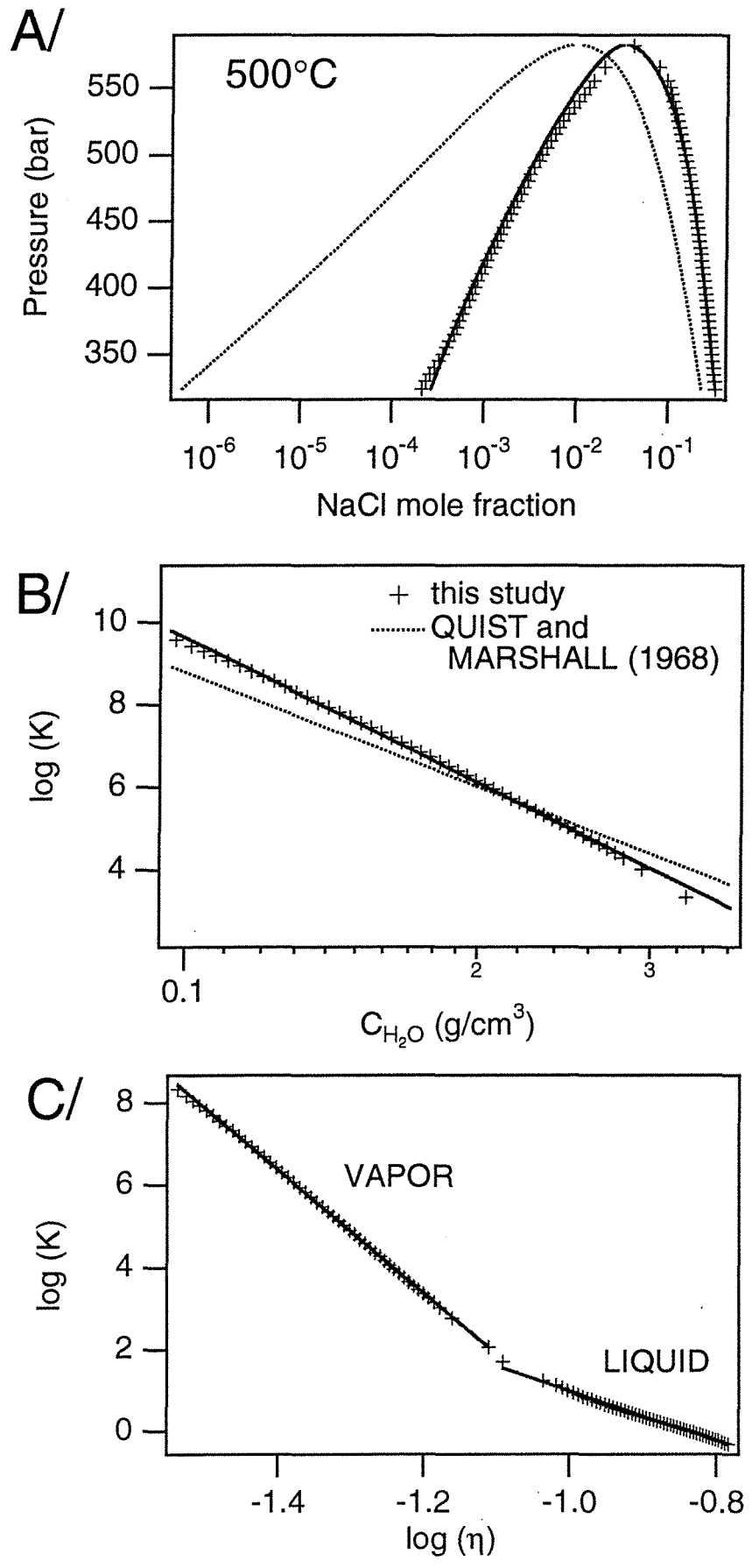


FIGURE 5

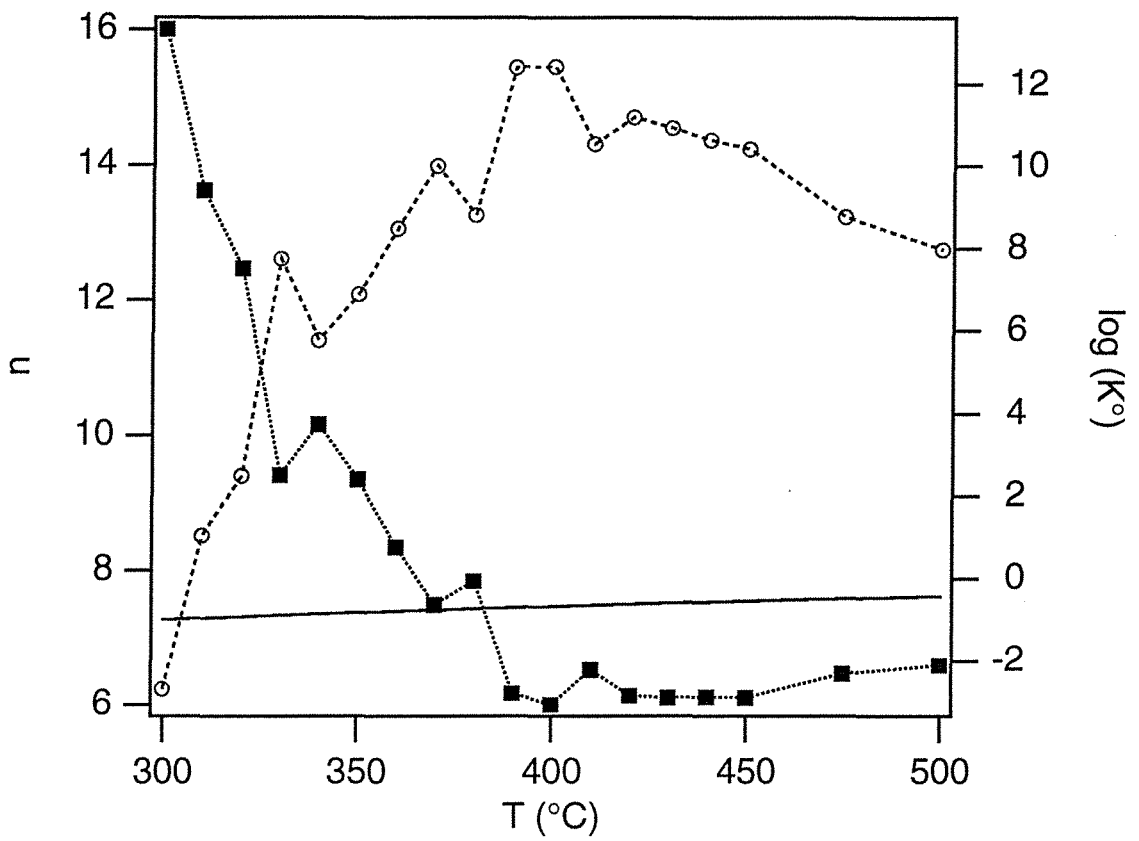


FIGURE 6

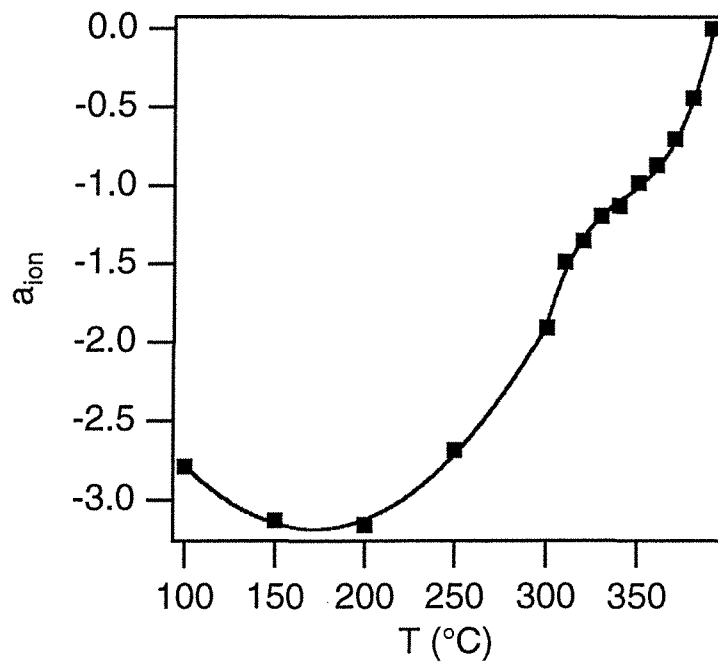


FIGURE 7

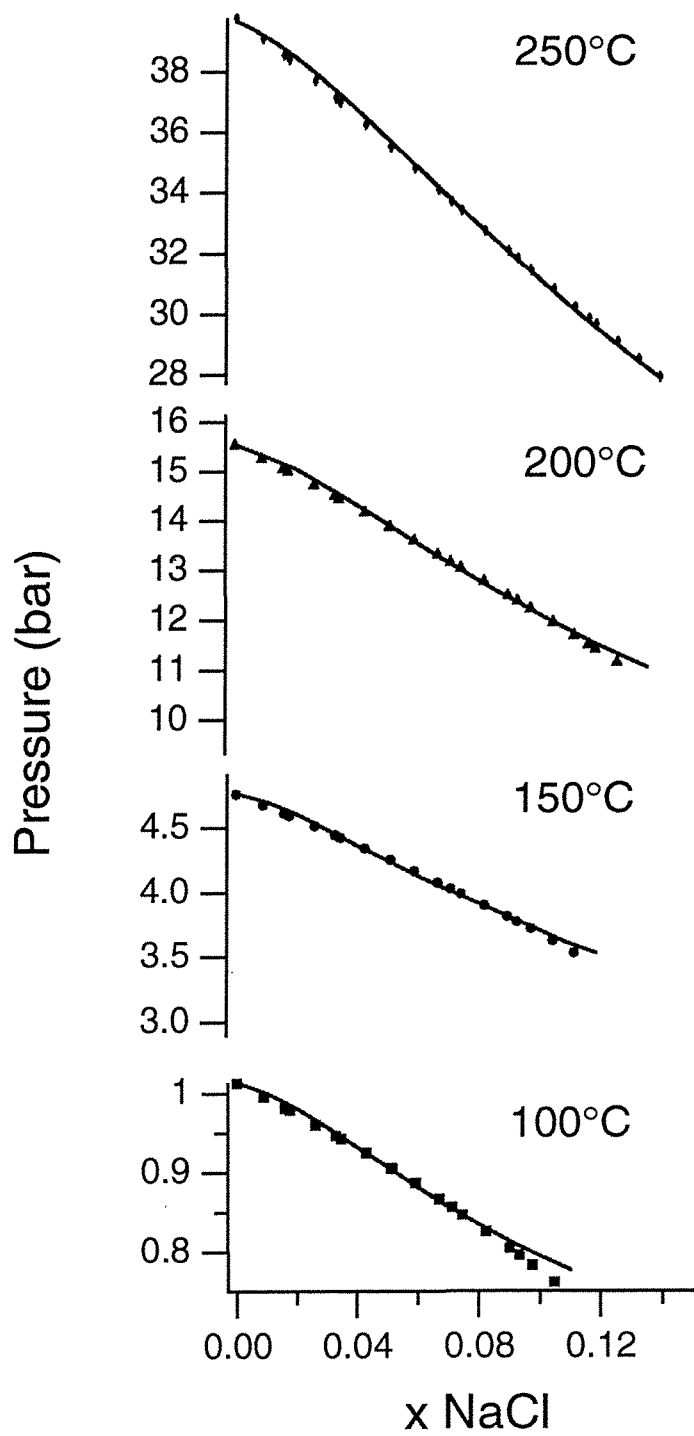


FIGURE 8

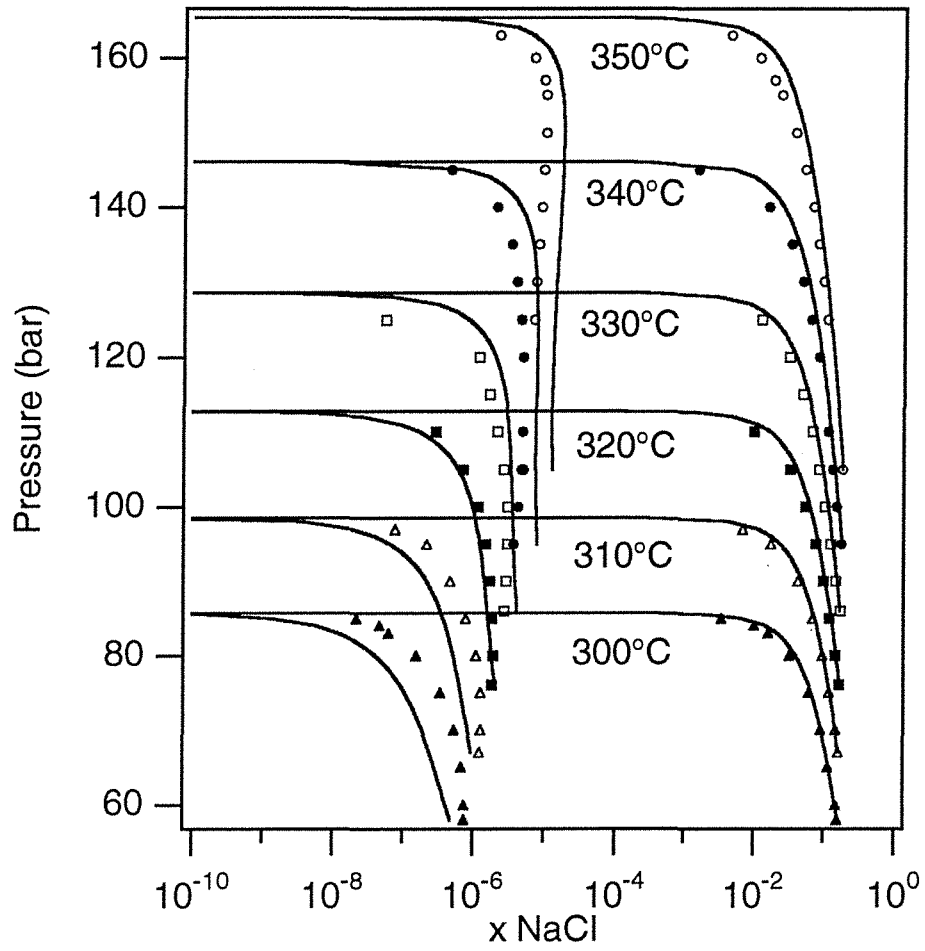


FIGURE 9

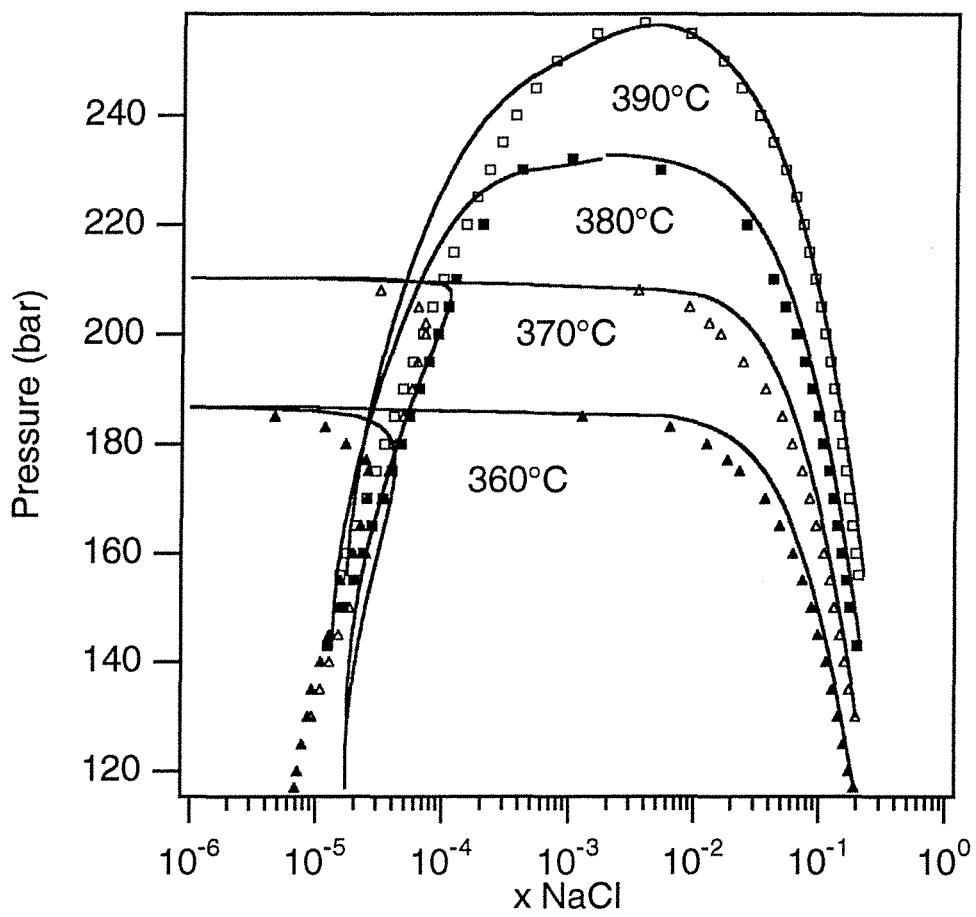


FIGURE 10

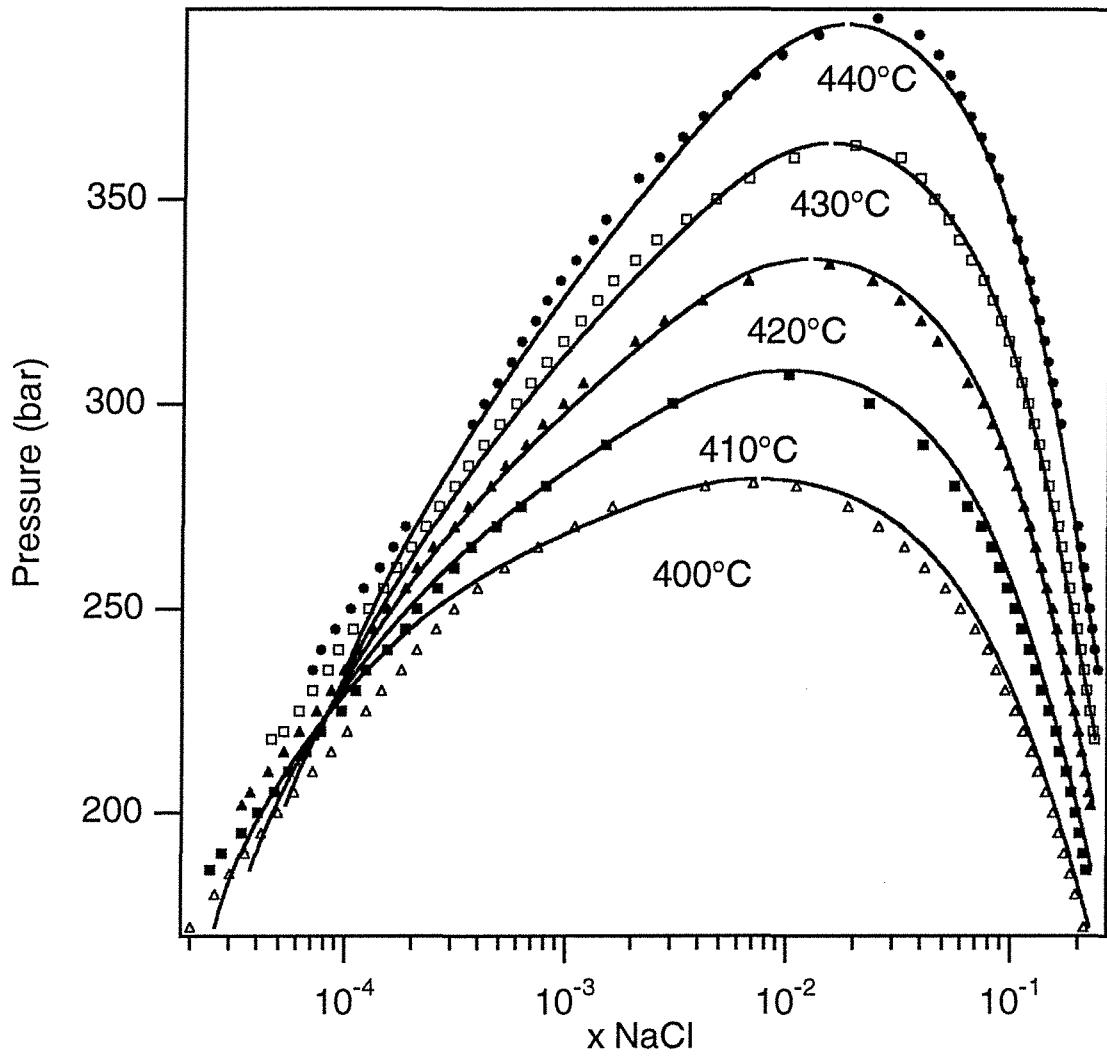


FIGURE 11

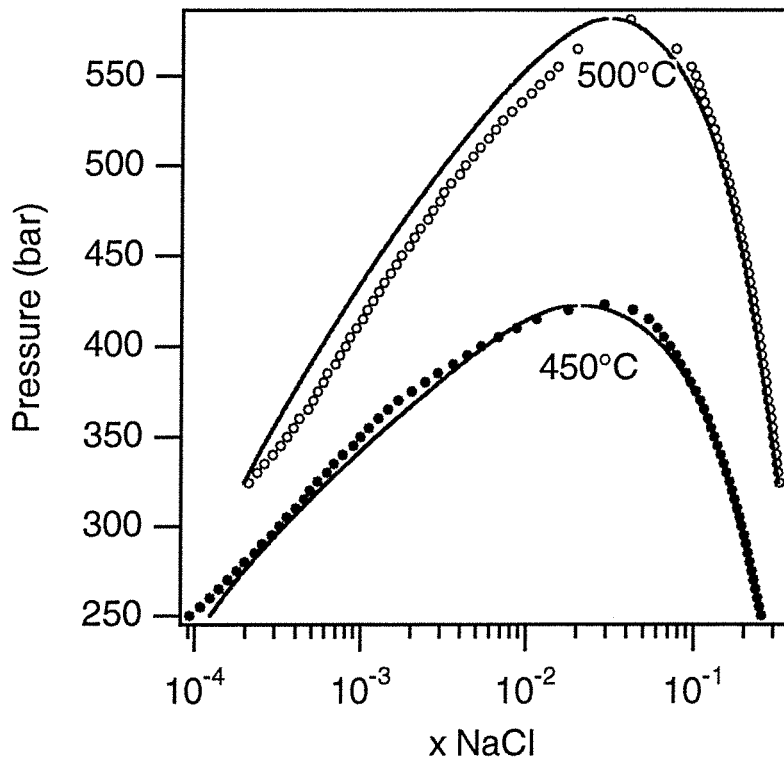


FIGURE 12

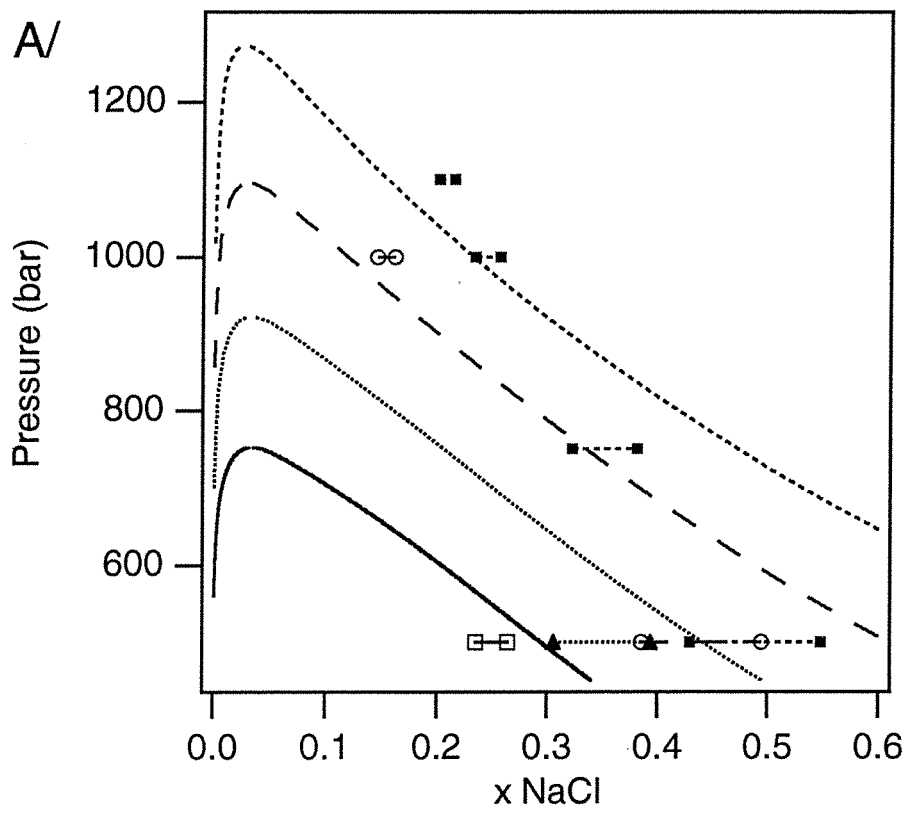


FIGURE 13A

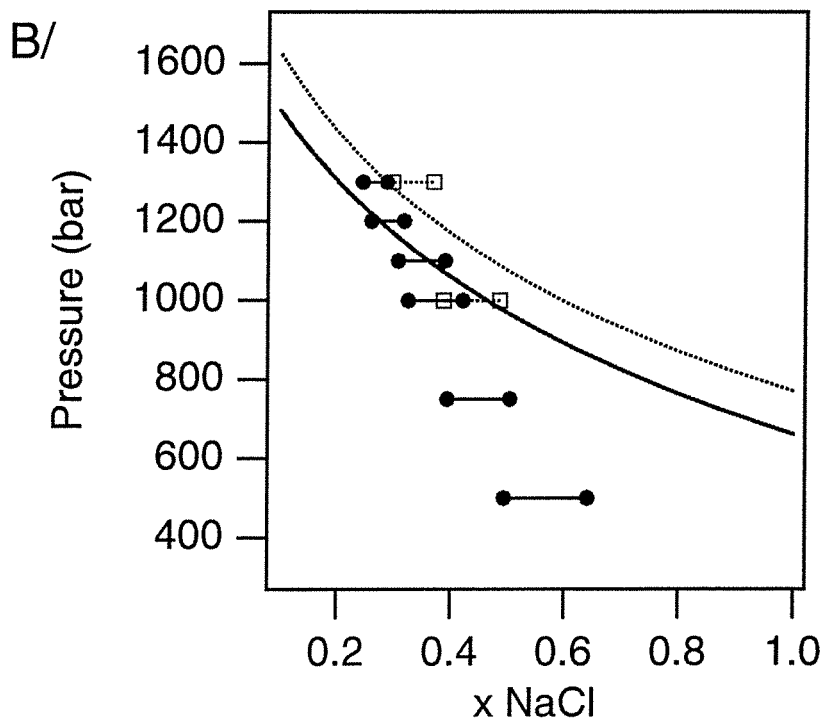


FIGURE 13B

CHAPITRE 5

Les hydrates de gaz.

Résumé

Les hydrates de gaz sont des composés solides composés d'eau et de gaz (méthane, dioxyde de carbone, azote, ...) se formant à basse température ($T < 30^{\circ}\text{C}$ en général) et sous de fortes pressions ($P > 1$ bar). De telles conditions se réalisent en particulier dans les inclusions fluides lors de leur étude par microthermométrie, et dans les sédiments des marges continentales. Le but de ce chapitre est de montrer l'intérêt de la modélisation thermodynamique des hydrates de gaz dans ces deux cas. Si de telles applications aussi concrètes et directes pour la géologie peuvent être abordées maintenant, c'est que la modélisation des hydrates de gaz a atteint un stade très avancé grâce au cadre théorique fourni par van der Waals et Platteeuw (1959). Van der Waals et Platteeuw (1959) ont en effet donné les bases théoriques solides, dérivées de la mécanique statistique et sur lesquelles sont construits les modèles thermodynamiques (Dubessy et al., 1992; Bakker et al., 1996) pouvant décrire les conditions de stabilité des hydrates de gaz dans les fluides naturels.

Le premier volet de ce chapitre concerne les hydrates de gaz dans les inclusions fluides. La température de dissociation des hydrates de gaz en l'absence de liquide hydrocarboné est fonction :

- de la salinité globale de l'inclusion (1),
- de la densité de la bulle de gaz (2),
- et de la fraction volumique de la bulle de gaz dans l'inclusion (3).

Une bonne connaissance des conditions de dissociation des hydrates de gaz grâce à la modélisation permet donc d'estimer les paramètres (1) et (2) cités ci-dessus.

Le deuxième volet de ce chapitre concerne les hydrates de gaz marins présents dans les sédiments de marge continentale, comme l'a confirmé le Leg ODP 164 (Ocean Drilling Program) sur le Blake Outer Ridge (à 700 km au large de la côte SW des Etats-Unis). Ce leg confirme également que la distribution des hydrates

de gaz est d'abord contrôlée par leurs conditions de stabilité. Les hydrates de gaz ne peuvent être présents que lorsque les conditions de température, pression sont favorables et lorsque le méthane est présent en quantité suffisante. De nombreuses données (températures in-situ, régime de pression, nature et composition des fluides interstitiels) ont été recueillies lors de ce leg, et leur interprétation nécessite l'utilisation de modèles thermodynamiques. Les principaux résultats (Thiéry et al., soumis) sont les suivants :

- l'analyse des anomalies en chlore dans les eaux interstitiels indique que les hydrates de gaz sont présents entre 190 et 450 mètres en dessous du fond de la mer à des concentrations moyennes comprises entre 1.5 et 3 % du volume total des sédiments.
- la nature du Bottom Simulating Reflector (BSR), un réflecteur souvent observé sur les profils sismiques des marges continentales, a été confirmée sur le Blake Outer Ridge. C'est un réflecteur provoqué par la présence de gaz libre situé juste en dessous des couches les plus profondes à hydrates de gaz.
- les hydrates de gaz se forment dans les pores interstitiels et réduisent la perméabilité des sédiments. Des fractionnements des différentes espèces chimiques (sels et gaz) entre les hydrates de gaz et les fluides interstitiels sont également observés. Les ions sont exclus des hydrates de gaz. Le méthane est incorporé préférentiellement par rapport au dioxyde de carbone dans les hydrates de gaz. Des surconcentrations locales en éthane et hydrocarbures lourds sont notées dans les couches sous-jacentes des zones riches en hydrates de gaz.

Références

Bakker, R.J., Dubessy, J., et Cathelineau, M. (1996) Improvements in clathrate modeling. I: the H₂O-CO₂ system with various salts. *Geochim. et Cosmochim. Acta*, **60**(10), 1657-1681.

Dubessy, J., Thiéry, R. et Canals, M. (1992) Modelling of phase equilibria involving mixed gas clathrates: application to the determination of molar volume of the vapour phase and salinity of the aqueous solution in fluid inclusions. *Eur. J. Min.*, **4**, 873-884.

Thiéry, R., Bakker, R., Monnin, C. and the Shipboard Scientific Party (ODP Leg 164) Geochemistry of gas hydrates and associated fluids in the sediments of a continental passive margin (The Blake Outer Ridge, Leg 164). (soumis à *Geochim. et Cosmochim. Acta*).

Van der Waals, J.H. and Platteuw, J.C. (1959) Clathrate solutions. In Prigogine, I. (ed.), *Advances in Chemical Physics*, Interscience, 1-57.

Modelling of phase equilibria involving mixed gas clathrates: Application to the determination of molar volume of the vapour phase and salinity of the aqueous solution in fluid inclusions

JEAN DUBESSY, RÉGIS THIERY and MARTIN CANALS

CREGU, GS-CNRS 77, BP 23, F-54501 Vandœuvre-lès-Nancy Cedex, France

Abstract: Modelling of clathrate stability in single component gases (CO₂, CH₄, N₂, H₂S and C₂H₆) and of mixtures in systems with or without NaCl is described, and then applied to fluid inclusions in which the dissociation of clathrate occurs in the presence of a vapour phase. The chemical potential of the water component in clathrate is calculated from a combination of the models of Parrish & Prausnitz (1972) and of Munck *et al.* (1988). The Langmuir constants have been recalculated to obtain the best fit of the available experimental data on single gas systems. The dependence of the activity of water on the salt concentration in the aqueous solution is described by the model of Pitzer. Pressure is calculated with an uncertainty of less than 10 % along the dissolution curve of clathrate for single component gas systems and gas mixtures. The bulk salinity, expressed in equivalent NaCl concentration, can be derived from the melting temperature of ice in presence of the assemblage clathrate + vapour phase + aqueous solution, but is shown to be a function of the volume fraction of the vapour phase. The fugacity coefficient of the gas components and the molar volume of the vapour phase are computed from the Soave equation of state.

Key-words: clathrate stability, thermodynamic properties, fluid inclusions, molar volume, salinity.

1. Introduction

To a first approximation, fluid inclusions are constant volume and mass systems, determination of their V–X properties is the first step in any quantitative interpretation of paleo-fluid circulation based on fluid inclusion studies. A combination of microthermometric and micro-Raman measurements allows fairly accurate estimations of the V–X properties of the non-aqueous volatile portions of fluid inclusions, except if a gas clathrate is present at the homogenization temperature of the volatile phase (Ramboz *et al.*, 1985; Seitz *et al.*, 1987; Dubessy *et al.*, 1989). Recently, experimental data (Diamond, 1992) and a combination of experimental data and modelling by Diamond (submitted) have been carried out in order

to achieve a better quantification of the salinity of fluid inclusions in the case of the homogenization of the carbonic phase in the presence of clathrate. However, the dissolution of clathrate in the presence of a vapour phase is often the only phase equilibrium which can yield information on the density of the vapour phase. Available experimental data on clathrate equilibria does not cover the whole range of compositions of natural fluid inclusions. Therefore, appropriate development of thermodynamic modelling of the stability of mixed gas clathrates (CO₂–CH₄–N₂–C₂H₆–H₂S) is essential (Seitz & Pasteris, 1990). The aim of this paper is to present the chosen model, to compare the model predictions with the experimental data and to discuss its application to fluid inclusions.

0935-1221/92/0004-0873 \$ 3.00

© 1992 E. Schweizerbart'sche Verlagsbuchhandlung, D-7000 Stuttgart 1

2. Symbols and constant values

- a_i^ϕ : activity of component i in phase ϕ
 aq: aqueous solution
 Cla: clathrate
 e : charge of the electron = $1.60219 \cdot 10^{-19}$ C
 g : vapour phase
 H : enthalpy
 k : Boltzmann constant = $1.38066 \cdot 10^{-23}$ (Joule K⁻¹)
 \ln : natural logarithm
 \log : decimal logarithm
 M_{wH_2O} : molecular weight of H₂O = 18 g·mol⁻¹
 M_{wNaCl} : molecular weight of NaCl = 58.5 g·mol⁻¹
 m_{NaCl} : NaCl molality
 N_A : Avogadro number = $6.022 \cdot 10^{23}$
 P : pressure in bar
 $P_{c,i}$ and $T_{c,i}$: critical pressure (bar) and temperature (°K) of gas component i
 $P_{r,i}$: reduced pressure ($P/P_{c,i}$) of gas component i
 R : perfect gas constant = 8.31441 (Joule °K⁻¹·mol⁻¹)
 T : temperature in ° Kelvin
 $T_{r,i}$: reduced temperature ($T/T_{c,i}$) of gas component i
 V_ϕ : volume fraction of phase ϕ
 v_ϕ : molar volume (cm³·mol⁻¹) of phase ϕ
 v_i^∞ : partial molar volume of gas i at infinite dilution in aqueous solution
 X_i^ϕ : mole fraction of component i in phase ϕ
 y_i : mole fraction of gas i in the vapour phase g
 Z : compressibility factor of the vapour phase g ;
 $Z = P \cdot v_g / (RT)$
 ϵ_0 : vacuum permittivity = $8.854188 \cdot 10^{-12}$ (Joule⁻¹ C² m⁻¹)
 ϵ_r : dielectric constant of pure water at 0 °C and 1 bar = 87.74
 Φ : practical osmotic coefficient
 ρ^{aq} : density of pure water at 1 bar and 0 °C = 1000 kg·m⁻³
 ρ_ϕ : density (g·cm⁻³) of phase ϕ
 $\mu_{H_2O}^\phi(P,T)$: chemical potential of H₂O in phase ϕ at T and P
 $\mu^{\circ H_2O}^\phi$: chemical potential of H₂O in phase ϕ at the reference state ($P^\circ = 1$ bar and $T^\circ = 273.15$ °K)
 γ_i : fugacity coefficient of gas species i
 γ_{sc}^* : Setchenow coefficient

3. Thermodynamic models for clathrates

The aqueous solution – clathrate – vapour phase assemblage at equilibrium is described by the following equation:

$$\mu_{H_2O}^{Cla}(P,T) = \mu_{H_2O}^{aq} \quad (1)$$

Therefore, the problem is reduced to the modeling of two chemical potentials. The chemical potential of water in the aqueous solution (section 3.1) is calculated as a function of the salinity, in terms of the NaCl molality, and of solubility of gases. This calculation is carried out by a combination of the model of Pitzer, to account for the NaCl content, and of Raoult's Law to account for the concentration of the dissolved gas in the aqueous solution. Calculation of the chemical potential of water in clathrate is based on a statistical thermodynamic model based on the pioneering work of Van der Waals & Platteuw (1959). The model is briefly outlined in section 3.2 with all the equations necessary for its practical use. However, readers are referred to Sloan (1990) for a comprehensive description of the theory.

3.1. Chemical potential of H₂O in aqueous solution

The chemical potential of water in aqueous solution, $\mu_{H_2O}^{aq}(P,T)$, is calculated from the activity of water. In salt-free aqueous solution, the activity of water is calculated from Raoult's Law taking into account the solubility of gases i using Henry's Law. Only CO₂ and H₂S will be considered here, since they are the most soluble gaseous species in water that lower the activity of water in the aqueous solution sufficiently enough to be measurable at the precision of microthermometric measurements.

$$a_{H_2O}^{aq} = 1 - [X_{CO_2}^{aq} + X_{H_2S}^{aq}] \quad (2)$$

$$X_i^{aq} = f(G)/K_{H,i}(P,T,0) \quad (3)$$

where $K_{H,i}(P, T, 0)$ is the Henry constant for the solubility of the gaseous species i in aqueous solution, at pressure P and temperature T , with a zero m_{NaCl} molality, and $f(i)$ is the gas fugacity calculated by the equation of state described below.

3.1.1. Henry constant

The equation of the Henry constant $K_{H,i}(1, T, 0)$ as a function of temperature is taken from Munck *et al.* (1988) based on the data and compilations of Wilhelm & Battino (1973) and Wilhelm *et al.* (1977):

$$\ln K_{H,i}(1, T, 0) = K_a + K_b/T + K_c \ln(T) + K_d T \quad (4)$$

where $K_a = 162.39$ (bar); $K_b = -8880.6$ (bar·K); $K_c = -22.014$ (bar/ln K); $K_d = 1.1201 \cdot 10^{-4}$ (bar·K⁻¹) for CO₂ and $K_a = 151.52$; $K_b = -8335.5$; $K_c = -20.499$; $K_d = -1.311 \cdot 10^{-3}$ for H₂S.

Theoretically, the Henry constant depends on pressure according to the following equation:

$$\ln K_{H,i}(P, T, 0) = \ln K_{H,i}(1, T, 0) + v_g^{\infty} (P-1) / (RT) \quad (5)$$

where v_g^{∞} is the partial molar volume of the dissolved gas at infinite dilution in the aqueous phase. For CO₂, $v_g^{\infty} = 33$ cm³·mol⁻¹ at 25 °C. For a maximum pressure of 50 bar, the second term of the right-hand-side of equation (5) is smaller than 0.05, resulting in negligible solubility variation. Therefore, the following approximation

$$\ln K_{H,i}(P, T, 0) = \ln K_{H,i}(1, T, 0) \quad (6)$$

is justified, as already used by several authors.

The dependence of the Henry constant on salinity is described by the empirical equation of Setchenow (Gerrard, 1980):

$$\ln \gamma_{sc}^* = \ln [K_{H,i}(P, T, m_{NaCl}) / K_{H,i}(P, T, 0)] = k_s \cdot m_{NaCl} \quad (7a)$$

where k_s is the salting out coefficient. As the temperature interval of interest is rather small in these calculations, the k_s value is considered to be constant and equal to its value at 0 °C for CO₂: 0.12 molal⁻¹ (Cramer, 1982).

For H₂S, the only available data are for temperatures higher than 25 °C (Drummond, 1981). The solubility data of Drummond (1981) in salt-free solution differs slightly from those of Wilhelm *et al.* (1977). Therefore, we have used the data of Drummond (1981) only for the calculation of the salt effect:

$$\begin{aligned} \ln [K_{H,H_2S}(P, T, m_{NaCl}) / K_{H,H_2S}(1, T, 0)] \\ = 0.294 \cdot m_{NaCl} - 0.0001595 \cdot m_{NaCl} \cdot T \\ - 46.81 \cdot m_{NaCl} / T - (578 + 0.0018 T) \\ \cdot m_{NaCl} / [m_{NaCl} + 1] \end{aligned} \quad (7b)$$

3.1.2. Water activity in salt-bearing aqueous solutions

For salt-bearing solutions, the model of Pitzer (1973) is used with fitted parameters between 0 and -40 °C (Thurmond & Brass, 1988), first to calculate the activity of water without gas. It is then multiplied by $\{1 - [X_{CO_2}^{aq} + X_{H_2S}^{aq}]\}$.

The water activity is calculated from the following equations:

$$\begin{aligned} \ln a_{H_2O}^{aq} &= -\Phi M_{wH_2O} (m_{Na} + m_{Cl}) / 1000 \\ &= -\phi M_{wH_2O} (2 m_{NaCl}) / 1000 \end{aligned} \quad (8)$$

where Φ is the practical osmotic coefficient calculated from equation (9)

$$\begin{aligned} \Phi - 1 &= -A_{\phi} m_{NaCl}^{1/2} / (1 + 1.2 m_{NaCl}^{1/2}) \\ &+ m_{NaCl} B_{\phi} + m_{NaCl}^2 C_{\phi} \end{aligned} \quad (9)$$

Detailed equations are given in Appendix 7.1 and values of all parameters (Thurmond & Brass, 1988) in Table 1.

3.1.3. Molar volume and fugacity coefficients of gas components

Four equations of state were checked on the P-v-T-X properties of CO₂ and CH₄: Soave (1972), Peng & Robinson (1976), Heyen (1982), Heyen *et al.* (1982) and Patel & Teja (1982). The sources of thermodynamic data are the IUPAC tables (CO₂: Angus *et al.*, 1976; CH₄: Angus *et al.*, 1978). The pressure and temperature ranges used to assess the quality of these equations is the following: P (from 1 to 50 bar for CO₂ and 1 to 400 bar for CH₄) and T (from 270 to 300 °K). The relative deviations of the calculated molar volume, at given P and T in the single phase field with respect to experimental data, show that the Soave as well as the Patel and Teja equations are the most accurate. The Soave equation was therefore chosen for all the present calculations. The formula of the Soave equation of state is the following:

$$P = \{RT / (v_g - b)\} - a(T) / \{v_g(v_g + b)\} \quad (10)$$

Table 1. Coefficients for the calculation of the osmotic coefficient from the model of Pitzer and the values of Thurmond & Brass (1988).

x_1	7.66249	x_2	$-1.00472 \cdot 10^3$	x_3	$-1.79001 \cdot 10^{-3}$
x_4	$1.15601 \cdot 10^{-5}$	x_5	$-1.90346 \cdot 10^{-8}$	x_6	2.57468·10
x_7	$-3.25771 \cdot 10^3$	x_8	$-6.58529 \cdot 10^{-3}$	x_9	$4.49459 \cdot 10^{-5}$
x_{10}	$-7.86640 \cdot 10^{-8}$	x_{11}	$-5.34139 \cdot 10^{-1}$	x_{12}	7.13101·10
x_{13}	$1.22262 \cdot 10^{-4}$	x_{14}	$-7.80262 \cdot 10^{-7}$	x_{15}	$1.27174 \cdot 10^{-9}$

Mixing rules are:

$$b_m = \sum y_i b_i \quad \text{and} \quad a_m(T) = \sum_i \sum_j y_i y_j a_{ij} \quad (11a)$$

$$\text{with } a_{ii} = a_i \text{ and } a_{ij} = (1 - \delta_{ij}) (a_i a_j)^{1/2} \quad (11b)$$

where δ_{ij} is an interaction parameter (Soave, 1972). All the equations required for the calculations are given in Appendix 7.2.

3.2. Chemical potential of H₂O in clathrate

The chemical potential of water in clathrate, $\mu_{\text{H}_2\text{O}}^{\text{Cla}}(P, T)$, is calculated using the model of Van der Waals & Platteuw (1959), established from statistical thermodynamics:

$$\mu_{\text{H}_2\text{O}}^{\text{Cla}}(P, T) = \mu^\beta(P, T) + RT \sum_i v_i \ln(1 - \sum_j \Theta_{j,i}) \quad (12)$$

where β refers to a hypothetical empty hydrate state, v_i is the number of cavities of type i , $\Theta_{j,i}$ is the fraction of type i cavity occupied by gas component j . All the clathrates of CO₂-CH₄-H₂S-C₂H₆ are of structure I and contain two small cavities and 6 large cavities for 46 H₂O molecules per unit cell (Davidson, 1973). Recent crystallographic data have demonstrated that the structure of the N₂ clathrate is of type-II (Davidson *et al.*, 1986). As the adjustments for a structure of type-I are valid for the pure N₂ system and the different gas mixtures, this structure was the only one considered, which simplifies the calculations. $\Theta_{j,i}$ depends on the fugacity of each gas component according to the equation established by the Langmuir adsorption theory:

$$\Theta_{j,i} = C_{j,i} \cdot f_j / (1 + \sum_k C_{k,i} \cdot f_k) \quad (13)$$

where $C_{j,i}$ is the Langmuir constant which accounts for the interaction between gas j and H₂O

molecules in the different cavities, and f_j is the fugacity of gas component j . Therefore, the calculation of the chemical potential of water requires an estimation of the Langmuir constants and $\mu^\beta(P, T)$ which is the chemical potential of the hypothetical empty clathrate lattice at P and T .

3.2.1. Calculation of $\mu^\beta(P, T)$

Munck *et al.* (1988) calculated $\mu^\beta(P, T)$ from the difference $\mu^\beta(P, T) - \mu_{\text{H}_2\text{O}}^{\text{aq}}(P, T)$ by integrating over P and T and using the corresponding differences in enthalpy, molar volume and constant pressure heat capacity at the reference state ($P^\circ = 1$ bar and $T^\circ = 273.15$) given in Table 2.

Table 2. Thermodynamic constants used for the calculation of $\mu^\beta(P, T) - \mu_{\text{H}_2\text{O}}(P, T)$ from Munck *et al.* (1988).

Property	Unit	Value
$\mu^\circ_\beta - \mu^\circ_{\text{aq}}$	J·mol ⁻¹	1264
$H^\circ_\beta - H^\circ_{\text{H}_2\text{O}}$	J·mol ⁻¹	-4858
$v^\circ_\beta - v^\circ_{\text{H}_2\text{O}}$	cm ³ ·mol ⁻¹	4.6
$Cp^\circ_\beta - Cp^\circ_{\text{H}_2\text{O}}$	J·mol ⁻¹ ·K ⁻¹	-39.16

3.2.2. Calculation of the Langmuir constants

The model of Parrish & Prausnitz (1972) is satisfactory for single gas clathrates but rather poor for some gas mixtures (Peng & Robinson, 1976). The model of Munck *et al.* (1988) is quite realistic for single gas systems and mixtures with $X(\text{CO}_2) < 0.5$: for pure CO₂ fluids, and a fixed pressure, the dissolution temperature of clathrate was shifted by 0.5 °C towards lower temperature values. The poor agreement of the model of Munck *et al.* (1988) for CO₂-rich fluids is probably due to their estimation of the Langmuir constants from the experimental data given by Berecz & Balla-Achs (1983). The experimental data of Deaton & Frost (1940), Unruh & Katz (1949), Robinson & Mehta (1971) and Bozzo *et al.* (1976) are mutually consistent but signifi-

cantly different from those of Berecz & Balla-Achs (1983). Therefore, we used the set of consistent experimental data to calculate the parameters of the Langmuir constant. The Langmuir constants are calculated from the following equation:

$$C_{j,i}(T) = 4\pi/kT \int \exp(-\omega_{j,i}(r)/kT) \cdot r^2 dr \quad (14)$$

where $\omega_{j,i}(r)$ is the cell potential of gas j in cavity i .

The cell potential can be calculated in two ways: (1) from the McKoy & Simanoglu (1963) formula, which assumes a Kihara potential $\Gamma_{j,i}(r)$ with a spherical core between water and gas molecules (appendix 3); Parrish & Prausnitz, 1972); or (2) assuming a square well potential $\Gamma(r)$ which simplifies the calculation of the integral in equation (14), thereby reducing equation (14) as follows:

$$C(T) = (A/T) \cdot \exp(B/T) \quad (15)$$

The first model was chosen because only three parameters (a , σ and ϵ) characteristic of the Kihara potential need to be determined and because the Langmuir constant is insensitive to variations of the a parameter. Values of the a , σ and ϵ parameters were obtained from a best-fit regression of the available experimental data (Table 3).

Table 3. a , σ and ϵ parameters of the Kihara potential used for the calculation of the Langmuir constants (appendix 7.3) and references of the experimental data.

	$a(\text{pm})$	$\sigma(\text{pm})$	$\epsilon/k(\text{K})$	References
CO ₂	70.3	295.8	170.00	(a), (b), (d)
CH ₄	30.0	327.0	152.00	(b), (c), (d)
N ₂	35.0	328.0	126.25	(c), (e)
C ₂ H ₆	40.0	344.0	175.0	(b)
H ₂ S	35.0	325	197.0	(f)

(a): Bozzo *et al.* (1975); (b): Deaton & Frost (1946); (c) Marshall *et al.* (1964); (d): Robinson & Mehta (1971); (e): van Cleeff & Diepen (1960); Selleck *et al.* (1952).

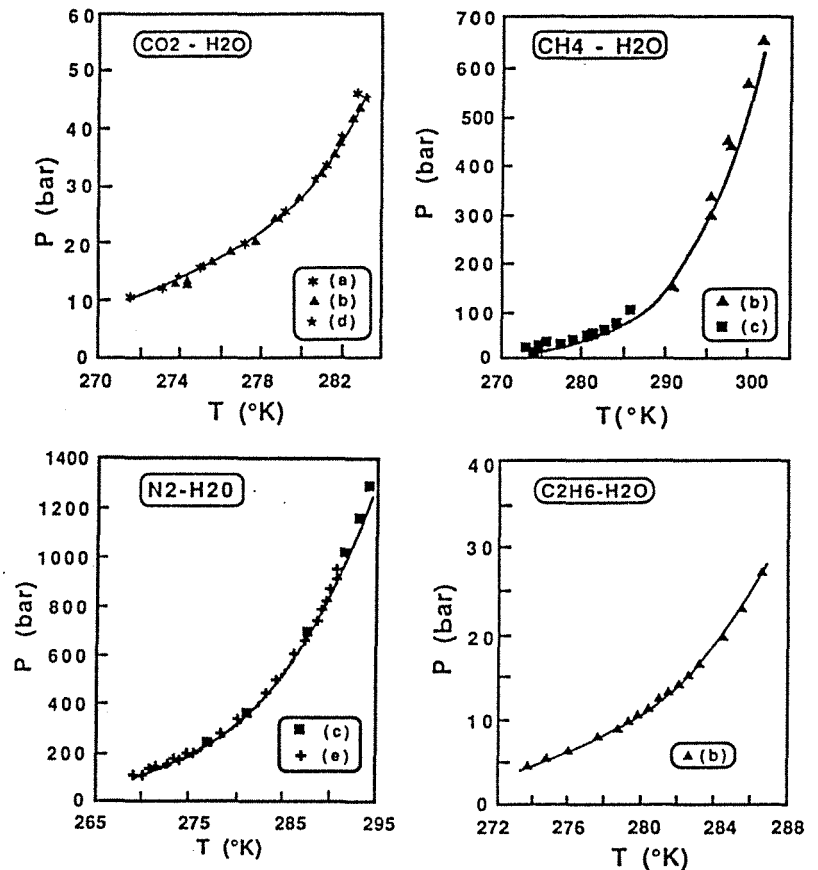


Fig. 1. Experimental and calculated pressure of pure gas clathrates versus temperature. References of experimental data are the same as those given in Table 3.

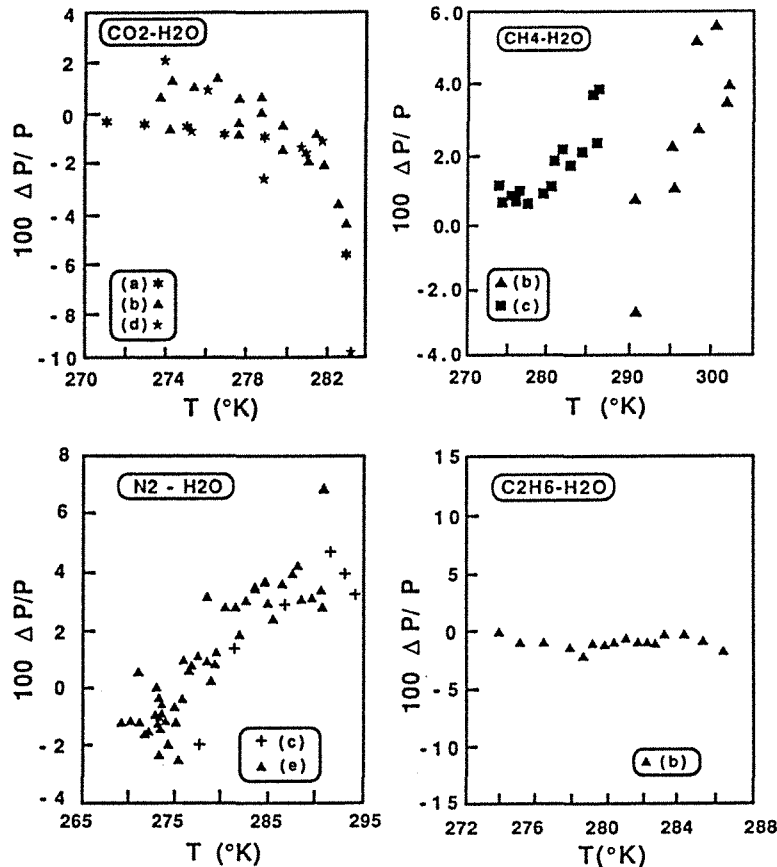


Fig. 2. Relative error $\{100 (P_{exp} - P_{calc}) / (P_{calc})\}$ versus temperature for pure gas clathrate systems. P_{exp} : experimental pressure; P_{calc} : calculated pressure from the model.

4. Results

4.1. Salt-free systems

Comparisons between experimental determinations of clathrate-gas-aqueous solution equilibria and the predictions of the present model are given in Figures 1 and 2. The relative deviation between experimental and calculated pressure at given temperature is always better than 6 %, which demonstrates the quality of the model and the adjusted parameters. Most of the calculated values show a smaller deviation. The relative deviation on pressure shows a trend with temperature except for CH_4 . Indeed, the experimental data of the CH_4 clathrate were obtained by three groups of experimentalists on different P-T interval ranges, and thus show some inconsistencies. Usually, authors check the validity of their clathrate models using the relative deviation of the dissociation temperature at a given pressure,

although temperature is a less sensitive parameter. The deviation in temperature is less than 0.3 K even for CO_2 .

The model has also been also checked for several binary mixtures: $\text{CH}_4\text{-CO}_2$ (Fig. 3); $\text{CH}_4\text{-C}_2\text{H}_6$; $\text{CH}_4\text{-N}_2$. The relative deviation of pressure is slightly greater than for the pure end-members and can reach 10 % on individual sets of experimental data. Even if the uncertainties in pressure are rather high, the model predictions are of the same quality as the model of John *et al.* (1985) and Munck *et al.* (1988).

4.2. The $\text{CO}_2\text{-H}_2\text{O-NaCl}$ system

The only available experimental data on a NaCl-bearing system are given by Bozzo *et al.* (1975). The relative uncertainty of the model predictions increases with the NaCl concentration, but remains always less than 10 % (Fig. 4).

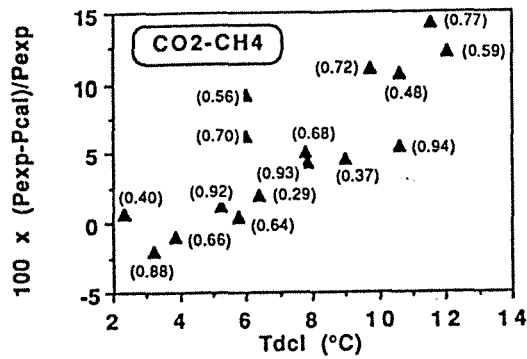


Fig. 3. Relative error $\{100 (P_{exp}-P_{calc})/P_{exp}\}$ versus temperature for the binary $\text{CO}_2\text{-CH}_4$ system. The mole fraction of CH_4 is given in parentheses. The experimental pressures are those of Unruh & Katz (1949).

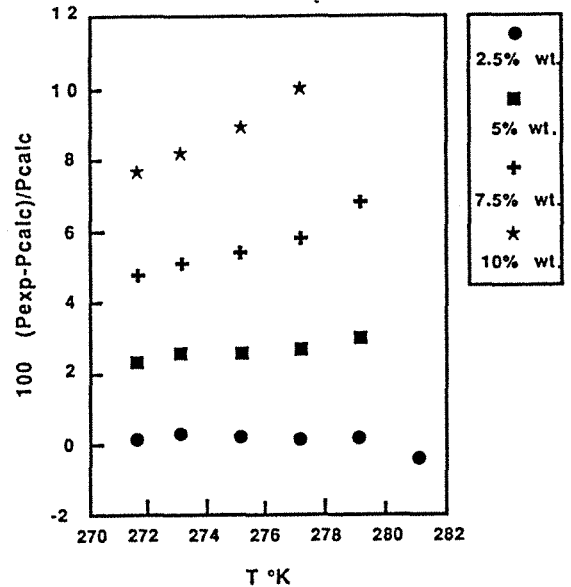


Fig. 4. Relative error $\{100 (P_{exp}-P_{calc})/P_{calc}\}$ versus temperature for the $\text{CO}_2\text{-H}_2\text{O-NaCl}$ system. The numbers indicate the NaCl concentration in weight %.

5. Application to fluid inclusions

5.1. Variance analysis

For the application of the clathrate model to fluid inclusions, the composition of the vapour phase is assumed to be known from Raman microspectrometric analysis. The water salinity, referred to the $\text{H}_2\text{O-NaCl}$ system, and the pressure of the vapour phase are the two unknowns which have to be determined from microthermometric measurements and the modelling of clathrate stability. At the melting temperature of ice, the phase assemblage is the following: ice - liquid water - clathrate - vapour phase. Since the temperature is known, the variance of the system is $v = c + 1 - 4 = c - 3$ where c is the number of independent components. For a fluid inclusion with only one gas component, $c = 3$ ($\text{H}_2\text{O-NaCl-Gas}$) and $v = 0$. Therefore, the composition of each phase is fixed. This implies that the salinity of the aqueous phase can be determined. If the system contains n gases, the variance of the system is increased by $n-1$ but, as analysis of the vapour phase yields $n-1$ mole fractions, the number of unknown variables remains zero. From the temperature of ice melting (T_{mIce}) to the temperature of clathrate dissolution (T_{dCla}), the clathrate releases water which lowers the salinity of the aqueous phase compared to its salinity at T_{mIce} . Thus, the salinity of the aqueous phase and the pressure of the vapour phase at T_{dCla} would be overestimated if the salinity were directly derived from T_{mIce} without taking into

account the trapping of water molecules by clathrate.

Cases are known to fractionate differently between the vapour phase and clathrate. Therefore, the composition of the vapour phase at T_{mIce} is not strictly equal to its composition at T_{dCla} . This point is addressed separately after the problem of salinity estimation.

5.2. Salinity calculation from T_{mIce}

The number of moles $N_{i(t)}$ of component i at T_{mIce} ($t=1$) and T_{dCla} ($t=2$) are given by the following equations:

For H_2O :

$$n_{\text{H}_2\text{O}(1)} = \rho_{\text{aq}(1)} \cdot V_{\text{aq}(1)} / \{M_{\text{WH}_2\text{O}}(1000 + M_{\text{WNaCl}} \cdot m_{\text{NaCl}(1)})\} + X_{\text{H}_2\text{O}(1)}^{\text{Cla}} \cdot V_{\text{Cla}(1)} / v_{\text{Cla}} \quad (16a)$$

where $X_{\text{H}_2\text{O}(1)}^{\text{Cla}}$ is the mole fraction of water molecules in clathrate at T_{mIce} .

$$n_{\text{H}_2\text{O}(2)} = \rho_{\text{aq}(2)} \cdot V_{\text{aq}(2)} / M_{\text{WH}_2\text{O}}(1000 + M_{\text{WNaCl}} \cdot m_{\text{NaCl}(2)}) \quad (16b)$$

$\rho_{\text{aq}(1)}$ and $\rho_{\text{aq}(2)}$ are calculated from the model of Potter & Brown (1977).

For NaCl:

$$n_{NaCl(1)} = \frac{\rho_{aq(1)} \cdot m_{NaCl(1)} \cdot V_{aq(1)}}{(1000 + M_{wNaCl} \cdot m_{NaCl(1)})} \quad (17a)$$

$$n_{NaCl(2)} = \frac{\rho_{aq(2)} \cdot m_{NaCl(2)} \cdot V_{aq(2)}}{(1000 + M_{wNaCl} \cdot m_{NaCl(2)})} \quad (17b)$$

For a gas component *i*, the mass balance equation involves the volume fraction of the vapour phase at *T_{mIce}* and *T_{dCla}*, which are respectively *V_{g(1)}* and *V_{g(2)}*:

$$n_{i(1)} = \frac{V_{g(1)}}{v_{g(1)}} + X_{i(1)}^{Cla} \cdot \frac{V_{Cla(1)}}{v_{Cla} + X_{i(1)}^{aq} \cdot (n_{H_2O(1)} + n_{NaCl(1)})} \quad (18a)$$

$$n_{i(2)} = \frac{V_{g(2)}}{v_{g(2)}} + X_{i(2)}^{aq} \cdot (n_{H_2O(2)} + n_{NaCl(2)}) \quad (18b)$$

where $X_{i(1)}^{Cla}$ is the mole fraction of gas component *i* in the clathrate at *T_{mIce}* and $X_{i(1)}^{aq}$ is the mole fraction of gas *i* in the aqueous solution at temperature (1).

The three equations of mass conservation of the type $n_{i(1)} = n_{i(2)}$ are written using equations (16a) to (18b). The unknowns are $n_{H_2O(2)}$, $n_{NaCl(2)}$ and $n_{i(2)}$. Other unknowns are $V_{g(1)}$, $V_{Cla(1)}$ and $m_{NaCl(2)}$. $V_{g(2)}$ is estimated optically under the microscope. $m_{NaCl(1)}$ is calculated from the melting ice temperature from the Pitzer model. $V_{g(1)}$,

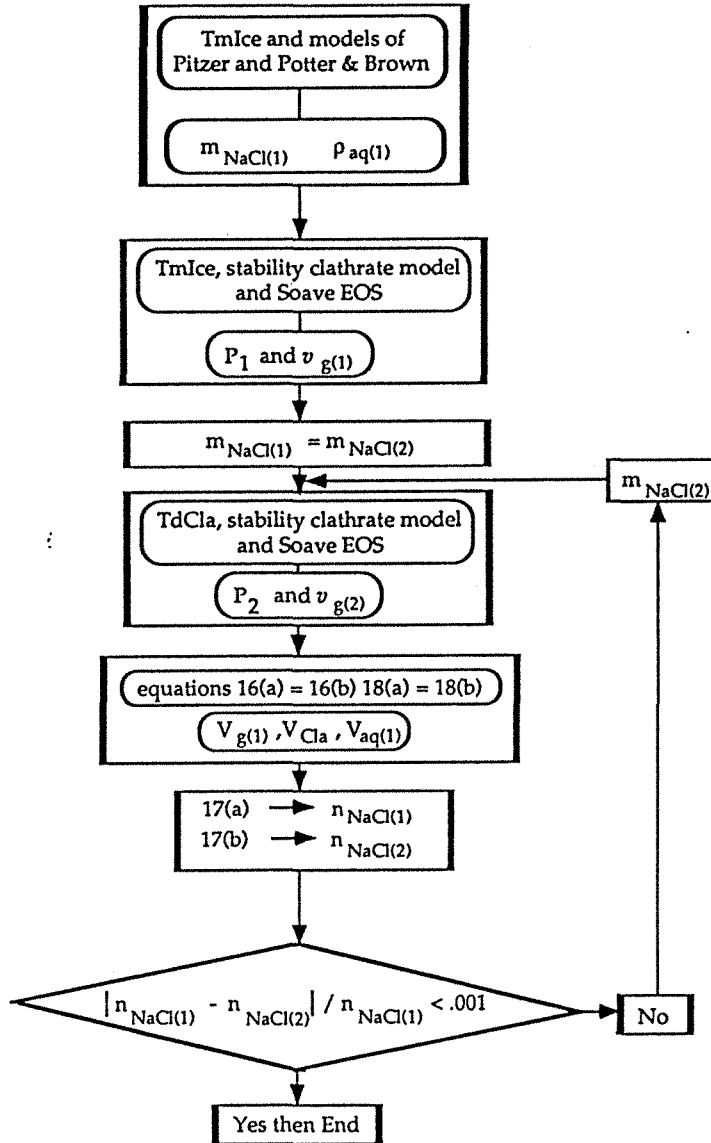


Fig. 5. Algorithm for the calculation of salinity from *T_{mIce}*, *T_{dCla}* and *V_{g(2)}*. EOS: equation of state.

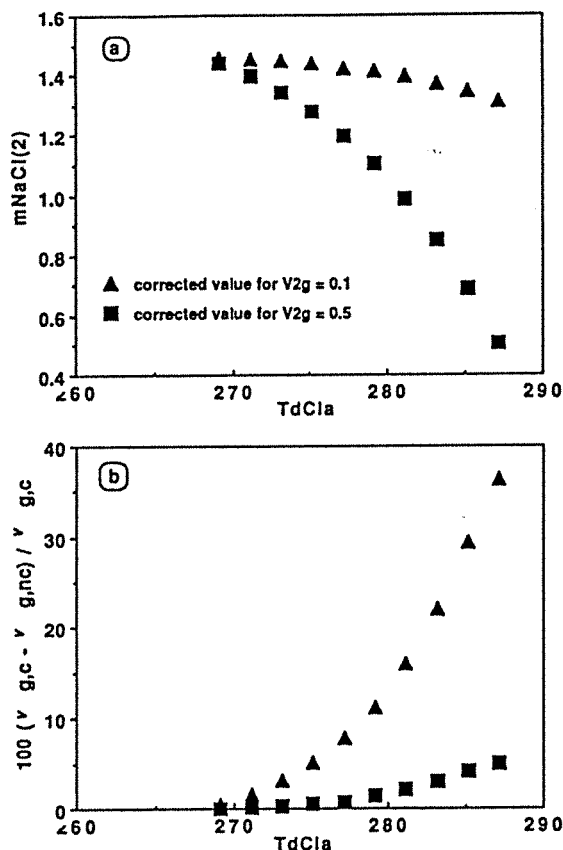


Fig. 6. Influence of the volume fraction of the vapour phase on the estimation of the correct salinity of the aqueous solution and the molar volume of the vapour phase. The vapour phase is assumed to contain only CH_4 . $T_{\text{mIce}} = -5^\circ\text{C}$. — a: variation of the NaCl molality of the aqueous solution versus T_{dCla} for two volume fractions of the vapour phase at T_{dCla} . b: relative error made on the molar volume of the vapour phase versus T_{dCla} if the salinity of the aqueous solution was directly derived from T_{mIce} . $v_{g,c}$: correct molar volume of the gas phase calculated at T_{dCla} for a salinity calculated iteratively by the procedure described in Figure 6; $v_{g,nc}$: uncorrected molar volume of the vapour phase if the salinity is derived from T_{mIce} and used for the calculation of the vapour pressure at T_{dCla} .

$V_{\text{Cl}(1)}$ and $m_{\text{NaCl}(2)}$ are calculated by trial and error, the molar volume of the vapour phase at T_{dCla} is calculated by the model from the pressure P_1 at T_{mIce} . The algorithm of this calculation is described in Appendix 7.4 and in Figure 5. Numerical results are strongly dependent on the

amount of vapour phase ($V_{g(2)}$) (Fig. 6a and 6b). For instance, $m_{\text{NaCl}(2)}$ is half of $m_{\text{NaCl}(1)}$ for $V_{g(2)} = 0.5$. Obviously, the greater is the difference $T_{\text{dCla}} - T_{\text{mIce}}$, the greater is $m_{\text{NaCl}(2)} - m_{\text{NaCl}(1)}$. In addition, the molar volume of the vapour phase is underestimated if the salinity at T_{dCla} is considered to be equal to $m_{\text{NaCl}(1)}$ instead of $m_{\text{NaCl}(2)}$ as calculated by the computer program. These calculations indicate that both the salinity and the vapour phase molar volume cannot be derived directly from T_{mIce} : $V_{g(2)}$ and T_{dCla} must be taken into account.

5.3. Influence of gas fractionation on salinity determination

The fractionation of the different gases between clathrate and vapour phase can be taken into account in the mass balance equations. The mass balance equations for H_2O and NaCl remain identical to equations (16) and (17). The modifications concerning the gas components i are:

$$n_{i(1)} = y_{i(1)} \cdot V_{g(1)} / v_{g(1)} + X_{i(1)}^{\text{Cl}} \cdot V_{\text{Cl}(1)} / v_{X\lambda\alpha} \\ X_{i(1)}^{\text{aq}} \cdot (n_{\text{H}_2\text{O}(1)} + n_{\text{NaCl}(1)}) \quad (19a)$$

$$n_{i(2)} = y_{i(2)} \cdot V_{g(2)} / v_{g(2)} \\ X_{i(2)}^{\text{aq}} \cdot (n_{\text{H}_2\text{O}(2)} + n_{\text{NaCl}(2)}) \quad (19b)$$

Calculations show that there is a negligible influence of gas fractionation between T_{mIce} and T_{dCla} on the estimation of salinity. Indeed, the molar volume $v_{g(1)}$ and $m_{\text{NaCl}(1)}$ are the only parameters affected by this effect. However, $m_{\text{NaCl}(1)}$ can be considered as constant since the variation of the activity coefficient of water does not vary significantly with pressure over an interval smaller than 10 bar, water being considered an incompressible fluid in the P - T interval of interest.

6. Conclusion

The model proposed in this paper predicts, with a satisfactory accuracy, the pressure of the vapour phase at the dissolution temperature of the gas clathrate in single component gas systems. The slightly larger uncertainty for gas mixtures is probably related to erratic variations in the quality of the experimental data. However, this model provides a good estimation of the molar volume of the vapour phase and salinity of the aqueous

solution using gas compositions determined by micro-Raman analysis and the microthermometry of phase equilibria involving gas clathrates. This resolves the problem of the determination of both the aqueous solution salinity and the vapour phase density in gas-bearing fluid inclusions, a difficult problem already pointed out by Ramboz *et al.* (1985) and Thomas & Spooner (1988). Such a model could also be used to derive the salinity of the aqueous solution in the case where clathrate dissolves in the presence of the CO₂-rich vapour and liquid phases, but this requires further research. Finally, this model may also be used to predict the behaviour of clathrates in natural environments, such as in permafrost in continental environments or in sediments (Makogon *et al.*, 1972; Kvenvolden, 1988; Sloan, 1990).

7. Appendices

7.1. Equations for the calculation of the osmotic coefficient (equation 9)

$$A\Theta = (2\pi N_A \rho_{aq}^0)^{1/2} \{e^2/(4\pi\epsilon_0\epsilon_r kT)\}^{1.5}$$

$$B\Theta = \beta^{(0)} + \beta^{(1)} \exp(-2 \cdot (m_{NaCl})^{1/2})$$

where $\beta^{(0)} = 2x_1 + 2x_2/T + x_3 T^2/6 + x_4 T^3/12 + x_5 T^4/20$

$$\beta^{(1)} = 2x_6 + 2x_7/T + x_8 T^2/6 + x_9 T^3/12 + x_{10} T^4/20$$

$$C\Theta/2 = 2x_{11} + 2x_{12}/T + x_{13} T^2/6 + x_{14} T^3/12 + x_{15} T^4/20$$

Values of x_i parameters are given in Table 1.

7.2. Equations related to the Soave equation of state (equations 10, and 11)

The $a_i(T)$ and b_i parameters for a gas i are calculated from the following equations:

$$a_i(T) = \{0.42747 (R T_{c,i})^2 / P_{c,i}\} \alpha_i(T)$$

with $\{\alpha_i(T)\}^{0.5} = 1 + F_i (1 - T_{r,i})^{0.5}$
and $F_i = 0.480 + 1.574 \omega_i - 0.176 \omega_i^2$
where ω_i is the acentric factor of gas species i calculated from the equation:
 $-1 - \omega_i = \log(P_{r,i})$ for $T_{r,i} = 0.7$ along the saturation curve.

$$b_i = 0.08664 R T_{c,i} / P_{c,i}$$

The fugacity γ_i coefficient of a pure component is calculated from the equation:

$$\ln(\gamma_i) = Z - 1 - \ln(Z - B_i) - A_i/B_i \ln\{(Z + B_i)/B_i\}$$

where $A_i = \alpha_i(T)P/(RT)^2$
 $= 0.42747 \alpha_i(T) P_{r,i}/\{T_{r,i}\}^2$
and $B_i = b_i P/RT = 0.08664 P_{r,i}/T_{r,i}$

The fugacity coefficient of the gas species i in a mixture is calculated from the equation:

$$\ln(\gamma_i) = (b_i/b_m)(Z-1) - \ln(Z-B_m) - A_m/B_m \{2(a_i/a_m)^{0.5} - (b_i/b_m)\} \ln(1+B_m/Z)$$

where $A_m = 0.42747 P/T^2 \{\sum y_i T_{c,i} a_i^{0.5}/P_{c,i}^{0.5}\}^2$
and $B_m = 0.08664 P/T \{\sum y_i T_{c,i}/P_{c,i}\}$

7.3. Derivation of the spherically symmetric cell potential $\omega(r)$ for equation (14)

The Kihara potential used by Parrish & Prausnitz (1972) and in this work, describes the interaction between the gas molecule inside its cavity and an H₂O molecule of the wall. It is defined by the following equations:

$$\Gamma(r) = \infty, r \leq 2a$$

$$\Gamma(r) = 4 \epsilon \{[\sigma/(r-2a)]^{12} - [\sigma/(r-2a)]^6\}$$

where ϵ is the characteristic energy,
 a is the core radius and $\sigma+2$ the collision parameter.

Summing over all the gas-H₂O interactions in the cell, Parrish & Prausnitz (1972) give the cell potential $\omega(r)$ (McKoy & Simanoglu, 1963):

$$\omega(r) = 2z\epsilon \{ \sigma^{12} (\delta^{10} + a/[R\delta^{11}]) / R^{11} r - \sigma^6 (\delta^4 + a/[R\delta^2]) / R^5 r \}$$

where $\delta^N = \{(1 - r/R - a/R)^{-N} - (1 + r/R - a/R)^{-N}\} / N$
with z , the coordination number in cavities (20 and 24), $2R$, the cell diameter (7.95 and 8.60 Å)

7.4. Algorithm for the calculation of salinity as a function of T_{mIce} , T_{dCl} , $V_{2,g}$

Step 1: the salinity of the aqueous solution at T_{mIce} is calculated from the model of Pitzer; the density of the aqueous solution is calculated from the equation of Potter & Brown (1977). Step 2: $v_{g(1)}$ is calculated at T_{mIce} from the pressure P_1 calculated by the model. Step 3: calculation of pressure P_2 and $v_{g(2)}$ at T_{dCl} . Step (4): calculation of $V_{g(1)}$, $V_{Cl(1)}$ and $V_{aq(1)}$ from mass balance equations on water and gas. Step (5): $n_{NaCl(1)}$ and $n_{NaCl(2)}$ are derived from equations (17a) and

(17b). Step 6: the convergence of the calculation is checked.

Acknowledgements: The authors thank D. Banks, L.W. Diamond and B. Yardley for their helpful reviews of the manuscript.

References

- Angus, S., Armstrong, B., De Reuck, K. M. (eds.) (1976): International thermodynamic Tables of the Fluid State. Carbon Dioxide. Pergamon Press, 385 p.
- (eds.) (1978): International thermodynamic Tables of the Fluid State. 5. Methane. Pergamon Press, 251 p.
- Berecz, E. & Balla-Achs, M. (1983): Gas hydrates. Studies in Inorganic Chemistry 4. Elsevier, 343 p.
- Bozzo, A. T., Chen, H. S., Kass, J. R., Barduhn, A. J. (1975): The properties of the hydrates of chlorine and carbon dioxide. *Desalination*, 16, 303-320.
- Cramer, S. D. (1982): The solubility of methane, carbon dioxide, and oxygen in brines from 0 to 300 °C. *U.S. Bur. Mines, Rep. of investigations* 8706, 14 p.
- Davidson, D. W. (1973): Clathrate hydrates. In Franks, F. (ed.), *Water: A comprehensive treatise*. Plenum Press, 2, 115-234.
- Davidson, D. W., Handa, Y. P., Ratcliffe, C. I., Ripmeester, J. A., Tse, J. S., Dahn, J. R., Lee, F., Calvert, L. D. (1986): Crystallographic studies of clathrate hydrates. Part I. *Mol. Cryst. Liq. Cryst.*, 141, 141-149.
- Deaton, W. M. & Frost, E. M. Jr. (1948): Gas hydrate and their relation to the operation of natural gas pipe lines. *U.S. Bur. Mines, Monogr.*, 8, 103 p.
- Diamond, L. W. (1992): Stability of CO₂ clathrate hydrate + CO₂ liquid + CO₂ vapour + aqueous KCl-NaCl solutions: Experimental determination and application to salinity estimates of fluid inclusions. *Geochim. Cosmochim. Acta*, 56, 273-280.
- (submitted): Salinity of multi-volatile fluid inclusions determined from gas-clathrate-hydrate stability. *Geochim. Cosmochim. Acta*.
- Drummond, S. E. (1981): Boiling and mixing of hydrothermal fluids: chemical effects on mineral precipitation. Unpub. PhD. Thesis, The Pennsylvania State University, 380 p.
- Dubessy, J., Poty, B., Ramboz, C. (1989): Advances in C-O-H-N-S fluid geochemistry based on Raman analysis of fluid inclusions. *Eur. J. Mineral.*, 1, 517-534.
- Gerrard, W. (1980): Gas solubilities. Widespread applications. Pergamon Press, 497 p.
- Heyen, G. (1982): Contribution à l'étude de la thermodynamique des systèmes non idéaux sous pressions élevées. Unpub. thesis, Liège Univ., 233 p.
- Heyen, G., Ramboz, C., Dubessy, J. (1982): Simulation des équilibres de phases dans le système CO₂-CH₄ en-dessous de 50 °C et de 100 bars. *C.R. Acad. Sci. Paris*, 294, 203-206.
- Holder, G. D. & Grigoriou, G. C. (1980): Hydrate dissociation pressures of methane + ethane + water. Existence of a locus of minimum pressures. *J. Chem. Thermodynamics*, A-150, 1093-1104.
- Jhaveri, J. & Robinson, D. B. (1965): Hydrates in the methane-nitrogen system. *Can. J. Chem. Eng.*, 43, 75-78.
- John, V. T., Papadopoulos, K. D., Holder, G. D. (1985): A generalized model for predicting equilibrium conditions for gas hydrates. *AIChE J.*, 31, 252-259.
- Kvenvolden, K. A. (1988): Methane hydrate - A major reservoir of carbon in the shallow geosphere? *Chem. Geol.*, 71, 41-51.
- Makogon, Yu. F., Trebin F. A., Trofimuk, A. A., Tsarev, V. P., Cherskiy, N. V. (1972): Detection of a pool of natural gas in solid (hydrated gas) state. *Dokl. Acad. Sci. USSR, Earth Sci. Sect.*, 196, 197-200.
- Marshall, D. R., Saito, S., Kobayashi, R. (1964): Hydrates at high pressures: Part I. Methane-water, argon-water and nitrogen-water systems. *AIChE J.*, 10, 202-205.
- McKoy, V. & Simanoglu, O. (1963): Theory of dissociation pressures of some gas hydrates. *J. Chem. Phys.*, 38, 2946-2956.
- Munck, J., Skold-Jorgensen, S., Rasmussen, P. (1988): Computations of formation of gas hydrates. *Chem. Eng. Sci.*, 43, 2661-2672.
- Parrish, W. R. & Prausnitz, J. M. (1972): Dissociation pressures of gas hydrates formed by gas mixtures. *Ind. Eng. Chem. Process. Develop.*, 11, 26-34.
- Patel, C. & Teja, A. S. (1982): A new cubic equation of state for fluids and fluid mixtures. *Chem. Eng. Sci.*, 37, 463-473.
- Peng, D. Y. & Robinson, D. B. (1976): A new two constants equation of state. *Ind. Eng. Chem. Fundam.*, 15, 59-64.
- Pitzer, K. S. (1973): Thermodynamics of electrolytes. I. Theoretical basis and general equations. *J. Phys. Chem.*, 77, 268-277.
- Potter, R. W. & Brown, D. L. (1977): The volumetric properties of aqueous sodium chloride solutions from 0° to 500 °C and pressures up to 2000 bars based on a regression of available data in the literature. *U.S. Geo Surv. Bull.*, 1421C, 36 p.
- Ramboz, C., Schnapper, D., Dubessy, J. (1985): The P-V-T-X-fO₂ evolution of H₂O-CO₂-CH₄ bearing fluid in a wolframite vein: reconstruction from fluid inclusion studies. *Geochim. Cosmochim. Acta*, 49, 205-219.
- Robinson, D. B. & Mehta, B. R. (1971): Hydrates in the propane-carbon dioxide-water system. *J. Can. Petr. Tech.*, 10, 33-35.
- Seitz, J. C. & Pasteris, J. D. (1990): Theoretical and practical aspects of differential partitioning of gases by clathrate hydrates in fluid inclusions. *Geochim. Cosmochim. Acta*, 54, 631-639.
- Seitz, J. C., Pasteris, J. D., Wopenka, B. (1987): Characterization of CO₂-CH₄-H₂O fluid inclusions by microthermometry and laser Raman microprobe spec-

- troscopy: inferences for clathrate and fluid equilibria. *Geochim. Cosmochim. Acta*, **51**, 1990.
- Selleck, F. T., Carmichael, L. T., Sage, B. H. (1952): Phase behavior in the hydrogen sulfide - water system. *Ind. Eng. Chem.*, **44**, 2219-2226.
- Sloan, E. D. Jr. (1990): Clathrate hydrates of natural gases. Marcel Dekker, 641 p.
- Soave, G. (1972): Equilibrium constants from a modified Redlich-Kwong equation of state. *Chem. Eng. Sci.*, **27**, 1197-1203.
- Thomas, A. V. & Spooner, E. T. C. (1988): Fluid inclusions in the system $H_2O-CH_4-NaCl-CO_2$ from metasomatic tourmaline within the border unit of the Tanco zoned granitic pegmatites, S.E. Manitoba. *Geochim. Cosmochim. Acta*, **52**, 1065-1075.
- Thurmond, V. L. & Brass, G. W. (1988): Activity and osmotic coefficients of NaCl in concentrated solutions from 0 to -40 °C. *J. Chem. Eng. Data*, **33**, 411-414.
- Unruh, C. H. & Katz, D. L. (1949): Gas hydrates of carbon dioxide-methane mixtures. *J. Petrol. Technol.*, **1**, 83-86.
- Van Cleeff, A. & Diepen, G. A. M. (1960): Gas hydrates of nitrogen and oxygen. *Rec. Trav. Chim.*, **79**, 582-586.
- Van der Waals, J. H. & Platteuw, J. C. (1959): Clathrate solutions. In Prigogine, I. (ed.), *Advances in Chemical Physics*. Interscience, 1-57.
- Wilhelm, E. & Battino, R. (1973): Thermodynamic functions of the solubility of gases in liquids at 25 °C. *Chem. Rev.*, **73**, 1-9.
- Wilhelm, E., Battino, R., Wilcock, R. J. (1977): Low-pressure solubility of gases in liquid water. *Chem. Rev.*, **77**, 219-262.

Accepted 6 February 1992

Geochemistry of gas hydrates and associated fluids in the sediments of a continental passive margin (The Blake Outer Ridge, Leg 164)

Régis THIÉRY*, Ronald BAKKER**, Christophe MONNIN***
and the Shipboard Scientific Party (ODP Leg 164).

* CREGU, Centre de Recherches sur la Géologie des Matières Premières et Minérales.
BP 23, 54 501 Vandoeuvre-les-Nancy, FRANCE.

** Geologisch-Paläontologisches Institut, University Heidelberg, im Neuenheimer Feld 234,
D-69120, Heidelberg, ALLEMAGNE.

*** Laboratoire de Géochimie, 38, rue des Trente-Six Ponts, 31 062 Toulouse, FRANCE.

(submitted to *Geochimica et Cosmochimica Acta*)

ABSTRACT:

Extensive sampling of in-situ gas hydrates and associated fluids have been carried out in the marine sediments of a continental passive margin (the Blake Outer Ridge) during the ODP Leg 164. Shipboard analyses of gases and interstitial waters have been interpreted with the help of thermodynamic models for gas hydrates and aqueous solutions. Gas hydrates are located between 190 and 450 mbsf (meters below the sea floor) throughout the sedimentary column with a mean concentration amount between 1.0 and 3 % of the bulk volume of the sediments. The Bottom Simulating Reflector (BSR) is shown to be an interface between gas hydrates and underlying zones rich in free gas. Gas hydrates reduce the permeability of sediments and fractionation of chemical species (salts, methane, carbon dioxide, ...) occurs between gas hydrates and associated fluids.

INTRODUCTION

Gas hydrates are crystalline compounds composed of water and low-molecular weight gases. Natural gas hydrates can form only under conditions of low temperature, high pressures and when sufficient amounts of gases are present. As a consequence, gas hydrates are not stable on the surface of the earth; and for a long time, gas hydrates were considered only as a scientific curiosity. Gas hydrates have regained new interest in the last decade, when it was realized that they can be present in large amounts in the permafrost and in the sediments of continental margins (CLAYPOOL and KAPLAN, 1974; SLOAN, 1989). About 10000 Gt of carbon could be stored in the gas hydrates of marine sediments (KVENVOLDEN, 1988b). This represents two times the estimate for the carbon in all other fossil fuel deposits. Natural gas hydrates trap a lot of methane, and are considered to be a potential source of energy for the future. Gas hydrates could have played too an important role in the past climatical changes. A lowering of the sealevel during a glaciation could cause the dissociation of a small fraction of the gas hydrates trapped in the marine sediments. Large amounts of methane, a greenhouse gas, would then be released in the atmosphere, and this would lead to a global warming of the earth. However, present estimates of marine gas hydrates are not reliable enough and need to be confirmed (KVENVOLDEN, 1988b). A good assessment of the amount and distribution of methane gas hydrates would be important too, if their economic recovery and exploitation should be undertaken one day. It is therefore important to control on natural case studies if thermodynamic models are able to predict the distribution of gas hydrates. Another important question related to gas hydrates is the signification of a reflector, that is commonly observed in seismic profiles of continental margins. This reflector mimics the topography of the seabottom, and thus it has been called the "Bottom-Simulating Reflector" (BSR). This reflector is believed to be caused by the high acoustic impedance contrast between a high-velocity gas hydrate-rich layer overlying a low-velocity free gas-rich layer (MINSHULL and WHITE, 1989; HYNDMAN and SPENCE, 1992; SINGH et al., 1993; KATZMAN et al., 1994). Thus, BSRs should correspond to the base of the gas hydrate stability (BGHS). If this interpretation is valid, the BSR would be a

useful indicator of gas hydrates and could be used for estimating local temperature gradients. In particular, the BSRs have been used by KVENVOLDEN (1988b) for estimating the amount of marine gas hydrates in the world. Again, too little is known to be confident about this interpretation, and it was necessary to drill through a BSR. But, up to now, drilling of BSRs were avoided due to safety considerations.

The formation of gas hydrates should modify clearly the geochemistry of fluids in the sediments. Indeed, salts are excluded in gas hydrates, and thus, more saline fluids are produced with formation of gas hydrates. Secondly, gas hydrates are solid phases that should probably cement the sediments. Therefore, the porosity and permeability should be reduced, limiting the migration of the fluids. In particular, the gas hydrate-rich zone may act as a barrier zone. However, these effects are not well known, and only the drilling and sampling of fluids in gas hydrates-rich zones could address more accurately these effects. Analyses procedures are first reviewed. Then, the nature of fluids, the amount and distribution of gas hydrates are investigated. And finally, the signification of the BSR is addressed.

GEOLOGICAL SETTINGS

ODP Leg 164 was devoted to the drilling of a gas hydrate-rich field in the Blake Outer Ridge (Fig. 1). Three holes along a transect were drilled up to 750 m depths (Sites 994, 995, and 997). Site 997 lies on the topographic crest of the Blake Ridge. Sites 994 and 995 are located at a few kilometers away (7 and 10 km respectively) from the 997 Site in the SSW direction. The BSR in this region is about 400-450 m below the sea floor. Thus, these holes extend well below the depths of the stability zone of gas hydrates. Sites 995 and 997 are characterized by a strong BSR, whereas no BSR is visible on the seismic records of Site 994. Two diapirs (Sites 991, 992, 993 and 996) have been investigated too by a series of shorter holes (50 m) in order to study the effects of diapiric intrusions into gas hydrate-rich zones. These sites will be considered in another study. The sediments in the upper few hundreds meters of the Blake Outer Ridge are very homogenous and consist primarily of nannofossil-rich clays. They are the result of a rapid detrital accumulation during the late Tertiary and Quaternary periods. Sedimentation rates were estimated from nannofossil zonations, and a

decrease from 260 m/m.y. at the late Miocene to 60 m/m.y. at the Quaternary has been estimated. Therefore, the Blake Outer Ridge constitutes an ideal region in order to investigate the geochemistry of gas hydrates and associated fluids in a passive margin.

ANALYTICAL PROCEDURES

Extensive sampling and analyses of gases and interstitial waters have been carried out on shipboard. Sampling was done on each core that is recovered. Gases are first collected using two different procedures, which are referred to as "headspace" and "free gas". In the technique of headspace sampling, 5 cm³ of sediments are sampled on the ship with a calibrated cork borer and sealed in small bottles. Samples are then heated to 60°C during 30 minutes. The heating process allows to extract residual gases that are trapped in the sediment. Headspace sampling has been done extensively for each core, i.e. at distances of about 9.5 meters. The free gas technique can be used only when sediments are gassy, i.e. pockets of free gases are then present in the core. Free gases are collected by piercing the plastic bag around the core with a special syringe. The gases collected by both techniques are then analyzed by gas chromatography. Air contamination is inevitable in both methods and must be taken into account for the interpretation of measured values.

A few number of gas hydrates could be sampled before they dissociate completely. They were placed in a plastic bag closed hermetically. After thermal equilibrium and decomposition, gases are collected by piercing the bag and analyzed on the gas chromatograph. A dissociation chamber as described by KVENVOLDEN and BARNARD (1983b) is used in order to measure the gas/water ratio of gas hydrates.

Interstitial waters are collected from a whole round sample of 30 cm³. In order to reduce the effects of contamination, all sides of the sediment are trimmed. The sample is then placed in a titanium sleeve and squeezed in the hydraulic press. The interstitial water is extruded in a large syringe by compressing the sample. After filtering, the water is analyzed for alkalinity, refractive index, and composition by ionic chromatography and atomic absorption spectroscopy. Seawater contamination of interstitial water samples is not uncommon. Thus, concentration of dissolved species must be corrected. This is done for samples that are below

the sulfate reduction zone by assuming that all SO_4^{2-} ions come from seawater. Thus, SO_4^{2-} were then used for estimating the degree of seawater contamination and for correcting the measured electrolyte composition of interstitial waters. Sediment samples were taken for index properties studies (density, water content, porosity). These parameters are deduced by measuring the weight before and after drying samples for 24 hours in an oven at 100°C .

Finally, a special and useful device, called the Pressure Core Sampler (PCS) has been used with success on this leg. The PCS allows to return a short pressurized core from the bottom of the hole, so that no gases are lost during the recovery (KVENVOLDEN et al., 1983). Sampling from the PCS give information on the in-situ water and gases content of the sediments. Pressures, that were measured in successful PCS, are close to hydrostatic values.

ANALYTICAL RESULTS

Headspace gases.

The methane content (expressed in μl per kilogram of sediment under standard conditions (25°C , 1 bar)) and the methane/ethane ratio measured on headspace samples are given in Fig. 2 for Sites 994, 995 and 997. The same pattern has been found for the three sites. In the first few meters (0-10 mbsf), methane is practically absent. Below this zone, a very strong increase of the methane content between 10 and 50 mbsf is observed from 40 to 180000 $\mu\text{l}/\text{kg}$. Below 50 mbsf, the methane concentration decreases steadily down to a depth of 200 mbsf; and at greater depths, the methane concentration remains nearly constant about 10000 $\mu\text{l}/\text{kg}$. Ethane headspace concentrations are low (0-8 $\mu\text{l}/\text{kg}$) in the upper 400 mbsf and increase between 400 and 700 mbsf to values of 160 $\mu\text{l}/\text{kg}$. The CO_2 content has not been measured systematically. CO_2 concentrations are highest from 200 to 450 mbsf, then decline with depth. A maximum value of 750 $\mu\text{l}/\text{kg}$ has been measured at a depth of 384.09 mbsf at Site 995. The methane/ethane ratio increases strongly in the first upper meters (0-40 mbsf) from values around 40 to 20000 (Fig. 2d,e,f). Below 100 mbsf, the ratio decreases exponentially with the depth. The methane/ethane ratio curve can be represented by a straight line on a logarithmic plot. A change of the slope of the curve can be observed at a depth of

about 400 mbsf. This change of the slope is most noticeable on the profile for Site 995 (Fig. 2e), where the methane/ethane ratio becomes almost constant below 400 mbsf.

Free gases.

Results of the analyses are given in Fig. 3. Free gases can only be sampled when pockets of free gas are present in the cores. As air contamination occurs during the sampling at various levels, only concentration ratios can be interpreted. The methane/ethane ratio is fairly constant at about 20000-30000 from 50 to 165 mbsf. Below 165 mbsf, the methane/ethane ratio decreases to values between 1000 and 2000 at 400 mbsf. The methane/ethane ratio profiles are similar to those obtained from headspace samples, but some differences are observable between the different profiles. First, the methane/ethane ratio is about 4-10 times higher for free gas samples than for headspace samples. For example, at 400 mbsf, the methane/ethane ratio is around 700 for headspace gases, whereas it is around 3000 for free gas samples. Like headspace samples, profiles are linear, when data are plotted against a logarithmic axis for the methane/ethane ratio. A change of the slopes of the lines occurs at 570 mbsf for Site 994, at 500 mbsf for Site 995 and at 450 mbsf for Site 997. A gradation of this effect can be observed respectively for Sites 994, 995 and 997 (Fig. 3a,b,c). Indeed, this slope change is most visible at Site 997, where the methane/ethane ratio becomes almost constant below 450 mbsf at a level of about 1200, whereas the change of the slope is less visible for Sites 994 and 995. Several peaks towards lower methane/ethane values occur occasionally along the methane/ethane profiles (at 190 and 280 mbsf at Site 994, at 270 and 430 mbsf at Site 995, and at 250, 310, and 449 mbsf at Site 997). The CO₂ concentrations vary widely (Fig. 3d,e,f), in particular below 500 mbsf. In some samples between 200 and 400 mbsf, carbon dioxide makes up surprisingly up to 30 % of the free gases. Between 100 and 200 mbsf, the methane/CO₂ ratio decreases by a factor one from 40 to 4. Between 200 and 500 mbsf, the methane/CO₂ remains roughly constant at a level of 4. Below 600 mbsf, the methane/CO₂ content increases up to values of 20-40 at 700 mbsf. At Site 994, a distinct maximum of 142 has been measured for the methane/CO₂ content at the depth of 272.69 mbsf, in a zone where gas hydrates have been recovered. Small amounts of liquid hydrocarbons have been recovered at Site 997. Visible oil has been observed in the sediments

from 500 to 650 mbsf, and a strong aromatic odor accompanied each core. In addition, concentrations greater around 10 ppm have been detected for hydrocarbons (propane, butane, pentane, hexane, heptane, referred to as C₃₊, as a variety of additional unidentified compounds) by gas chromatography. The contents of isobutane and iso-pentane sometimes exceed that for propane. Iso-alkanes are more abundant than the normal alkanes. The methane/C₃₊ ratio is about 45 000 between 180 and 450 mbsf, and around 20 000 between 450 and 700 mbsf.

Gas Hydrates.

Few gas hydrates have been recovered at Sites 994, 995 and 997. However, numerous evidences, as shown below, indicate their presence between 200 and 450 mbsf.

A piece of gas hydrate (3 cm³) was recovered first at Site 994 at 259.9 mbsf. Dissociation of the gas hydrate yields a gas of composition of 98.78 % CH₄ and 1.22 % CO₂. Only minor amounts of ethane and propane are present, respectively 86 and 2 ppm. The gas/water volumetric ratio is 154, giving a ratio of H₂O/CH₄ molecules of 8.08. The theoretical chemical formula of a CH₄-rich gas hydrate, which forms a structure I is M₅.75 H₂O, where M designates a cavity that can be filled by a gas molecule. No gas hydrate has been sampled at Site 995. Massive gas hydrates have been recovered at 330-331 mbsf at Site 997. A sample was placed in a dissociation chamber, and the ratio of evolved gas volume to water is 138.7, giving a ratio of H₂O/CH₄ molecules of 7.27 and indicating that at least 79 % of the cavities are filled. The composition of the released gas is 98.43 % CH₄ and 1.57 % CO₂. Ethane and propane are present at very low levels (respectively 196 and 4 ppm). The methane/ethane ratio is 4936. This ratio falls within the range of the methane/ethane ratios measured for headspace gases (1880) and free gases (6748) taken from the same core.

Interstitial waters.

Interstitial waters are mainly composed of chloride ions (see below) and sodium ions (not measured). Sulfate is present in the few upper meters of the sediments (0.025 molal at the seafloor), but their concentrations tend to zero below 23 mbsf (Fig. 4a). The content of ammonium (Fig. 4b) increases linearly with the depth between 0 and 170 mbsf (reaching a value of 0.016 mM at 170 mbsf). The ammonium content continues to increase in small

amounts between 200 and 450 mbsf with an intensive scatter. A maximum value of 0.0223 molal is reached at the depth of 500 mbsf. Ammonium then decreases with depth. Potassium (Fig. 4c) increases slightly with depth (0.0125 molal at the seafloor and with scatter up to 0.015 molal at 473 mbsf, and then decreases to lower values (0.012 at 700 mbsf). Calcium (Fig. 4d) decreases strongly from 0.010 molal near the sediment-water interface to 0.002 molal at 40 mbsf. Calcium content remains constant at 0.002-0.003 molal between 40 and 400 mbsf. A linear increase of the calcium is observed between 400 and 700 mbsf (0.006 molal at 700 mbsf). Magnesium (Fig. 4e) also decreases strongly in the 60 upper meters (0.05 molal at the seafloor and 0.022 molal at 60 mbsf). Then the magnesium content decreases linearly to 0.014 at 700 mbsf. The pH (Fig. 4f) of sampled waters oscillates between 7 and 8.

Profiles of the chloride content and alkalinity are given for the Sites 994, 995 and 997 in Fig. 5. Concentration values have been corrected for seawater contamination. The correction effect is small and tends to lower slightly the concentrations values in chloride by less than 0.006 molal. The chloride profiles of the 994, 995 and 997 sites are very similar. In the first upper meters (0-12 mbsf), the chloride content increases slightly (from 0.557 molal near the sediment-water interface to 0.560 at 12.3 mbsf at Site 994). Below this depth, chloride steadily decreases to values around 0.51 molal at 190 mbsf. Between 190 and 440 mbsf, a zone with considerable scattering is observed. A general baseline concentration of about 0.5 molal can be distinguished, but this trend is superimposed by numerous excursions to lower saline values (down to 0.44 molal at 400-410 mbsf). Two main subzones of irregular chloride variations are noticeable, one between 200 and 280 mbsf, and the other between 380 mbsf and 420 mbsf. Below 450 mbsf, the chloride content increases linearly at Sites 994 and 995 (0.52 and 0.515 molal at 700 mbsf for Sites 994 and 995). The chloride content remains practically constant at 0.51 molal at Site 997.

Alkalinity profiles are plotted in Fig. 5d, e and f. Alkalinity values increase linearly with the depth between 0 and 230 mbsf (0 molal near the water-sediment interface and 0.1 molal at 230 mbsf). Alkalinity then increases slightly with depth reaching a maximum value of 0.126 molal at 300 mbsf. From 250 to 450 mbsf, the alkalinity values exhibit several trends towards

lower values (up to 0.075 molal). Below 450 mbsf, the alkalinity values are less scattered and decrease linearly with the depth. A shift of the alkalinity to higher values is observed from Site 994 to Site 997.

PCS samples.

A pressure core sampler (PCS) has been used with success several times. The great advantage of this device is clearly its ability to sample gases and fluids with in-situ sediments by minimizing the losses during recovery (KVENVOLDEN et al., 1983). Several cores, that have been recovered with the PCS, were at pressures only slightly below the hydrostatic pressure, indicating that the losses of fluids are effectively small. Composition gases are similar with that measured shipboard on free gas samples, with the exception of two notable differences. First, higher concentrations of isobutane and *n*-heptane (respectively up to 618 and 85 ppm) were observed in most gas samples from the PCS cores below 434 mbsf. Secondly, the CO₂ concentrations of gases recovered from the PCS are ten times lower. This discrepancy results probably from the sampling technique of gases from the PCS. Indeed, the gas from the PCS core travels through a four-liter volume of water before being sampled from the manifold. The water is undersaturated in CO₂ at these high pressures (0-300bar). Thus, this volume of water is sufficient to dissolve a large fraction of the CO₂ released from the PCS core.

DISCUSSION

Chloride anomalies.

Fluid analyses reveal first that there is a zone between 190 and 450 mbsf where the chemistry of the fluids shows irregular and anomalous trends. This is most clear on the chloride profiles. For the three holes (Sites 994, 995 and 997), the chloride content is highly irregular with many freshening anomalies. High chloride concentration contrasts (up to 0.06 molal) are observed between adjacent samples. Diffusion should normally eliminate such chloride differences. Thus, these chloride excursions must have occurred during cores retrieval and they result from the dissociation of locally-concentrated gas hydrates. These effects of dilution of interstitial waters by the decomposition of gas hydrates have already

been abundantly documented on other drilling sites (HESSE and HARRISON, 1981; JENDEN and GEISKES, 1983; KVENVOLDEN and BARNARD, 1983b; HESSE et al., 1985; KASTNER et al., 1990; KVENVOLDEN and KASTNER, 1990; USSLER and PAULL, 1995). Dissolved ions are excluded from the hydrate lattice during the formation of gas hydrate. The marine sediments behave probably as an open system; and thus, the excluded ions diffuse away from the zone of formation of gas hydrates. The sediment compaction results also to a porosity reduction, and thus to the expulsion of these more saline waters. During core recovery and sampling, fresh waters are released by gas hydrates, leading to freshening of interstitial waters. This freshening of waters is visible too on the profiles of other ions (ammonium, calcium, magnesium, potassium, strontium, ...), where concentration decrease up to 15 % occurs in gas hydrates-bearing zones. The chloride profiles indicate too that the distribution of inferred gas hydrates is heterogeneous. Two zones contain apparently higher amounts of gas hydrates. One is located between 380 and 420 mbsf, and the other between 200 and 280 mbsf. Another point of discussion is the presence or not of gas hydrates at background concentrations when no anomalous chloride concentrations have been observed. Interstitial waters have been sampled downhole by a WSTP (Water Sampler - Temperature Probe) tool. Corrected chloride concentrations measured in the WSTP samples are consistent with the baseline concentrations (about 0.52 molal) of the interstitial waters in the zone between 190 and 450 mbsf. Therefore, gas hydrates are largely confined to the short freshening intervals. No chloride anomalies have been observed below 456 mbsf at Site 994, below 438 mbsf at Site 995 and below 460 mbsf at Site 997. This suggests that these depths represent the limit of gas hydrate occurrence. This inference is also consistent with certain logging results. More unexpectedly, chloride concentrations have been observed to increase slightly in the first few meters (0-12 mbsf) below the sediment-water interface from 0.555 to 0.56 molal. Less saline waters are present below 12 mbsf. The existence of this local maximum in chloride concentrations at 12 mbsf is not yet explained. One explanation is that it represents ultrafiltration by compacted clays (McKELVEY and MILNE, 1962; DESITTER, 1949; MATSUHISA and MATSUMOTO, 1986).

The phase diagram.

As shown above, gas hydrates seem to influence too the composition of gases. But, before any interpretation, it is necessary at first to know from which phase the gases come. A phase diagram showing the saturation boundaries of fluids at the Site 995 is given in Figure 6. The diagram has been calculated by using thermodynamic models, described in DUBESSY et al. (1992), BAKKER et al. (1995) and DUAN et al. (1992). A geothermal gradient of 33.7°C/km associated with an hydrostatic pressure regime has been established at Site 995 based on measurements of in-situ temperatures. Water content of sediments measured on the ship has been used for the calculations. This explains the jagged nature of the calculated phase boundaries, as the water content has not been smoothed before the calculations. In the upper section (0-540 mbsf), and depending upon the methane content in sediments, pore waters can either be undersaturated or oversaturated with respect to gas hydrates. Below 540 mbsf, gas hydrates are not stable because of the too high temperatures (above 21.8°C). Therefore, below 540 mbsf, pore waters are either undersaturated or oversaturated with respect to free gas. The depth of 540 mbsf corresponds to the larger depth, at which gas hydrates are stable. This level is commonly referred to as the BGHS (Base of Gas Hydrate Stability). Note here that the BGHS calculated for Site 995 lies at greater depth than that inferred from seismic profiles and geochemical studies (450 mbsf). This is the reason why in Fig. 6, a small field above the BGHS has been labelled as a possible zone of metastable free gas. This point will be discussed further. In the zone 0-190 mbsf, no gas hydrates are present. This means that the pore waters are undersaturated with respect to gas hydrates in this zone. Then, the methane content should be less than 800 ml/kg sediment. Thus, all sampled gases in this zone (0-190 mbsf) result from the degassification of the interstitial waters caused by the pressure drop during the core retrieval. In the zone 190-450 mbsf, gas hydrates are present (as discussed above), and the methane content must be at least locally higher than the saturation values (0.8 l/kg at 200 mbsf and 1.0 l/kg of sediment at 450 mbsf). Gas hydrates are solid phases, that are able to retain high amounts of methane, even when they are present only at low amounts. An illustration of this is given by the dotted curve of Fig. 6, that represents the amount of methane in sediments containing three percent in volume of gas hydrates. In such a case, a significant fraction (up to 60 % of the methane) of the collected gases would come

from the gas hydrates. Therefore, gas released from gas hydrates are expected to influence the composition pattern of free gas samples. However, the sampling of free gases in the gas hydrate-rich zone was difficult because of the very gassy nature of the cores. Cores extrude from the core liner, resulting in a low recovery. Nevertheless, some data have been obtained in the same cores where gas hydrates have been sampled. Finally, below the BGHS, collected gases come from pore waters and from free gases (if the pore waters are saturated in methane).

The carbon dioxide.

Fractionation between the different phases may be first revealed by considering the methane and carbon dioxide. Both gases have indeed physico-chemical properties, that are very different. At Site 994, a distinct maximum value of 142 for the methane/carbon dioxide ratio has been measured at 272.69 mbsf near a core containing gas hydrates. This value is in large contrast with values obtained from cores recovered above and below (between 10 and 20). The piece of gas hydrate sampled at 259.9 mbsf at Site 994 yields a methane/CO₂ ratio of 83. Another piece has been recovered at the Site 997 with a methane/CO₂ ratio of 63. Again, these values are stronger than the mean values (around 10) obtained from free gas samples between 190 and 450 mbsf at Site 997, and which are believed to represent the methane/CO₂ ratio of pore waters. All these data suggest that very different fractionations of methane and carbon dioxide occur between gas hydrates and interstitial waters. Gas hydrates would incorporate more easily methane molecules than carbon dioxide molecules. As a gas hydrate relatively enriched in methane dissociates, it would release more methane than carbon dioxide. This would lead to a relative depletion of carbon dioxide with respect to methane. There is no experimental data to confirm this fractionation effect. However, thermodynamic models for gas hydrates (DUBESSY et al., 1992; BAKKER, 1996) are now available for quantifying this effect. For instance, at about 12°C (which is the temperature at about 272.69 mbsf), a gas hydrate characterized by a methane/CO₂ ratio of 80 is predicted to be in equilibrium with seawater containing dissolved methane and carbon dioxide in a ratio of 3. Therefore, the behaviour of methane and carbon dioxide between gas hydrates and pore waters, that is calculated by the theory, is quite in agreement with our observations. In the

zone between 450-700 mbsf, gas hydrates are absent (see above). Thus, if the pore waters are saturated, a part of the sampled gases comes from the gaseous phase, which is the stable methane-rich phase at these depths. Fractionation of gases occurs too between the aqueous solution and the gaseous phase. Indeed, carbon dioxide is about ten fold more soluble than methane. As a consequence, the methane/CO₂ ratio in liquid waters is ten fold lower than the corresponding ratio in gases. This could explain the higher variability of the methane/CO₂ ratio below 500 mbsf observed for free gas samples in Fig. 3d, e and f. Oscillations of one order of amplitude are indeed measured for the methane/CO₂ ratio. These oscillations could result from the heterogeneous sampling of methane and carbon dioxide coming from two different coexisting sources (pore waters and gas phase). Moreover, the dissolved carbon dioxide is related to the alkalinity (HCO₃⁻). A rough relationship is observed between the alkalinity and the CO₂ concentrations in free gases. When the alkalinity is low (varying from 0 to 60 mMolal between 0 and 150 mbsf), high methane/CO₂ ratio are observed in free gas samples (above 20). The alkalinity is maximum in the gas hydrate-rich zone (190-450 mbsf), where the methane/CO₂ ratio of free gas samples is globally low (around 10). These observations prove too that the largest part of CO₂ in free gas samples was probably released from pore water bicarbonates above 450 mbsf. Freshening spikes are seen too along the alkalinity profiles in the gas hydrate zone. This is probably due to the dilution caused by the freshening of waters during the dissociation of gas hydrates. Below 450 mbsf, alkalinity decreases smoothly, indicating a smooth decrease of the dissolved carbon dioxide in the pore waters. This observation confirms that the large oscillations of the methane/CO₂ ratio in free gas samples cannot result from an heterogenous distribution of the carbon dioxide in the sediments.

The methane and other hydrocarbons.

Similarities and differences have been noticed too for the methane and methane/ethane profiles obtained on this leg when compared to other drilling sites. The upper sediment column (0-30 mbsf) is strongly depleted in methane (Fig. 2). This zone corresponds to the sulfate reduction zone, where organic matter is oxidized by sulfate :



Sulfate ions diffuse downwards from the oceanic waters and are progressively reduced by bacteria to produce sulfur. Below this zone, the methane concentration increases strongly. The ethane content is very low, resulting to a very high methane/ethane ratio (above 10000 at 50 mbsf in headspace samples and above 40000 in free gas samples). This high ratio indicates that methane is of biologic origin (BERNARD et al., 1976). Methane is produced by bacterial oxidation of organic matter (PAULL et al., 1994):



Another evidence of the occurrence of this reaction is the strong increase of the alkalinity in this zone (Fig. 5), caused by the production of carbon dioxide. Upwards migration from underlying sediments superimposes probably the methanogenesis to produce the high methane concentration of methane observed in headspace samples between 50 and 100 mbsf. Below 200 mbsf, the amount of methane extracted from headspace samples decreases to about 10 ml/kg of sediment at 200 mbsf and then remains roughly constant. This decrease of the headspace methane content should not be taken into account too seriously, as it corresponds certainly to an artefact. Indeed, it will be demonstrated below that the methane concentration does increase with the depth. A change of the coring techniques occurs below around 100 mbsf, causing a greater disturbance of the sediments, and thus a greater loss of gas. As observed above, the methane/ethane ratio is about ten fold greater in free gas samples than in headspace samples. Gas extracted from headspace samples corresponds to residual molecules that are bound strongly to the sediments (adsorption); and it is likely that ethane and higher molecular weight hydrocarbons adsorb more favorably on minerals than methane. However, the same trends for the methane/ethane ratio are observed between headspace samples and free gas samples. The methane/ethane ratio decreases exponentially with depth, as it has been already documented on other sites (KVENVOLDEN and BARNARD, 1983a,b). However, a sudden change of the exponential slope occurs approximately at 450 mbsf (Fig. 2 and 3); and below 450 mbsf, the methane/ethane ratio still decreases exponentially with the depth, but more slowly. The exponential decrease of the methane/ethane ratio, which is commonly observed in sediments of continental margins, is usually interpreted as the result of upwards migration from deep zones where ethane and

higher molecular weight hydrocarbons are produced by thermogenic processes. Thus, hydrates-rich layers seem to hinder at least partially the upwards diffusion of ethane and other hydrocarbons. Another argument in favor of this hypothesis is the presence of high concentrations of isobutane and *n*-heptane observed in PCS cores and free gas samples below 434 mbsf at Site 997. These hydrocarbons could constitute a residual pool of hydrocarbons, that have formed by higher migration rates and incorporations of methane in gas hydrates. Several large offsets of the methane/ethane ratio to lower values have been noted in free gas samples (at 280 mbsf at Site 994, at 300 and 440 mbsf at Site 995). These offsets could be due to the dissociation of gas hydrates relatively enriched in ethane. However, gas hydrates, that have been recovered at Site 994 and 997, are characterized by very low concentrations of ethane (the methane/ethane ratios of the gas hydrate sampled at 259.9 mbsf at Site 994 and at 330 mbsf at Site 997 are respectively 11486 and 5022. These ratios are of the same order than the background values measured for free gas samples). No data exist on the fractionation of methane and ethane between gas hydrates and an aqueous solution. However, gas hydrates are expected to incorporate more easily methane molecules than ethane. Therefore, the hypothesis of ethane-concentrated gas hydrates is difficult to defend and decomposition of gas hydrates leads certainly to an increase of the methane/ethane ratio. Another explanation would be the presence of zones, where the pore waters are locally enriched in ethane. Indeed, it is interesting to note that these zones of higher ethane concentrations are located just below layers, that are more concentrated in gas hydrates (compare Fig. 3a, b and c with Fig. 5a,b,c). Thus, these gas hydrates-concentrated layers would act as a partial seal, that would slow down the upward migration of ethane.

AMOUNTS AND DISTRIBUTION OF GAS HYDRATES

One of the objectives of this leg is to assess the amounts and the distribution of gas hydrates in the sediments of a passive margin. This can be achieved by two independent ways, either by using the chloride anomalies or the PCS samples.

As seen above, anomalously freshening of pore waters indicates the presence of gas hydrates and it is possible to estimate quantitatively the amount of gas hydrates responsible for the

salinity decrease of waters. Consider one liter of aqueous solution of molality m° containing p moles of gas hydrates. The dissociation of p moles of gas hydrates yields $p \times 5.75$ moles of H_2O (if all cages are occupied by gas molecules), thus decreasing the molality of the interstitial water to a molality m . The molality decrease dm is related to the amount of initial gas hydrates by :

$$dm = m - m^\circ = nCl / 18 \times (1/n - 1/n^\circ) \quad (3)$$

where nCl is the number of Cl^- ions in one kilogram of water, n° is the initial number of H_2O molecules ($n^\circ = 55.55$ moles) in one liter of water and n is the number of H_2O molecules after dissociation of gas hydrates ($n = 55.55 + 5.75 p = n^\circ + 5.75 p$). Then, the molality decrease can be explicated as follows:

$$dm = m^\circ (n^\circ/n - 1). \quad (4)$$

Therefore,

$$n^\circ/n = dm / m^\circ + 1, \quad (5a)$$

and finally after some algebra,

$$p = (m^\circ/m - 1) \times 55.55 / 5.75 \quad (5b)$$

One mole of gas hydrate occupies a space of $22.8 \text{ cm}^3/\text{mole}$. The filling F of interstitial porous space by gas hydrates prior the drilling can be estimated by :

$$F = 22.8 p / (22.8 p + 1000) \quad (6)$$

Use of Equation (5b) and (6) with chloride concentration data of Sites 994, 995 and 997 yields values that reach values as high as 6 vol. % (at 330 mbsf at Site 997) for the degree of filling of gas hydrates in the porous interstitial space. A median value of 3 % is found in all the interstitial water samples presenting anomalously low chloride values between 200 and 450 mbsf.

The other way to estimate the amount of gas hydrates is to use PCS samples data with a saturation phase diagram, as given in Fig. 6. This has been carried out in Fig. 7, where the calculated methane saturation in pore waters are compared with data obtained from PCS samples from Sites 994, 995 and 997. Saturation values with respect to gas hydrates, as calculated from the thermodynamic models described in DUBESSY et al. (1992) and BAKKER et al. (1996) are plotted as a function of the depth. Saturation values increase

slightly with the depth from 0.7 to 1.3 liter per kg of sediment between 0 and 450 mbsf. For these calculations, a mean geothermal gradient of 37°C/km (as measured on Sites 994 and 997) has been used with the mean water content of sediments of Sites 994, 995 and 997. Pore waters have been assimilated to a NaCl aqueous solution of molality 0.575. The BGHS is calculated to be at 450 mbsf. Below the BGHS, the model of DUAN et al. (1992) has been used for calculating the methane saturation in seawater. Comparison of PCS data with calculated saturation curves is in quite good agreement with conclusions inferred from the chloride profiles. In the upper section (0-200 mbsf), PCS samples are undersaturated and no gas hydrate can form. At 200 mbsf, one sample is slightly oversaturated and should have contained a small amount of gas hydrates (around 0.3 % of the bulk volume of sediments). Between 220 and 350 mbsf, all sampled PCS cores are undersaturated. Between 380 and 450 mbsf, all PCS cores (except one) are clearly oversaturated in methane. Amounts of gas hydrates can reach three percent of the bulk volume of the sediments in the most gas hydrates-concentrated layers.

THE SIGNIFICATION OF THE BSR

Another important question is related to the nature of the BSR. First, PCS samples of sediments, that were recovered in the zone below the BSR, contain very large quantities of methane (up to eight liters per kg of sediment, see Fig. 7). Moreover, no anomalous freshening anomalies have been detected in the interstitial waters of these samples. This confirms that the BSR corresponds to the interface between a zone rich in gas hydrates overlying a zone containing high amounts of free gas. As a consequence, the BSR should correspond to the BGHS. Another important question is why there is no BSR at Site 994. A working hypothesis is that the BSR occurs because of the presence of free gas rather than gas hydrate (MINSHULL and WHITE, 1989; SINGH et al., 1993), and that there is less free gas below 440 mbsf at Site 994 than at Site 997.

The BGHS was calculated for Sites 994, 995 and 997 by locating the intersection of the geothermal gradient with the experimental stability curve of methane hydrate in seawater in a pressure-temperature diagram (Fig. 8). Geothermal gradients, as determined by the in-situ

temperature measurements during the leg, were used for the calculations. The temperature at the water-sediment interface is 3.6°C. The geothermal gradients were measured respectively at Sites 994, 995 and 997 (37.3 ± 0.13 , 33.7 ± 0.09 and 36.9 ± 0.04 °C/km). Levels of the BGHS are calculated respectively at 491 ± 20 , 536 ± 15 , and 482 ± 5 mbsf. No BSR has been recorded at Site 994. Vertical Seismic Profile (VSP) experiments place the BSR at 440 ± 10 mbsf at Site 995, and at 450 ± 10 mbsf at Site 997. These depths are coincident with the base of the lower zone of Cl⁻ excursions observed on chloride profiles. Discrepancies do appear between the calculated BGHS and the observed BSR. This is particularly true for the Site 995, where the BGHS is estimated to be 86 mbsf below the BSR. A better agreement is found at Site 997, where the BGHS is found at 28 mbsf below the BSR. The discrepancy at Site 997 is well within the range of uncertainties of parameters. However, this is not the case at Site 995. The geothermal gradient at Site 995 is around ten percent lower than at Sites 994 and 997. The first question, that arises, is how the geothermal gradient can vary to such extent from one site to the other distanced only by less than five kilometers. Problems with the in-situ temperature measurements cannot be discarded. Another hypothesis is that fined grained sediments modify the stability conditions of gas hydrates. Porosity could shift the dissociation temperature of gas hydrates by a few tenths of degrees (CLENNELL et al., submitted). A third explanation would be that Site 995 has not yet reached its equilibrium state. The BGHS is expected to move through the sediment column during geological times as a result of sedimentation and sea-level changes (see below). The depth of the BSR at Site 995 would correspond to a fossil depth to the BGHS that occurred during some previous change of the sea level and/or the bottom water temperature (PAULL et al. 1991). Limitation of the diffusion rate of the heat and/or the salinity could support such an hypothesis. However, it is difficult to understand why such a phenomenon would occur only at Site 995, and not at Site 997.

CONCLUSION

Drilling operations of a gas hydrate rich field during the ODP Leg 164 in the Blake Outer Ridge has brought several new and important information on marine gas hydrates. The

recovery of gas hydrates was difficult. However, the analysis of the chloride profiles and PCS samples yields important information on the amounts and distribution of gas hydrates throughout the sedimentary column. Gas hydrates are present between 190 mbsf and 450 mbsf. Two zones are locally more concentrated (between 240 and 280 mbsf, and between 380 and 420 msf) respectively with a mean amount of 1.5 and 3 percent of the bulk volume occupied by gas hydrates. Between 280 and 380 mbsf, the amount is estimated around 1 percent of the bulk volume. These values confirm that gas hydrates represent an enormous reservoir of methane in marine sediments. This represents 275 kg of methane per square meter; and by considering the extent of the Blake Ridge (24000 km²), where a BSR has been recorded, this represents a total amount of around one Gt of methane. Moreover, free gases are present throughout a zone a few hundred meters thick beneath the gas hydrate-bearing zone and constitutes an important resource of methane. The leg has confirmed the nature of the BSR in this region as a reflector between a gas hydrate-rich layer overlying a zone containing free gas. Thus, the BSR is clearly an indicator of gas hydrates in this region. The Leg 164 reveals too that gas hydrates are present even when the BSR is absent (Site 994). Gas hydrates are shown to modify the circulation of fluids. Free gas and pore waters below gas hydrates zones are shown to be enriched in ethane and higher hydrocarbons. Gas hydrates cement the pore spaces, and thus, may act as a barrier seal. The profile of carbon dioxide is influenced by its fractionation between gas hydrates and pore waters above the BSR, and between free gas and pore waters below the BSR.

REFERENCES

- BAKKER R.J. (1996) Application of clathrate melting temperatures to fluid inclusions studies (under press, *Computers & Geosciences*).
- BAKKER R.J., DUBESSY J. and CATHELINÉAU M. (1995). Improvements in clathrate modeling. I: the H₂O-CO₂ system with various salts. *Geochim. et Cosmochim. Acta*, **60**, 1657-1681.
- BERNARD B., BROOKS J.M. and SACKETT W.M. (1976). Natural gas seepage in the Gulf of Mexico. *Earth and Planet. Sci. Lett.*, **31**, 48-54.
- CLAYPOOL G.E. and KAPLAN I.R. (1974). Methane in marine sediments. In Kaplan, I.R. (Ed), *Natural Gases in Marine Sediments*, New York (Plenum Press), 99-139.
- CLENNEL M.B., HOVLAND M. and BOOTH J.S. (1996). Role of host sediment pore size in the stability and growth habits of natural gas hydrates (submitted).
- DUAN Z.N., MØLLER J., GREENBERG J. and WEARE J.H. (1992). The prediction of methane solubility in natural waters to high ionic strength from 0 to 250°C and from 0 to 1600 bar. *Geochim. Cosmochim. Acta*. **56**, 1541-1460.
- DUBESSY J., THIÉRY R. and CANALS M. (1992). Modeling of gas phase equilibria involving mixed gas clathrates: Application to the determination of molar volume of the vapour phase and salinity of the aqueous solution in fluid inclusions. *Eur. Jour. Min.*, **4**, 872-884.

HESSE R. and HARRISON W.E. (1981). Gas hydrates (clathrates) causing pore water freshening and oxygen isotope fractionation in deep-water sedimentary sections of terrigenous continental margins. *Earth and Planetary Science letters*, **55**, 453-462.

HESSE R., LEBEL J. and GIESKES J.M. (1985). Interstitial water chemistry of gas-hydrate bearing sections of the middle America Trench, DSDP Leg 84. In VON HUENE R., AUBOUIN J., et al., *Init. Repts DSDP*, **84**, Washington (U.S. Govt. Printing Office), 727-737.

HYNDMAN R.D. and SPENCE G.D. (1992). A seismic study of methane hydrate marine bottom simulating reflectors. *J. Geophys. Res.*, **97**, 6683-6698.

JENDEN P.D. and GIESKES J.M. (1983). Chemical and isotopic composition in interstitial water from Deep Sea Drilling Project sites 533 and 534. In Sheridan R.E., Gradstein F.M., et al., *Init. Repts. DSDP*, **76**, 453-467.

KASTNER M., ELDERFIELD H., MARTIN J.B., SUESS E., KVENVOLDEN K.A., and GARRISON R.E. (1990). Diagenesis and interstitial-water chemistry at the Peruvian Continental Margin - Major constituents and strontium isotopes. In SUESS, E., VON HUENE, R., et al., *Proc. ODP Sci. Results*, 112 College Station, TX (Ocean Drilling Program), 413-440.

KATZMAN R., HOLBROOK W.S. and PAULL C.K. (1994). Combined vertical-incidence and wide-angle seismic study of a gas hydrate zone, Blake Ridge. *J. Geophys. Res.*, **99**, 17975-17995.

KVENVOLDEN K. (1988a). Methane hydrates and Global Climate. *Global Biochem. Cycles*, **2**, 221-229.

KVENVOLDEN K. (1988b). Methane hydrate - A major reservoir of carbon in the shallow geosphere ? *Chem. Geol.*, **71**, 41-51.

KVENVOLDEN K. and BARNARD L.A. (1983a). Hydrates of natural gas in continental margins. In WATKINS J.S. and DRAKE C.L. (Eds), *Studies in Continental Margin Geology*, AAPG Mem., **34**, 631-640.

KVENVOLDEN K. and BARNARD L.A. (1983b). Gas hydrates of the Blake Outer Ridge, Site 533, Deep Sea Drilling Project Leg 76. *Init. Repts. DSDP*, **76**: 353-365.

KVENVOLDEN K., BARNARD L.A. and CAMERON D.H. (1983). 7. Pressure core barrel: application to the study of gas hydrates Deep Sea Drilling Project Site 533, Leg 76. *Init. Rep. of the Deep Sea Drilling Project*, **76**, 453-467.

KVENVOLDEN K.A. and KASTNER M. (1990). Gas hydrates of the Peruvian outer continental margin. In SUESS E., VON HUENE R. et al., *Proc. ODP Sci. Results*, 112 College Station, TX (Ocean Drilling Program), 517-526.

MATSUHISA Y. and MATSUMOTO R. (1986). Oxygen isotope ratios of interstitial waters from the Nankai Trough and the Japan Trench, Leg 87. In KAGAMI H., KARIG D.E., COULBOURN W.T. et al., *Init. Repts. DSDP*, **87**, 853-856.

McKELVEY, I.G. and MILNE, J.H. (1962). The flow of salt solutions through compacted clay. *Clays and Clay Minerals*, 9th Conference, Pergamon Press, p 240-259.

MINSHULL T. and WHITE R.S. (1989). Sediment compaction and fluid migration in the Makran accretionary prism. *J. Geophys. Res.*, **94**, 7387-7402.

PAULL C.K., USSLER III W. and DILLON W.P. (1991). Is the extent of glaciation limited by marine gas hydrates ? *Geophys. Res. Lett.* **18**, 432-434.

PAULL C.K., USSLER III W. and BOROWSKI W.S. (1994). Sources of Biogenic Methane to Form Marine Gas Hydrates. In situ production or upward migration ? *In International Conference on Natural Gas Hydrates. Annals of the New York Academy of Sciences*, **715**, 392-409.

SINGH C.S., MINSHULL T.A. and SPENCE G.D. (1993). Velocity structure of a gas hydrate reflector. *Science*, **260**, 204-207.

SITTE, L.U. de (1947) Diagenesis of oil field brines. *Bull. Am. Assoc. Petr. Geol.*, **31**, 2030-2040.

SLOAN E.D. (1989). Clathrate Hydrates of Natural Gases; New York (Marcel Decker, Inc.), 641 p.

USSLER III W. and PAULL C. K. (1995). Effects of ion exclusion and isotopic fractionation on pore water geochemistry during gas hydrate formation and decomposition. *Geo-Marine Letters*, **15**, 37-44.

LIST OF FIGURES

Figure 1. Map showing the location of the drilling sites. The dotted zone corresponds to the extent of gas hydrates-rich field based on the presence of the BSR on seismic profiles.

Figure 2. Profiles of the headspace methane amounts at Site 994 (a), 995 (b) and 997 (c). The corresponding profiles of the methane/ethane ratio are given in Fig. 1d, e and f.

Figure 3. Profiles of the methane/ethane ratio at Sites 994 (a), 995 (b) and 997 (c), and profiles of the methane/CO₂ ratio at Sites 994 (d), 995 (e) and 997 (f) measured for free gas samples.

Figure 4. Profiles measured at Site 997 of the sulfate (a), ammonium (b), potassium (c), calcium (d), magnesium (e) and pH (f).

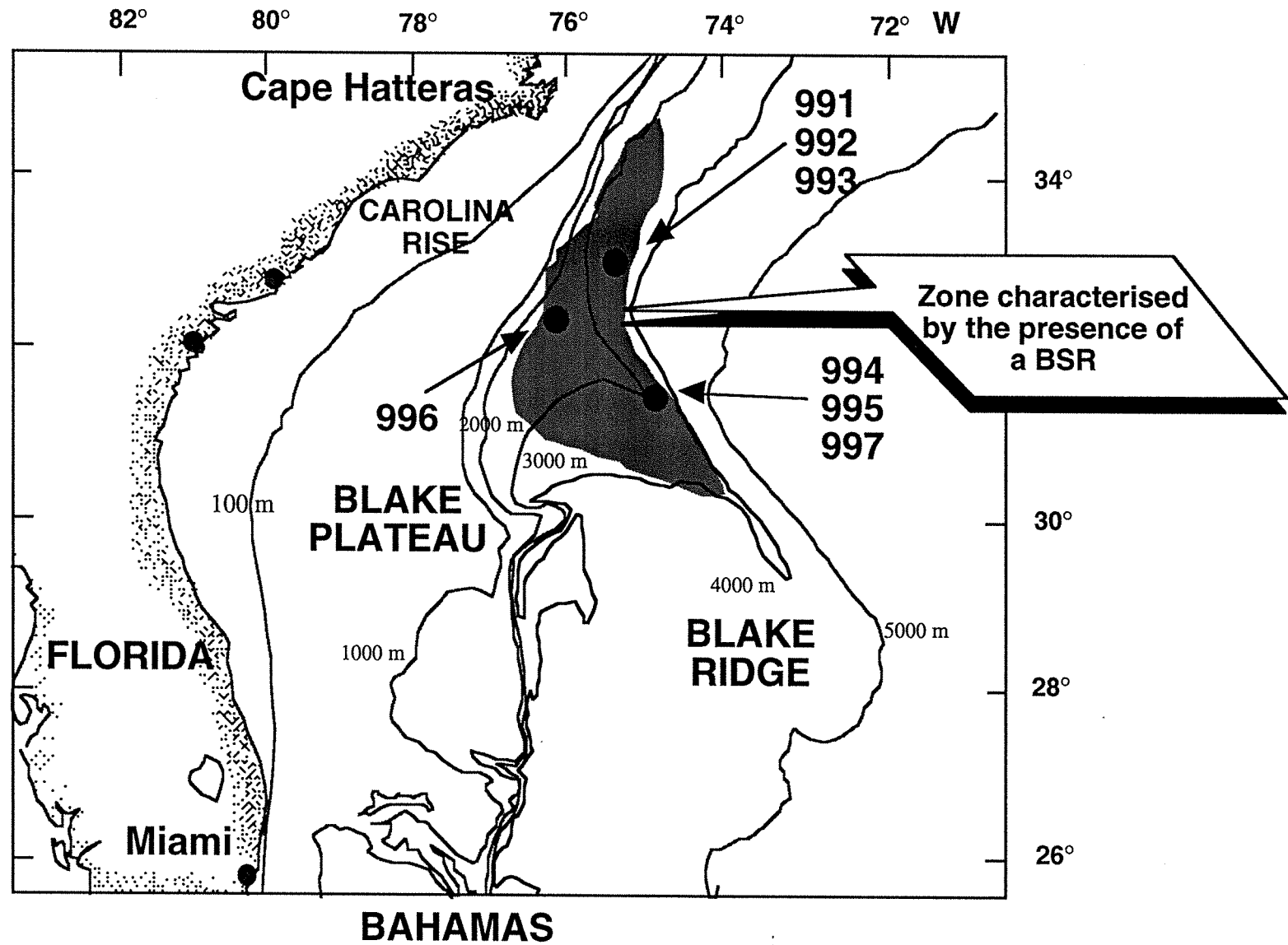
Figure 5. Chloride and alkalinity profiles at Site 994 (a and d), at Site 995 (b and e) and at Site 997 (c and f) are given on (depth vs molality) diagrams.

Figure 6. Theoretical phase diagram (depth vs methane amounts) showing the stability fields of gas hydrates and free gas at Site 995. Saturation curves of the methane with respect to gas hydrates (thick full line) and the vapor phase (thick dashed line) have been drawn. The intersection of these two curves is the BGHS and delimits the phase boundary between the gas hydrate and the free gas stability fields. Saturation curves have been calculated from the water content of the sediments. Note that the calculated BGHS is located at depths (at 536 ± 15 mbsf) well below from the observed BGHS inferred from chloride profiles and seismic records (at 450 ± 10 mbsf). The dotted curve indicates the amount of methane required for forming three percent in volume of gas hydrates in the sediments.

Figure 7. (Depth vs methane amount) diagram. The horizontal dashed line at 450 mbsf indicates the level of the BSR at Site 995 and 997. The solid line is the saturation curve of methane in aqueous solution. Above the BSR, gas hydrates form when pore waters are saturated with respect to methane; and below the BSR, free gas appears when the saturation of pore waters is reached. Symbols indicate the methane amounts collected from PCS samples (empty square: Hole 994A; empty triangle: Hole 994B; empty circle: Hole 994C; filled circle: Hole 997A; filled square: Hole 997B).

Figure 8. (Depth vs temperature) diagrams for the Site 994 (a), 995 (b) and 997 (c). On the left axis, the depth is indicated in meters below the ocean surface (mbos), whereas it is given in meters below the sea floor (mbsf) on the right axis. The seafloor is represented by the horizontal solid line. The geothermal gradient is given by the two dashed lines, and is estimated from in-situ temperature measurements done during this leg (diamond points; uncertainties on the temperature measurements are represented by the small horizontal lines). The dissociation curve of gas hydrates is indicated by both non-horizontal solid lines. The first line on the right side gives the dissociation temperature of a methane gas hydrate in pure water, whereas the second one on the left indicates the dissociation temperature of a methane gas hydrate in seawater. These lines have been calculated by the model of BAKKER (1996).

Figure 1



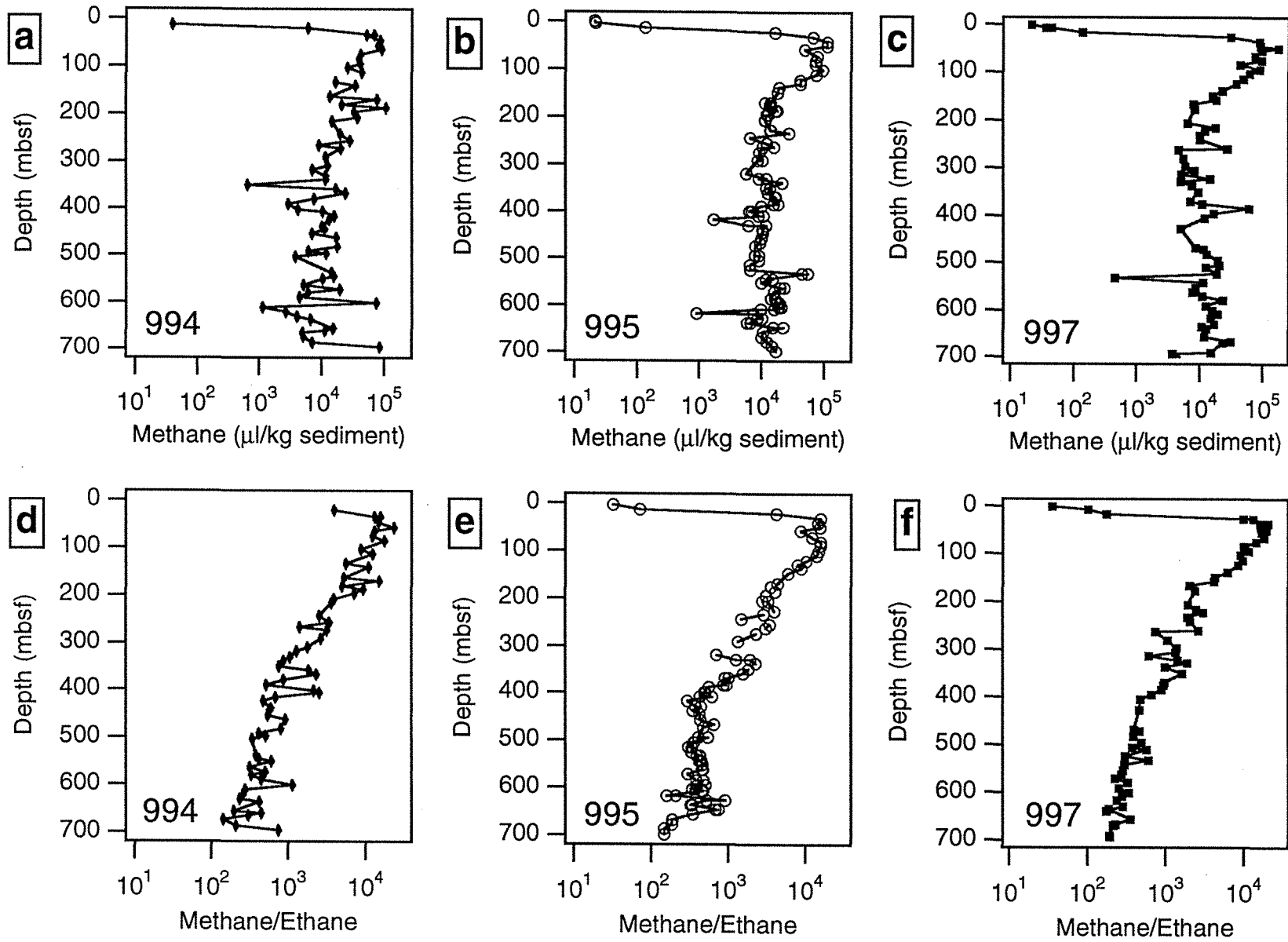


Figure 2

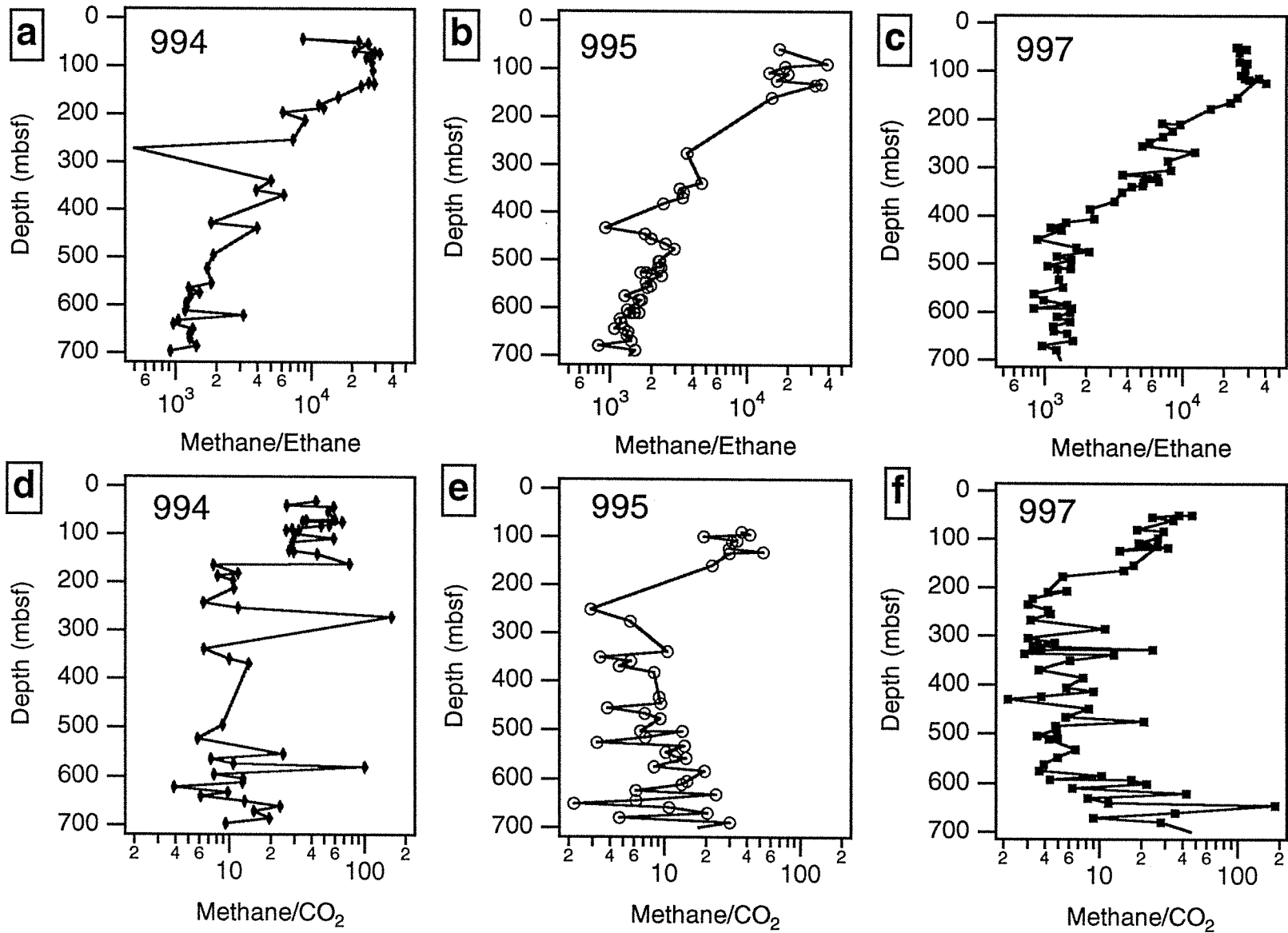
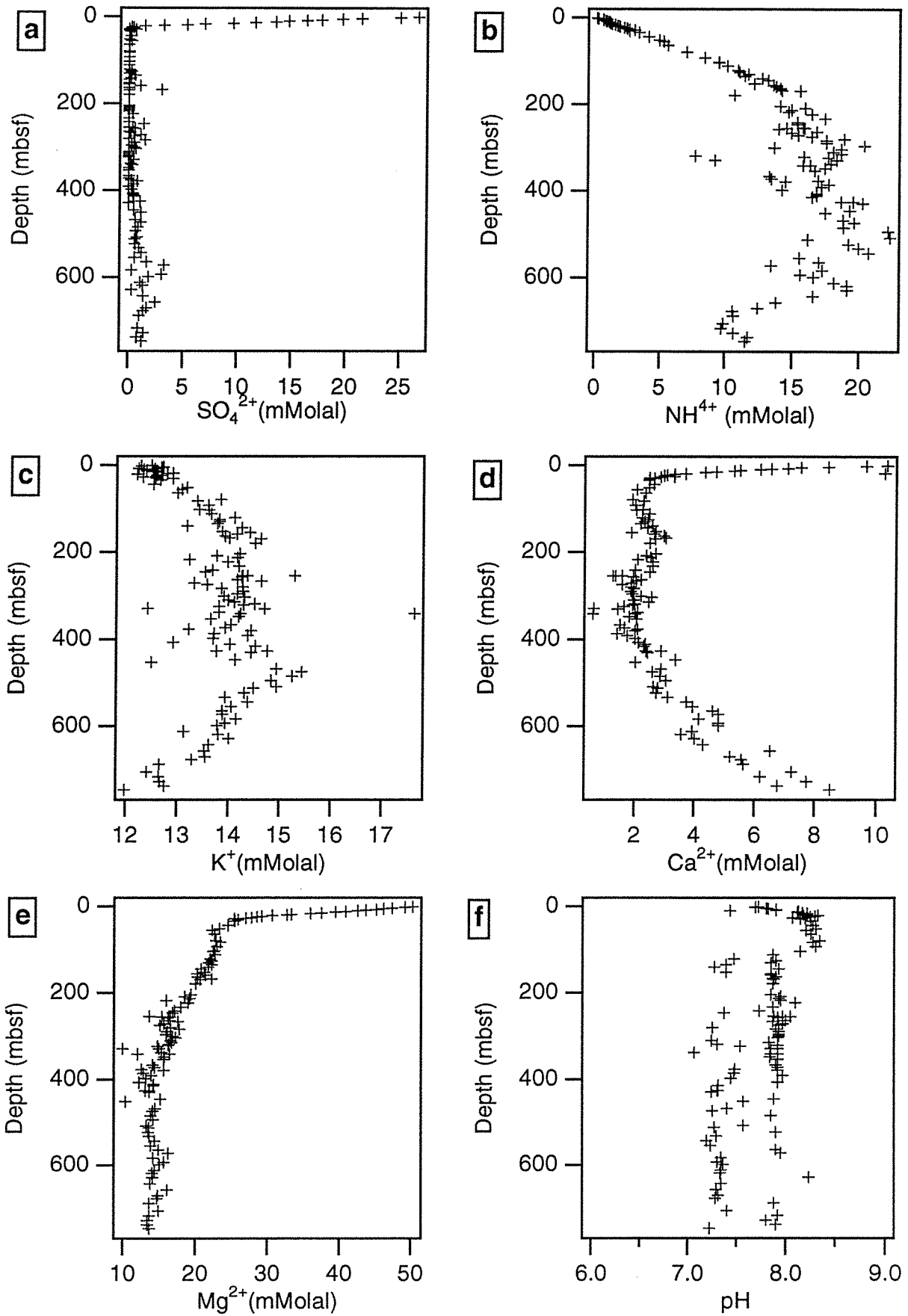


Figure 3

Figure 4



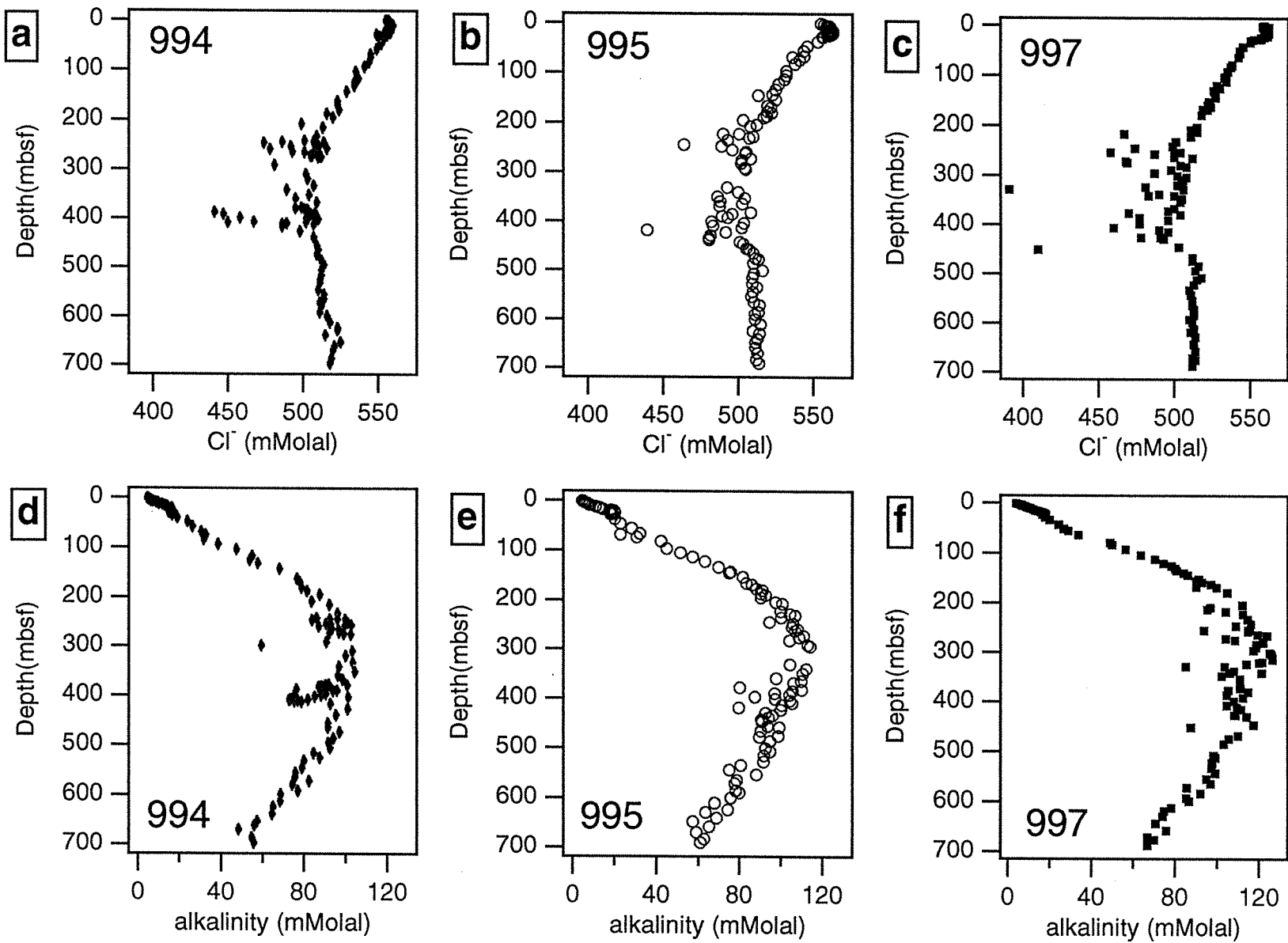


Figure 5

Figure 6

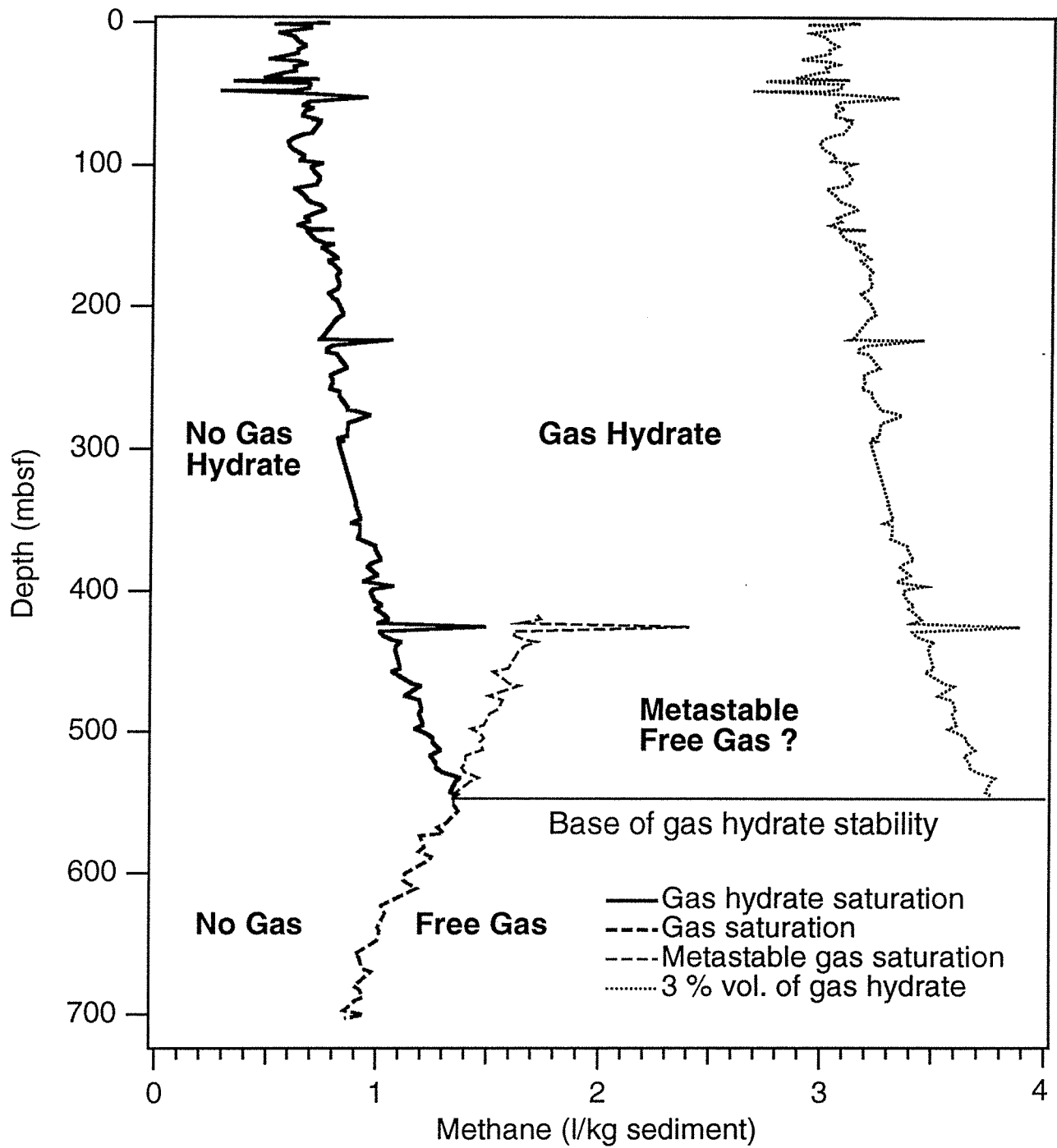
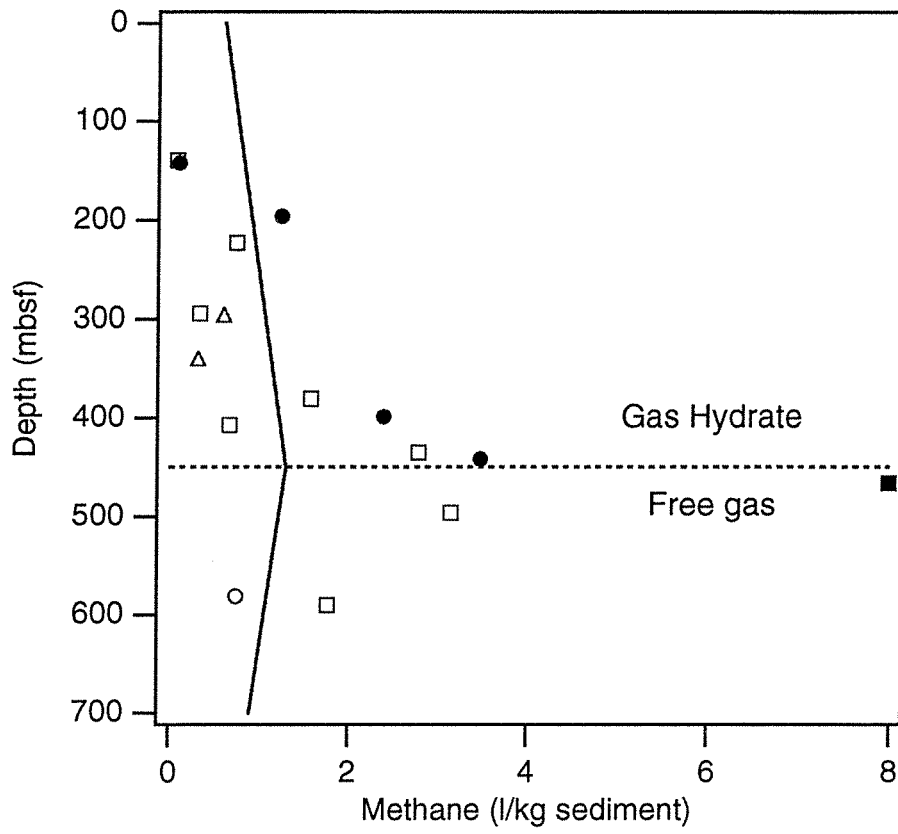


Figure 7



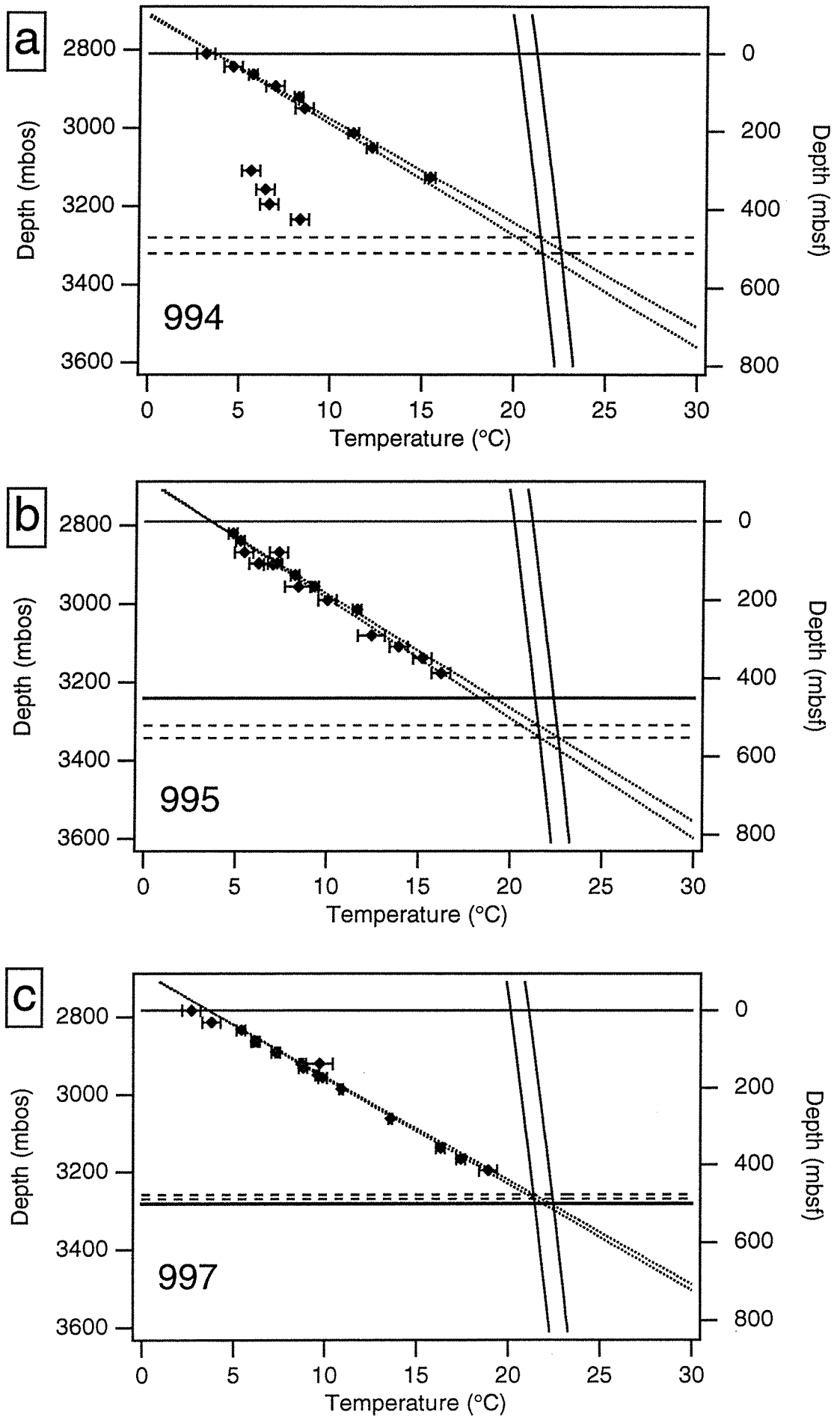


Figure 8

CONCLUSION

Conclusion

Ce mémoire a couvert trois aspects des équilibres de phases dans les systèmes eau-gaz-sels et de leur application à la géologie: les équilibres de phases dans le système $\text{CO}_2\text{-CH}_4\text{-N}_2$, les équilibres liquide-vapeur des systèmes eau-sels, et les équilibres de phases impliquant des hydrates de gaz dans les systèmes eau-gaz-sels.

Les équilibres de phases dans le système $\text{CO}_2\text{-CH}_4\text{-N}_2$ sont ceux qui paraissent être les plus simples à traiter. Tous les équilibres de phases (liquide-vapeur, liquide-liquide, solide-liquide-gaz, solide-liquide, solide-gaz) ont été calculés avec l'aide d'une simple équation cubique à deux paramètres (Soave, 1972). Un bon accord avec les données expérimentales en dehors du domaine critique est obtenue en utilisant un seul paramètre d'interaction pour chaque système binaire $\text{CO}_2\text{-CH}_4$, $\text{CH}_4\text{-N}_2$ et $\text{CO}_2\text{-N}_2$. Dans le domaine critique, les pressions calculées surestiment de manière significative les pressions expérimentales. Une amélioration du modèle a été proposée en utilisant des paramètres d'interactions binaires dépendant de la densité des phases liquide et vapeur en équilibre. Cette modification conduit à une amélioration sensible des prédictions dans le domaine critique, à la fois pour les systèmes binaires $\text{CO}_2\text{-N}_2$ et $\text{CO}_2\text{-CH}_4$, mais aussi sur le système ternaire $\text{CO}_2\text{-CH}_4\text{-N}_2$. Les propriétés v-x des fluides $\text{CO}_2\text{-CH}_4\text{-N}_2$ peuvent donc être maintenant déterminées en combinant ce modèle avec un modèle de calcul des densités des fluides.

La deuxième application concerne la prédiction des équilibres liquide-gaz des systèmes eau-sels. Le modèle de Lvov (LVOV et WOOD, 1990) assimilant le fluide à un mélange d'ions et de dipôles ion-dipôle, développé à partir de la "Mean Spherical Approximation", a été exploité. Ce modèle de mécanique statistique est basé sur des bases théoriques solides et rend compte des interactions majeures ion-ion, ion-dipôle et dipôle-dipôle existant dans les solutions électrolytiques. L'influence des paramètres physiques (moment dipolaire, diamètre des ions et des dipôles, valence et charge des ions) sur la topologie des diagrammes de phases a d'abord été étudiée et représentée sous la forme d'un

diagramme de phase global. Le modèle ion-dipôle a été ensuite appliqué aux équilibres liquide-vapeur dans le système $\text{H}_2\text{O-NaCl}$. Il est apparu très vite que le système $\text{H}_2\text{O-NaCl}$ ne peut être représenté uniquement par un fluide composé d'ions et de dipôles. A haute température ou dans les phases de faible densité, la formation des paires d'ions NaCl doit être prise en compte. Les constantes d'association ont été déterminées par ajustement sur les écarts de composition entre les prédictions du modèle ion-dipôle et les données expérimentales d'équilibre liquide-vapeur. Les constantes d'association obtenues varient en fonction de la température, densité et composition. Les variations des constantes d'associations à dilution infinie en fonction de la densité peuvent être reliées au nombre de molécules d'eau, qui sont libérées hors de la sphère d'hydratation des ions lors de la formation des paires d'ions. Les nombres d'hydratation estimés sont en bon accord avec les valeurs estimées par d'autres méthodes. A basse température (en dessous de 400°C), le modèle ion-dipôle doit être associé avec un terme de van der Waals afin d'obtenir un bon accord avec les données expérimentales. Une signification physique claire ne peut pas être attribuée ce terme de van der Waals. Cependant, la bonne qualité des prédictions, le nombre réduit des paramètres d'ajustement, la signification physique de la plupart des paramètres, toutes ces raisons militent en faveur du modèle ion-dipôle. Des améliorations peuvent être encore apportées, et il est pensable que le modèle ion-dipôle pourra servir de base de développement pour une équation d'état générale pour les équilibres liquide-vapeur dans les systèmes eau-sels et eau-gaz-sels.

La troisième application concerne les équilibres de phase à basse température (en dessous de 30°C) des systèmes eau-gaz-sels. Des hydrates de gaz peuvent alors se former. Ceci se produit dans les inclusions fluides lors des mesures microthermométriques à basse température. Un modèle de stabilité des hydrates de gaz, basé sur le cadre théorique de van der Waals et Platteuw (1959), a été établi et utilisé pour déterminer la salinité globale et la densité de la partie volatile à partir des mesures de la température de fusion de la glace et de la température de dissociation du clathrate en l'absence de phase carbonique dense. Les conditions de pression-température sont favorables aussi à la formation d'hydrates de

ont été collectées. Les analyses des fluides collectées (eaux interstitielles, gaz) révèlent clairement l'influence des hydrates de gaz sur la circulation des fluides. Des enrichissements de la fraction lourde des hydrocarbures sont observés en dessous des zones riches en hydrates de gaz. Ceci suggère que les couches riches en hydrates de gaz agissent au moins partiellement comme des barrières de perméabilité. Les hydrates de gaz modifient également la composition des fluides. Les sels sont exclus de la structure des hydrates de gaz, et le méthane est incorporé préférentiellement par rapport au dioxyde de carbone. Le Leg 164 confirme également que la distribution des hydrates de gaz est d'abord contrôlée par leur conditions de stabilité (pression, température et quantité de méthane). Ceci illustre l'importance de la modélisation thermodynamique pour la compréhension des processus géologiques.

Références.

LVOV S.N. and WOOD R.H. (1990) Equation of state of aqueous NaCl solutions over a wide range of temperatures, pressures and concentrations. *Fluid Phase Equilibria* **60**, 273-287

Soave, G (1972) Equilibrium constants from a modified Redlich-Kwong equation of state. *Chem. Eng. Sci.*, **27**, 1197-1203.

Van der Waals, J.H. and Platteuw, J.C. (1959) Clathrate solutions. In Prigogine, I. (ed.), *Advances in Chemical Physics*, Interscience, 1-57.

AUTORISATION DE SOUTENANCE DE THESE
DU DOCTORAT DE L'INSTITUT NATIONAL POLYTECHNIQUE
DE LORRAINE

o o o

VU LES RAPPORTS ETABLIS PAR :

Monsieur MONNIN, Labo de Géochimie, TOULOUSE,
Monsieur MONTEL, Ingénieur de recherche, PAU,
Monsieur YARDLEY, Professeur, Université Géologie Royaume-Uni.

Le Président de l'Institut National Polytechnique de Lorraine, autorise :

Monsieur THIERY Régis

à soutenir devant l'INSTITUT NATIONAL POLYTECHNIQUE DE LORRAINE,
une thèse intitulée :

"Les Systèmes eaux-gaz-sels. Modélisation des équilibres de phase et
application aux fluides géologiques".

en vue de l'obtention du titre de :


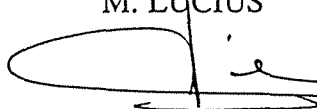
DOCTEUR DE L'INSTITUT NATIONAL POLYTECHNIQUE DE
LORRAINE

Spécialité : "GÉOSCIENCES"

Fait à Vandoeuvre le, 29 AOÛT 1996

Le Président de l'I.N.P.L.

M. LUCIUS



NANCY BRABOIS
2, AVENUE DE LA
FORET-DE-HAYE
BOITE POSTALE 3
F - 5 4 5 0 1
VANDŒUVRE CEDEX